SMIP18

SMIP18 SEMINAR ON
UTILIZATION OF STRONG-MOTION DATA

Sacramento, California
October 25, 2018

PROCEEDINGS

Sponsored by

California Strong Motion Instrumentation Program
California Geological Survey
California Department of Conservation

Co-Sponsors

California Seismic Safety Commission
California Governor's Office of Emergency Services
Office of Statewide Health Planning and Development
California Department of Transportation

California
Department of
Conservation
California Geological Survey

The California Strong Motion Instrumentation Program (CSMIP), a program within the California Geological Survey (CGS) of the California Department of Conservation, records the strong shaking of the ground and structures during earthquakes for analysis and utilization by the engineering and seismology communities, through a statewide network of strong motion instruments (www.conservation.ca.gov/CGS/smip). CSMIP is advised by the Strong Motion Instrumentation Advisory Committee (SMIAC), a committee of the California Seismic Safety Commission. Major program funding is provided by an assessment on construction costs for building permits issued by cities and counties in California, with additional funding from the California Governor's Office of Emergency Services (Cal OES), the Office of Statewide Health Planning and Development (OSHPD) and the California Department of Transportation (Caltrans)

In July 2001, the California Governor's Office of Emergency Services (Cal OES) began funding for the California Integrated Seismic Network (CISN), a newly formed consortium of institutions engaged in statewide earthquake monitoring that grew out of TriNet, funded by FEMA, and including CGS, USGS, Caltech and UC Berkeley. The goals are to record and rapidly communicate ground shaking information in California, and to analyze the data for the improvement of seismic codes and standards (www.cisn.org). CISN produces ShakeMaps of ground shaking, based on shaking recorded by stations in the network, within minutes following an earthquake. The ShakeMap identifies areas of greatest ground shaking for use by OES and other emergency response agencies in the event of a damaging earthquake.

The Center for Engineering Strong Motion Data (CESMD) is operated by the CSMIP in cooperation with the National Strong-Motion Project (NSMP), a part of the Advanced National Seismic System (ANSS) of the U.S. Geological Survey (USGS). The CESMD builds on and incorporates the CISN Engineering Data Center and will continue to serve the California region while expanding to serve other ANSS regions. The Data Center provides strong-motion data rapidly after a significant earthquake in the United States. Users also have direct access to data from previous earthquakes and detailed information about the instrumented structures and sites. The CESMD also provides access to the U.S. and international strong ground motion records through its Virtual Data Center (VDC). The Data Center is co-hosted by CGS and USGS at www.strongmotioncenter.org

DISCLAIMER

SMIP18

SMIP18 SEMINAR ON
UTILIZATION OF STRONG-MOTION DATA

Sacramento, California
October 25, 2018

PROCEEDINGS

Edited by

Daniel Swensen

Sponsored by

California Strong Motion Instrumentation Program
California Geological Survey
California Department of Conservation

Co-Sponsors

California Seismic Safety Commission
California Governor's Emergency Services
Office of Statewide Health Planning and Development
California Department of Transportation

PREFACE

The California Strong Motion Instrumentation Program (CSMIP) in the California Geological Survey of the California Department of Conservation established a Data Interpretation Project in 1989. Each year CSMIP funds several data interpretation contracts for the analysis and utilization of strong-motion data. The primary objectives of the Data Interpretation Project are to further the understanding of strong ground shaking and the response of structures, and to increase the utilization of strong-motion data in improving post-earthquake response, seismic code provisions and design practices.

As part of the Data Interpretation Project, CSMIP holds annual seminars to transfer recent research findings on strong-motion data to practicing seismic design professionals, earth scientists and post-earthquake response personnel. The purpose of the annual seminar is to provide information that will be useful immediately in seismic design practice and post-earthquake response, and in the longer term, useful in the improvement of seismic design codes and practices. Proceedings and individual papers for each of the previous annual seminars are available at http://www.conservation.ca.gov/cgs/smip/seminar in PDF format. Due to the State budget restraints, CSMIP did not hold an annual seminar in 2010 or 2011. The SMIP18 Seminar is the twenty-seventh in this series of annual seminars.

The SMIP18 Seminar is divided into two sessions in the morning and two sessions in the afternoon. There are seven presentations on the results from CSMIP-funded projects and one presentation by CSMIP. The sessions in the morning include four presentations. The first session will focus on ground motions. Professor Archuleta of UC Santa Barbara will present on strong ground motions from earthquakes with multiple faults. It will be followed by a presentation by Professor Stewart of UCLA on reconsidering basin effects in ergodic site response models. The second session will focus on results from building response data: building code accidental torsion provisions for buildings with symmetric plans by Professor Zareian of UC Irvine and building soil-structure interaction mechanisms by Professor Asimaki of Caltech.

The third session in the afternoon will focus on lifeline structures. Professor Armstrong of CSU Sacramento will present on earthquake-induced earth dam deformations. Professor Elgamal of UC San Diego will present on the seismic response of bridge-ground systems. The last session will include presentations on building damage detection using cumulative absolute velocity by Professor Mosalam of UC Berkeley, and the instrumentation of two new super tall buildings in California by Dr. Huang of CSMIP. Individual papers and the proceedings are available for the SMIP18 participants in a USB flash drive, and will be available at the CSMIP website.

Daniel Swensen
CSMIP Data Interpretation Project Manager

Appreciation to Members of the Strong Motion Instrumentation Advisory Committee

Main Committee

Farzad Naeim, Chair, Farzad Naeim, Inc.
Norman Abrahamson, Pacific Gas & Electric Company
Bruce Clark, Leighton & Associates
Martin Eskijian, California State Lands Commission (retired)
David Gutierrez, GEI Consultants
Wilfred Iwan, California Institute of Technology
Mark Mahan, Caltrans
Marshall Lew, Wood
Bret Lizundia, Rutherford + Chekene
Chris Tokas, Office of Statewide Health Planning and Development
Robert Anderson (ex-officio), Seismic Safety Commission

Ground Response Subcommittee

Marshall Lew, Chair, Wood
Abbas Abghari, Caltrans
John Egan, SAGE Engineers
Geoffrey Martin, Univ. of Southern California

Buildings Subcommittee

Bret Lizundia, Chair, Rutherford + Chekene
Lucie Fougner, Degenkolb Engineers
Ifa Kashefi, City of Los Angeles
Jimmy Cheung, City of San Francisco
Eduardo Miranda, Stanford University
Roy Lobo, Office of Statewide Health Planning and Development
Chia-Ming Uang, UC San Diego

Lifelines Subcommittee

Martin Eskijian, Chair, California State Lands Commission (retired)
Craig Davis, Los Angeles Dept. of Water and Power
David Gutierrez, GEI Consultants
Mark Mahan, Caltrans
Faiz Makdisi, SAGE Engineers

Data Utilization Subcommittee

Wilfred Iwan, Chair, California Institute of Technology
Representatives from each Subcommittee

TABLE OF CONTENTS

SMIP18 SEMINAR ON UTILIZATION OF STRONG-MOTION DATA

October 25, 2018

California State Lottery Headquarters
700 N. 10th Street, Sacramento, California

PROGRAM

8:15 am **REGISTRATION**

9:15 am **WELCOMING REMARKS**
Farzad Naeim, Chair, Strong Motion Instrumentation Advisory Committee (SMIAC)
David Bunn, Director, Department of Conservation
Bill Short, Acting State Geologist, California Geological Survey

9:25 am **RECOGNITION of Dr. Tony Shakal for his 35 Years of Service as the Manager of California Strong Motion Instrumentation Program**

9:30 am **INTRODUCTION**
Moh Huang, Acting Manager, California Strong Motion Instrumentation Program
Dan Swensen, California Strong Motion Instrumentation Program

Session I

Moderator: *Marshall Lew*, Wood and SMIAC

9:35 am **Strong Ground Motion from Earthquakes with Multiple Faults**
Ralph Archuleta, Chen Ji and Mareike Adams, UC Santa Barbara

10:05 am **Reconsidering Basin Effects in Ergodic Site Response Models**
Chukwuebuka Nweke, Pengfei Wang, Scott Brandenberg and *Jonathan Stewart*, UC Los Angeles

10:35 am Break

Session II

Moderator: *Chris Tokas*, OSHPD and SMIAC

11:00 am **Critical Assessment of Accidental Torsion in Buildings with Symmetric Plans using CSMIP Data**
Yijun Xiang, Farzad Naeim and *Farzin Zareian*, UC Irvine

11:30 am **System Identification of Soil-Structure Interaction Mechanisms for Building Structures**
D. Kusanovic, E. Esmaeilzadeh Seylabi and *Domniki Asimaki*, Caltech

12:00 pm **Lunch**
Lunch will be provided

Session III

Moderator: *Martin Eskijian*, California State Lands Commission and SMIAC

1:00 pm **Efficiency of Ground Motion Intensity Measures with Earthquake-Induced Earth Dam Deformations**
Richard Armstrong, Tadahiro Kishida and DongSoon Park, CSU Sacramento

1:30 pm **System Identification of Bridge-Ground Systems from Recorded Seismic Response**
Ahmed Elgamal, Ning Wang and John Li, UC San Diego

2:00 pm Break

Session IV

Moderator: Roy Lobo, OSHPD and SMIAC

2:25 pm **Localized Damage Detection of CSMIP Instrumented Buildings using Cumulative Absolute Velocity: A Machine Learning Approach**
Sifat Muin and *Khalid Mosalam*, UC Berkeley

2:55 pm **Strong-Motion Instrumentation of Two New Super Tall Buildings in California and Results from Ambient and Earthquake Response Data**
Moh Huang, Dan Swensen, Hamid Haddadi and Troy Reitz, CGS/CSMIP

3:25 pm **Adjourn**

STRONG GROUND MOTION FROM EARTHQUAKES WITH MULTIPLE FAULTS

Ralph J. Archuleta, Chen Ji and Mareike N. Adams

Department of Earth Science and the Earth Research Institute
University of California, Santa Barbara

Abstract

The 2016 M_W 7.8 Kaikoura earthquake in New Zealand may have involved co-seismic slip on more than 10 distinct faults. We attempt to assess the sequence of rupture on the segments as well as the contribution of the different segments to the recorded ground motion in New Zealand. First, we approximate the segments as points sources to determine the temporal sequence of faulting and to determine the relative contribution to the seismic moment. We reduce the overall number of segments to 10 crustal faults. We invert strong motion, geodetic and teleseismic body and surface wave data to provide a spatio-temporal map of slip and rupture time.

Introduction

Large earthquakes often involve slip on more than one fault. Four notable examples are 1) the 1992 M_W 7.3 Landers, California, earthquake with slip on five different faults; 2) the 2012 M_W 8.6 Indian Ocean earthquake with slip on four faults—three of which are perpendicular to the primary fault; 3) the 2010 M_W 7.1 Darfield, New Zealand, earthquake, with slip on as many as eight segments and 4) the 2010 M_W 7.2 El Mayor–Cucapah, Mexico, earthquake comprised of seven faults. The latest hazard assessment for California (Figure 1) includes ruptures that involve

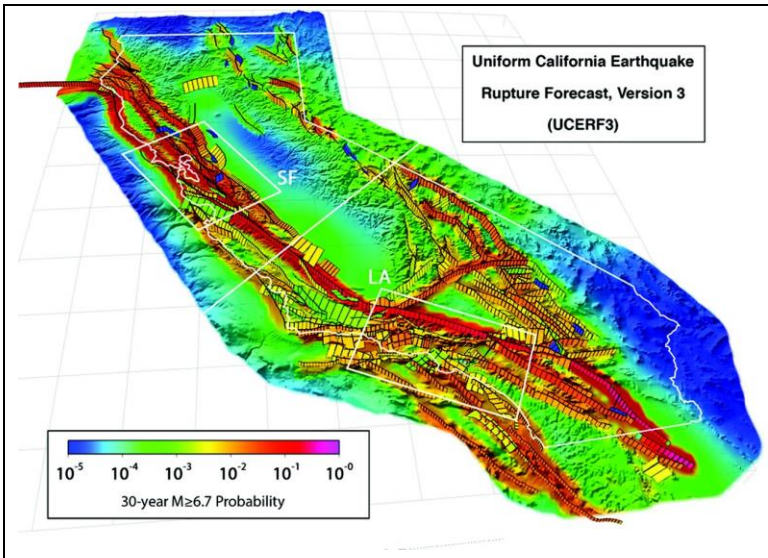

Figure 1. "Three-dimensional perspective view of the third Uniform California Earthquake Rupture Forecast (UCERF3). The small black rectangular elements represent the 2606 fault subsections used in the forecast (for one of the two fault models, FM3.1) … Colors depict the mean participation probability, the likelihood that each point will experience one or more $M \geq 6.7$ earthquakes in the 30 years following 2014 ... The white boxes define the San Francisco (SF) Bay and Los Angeles (LA) regions, respectively, and the white line crossing the state is our definition of northern versus southern California. ..." From Field et al. (2015).

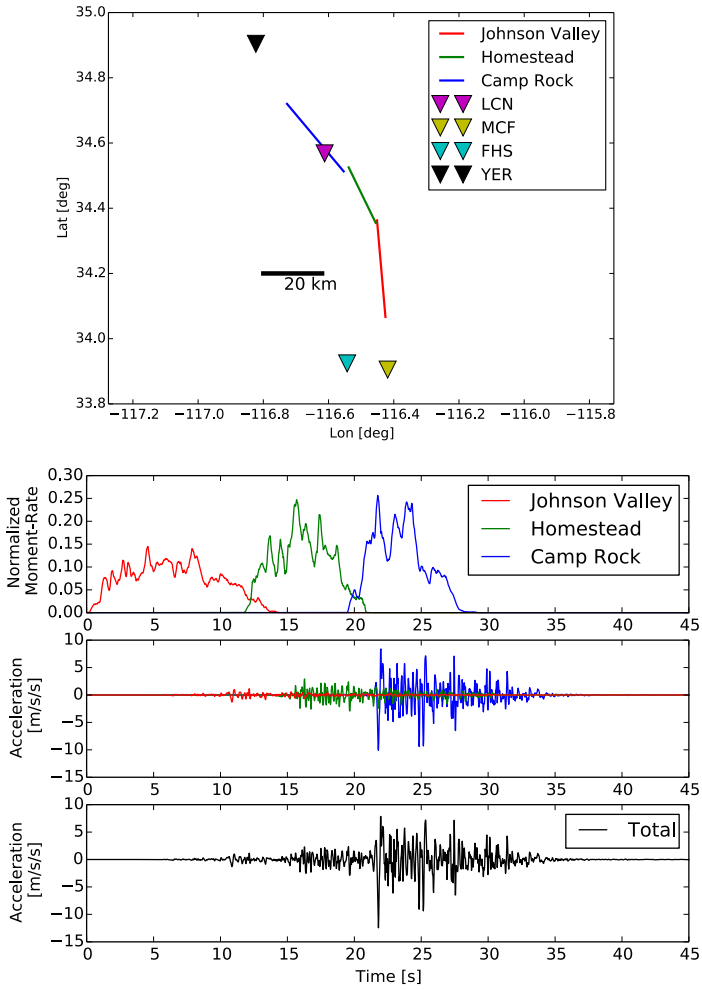

Figure 2. Simulation of Landers ground motion at the Lucerne Valley station (LCN), 0.5 km off the Camp Rock Fault. Contributions from three fault segments: Johnson Valley, Homestead and Camp Rock are shown. Each segment has approximately the same seismic moment, i.e., magnitude. Faulting on the Camp Rock segment dominates the ground motion.

multiple faults (Field et al., 2015). If these earthquakes are looked at from great distances (1000's of kilometers), i.e., treated as point sources, there are standard methods for assigning a seismic moment/magnitude. However, when considering the near source ground motion where the largest amplitudes generally occur, there is a fundamental question that needs to be examined. Should near source ground motion be assigned to the magnitude of the closest segment or the magnitude of the entire complex rupture?

As an example, Crempien and Archuleta (2016) computed ground motion based on a kinematic rupture simulation that uses heterogeneous faulting on three segments representing the M 7.3 Landers earthquake in 1992 (Figure 2). The three fault segments are the Johnson Valley fault (on which the rupture starts)—the southern-most segment, the Homestead Fault segment in the middle, and the Camp Rock Fault on which the rupture terminates. The station closest to the overall rupture is Lucerne Valley which is next to the Camp Rock segment. It also had the largest recorded peak ground acceleration (PGA) and peak ground velocity (PGV). The peak ground acceleration is clearly dominated by rupture on the Camp Rock Fault, which has one-third of the total moment—a magnitude of 7.0 compared to 7.3 for the entire earthquake.

2016 Kaikoura Earthquake

The complexity of faulting during the 2016 Kaikouora earthquake is illustrated in Figure 3 (taken from Hamling et al., 2017). At least 10 faults in the Marlborough Fault System (MFS) were activated in this earthquake. Hamling et al. (2017) further modeled it using 19 rectangular

fault segments, with the possibility of a 20th with slip on the Hikurangi subduction zone interface (HSZI) (Figure 3). Whether or not slip occurred on the HSZI that underlies the MFS is an open question (Hamling et al., 2017). Clark et al. (2017) improved on the fit to geodetic data of Hamling et al. (2017) by allowing slip on the Point Kean fault, a crustal thrust fault with coseismic outcrop offshore. In allowing slip on the Point Kean fault they found that the inverted

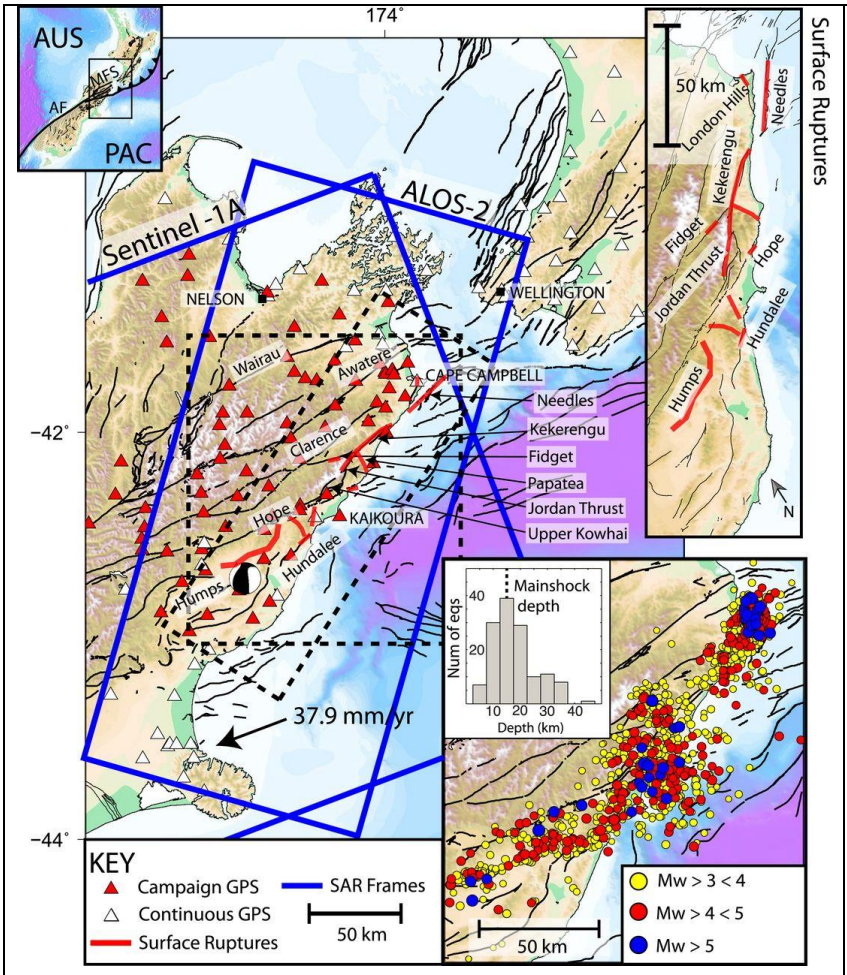

Figure 3. "The main panel shows the location of the continuous (white triangles) and campaign (red triangles) GPS site. … Labels in all capital letters show the towns and cities of Kaikōura, Wellington, and Nelson, as well as the Cape Campbell region. The dashed black boxes indicate the regions shown by the two panels inset at right. The vector shows the relative plate motion between the Pacific (PAC) and Australian plates (AUS), as indicted in the top left inset. AF, Alpine fault. The beach ball icon denotes the W-phase moment tensor generated by the U.S. Geological Survey (USGS) at the epicentral location. Bottom right inset: Distribution of relocated aftershocks with $M_w > 3$ occurring in the first 2 weeks after the mainshock. Earthquakes are color coded by moment magnitude. The histogram shows the depth distribution of M_w4.5 and above. Top right inset: Map showing

slip on HSZI decreased. Both studies ignored the contribution of Papatea fault, which produced over 6 meters of uplift, and was interpreted as non-elastic deformation. The contribution of Papatea fault was included in the models of two recent papers (Xu et al., 2018; Wang et al., 2018). Xu et al. (2018) constructed three models with different geometries, using only geodetic observations. Fault slip in their Model I was limited to crustal faults but did not include the Point Kean fault. Model II further included the contribution of HSZI; while Model III included the contribution of Point Kean fault but did not include the HSZI. Xu et al. (2018) indicated that because every model can explain the geodetic observations well, whether slip occurred on the HSZI cannot be answered by the geodetic data alone, as concluded by Hamling et al. (2017) and Clark et al. (2017). In contrast, Wang et al. (2018) did a joint inversion with geodetic

measurements, strong motion and teleseismic body waves. They argued that the rupture of HSZI is required by the seismic data. Their preferred model has about 45% of total seismic moment on the HSZI. It is important to note that Wang et al. (2018) did not include any contribution from the Point Kean fault. A good review of other researchers who have explored the multi-fault Kaikoura earthquake can be found in Chapter 4 of Adams (2018).

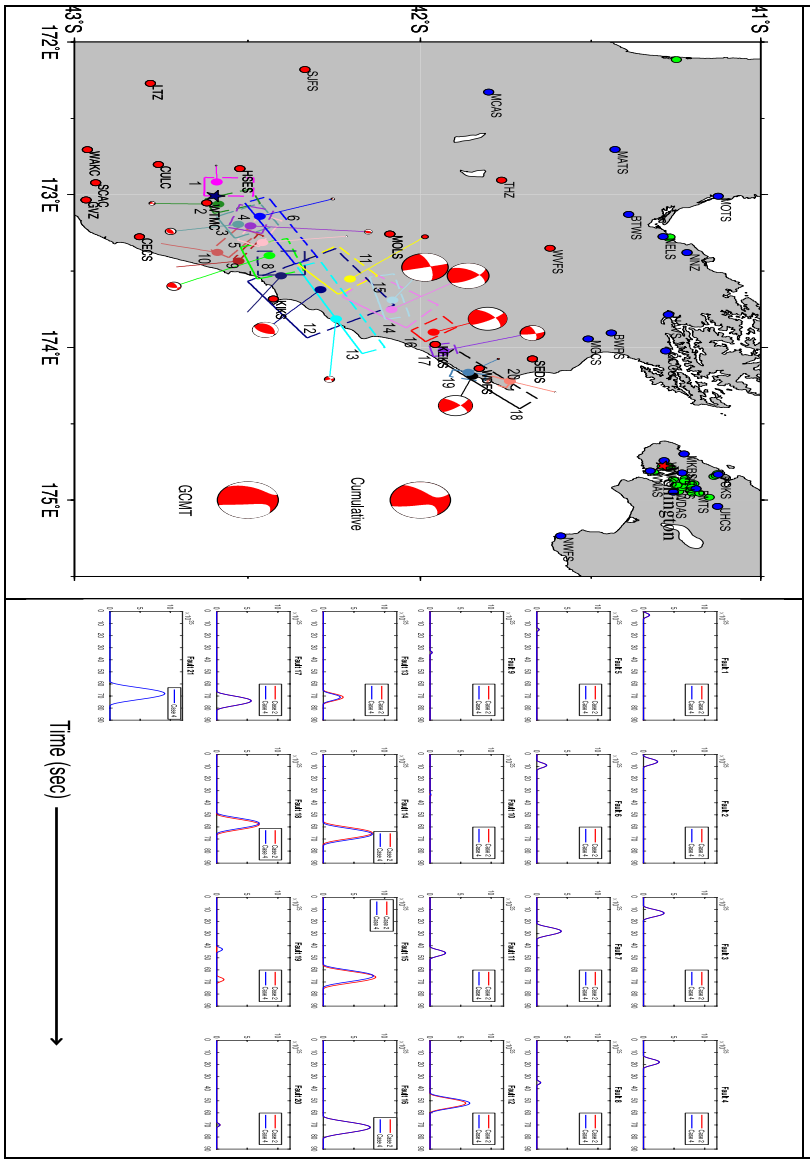

Figure 4. In the upper figure twenty crustal fault segments are shown as rectangles. Solid line indicates upper extent of the fault, from which one can infer the strike and dip. Epicenter is black star. Strong motion stations are red disks with 4-letter labels. Focal mechanisms are the red/white balls with the size proportional to the seismic moment. Focal mechanisms indicate both thrust and strike-slip faulting. The cumulative moment tensor is similar to that of the global CMT, which is a single point source representation of faulting. The lower figure shows the moment rate as a function of time for each fault segment (1-21) with origin time at 0. Fault segments 12, 14, 15, 16, 17, and 18 contribute the largest seismic moment in the time window 45-80 seconds after origin time.

Because so many faults are involved, our first effort is to determine the timing among the faults and the relative seismic moment contribution of each segment, assuming the slip distributions inferred from geodetic observations are correct. We use the slip model of Clark et al. (2017), which includes 21 fault segments. The 21th fault segment is the plate interface. We treat every fault segment as one subevent and model it as a double-couple point source. We fix the point source locations as the centroid locations inferred from the fault slip on the corresponding fault segments, and constrain both centroid time and seismic moment of every

point source using the close-fault strong motion records with the multiple double-couple (MDC) inversion approach (Li et al., 2011; Shao et al., 2011). The slip rate function of each point source is modeled as symmetric cosine function (Ji et al., 2002) with a half duration calculated using the empirical scaling relationship between seismic moment and half duration ($T_h = 2.24 \times 10^{-6} \times M_0^{1/3}$, Ekström et al., 2005).

Table 1: Strong Motion Stations with maximum values of PGA and PGV

STA	Lat.	Long.	H1 (cm/s/s)	H2 (cm/s/s)	HR (cm/s/s)	HT (cm/s/s)	CESMD (cm/s)	Rrup (km)
CECS	-42.813	173.275	123.12	213.12	284.96	276.80	31.7	27.7
CULC	-42.759	172.803	246.75	336.75	241.90	242.07	33.2	15.6
GVZ	-42.967	173.035	177.71	267.71	112.60	146.64	12.0	37.8
HSES	-42.523	172.83	320.02	50.02	268.69	258.52	29.9	11.8
KEKS	-41.956	173.981	43.85	133.85	1337.88	382.30	79.8	3.0
KIKS	-42.426	173.682	61.43	151.43	200.09	252.09	44.5	0.7
LTZ	-42.782	172.271	260.79	350.79	84.25	67.48	6.0	52.8
MOLS	-42.088	173.257	16.19	106.19	294.90	445.84	14.1	29.5
SCAC	-42.939	172.922	196.19	286.19	268.50	210.43	26.5	34.5
SEDS	-41.672	174.076	37.3	127.3	571.16	746.22	52.8	22.7
SJFS	-42.335	172.18	300.02	30.02	42.71	58.35	7.6	65.1
THZ	-41.762	172.905	354.78	84.78	48.27	38.36	7.2	72.7
WAKC	-42.963	172.705	220.45	310.45	146.63	141.34	17.3	39.8
WDFS	-41.827	174.138	43.53	133.53	769.16	1175.55	83.2	8.5
WTMC	-42.619	173.054	19.45	109.45	943.14	995.19	101.7	0.7
WVFS	-41.620	173.351	12.85	102.85	147.70	149.02	25.9	55.5

All values in the table are taken from the unprocessed records. H1 and H2 are the original horizontal orientations, which vary from station to station. HR and HT are the radial and transverse orientations as measured from the epicenter. The maximum ground velocity is from the processed records at the Center for Engineering Strong Motion Data (CESMD). Rrup is closest distance to the fault from CESMD.

We select three components of ground motion velocity at 16 close-fault strong motion stations (Table 1) and bandpass filter the signals to periods between 10 s and 90 s. Note that half of the strong motion stations are in the southern end of the rupture where slip on the faults is generally small relative to slip on faults northeast of the hypocenter (Figure 4). In Figure 4, we show the results of two cases. In Case 2 we only investigate the crustal faults, i.e., the point source associated with the 21th fault segment is ignored. In case 4, all fault segments are considered. This study provides a temporal sequence of when the different fault segments contributed to the overall rupture and the relative contribution to the overall seismic moment (Figure 4). For example, the MDC result suggests that strong motion stations south of the hypocenter were mostly affected by the early part (Faults 1-9) of the Kaikoura earthquake, which

was effectively a M_W 7.27 earthquake. The rupture generally unilaterally propagated to the northeast and the rupture of the plate interface occurred from 60 s to 80 s.

To invert for spatio-temporal kinematic parameters we consolidated the 20 crustal fault segments to 10 (Table 2). We further divided them into 3.5 km by 4 km subfaults and simultaneously invert slip, rake angle, rupture initiation time, and the shape of analytic slip rate function of each subfault, using both seismic and geodetic observations. Our seismic data is composed of: i) three components of ground motion velocity at the same 16 stations (Table 1). The velocity time histories are 125 seconds in length and bandlimited to periods between 50 s and 2 s (Figure 5). Note that the horizontal motion has been rotated to radial (R) and transverse (T) components relative to the Kaikuara epicenter; ii) displacement waveforms at 6 high-rate GPS stations (sampling rate 10Hz). A lowpassed filter with a corner of 1.0 Hz has been applied (Figure 6); iii) teleseismic broadband P and SH recordings at 26 stations (Figure 7); iv) long-period (4-6mHz) whole waveforms in vertical and transverse components of 33 stations (Figure 8). The geodetic data include static offsets from 20 continuous GPS sites and 64 campaign sites (Hamling et al., 2017).

Table 2. Fault Description

Fault ID	Fault Name Wang et al. (2008)	Length (km)	Width (km)	Strike^o/ dip^o/rake^{o*}	M_0 (Nm)	Mw	Ave. Slip* (m)	Ave. Rise time* (s)	Ave. Slip rate* (m/s)	Ave. Stress* (MPa)
1	Humps-west	21	20	77/65/(-8)	$5.6x10^{18}$	6.5	1.2	5.1	0.4	3.3
2	Humps-east	21	20	255/70/(166)	$7.7x10^{19}$	7.2	4.9	5.0	1.2	8.0
3	Leader	21	24	195/50/(78)	$2.8x10^{19}$	6.9	3.1	4.4	0.8	7.6
4	Hundalee-west	28	32	230/45/(85)	$8.0x10^{19}$	7.2	3.8	4.0	1.1	4.8
5	Whites	24.5	32	172/45/(86)	$3.3x10^{19}$	7.0	1.9	2.9	0.8	5.5
6	Point Kean	28	40	243/35/(126)	$2.3x10^{19}$	7.5	5.0	4.8	1.6	9.5
7	Papatea	21	32	172/50/(61)	$1.1x10^{20}$	7.3	7.8	6.0	1.4	10.7
8	Jordan_ Kekerengu	59.5	32	223/50/(170)	$2.5x10^{20}$	7.6	7.5	4.9	1.9	10.0
9	Kekerengu	21	32	242/50/(161)	$1.5x10^{20}$	7.4	8.7	6.6	1.8	15.6
10	Needles	35	32	222/50/(162)	$1.1x10^{20}$	7.3	5.4	5.0	1.3	12.4

* rake angle, slip, rise time, slip, stress drop are average values weighted by fault slip (Ji et al., 2002). The slip rate at individual subfault is simply defined as ratio of fault slip and rise time. Note that the average slip rate is larger than the ratio of average fault slip and average rise time. The stress drop is in the direction of average rake angle.

As shown in Figures 5-8, synthetic seismograms predicted with our preliminary model generally match data well. The fit to the strong motion and high rate GPS data is good for both amplitude and duration though there are some noticeable exceptions such as the peak amplitude of the transverse (T) component of KEKS and WTMC (Figure 5), and the polarity discrepancy at vertical component (Z) of station MRBL (Figure 6). The fit to the teleseismic P and SH waves and the long-period surface waves is better.

The slip distribution of the preliminary model is shown in Figure 9. We also illustrate the contribution of each fault segment and its individual moment rate function in Figure 10. All of the moment rate functions are scaled to the same maximum in order to show the relative

contribution from the 10 faults. Zero time is the origin time for the earthquake. The cumulative moment rate function is shown in Figure 11. The fault parameters of our preliminary slip model are summarized in Table 2. Initial rupture on the Humps-west fault is equivalent to M_W 6.5 (Table 2). In Figure 12 the sequence of slip is shown as a series of snapshots of the slip

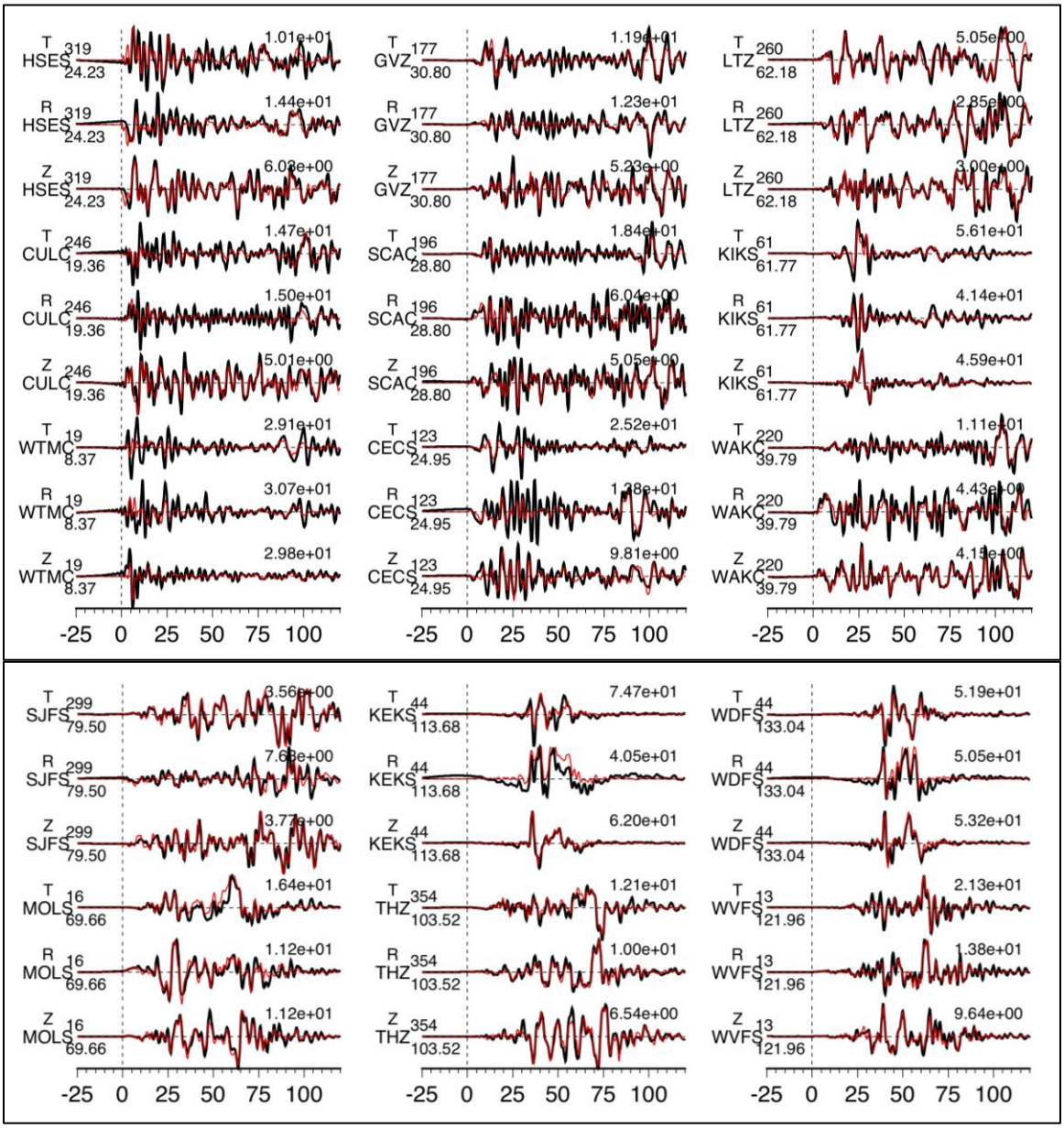

Figure 5. Comparison of 16 three-component velocity waveforms (black) and synthetic seismograms (red). Station names are left of the traces along with the epicentral distance (km) and azimuth relative to the epicenter. Peak amplitude (cm/s) of the observation is on the right side of the trace.

accumulated in 10 s intervals. One of the most interesting features is the jump to the northern part of the Kekerengu fault around 50-60 seconds. The rupture then proceeds southwest on the Kekerengu fault and then moves northeast after about 10 seconds. It reveals that 2016 Kaikuara earthquake has a complex rupture process.

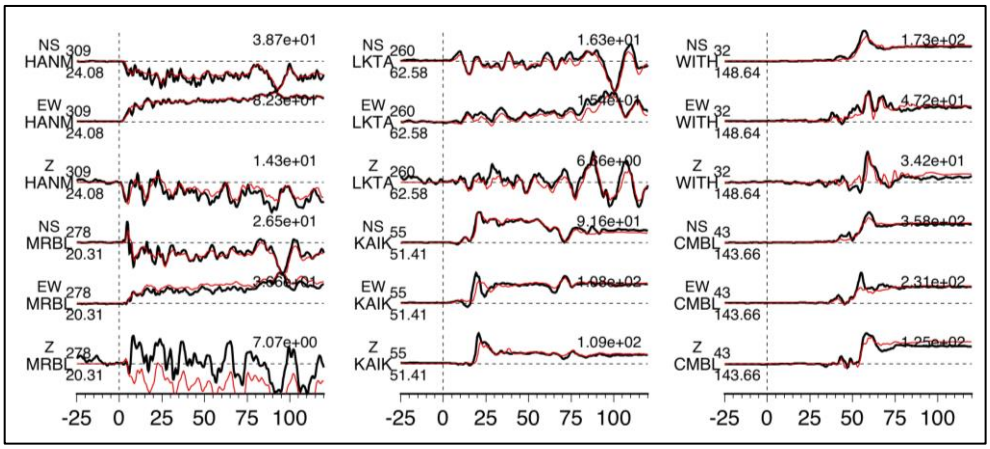

Figure 6. Comparison of synthetics (red) with data (black) of continuous, high-rate GPS low-passed filtered with a 1.0 s corner. Units are cm, shown on the right of each trace. On the left is the station code, component, azimuth and distance (km) from epicenter. The station MRBC is close to the end of the Humps fault which we approximated as a straight fault but may be curved. All other fits are good including the static offset.

***Rupture Process**:*

1. Although we let rupture initiate at south dipping Humps-west fault, most inverted fault slip occurred on north-dipping Humps-east fault as right-lateral strike slip in the first 25 s and unilaterally propagated to the northeast. The rupture on this segment ended with a transpressional motion on the west-dipping Leaders fault. The rupture of the Humps-Leaders fault system is associated with relatively high stress drop of 7.6-8.0 MPa as compared with global average 3-4 MPa (Kanamori and Anderson, 1975; Allmann and Shearer, 2009).

2. About 12 s after the event started, rupture on the Hundalee fault initiated. The rupture of this fault segment is nearly pure thrust with an average rake angle of 85º. The rupture of this fault segment reached its peak moment rate around 25-30 s and ceased sharply at 35 s. The cumulative seismic moment is 8.0×10^{19} Nm (M_W 7.3). Rupture on Whites fault initiated at about 25 s and continued about 40 s— again with a pure thrust focal mechanism. Though the cumulative seismic moment is still significant (3.3×10^{19} Nm, M_W 7.0), this rupture duration is much longer than a typical rupture of this magnitude (~14 s). The stress drop on these two segments is around 5 MPa.

3. Rupture of Point Kean fault initiated at 25 s on the shallow portion of the fault plane with an oblique focal mechanism (average rake angle of 126º). The total rupture duration is about 50 s and the cumulative seismic moment is 2.3×10^{20} Nm (M_W 7.5). Note that from 60 to 80 s, the rupture is limited to subfaults with depth >20 km. The cumulative seismic moment during this period is 1.2×10^{20} Nm (M_W 7.4).

4. The rupture of Jordan thrust- Kekerengu-Needles fault, which we modeled using three fault segments, might start as earlier as 25 s from its southwest end. However, the major asperity extending from roughly 70 km to 150 km northeast of the Kaikuara epicenter failed first in the middle on the shallow portion of Kekerengu fault, near the strong motion station KEKS,

at 53 s. This subevent sharply ceases at 62 s. The cumulative seismic moment during this period is 1.7×10^{19} Nm (M_W 6.8), consistent with previous result of Holden et al. (2017). The southwest edge of this asperity rupture initiated at about 60 s and gradually propagated to the northeast. About half of the total seismic moment occurred on these three fault segments.

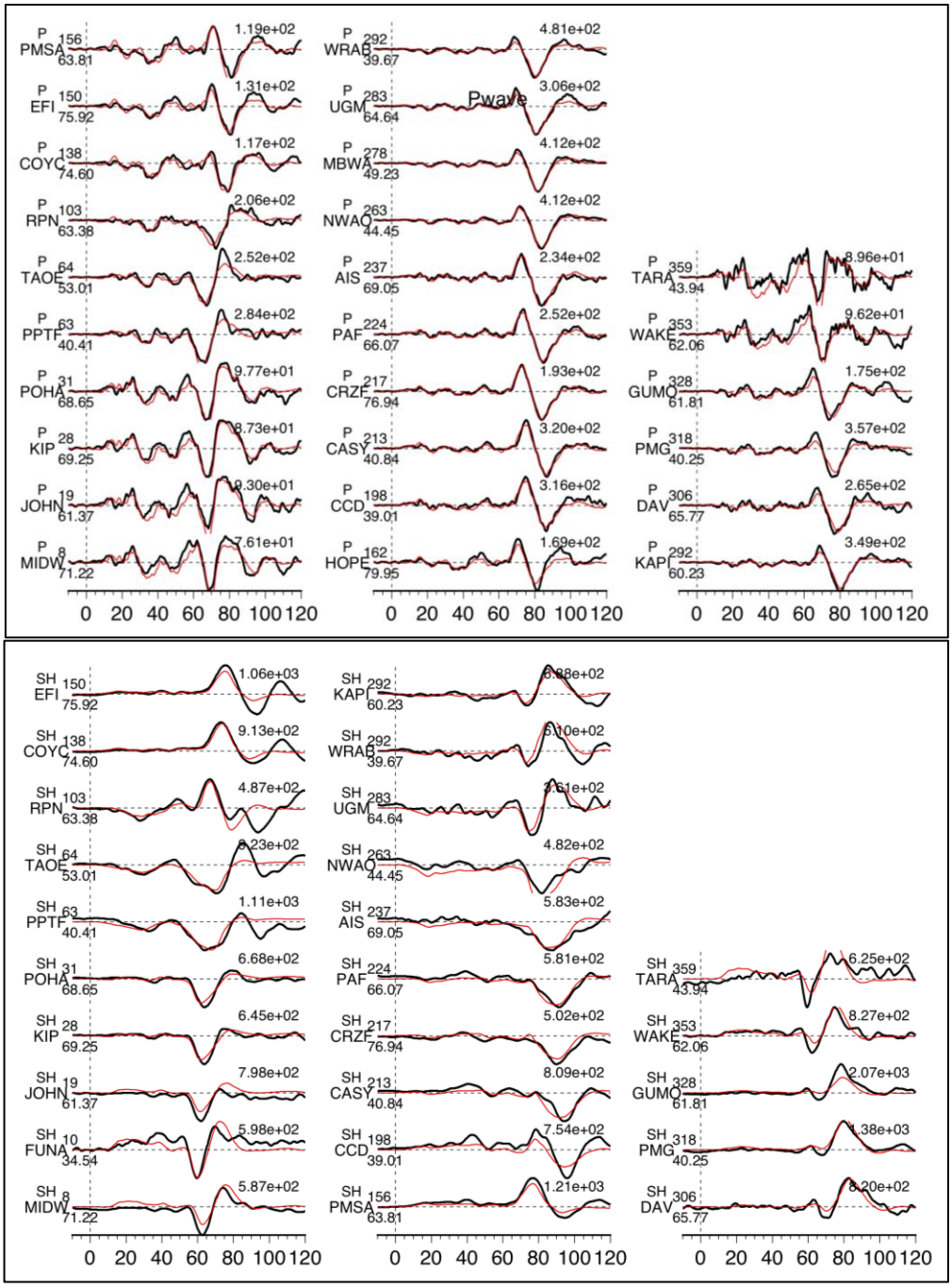

Figure 7. Displacement of P and SH waves vs time (s). Data in black and synthetics in red. Left of each trace is the station code. Upper number is the azimuth relative to the epicenter and lower number is the angular distance in degrees. On the right is the maximum amplitude (units are 10^{-6}m) of the observation.

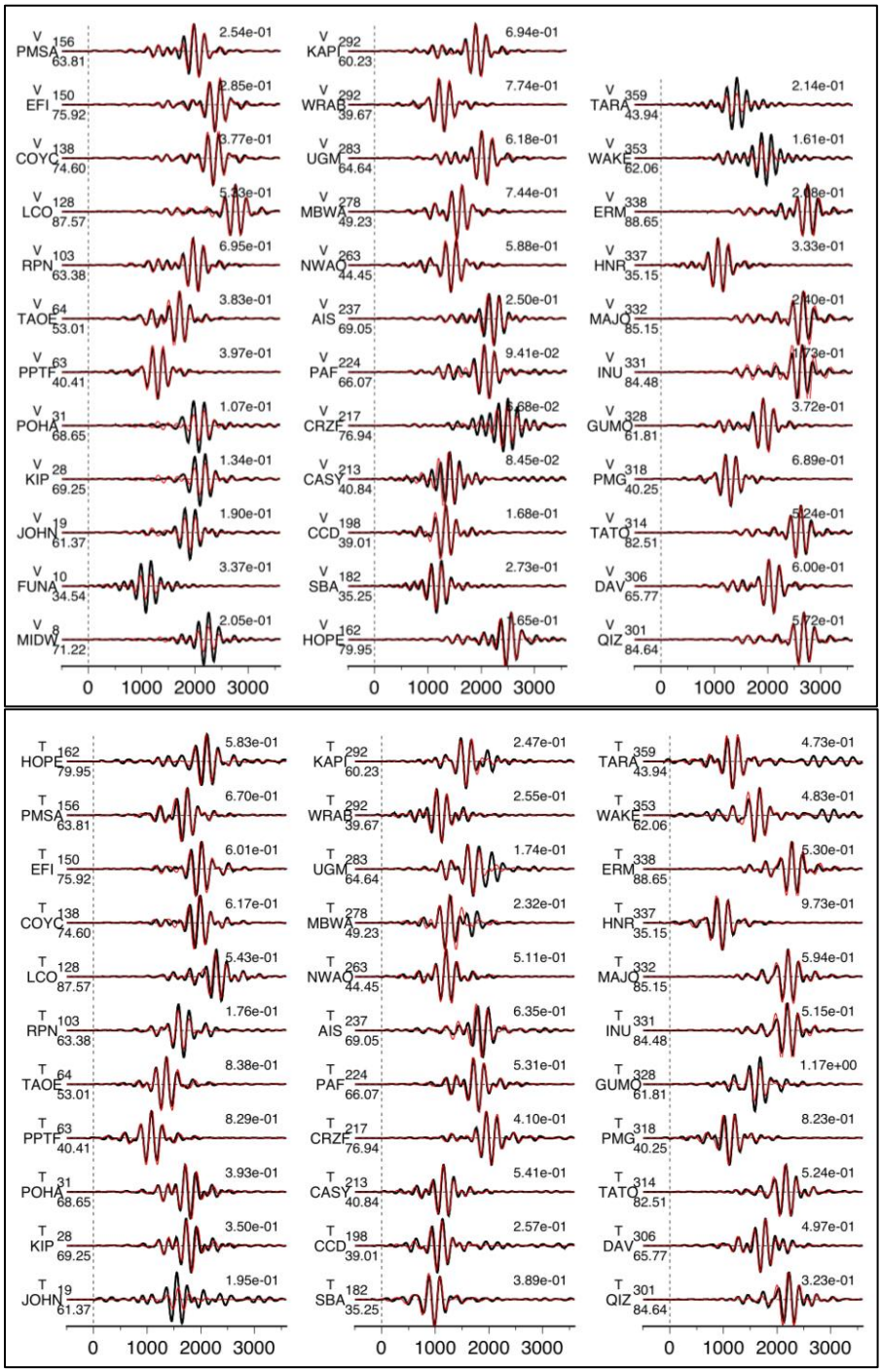

Figure 8. Long period surface waves (vertical-upper and transverse-lower) vs time (s). Data in black and synthetics in red. Left of each trace is the station code. Upper number is the azimuth relative to the epicenter and lower number is the angular distance in degrees. On the right is the maximum amplitude (10^{-3}m) of the observation.

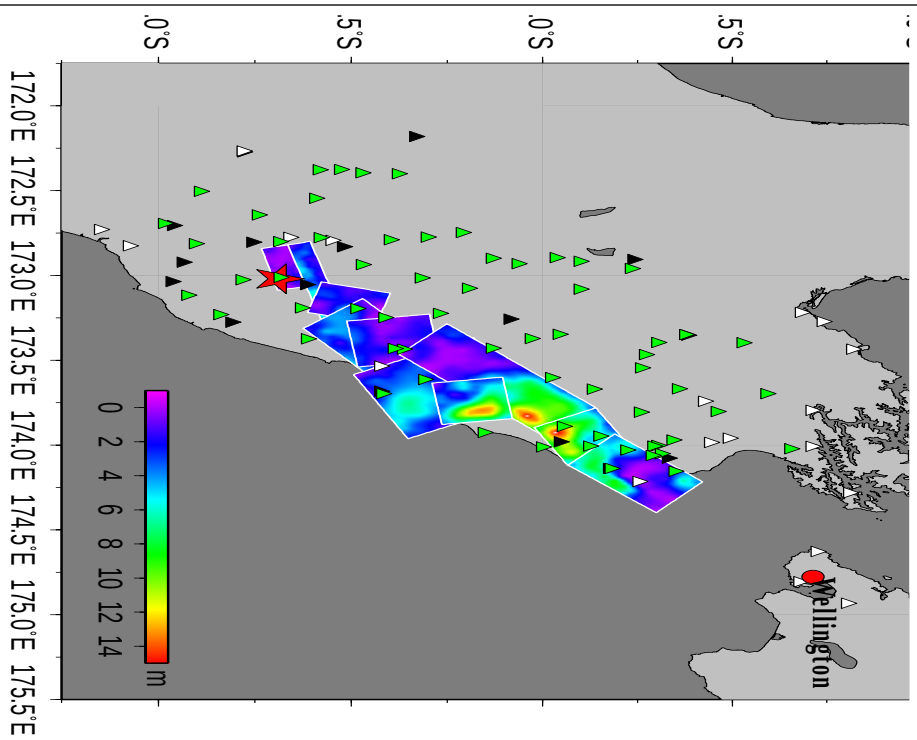

Figure 9. Slip distribution on the 10 faults constructed by inversion (see text for the data used).

5. The rupture on the Papatea fault has an oblique focal mechanism with average rake angle of 61°. The cumulative seismic moment is 1.0×10^{20} Nm, equivalent to a moment magnitude 7.3. Both the average rake angle and seismic moment are similar to the results of Xu et al. (2018) using both GPS and INSAR data. Their estimates are 50° and 1.3×10^{20} Nm, respectively in fault model I. It is noteworthy that the Model I didn't consider the contribution of the Point Kean fault. While the rupture initiation of Papatea fault is poorly constrained, about 90% of its total seismic moment occurred between 55 s and 85 s.

A scalar summation of the seismic moments of 10 fault segments yields an estimate of total seismic moment of 1.08×10^{21} Nm (M_W 8.0).

Table 3: Comparison of the centroid moment tensor of this study and GCMT

Solution	M_0 (10^{20} Nm)	CLVD	T axis		N axis		P axis	
			plunge	azimuth	plunge	azimuth	plunge	azimuth
GCMT	6.7	31%	56°	225°	25°	360°	21°	100°
This study	7.2	27%	54°	212°	7°	33°	12°	105°

(a)

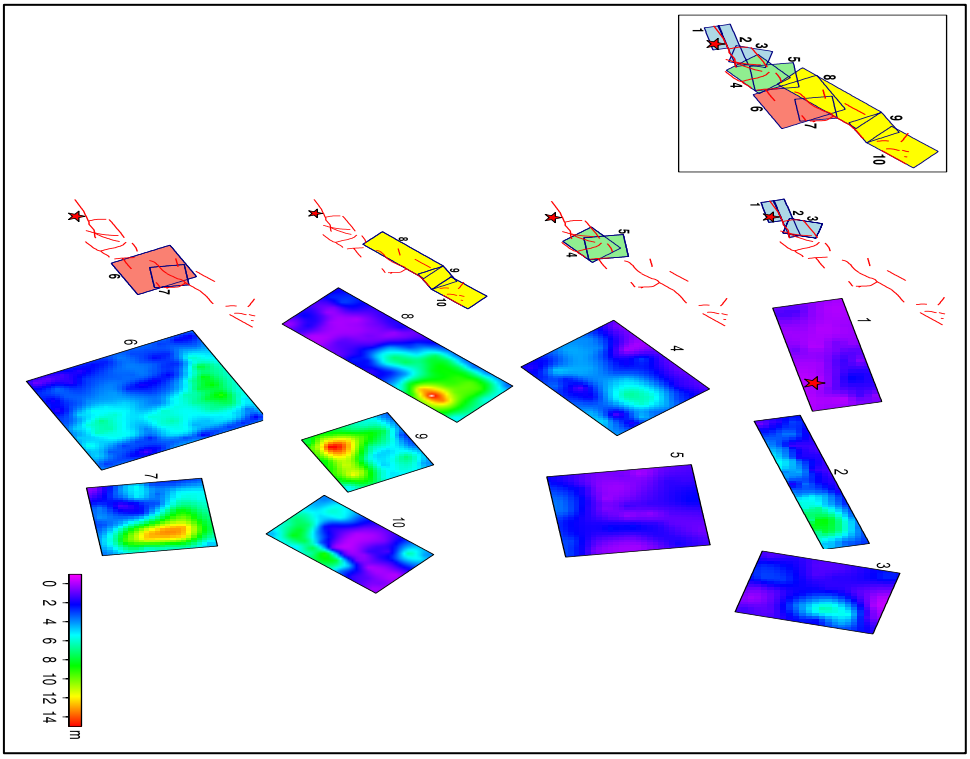

(b)

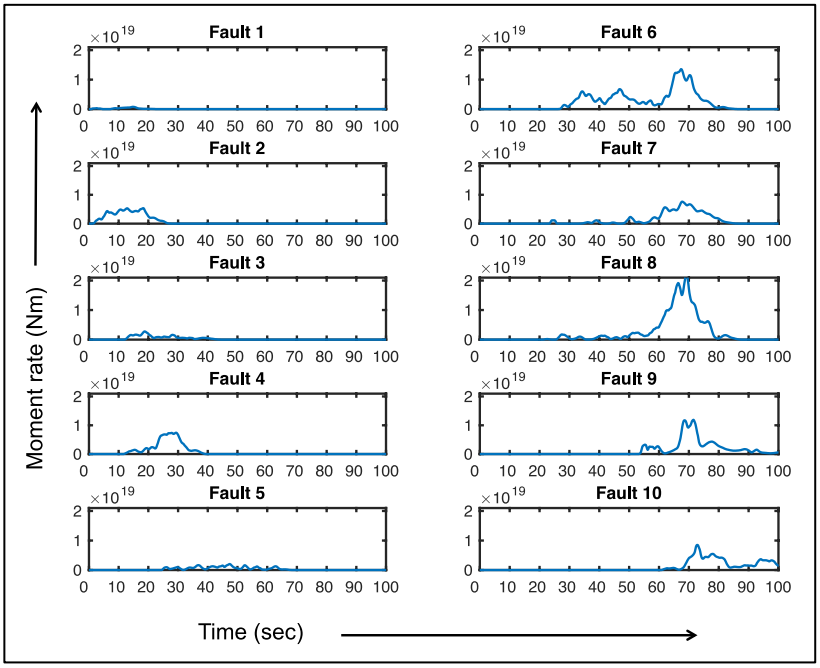

Figure 10. (a) Detailed slip history of all ten fault segments used in the finite fault inversion of strong motion data only. Faults are numbered according to the sequence seen in Figure 5. The red lines are the mapped surface fault traces. (b) Moment rate functions (in Nm/sec) for each individual fault segment in (a).

Including the GPS and teleseismic data, rather than inversion of strong motion data only, leads to larger slip and overall larger seismic moment. This is seen in Figure 12 where we compare the overall moment rate functions of the two models. The cumulative moment rate shows that the Kaikoura earthquake generated about two thirds of the seismic moment after 60 seconds. However, many of the largest accelerations are to the south of the hypocenter.

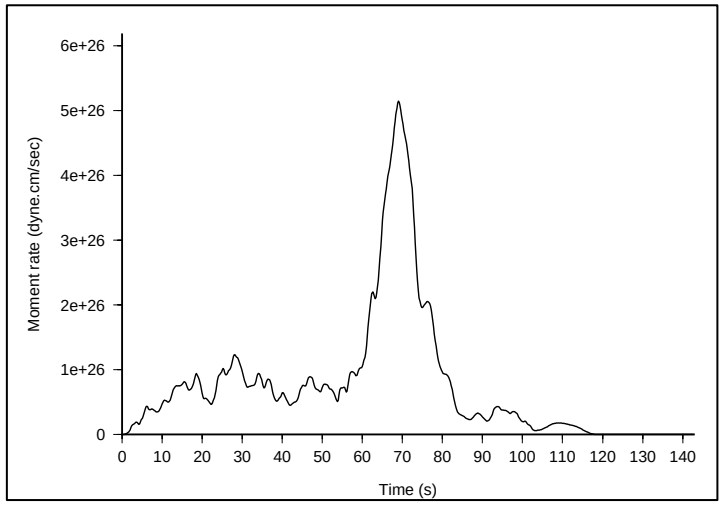

Figure 11. Cumulative moment rate function from joint inversion of strong motion data, GPS static and high-rate, teleseismic body waves (P and SH) and teleseismic surface waves.

Discussion

The tensor summation of these sub-sources leads to our estimate of the centroid moment tensor (Table 3), which has a scalar seismic moment of 7.2×10^{20} Nm (M_W 7.9). This is nearly identical to the GCMT estimate of 6.7×10^{20} Nm but one third smaller than the value of scalar summation. Hence, for such complex rupture processes, point source moment tensor inversion such as GCMT often underestimates the cumulative scalar seismic moment of a large earthquake.

With many parameters being used in finite fault inversions to represent the earthquake process during, some of them are inevitably correlated. For example, Ji et al. (2003) noticed the trade-off between the rupture initiation time and starting time of each subfault. The time of peak slip rate (peak time), which can be represented as a summation of rupture initiation time and starting time, is often better constrained. We show the peak time and hypocenter distance at the center of every subfault as a red dot in Figure 13. It reveals that the migration speed of the peak time from the hypocenter is clearly less than 2 km/s, consistent with previous studies. However, the local rupture velocity varies significantly. In particular, the subfaults with hypocenter distances from ~70 km to ~130 km (60 km), involving five fault segments—Point Kean, Jordan_Kekerengu, Kekerengu, Needles, Papatea—with different focal mechanisms, reach the peak slip rate all around 70 s. This is associated with the largest moment rate peak in cumulative moment rate function (Figure 11).

In this study, we present a slip model that matches the available near and far field observations without a contribution from the plate interface. However, whether the plate interface ruptured during the Kaikoura earthquake is still a question that remains unresolved. Note that the rupture of Point Kean fault during the period of 60 to 80 s is limited to subfaults with depths greater than 20 km, about 5 km above the plate interface. The cumulative seismic moment during this period is 1.2×10^{20} Nm (M_W 7.4), which is about 11% of the total seismic moment. The rupture of this slip patch dominates the later phase of station MOLS, which is the closest strong motion station to this slip patch. However, as shown in Wang et al. (2018), slip on plate interface can also match this record.

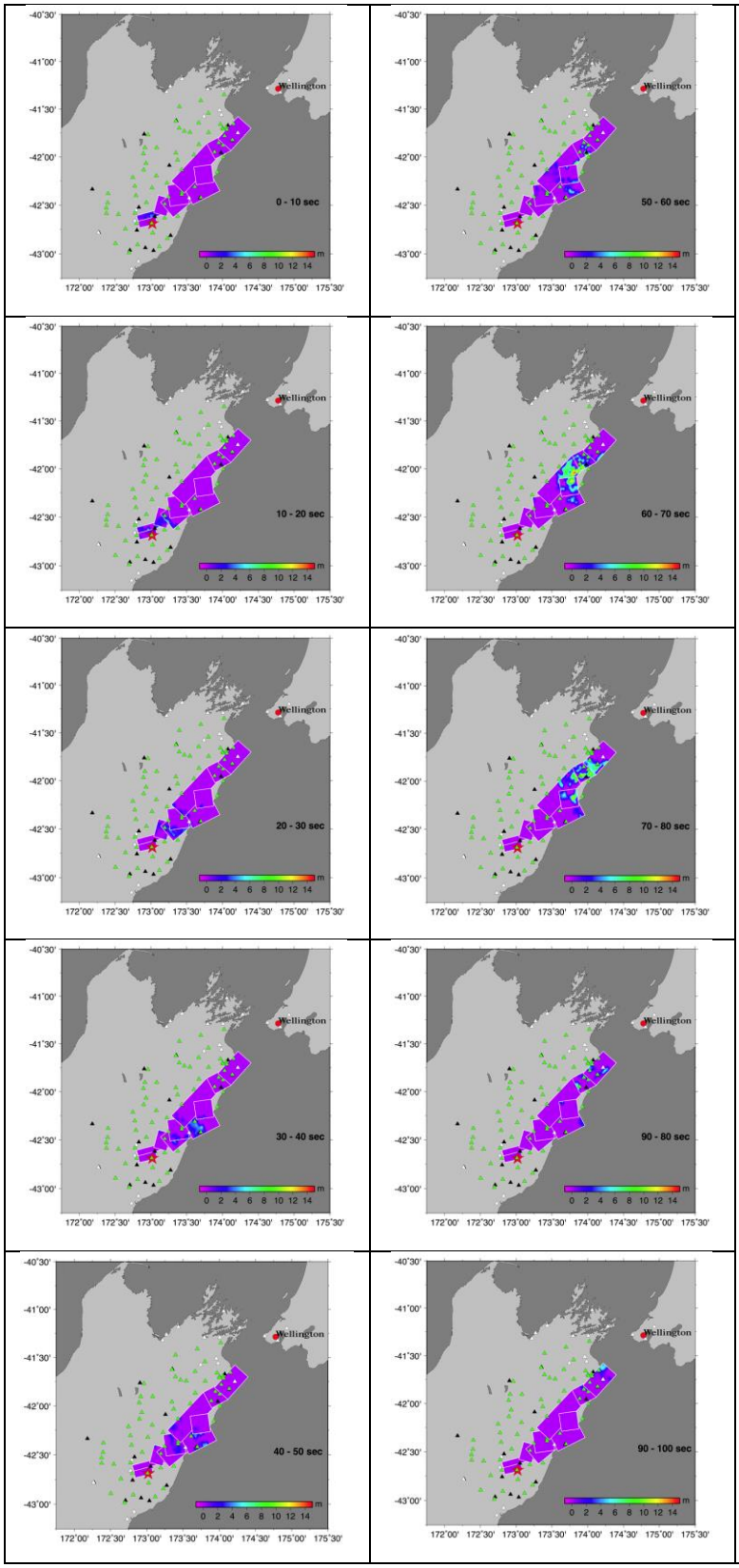

Figure 12. There are 10 snapshots of the slip on the fault accumulated in 10-second intervals. The snapshots are at 0-10 s, 10-20 s, … , 90-100 s going from top to bottom on the left column and continuing onto the right column. In each snapshot, the contours show the accumulated slip for the 10-second interval. Initially the rupture proceeds rather smoothly on the Humps fault with most slip on the Humps-east fault. The rupture continues onto the Leader fault and Hundalee fault by 30 s. It jumps onto the Point Kean Fault in the 30-40 s frame. At 40-50 s, slip is accumulating on the Hundalee, Point Kean, Jordan-Kekerengu and the Papatea faults. At 50-60 s, the rupture has large slip on the Papatea fault and has jumped to the Kekerengu, far to the north. At 60-70 s, the slip is about 6-8 m on the Papatea, Point Kean, Jordan-Kekerengu and Kekerengu faults. The same faults are active at 70-80 s but also the Needles Fault. At 80-90 s there is still slip on the Papatea and Jordan-Kekerengu faults.

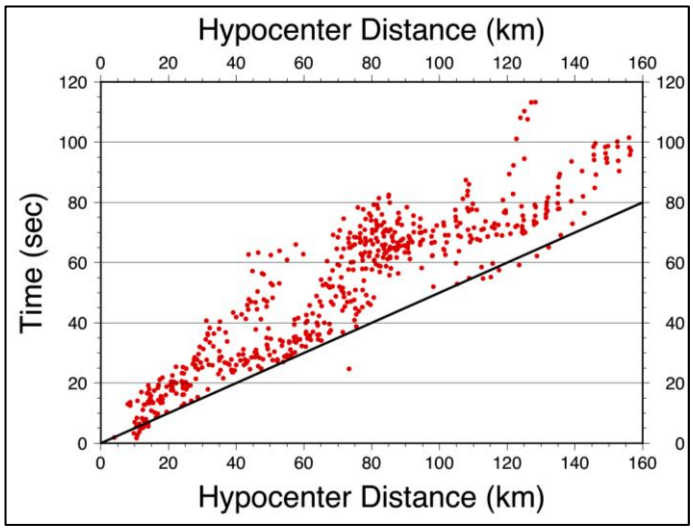

Figure 13. Individual peak time of slip rate in each subfault is plotted against hypocentral distance. Black line is for a constant rupture velocity of 2.0 km/s. There is a lot of variation. Note that for distances 70-120 km, the peak time is between 60-80 s corresponding to the largest moment release during the earthquake. Thus, large parts of the fault system are radiating nearly simultaneously.

The rupture Papatea fault produced up to 8 m uplift. But Holden et al. (2017) noted that it has relatively minor contribution to local waveforms despite its large slip. As shown in Figure 10b, ~90% of the seismic moment occurred within the time window of 55 s to 85 s, when rupture of the deep portion of the Point Kean fault, Jordan_Kekerengu fault, Kekerengu fault and Needles fault also reach their peak moment rates. The cumulative seismic moment of the rupture on these four fault segments during this period is 5.4×10^{20} Nm, 5-6 times of the Papatea fault rupture. Further considering the fact that north of Kaikoura, all strong motion and high rate GPS stations locate west of the Kaikoura fault zone. Therefore, these stations are more sensitive to the rupture of the four fault segments than Papatea fault segment. It is then not surprising that it was difficult to uniquely resolve rupture of the Papatea fault segment using only strong motion observations (Holden et al., 2017).

Conclusions

The M_W 7.8 Kaikoura earthquake is a complex event involving slip on at least 10 faults. Inversion that joined the seismic waveforms of strong motion, high-rate GPS, and teleseismic observations with GPS static field observations shows multiple faults simultaneously rupturing. The results also indicate that strong motion is not controlled by the fault segments with the largest slip. For example, the Papatea fault, which has large slip over a long time, has little effect on strong motion. Most of the seismic moment is released in a 30 second window (55-85s) on five faults: Point Kean, Jordan_Kekerengu, Kekerengu, Needles, Papatea, all of which are well north of the hypocenter. Near the hypocenter, the Humps and Leader faults produce smaller amounts of slip but with significant stress drop, ~8 MPa. This leads to high amplitude ground motion in the southern part. However, the combined seismic moment is only 1.06×10^{20} Nm (M_W 7.3, 10% of total moment).

References

Adams, M.N., (2018), Subject-oriented finite fault inversions and their applications, PhD dissertation, University of California, Santa Barbara.

Clark, K.J., Nissen, E.K., Howarth, J.D., Hamling, I.J., Mountjoy, J.J., Ries, W.F., Jones, K., Goldstein, S., Cochran, U.A., Villamor, P., Hreinsdóttir, S., Litchfield, N.J., Mueller, C., Berryman, K.R. and Strong, D.T. (2017), Highly variable coastal deformation in the 2016 M_W7.8 Kaikōura earthquake reflects rupture complexity along a transpressional plate boundary. *Earth and Planetary Science Letters*, **474**, 334–344. http://doi.org/10.1016/j.epsl.2017.06.048.

Crempien, J.G.F. and Archuleta, R.J., (2015), UCSB method for simulation of broadband ground motion from kinematic earthquake sources, *Seismological Research Letters*, **86,** 61-67.

Ekström, G., Dziewoński, A.M., Maternovskaya, N.N. and Nettles, M. (2005). Global seismicity of 2003: Centroid-moment-tensor solutions for 1087 earthquakes. *Physics of the Earth and Planetary Interiors*, **148**(2–4), 327–351. http://doi.org/10.1016/j.pepi.2004.09.006.

Field, E. H., Biasi, G.P., Bird, P., Dawson, T.E., Felzer, K.R., Jackson, D.D., Johnson, K.M., Jordan, T.H., Madden, C., Michael, A.J., Milner, K.R., Page, M.T., Parsons, T., Powers, P.M., Shaw, B.E., Thatcher, W.R., Weldon, R.J., and Zeng, Y. (2015), Long-term time-dependent probabilities for the Third Uniform California Earthquake Rupture Forecast (UCERF3), *Bull. Seismol. Soc. Am.* **105**, 511-543, DOI: 10.1785/0120140093.

Hamling, I.J., Hreinsdóttir, S., Clark, K., Elliott, J. , Liang, C., Fielding, E., Litchfield, N., Villamor, P., Wallace, L. , Wright, T.J., D'Anastasio, E., Bannister, S., Burbidge, D., Denys, P., Gentle, P., Howarth, J., Mueller, C., Palmer, N., Pearson, C., Power, W., Barnes, P., Barrell, D.J.A., Van Dissen, R., Langridge, R., Little, T., Nicol, A., Pettinga, J., Rowland, J. and Stirling M. (2017), Complex multifault rupture during the 2016 Mw 7.8 Kaikoura earthquake, New Zealand, *Science* 10.1126/science.aam7194.

Holden, C., Kaneko, Y., D'Anastasio, E., Benites, R., Fry, B. and Hamling, I.J. (2017). The 2016 Kaikōura earthquake revealed by kinematic source inversion and seismic wavefield simulations: Slow rupture propagation on a geometrically complex crustal fault network. *Geophysical Research Letters*, **44**(22), 11,320-11,328. http://doi.org/10.1002/2017GL075301.

Ji, C., Wald, D.J. and Helmberger, D.V. (2002), Source description of the 1999 Hector Mine, California, earthquake, part I: Wavelet domain inversion theory and resolution analysis, *Bulletin Seismological Society of America*, **92**, 1192-1207.

Li, X.Y., Shao, G. and Ji, C. (2011), Multiple double-couple analysis for M6-7 earthquakes, *SCEC 2011 Annual Meeting*.

Shao, G.F., Li, X.Y., Ji, C. and Maeda, T. (2011), Focal mechanism and slip history of the 2011 Mw 9.1 off the Pacific coast of Tohoku earthquake, constrained with teleseismic body and surface waves. *Earth Planets Space* **63**, 559-564.

Wang, T., Wei, S., Shi, X., Qiu, Q., Li, L., Peng, D., Weldon, R.J. and Barbot, S. (2018), The 2016 Kaikōura earthquake: Simultaneous rupture of the subduction interface and overlying faults. *Earth and Planetary Science Letters*, **482**, 44–51. http://doi.org/10.1016/j.epsl.2017.10.056.

Xu, W., Feng, G., Meng, L., Zhang, A., Ampuero, J.P., Bürgmann, R. and Fang, L. (2018), Transpressional rupture cascade of the 2016 Mw7.8 Kaikoura earthquake, New Zealand. *Journal of Geophysical Research: Solid Earth*, **123**, 2396–2409. https://doi.org/10.1002/2017JB015168.

RECONSIDERING BASIN EFFECTS IN ERGODIC SITE RESPONSE MODELS

Chukwuebuka C. Nweke, Pengfei Wang, Scott J. Brandenberg, and Jonathan P. Stewart

Department of Civil & Environmental Engineering
University of California, Los Angeles

Abstract

We investigate benefits of regionalizing basin response in ergodic ground motion models. Using southern California data, we find average responses between basin structures, even when the primary site variables used in ground motion models (V_{S30} and depth parameters) are controlled for. For example, the average site response in relatively modestly sized sedimentary structures (such as Simi Valley) are under-predicted at short periods by current models, whereas under-prediction occurs at long periods for larger sedimentary structures. Moreover, site-to-site within-event standard deviations vary appreciably between large basins, basin edges, smaller valleys, and non-basin (mountainous) locations. Such variations can appreciably impact aleatory variability.

Introduction

Seismic site response can be influenced by a variety of physical mechanisms, including amplification above impedance contrasts, resonance, nonlinearity, topographic effects, and amplification related to two- or three-dimensional wave propagation in sedimentary basins. For the purposes of site response modeling using ergodic procedures (including the site terms in NGA-West2 ground motion models), these effects are averaged over many sites globally with conditioning on time-averaged velocity in the upper 30 m (V_{S30}) and, in some cases, on basin depth parameters.

The portion of the site amplification model conditioned on V_{S30} reflects, in an average sense, all of these physical mechanisms, including basin effects to the extent they are present in the empirical data from which the V_{S30} term is derived. The contribution of basin amplification can be loosely associated with an average depth conditional on that V_{S30}. The basin amplification models are 'centered', in the sense that they predict changes in amplification at long periods for depths different from that average. For long-period ground motions, such models predict de-amplification (less than provided by the V_{S30}-scaling function) for shallower depths, and amplification for larger depths.

The NGA-West2 V_{S30}-based site amplification models form the primary basis for ergodic site effect modeling in the development of the USGS seismic hazards mapping program in the western US (Petersen et al. 2015). Many other site-specific applications, as well as ongoing work related to the 2018 version of the USGS maps, consider basin effect modeling using the NGA-West2 depth terms. This work has caused a number of important questions to be raised. There are two principle considerations related to the prediction of mean amplification in basins:

- Centering: Because the basin amplification model operates on a depth difference (depth minus V_{S30}-conditioned mean), it is sensitive to the mean depth model. Current relations for the mean depth apply for broad regions (California, Japan) and have large scatter.
- Amplification function: Basin amplification models were derived using data from basins in Japan and California. Variability in basin-related amplification between regions, and between basins within a given region, is likely present but is not captured with current procedures.

We are in the midst of a long-term research effort in which these and other issues pertaining to mean site amplification are being addressed. As part of this work, we are also investigating the dispersion of ground motion, also known as aleatory variability. This variability is represented in seismic hazard analyses using a total standard deviation (σ_{ln}), which has contributions from between-event variability (τ_{ln}) and within-event variability (ϕ_{ln}).

$$\sigma_{ln} = \sqrt{\tau_{ln}^2 + \phi_{ln}^2} \tag{1}$$

Within-event variability has contributions from region-to-region and site-to-site variations in path and site effects. Regional and azimuthal variations in path effects account for different attenuation rates as ground motions propagate from source to site along different paths. Ground motion models provide average attenuation rates, and the aleatory variability associated with variations from that average is denoted ϕ_{P2P}. Similarly, regional and site-to-site variations in geologic structure cause variable levels of site amplification, even when 'primary' site variable V_{S30} and basin depth terms are specified. Regional variations are accounted for in region-specific ergodic models, which may have different levels of ground motion scaling with V_{S30} (e.g., Parker et al. 2019). Site-to-site variations in site response relative to regional models is appreciable, due to the many aforementioned factors not considered in ergodic models; the dispersion associated with these variations is denoted ϕ_{S2S}. Assuming statistical independence, these different sources of within-event variability combine as follows (modified from Al Atik et al. 2010):

$$\phi_{ln} = \sqrt{\phi_{P2P}^2 + \phi_{S2S}^2 + \phi_{lnY}^2} \tag{2}$$

where ϕ_{lnY} is the remaining variability when path- and site-specific models are used, which appears to be principally associated with event-to-event variations in site response at a particular site (Stewart et al., 2017).

Given the limited information on basins that is considered in current GMMs (depth only), we investigate here the potential for regional variations in site response associated with particular basin structures. Likewise, given the limited information on site condition (V_{S30}) that is considered in models of aleatory variability, we investigate variations of site-to-site variability between site categories selected to reflect different morphological conditions. Our study region is southern California, which was selected due to large volumes of ground motion data and the availability of models describing the velocity structure in sedimentary basins.

Following this introduction, we describe the database compiled for the present study. We then present a site categorization scheme intended to distinguish sites having different levels and types of basin response (e.g., basins, mountain/hill areas, etc.). All sites in the ground motion

database are classified following this scheme for use in ground motion data analysis. The data analysis examines residuals of the data set relative to NGA-West2 models. These residuals analyses investigate model bias with respect to site categories and specific geologic structures such as the Los Angeles basin. The dispersion of residuals is used to investigate changes in site-to-site variability between categories and between specific basins. The results are interpreted to provide insights into how basin models can be improved for ground motion modeling in southern California.

Database

We begin with the NGA-West2 database (Ancheta et al., 2014), which is a global database for active tectonic regions. There is a significant contribution of data from southern California to the NGA-west2 database (191 events, 898 stations, 8245 recordings) over the time period 1938 to 2010. The site portion of the database (Seyhan et al. 2014) was developed to provide the principle site parameters used in model development − V_{S30} and various depth parameters denoted as z_x. These depths indicate the vertical distance from the ground surface to the first crossing of a shear wave velocity isosurface; the mostly widely used values are $z_{1.0}$ and $z_{2.5}$ for depths to the 1.0 km/s and 2.5 km/s isosurfaces. As part of this project and other complimentary projects, we converted the spreadsheet files that comprised the original NGA-West2 flatfile (pertaining to sources, sites, and ground motions) into a formal relational database, which is housed on a local server. Additions of data are made within the relational database. The database is accessed using Python scripts within Jupyter notebooks on DesignSafe (Rathje et al. 2017).

We have identified earthquakes and recordings since 2011 in California, which significantly extend the NGA-West2 database. In this extension of the database, we only consider **M** > 4 events, due to difficulties that can be encountered in the analysis of site terms using smaller magnitude data (Stafford et al., 2017). Figure 1 shows the locations of events sorted by magnitude, most of which occur in five main regions: Bay Area, Eastern Sierra and Nevada, central California, southern California, and Imperial Valley and northern Mexico. These five zones incorporate most of the urban areas in the state, and contain a large fraction of the ground motion stations. There are over 33,000 three-component recordings from 179 events. As explained further in the next section, we focus here on the southern California region. The data from events within the Southern California region in Figure 1 is derived from 22 earthquakes that have produced about 9,300 three-component recordings within the distance cutoffs suggested by Boore et al. (2014). The data are screened to remove duplicate recordings (e.g., seismometers and accelerometers at the same location) and recordings that appear to be unreliable from instrument malfunctions or similar, which leaves about 4260 usable three-component records. Figure 2 shows the locations of these events and of the 362 recording stations that have provided recordings.

Each of the three-component records has been processed according to standard protocols developed during Pacific Earthquake Engineering Research center (PEER)-NGA projects, as described in Ancheta et al. (2014). This processing provides a lowest usable frequency for each ground motion component. Horizontal ground motion components are combined to median-component (RotD50) as defined by Boore (2010) using the routines given in Wang et al. (2017). We take the lowest useable frequency for RotD50 as the higher of the two as-recorded values.

Figure 3 shows the number of usable RotD50 horizontal-component ground motions as a function of oscillator period. The fall-off begins at about 1.0 sec and the data is reduced by 50% by 2.5 sec.

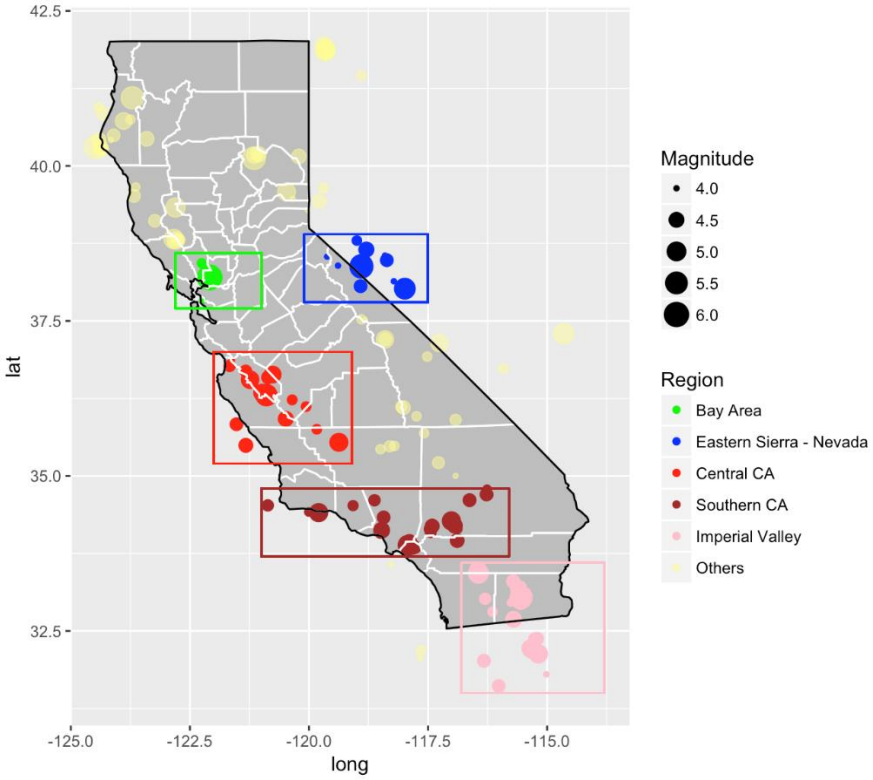

Figure 1. Locations of earthquakes in California and northern Mexico with **M** > 4 since 2011 that have for which ground motion data has been compiled for addition to the NGA-West2 database

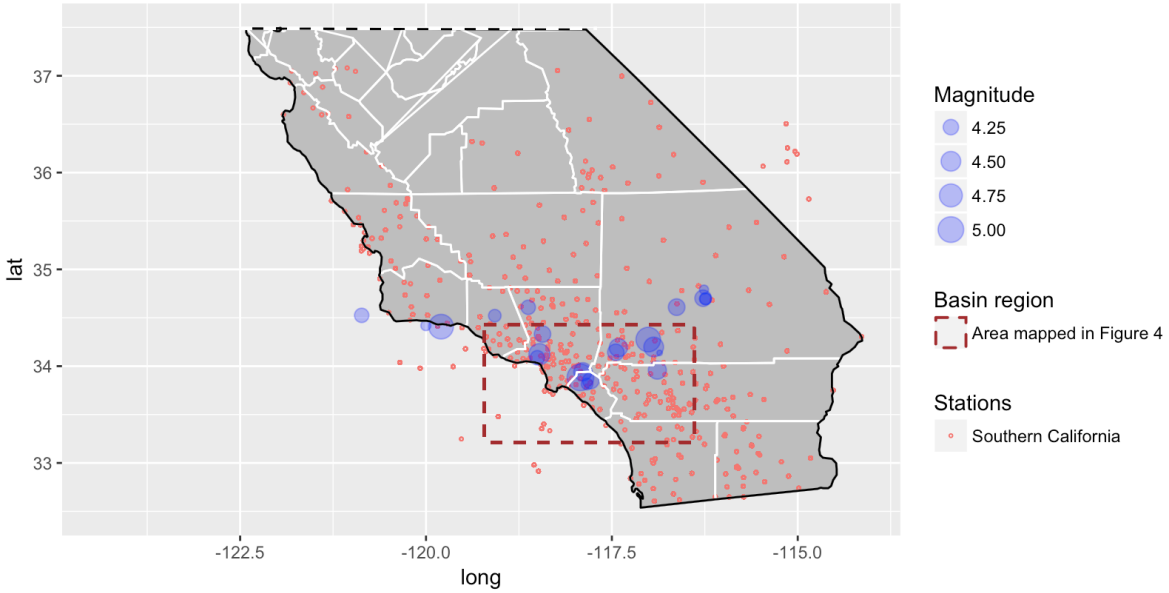

Figure 2. Map of southern California region showing locations of considered earthquakes with **M** > 4 since 2011 and locations of stations that recorded the event

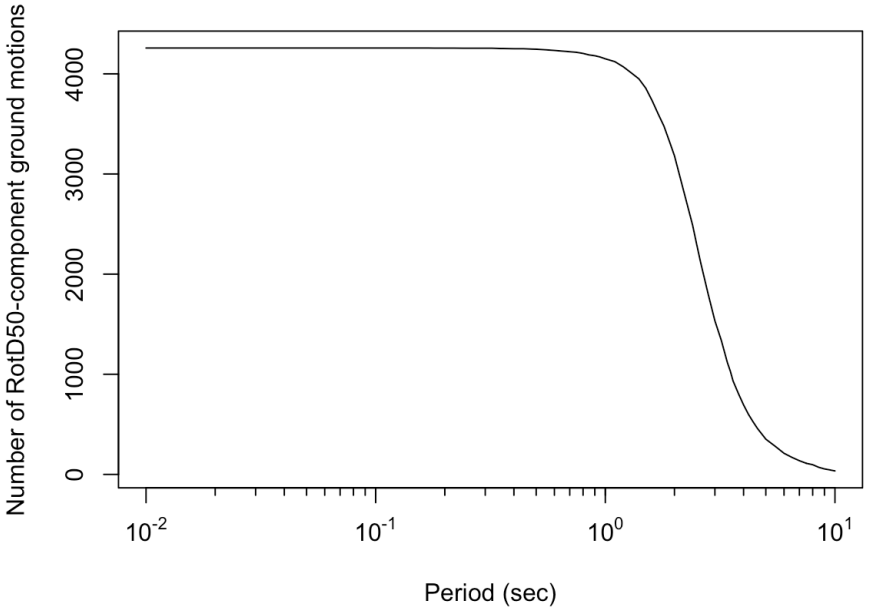

Figure 3. Number of usable RotD50-component ground motions as a function of oscillator period for the data added for the southern California region.

Considering both the NGA-West2 data and new data, there are 777 recording sites within the rectangular area shown in Figure 2, which is shown in greater detail in Figure 4. Of those, 736 are sites that were included in the NGA-West2 site database. Hence, there are 41 new sites that require assignment of site parameters. Following protocols given in Seyhan et al. (2014), V_{S30} was assigned using local shear wave velocity measurements where available – this applies to four sites (data obtained from USGS V_{S30} Compilation Database[1]). For sites without V_{S30} measurements, we use the V_{S30} map derived from geologic- and topographic-based proxy relationships by Thompson et al. (2014), as updated by Thompson (2018) (2/3 weight). We also consider the terrain-based proxy model of Yong et al. (2012), as updated by Yong (2016) (1/3 weight).

Basin depth parameters $z_{1.0}$ and $z_{2.5}$ were obtained for all of the considered sites, including the NGA-West2 sites and the newly added sites. Older values were replaced because of updates, and expansion, of the southern California basin models. Table 1 shows the basin models, including version numbers, used in this compilation. Regions for which basin models have been developed since the close of the NGA-West2 project include the central valley region of California (San Joaquin valley and Santa Maria River valley) and Mojave Desert region.

[1] https://earthquake.usgs.gov/data/vs30/

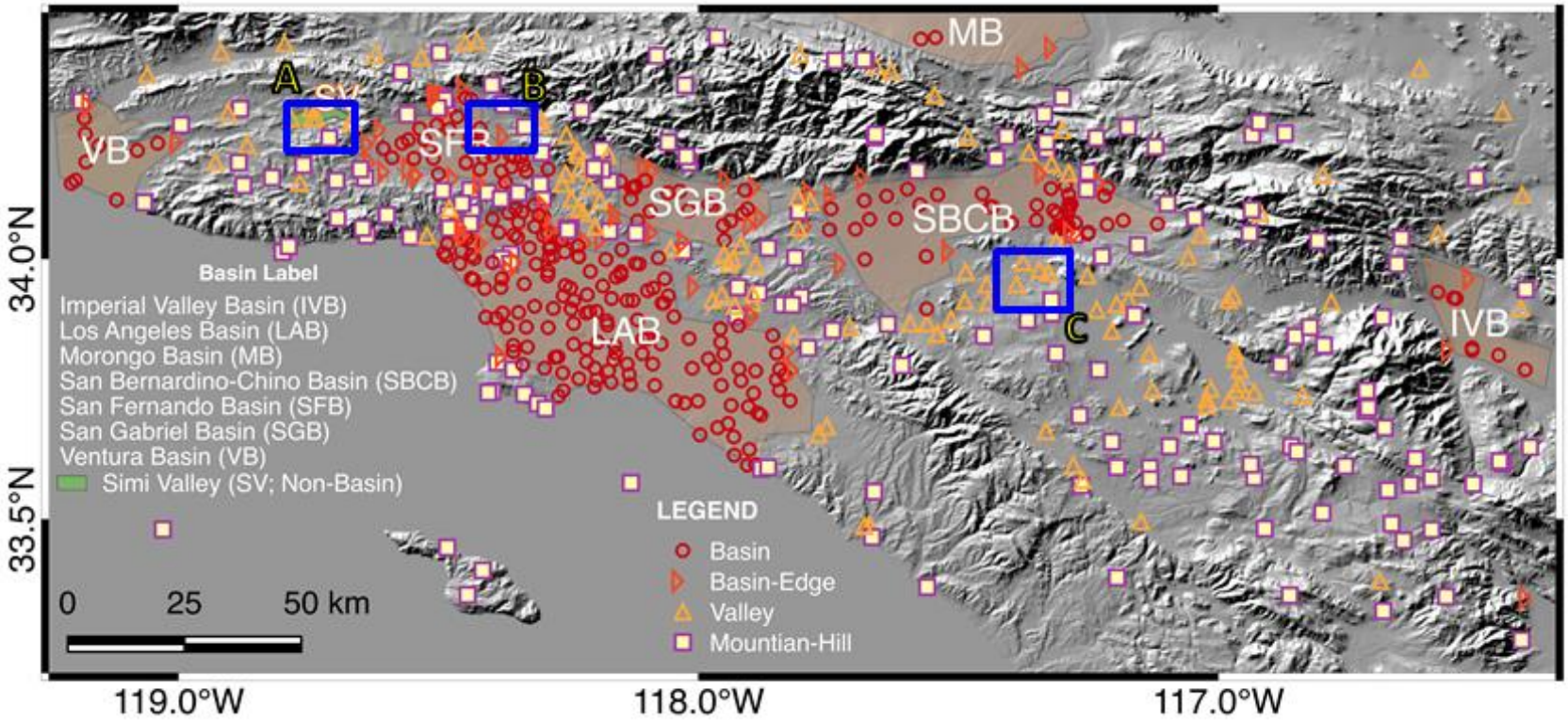

Figure 4. Detail map of southern California showing ground motion stations and sedimentary basins and related features considered in this paper. Ground motion sites are plotted according to a morphology-based site categorization scheme proposed in this paper. Boxes A, B, and C are detailed in subsequent figures in this paper.

Table 1. Seismic velocity models registered into the Unified Community Velocity Model (UCVM) modified from Small et al. (2017)

Model Name UCVM Abbreviation	Description	Region, Coverage Coordinates	References
SCEC CVM-H, v.15.1, (cvmh)	3D velocity model defined on regular mesh, no geotechnical layer. Based on 3D tomographic inversions of seismic reflection profiles and direct velocity measurements from boreholes	So. CA; −120.8620, 30.9565; −113.3329, 30.9565; −113.3329, 36.6129; −120.8620, 36.6129	Süss and Shaw 2003; Shaw et al. 2015
SCEC CVM-S4, (cvms)	3D velocity model defined as rule-based system with a geotechnical layer. Uses query of velocity by depth using empirical relationships from borehole sonic logs and tomographic studies	Irregular area in So. CA	Kohler et al. 2003
SCEC CVM-S4.26, (cvms5) SCEC CVM-S4.26.M01, (cvmsi)	3D velocity model defined on regular mesh, no geotechnical layer. Uses query of velocity by depth based on CVM-S4 as starting model, improved using full 3D tomography. 3D velocity model defined on regular mesh with query by depth that adds a GTL to CVM-S4.26	So. Central CA, So. CA; −116.0000, 30.4499; −122.3000, 34.7835; −118.9475, 38.3035; −112.5182, 33.7819	Lee et al. 2014
USGS Hi-res and Lo-res etree v.08.3.0, (cencal)	3D velocity model defined on regular mesh with geotechnical layer that uses velocity query by depth	Bay Area, No. & Central CA; −126.3532, 39.6806; −123.2732, 41.4849; −118.9445, 36.7022; −121.9309, 35.0090	Brocher et al. 2006
Central CA model, SCEC CCA06, (cca)	3D tomographic inversions done on a coarse mesh (500 m), trilinear interpolation between nodes	Central CA; -122.9362, 36.5298; -118.2678, 39.3084; -115.4353, 36.0116; -120.0027, 33.3384	Still in beta; Chen & Lee (2017)
SCEC CS17.3, (cs173) SCEC CS17.3-H, (cs173h)	CyberShake 17.3 velocity model with added geotechnical layer (UCVMC18.5) 17.3 model integrated with Harvard Santa Maria and San Joaquin basin models with geotechnical layer	Central CA; -127.6187, 37.0453; -124.5299, 41.3799; -112.9435, 35.2956; -116.4796, 31.2355	Still in beta; Ely et al. 2010, 2017
Mod. Hadley Kanamori (1d)	1D velocity model in nine layers that defines V_p and scaling relationship for V_s. Non-basin areas.	So. CA, irregular boundary	Hauksson 2010
Northridge region (bbp1d)	1D velocity model defined in 18 layers, derived from velocity profiles at SCSN stations. Non-basin areas	Northridge region, irregular boundary	Graves and Pitarka 2010

Source parameters were compiled for each of the 22 new events. The range of moment magnitudes is 4.0 to 5.1, and as such finite fault effects are not considered to be significant for the derivation of site-to-source distances. Finite fault models are not available for any of the considered events, to our knowledge. Parameters compiled for each event include hypocenter location (latitude, longitude, depth), focal mechanism, moment magnitude, and rake angle. Focal mechanisms were assigned from rake angles (λ) as follows (e.g., Campbell and Bozorgnia, 2014):

- Reverse, λ = 30 to 150 deg
- Normal, λ = -150 to -30 deg
- Strike-slip, otherwise

Site-to-source distances were computed using the CCLD5 program that was updated as part of the NGA-Subduction project, as described by Contreras (2017).

Figure 5 summarizes attributes of the compiled data. Figure 5a shows the newly added data in magnitude distance-space in comparison to the NGA-West2 data. Figure 5b shows the distribution of site data in V_{S30}-$z_{1.0}$ space, with data from particular basins (as defined in the next section) delineated. The plots in Figure 5 show that that data set has been significantly expanded. This was critical for the present study because our analysis of site terms (defined below) becomes increasingly robust as stations have more usable records. Prior to the present work, there were 110 stations with 10 or more recordings in the study region; whereas the current data set now has 174 such stations.

Figure 5b shows the model for predicting $z_{1.0}$ given V_{S30} proposed by Chiou and Youngs (2014) along with the southern California data. The Chiou and Youngs model is meant to apply for all of California, including San Francisco Bay Area sites. Comparing the binned means of the data to the model, it is apparent that the increase in depth as V_{S30} decreases is stronger in the southern California data than in the model. As a result, the NGA-West2 basin terms may not be optimally centered. The functional form for the Chiou and Youngs (2014) model is,

$$\ln(\overline{z_{1.0}}) = \mathrm{v}_0 ln\left(\frac{V_{S30}^4+v_1^4}{1360^4+v_1^4}\right) - \ln(1000) \quad (3)$$

where V_{S30} is in m/s and $z_{1.0}$ is in km. The coefficients recommended by Chiou and Youngs (2014) are listed in Table 2.

Table 2. Basin depth predictive model coefficients (Eqs. 3-4)

Parameters (CY14)	Value	Parameters (this study)	Value
v_0	-1.7875	c_0	1.02
v_1	570.94	c_1	-0.5
		v_μ (m/s)	266.4
		v_σ	0.20

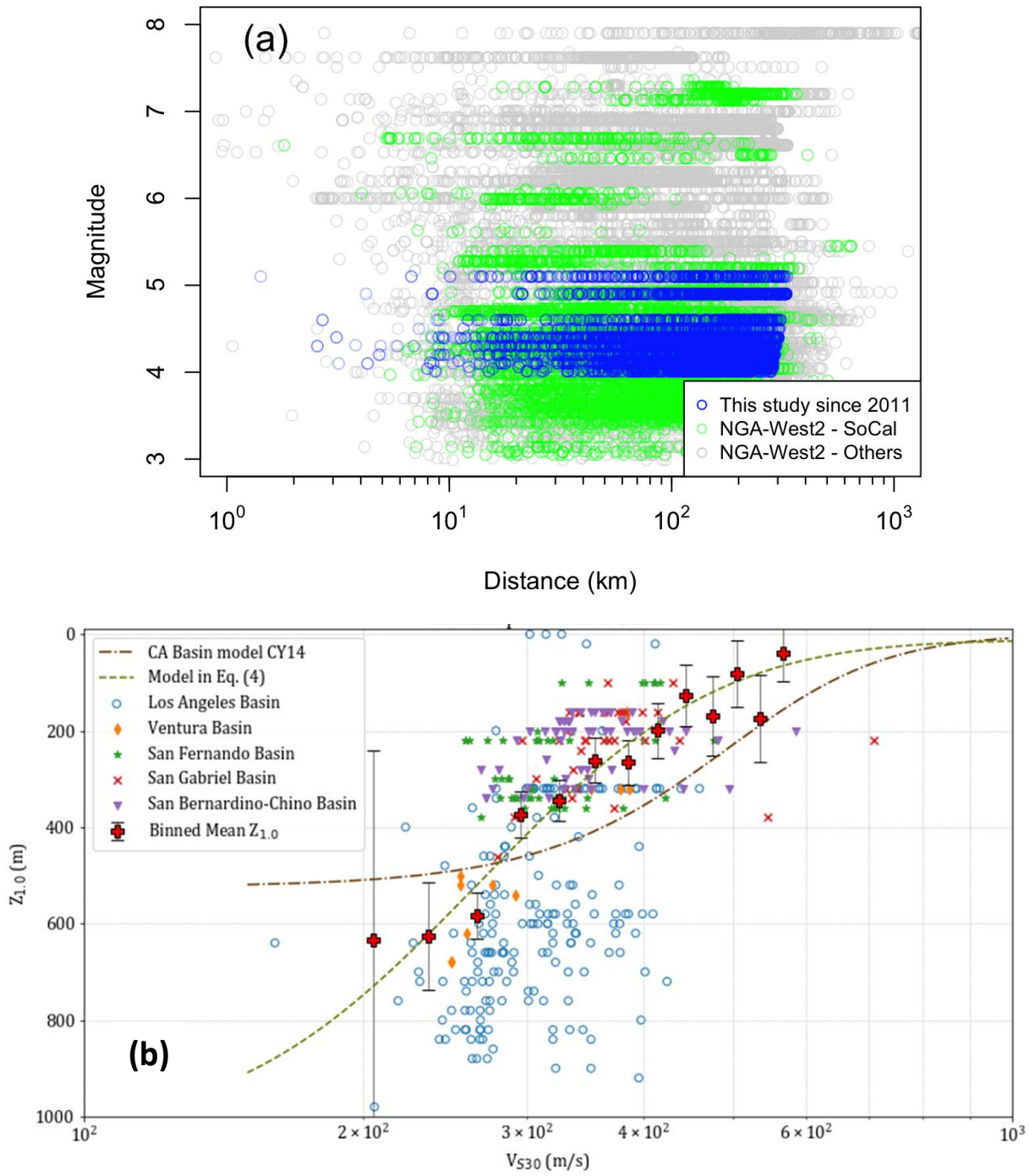

Figure 5. (a) Added data points (from southern California region as shown in Figure 2) in magnitude-distance space; (b) distribution of new and previous data in V_{S30}-$z_{1.0}$ space, including model for the relationship between these parameters by Chiou and Youngs (2014) for California.

We sought to develop an improved fit to the data. Our objective was to fit the trend shown by the binned mean while also enforcing physical bounds at the limits, whereby the depth scaling would flatten with respect to V_{S30}. We suggest the following function to provide the desired shape:

$$\overline{z_1} = c_1 \left[1 + erf\left(\frac{log(V_{S30}) - log(v_\mu)}{v_\sigma \sqrt{2}}\right)\right] + c_0 \quad (4)$$

where v_μ defines the center of the scaling relationship where the slope is steepest and v_σ defines the width of the ramp. Eq. (4) returns the mean $z_{1.0}$ in units of km. Values for all coefficients are given in Table 2. The *erf* function can be solved for in most numerical software packages. In Excel, *erf*(*x*) is given by ERF(*x*).

The fit of the proposed model to the southern California data is given in Figure 5b. Even with this improved fit, it is apparent that the model fits some basins better than others. The fit is good for the relatively deep near-coast basins (Los Angeles, Ventura), whereas depths are generally over-predicted for inland basins (San Fernando, San Gabriel, San Bernardino-Chino).

Basin Classification

A basin is a depression in the earth's surface filled by deep deposits of soft sediments that decrease in thickness towards their margins (Allen and Allen 2013). Two major types of basins are those formed in continental and oceanic settings. Further classifications have been proposed by Dickinson (1974, 1976) and Kingston et al. (1983) that consider tectonic setting (divergent, convergent, subduction) and the *state* of the deposited sediments (i.e., environment present at time of sediment deposition, which can change over time). Our objective is a simple and repeatable (i.e., different users would make identical assignments) basin classification system useful for ground motion amplification purposes. Such classifications have not been provided in prior work, to our knowledge.

Southern California Study Region

The present research on basin response effects is in its early stages. While we ultimately anticipate considering several regions with pronounced basin features and ample earthquake recordings, we have initially focused on the southern California region shown in Figure 4. The approximate limits of the region are (from west to east) Ventura to Landers and (from south to north) Borrego Springs to Phelan. Several factors motivated our selection of this region:

- Ground motion data is abundant, both in terms of the number of earthquakes and the average number of recordings per event.

- The region spans a range of geological conditions, including regions with basins of different sizes and origins, and mountainous non-basin regions.

- There is a large body of work, spanning several decades, to develop seismic velocity models for the region's sedimentary basin structures (i.e., Magistrale et al. 2000; other documents cited in Table 1).

We have identified five major basin structures within the study region, the approximate outlines of which are shown in Figure 4. These are the Los Angeles basin, the Ventura basin, the San Fernando basin, the San Gabriel basin, and the San Bernardino-Chino basin.

The three western-most basins (Ventura, Los Angeles, and San Fernando) have experienced a complex evolution associated with the transformation of the southern California region from a convergent plate boundary to a transform plate boundary (Ingersoll and Rumelhart 1999). Intermitted uplift and subsidence of mountains and basin floors provided continental and oceanic sediment depositional environments. Moreover, the three basins were connected at some points in their history, later becoming separated by uplifts of the Santa Monica and Santa Susana Mountains in conjunction with formation of complex fault systems (Langenheim et al. 2011).

The eastern-most basins within the study area (San Gabriel, San Bernardino-Chino) are continental pull-apart/graben basins that formed as a result of regional faulting. The San Gabriel and San Bernardino-Chino basins are adjacent alluviated lowlands with sediments deposited via erosion from the San Gabriel and San Bernardino Mountains. Both basins are separated by the Glendora Volcanics in the San Jose Hills as well as the Cucamonga Fault Zone (Anderson et al. 2004; Yeats 2004).

The intermitted subsidence and uplift experienced by the western-most basins likely led to the large depths that exists in those basins compared to the shallower depths observed in the eastern-most basins which formed from transform-graben induced valleys adjacent to uplifted blocks. As a result of these differences in geologic history, differences in site response might reasonably be expected. This hypothesis is tested in the present study.

Basin Categorization

In this study, we investigate the impact of information beyond V_{S30} and sediment depth in the analysis of ground motions in basins. This requires a site categorization scheme to indicate whether a site is located within or outside a basin. Because basin effects tend to occur at long periods, which is presumably related to the approximate alignment of long wavelengths with the large dimensions of many of these sedimentary structures, we represent basin size in the site categories.

The proposed categorization scheme is given in Table 3. Two of the categories are obvious – representing 'within basin' and 'outside basin' conditions (Categories #3 and #0, respectively). The valley category (#1) is intended to introduce lateral dimension to the categorization. We considered Simi Valley (identified in Figure 4 as Box A, detail in Figure 6) to

be a good example of a sedimentary depression of modest dimension that should be differentiated from those of large dimension, like the Los Angeles basin. Driven by this admittedly arbitrary example, we selected a limiting width of 3 km to differentiate basins (larger dimensions) from valleys (smaller dimensions). The basin edge category (#2) is intended to account for physical processes known to occur at basin edges, including basin edge generated surface waves (e.g., Graves, 1993; Graves et al. 1998; Kawase, 1996; Pitarka et al., 1998), and in some cases, focusing effects associated with lens-like structures (Baher and Davis, 2003; Stephenson et al., 2000). By differentiating basin edge sites from interior basin sites, we enable investigation of potential differences between ground motions in these domains.

Ground motion recording sites within the study area (i.e., Figure 4) were manually classified according to the categories in Table 3. The manual classification was performed using terrain maps from Google Maps™, where a visual assessment of slope and terrain roughness/texture were used along with information on the short dimension of the sedimentary structure and (as applicable) distance from edge. These classifications are admittedly subjective, although we sought to be as systematic as possible in the process. Figure 7a (detail of Box B from Figure 4) shows an example of three sites comprising mountain-hill, basin edge, and basin conditions located near the northern edge of the San Fernando basin. The eastern-most site categorized as mountain-hill is located on an outcrop rock mass, while the western-most site categorized as a basin is located within a region that is relatively flat. The basin edge site in Figure 7a is just west of an adjacent break in slope between the basin and non-basin areas. These classifications were relatively straightforward based on the differences in morphology in this region. Figure 7b (detail of Box C from Figure 4) shows a more ambiguous case, consisting of a mountain-hill site and several valley sites located in Riverside. The combination of basin and non-basin features (i.e., sites located in modestly-sized or narrow flat areas surrounded by rock outcrops or hills) at these sites partially motivated establishment of the "valley" category.

Table 3. Proposed basin classification criteria for Southern California

Category	Description	Criteria	Cat. #	Number of Sites
Basin	Site location in basin interior	Basin width in short direction > 3 km	3	281
Basin Edge	Sites along basin margin	Within 300 m of basin edge[1]	2	71
Valley	Site location in 'small' sedimentary structure	Valley width in short direction < 3 km	1	125
Mountain-Hill	Sites without significant sediments, generally having topographic relief	Generally identified on basis of appreciable gradients and/or irregular morphology	0	190

[1] Basin edge defined visually from break in slope (topographic features)

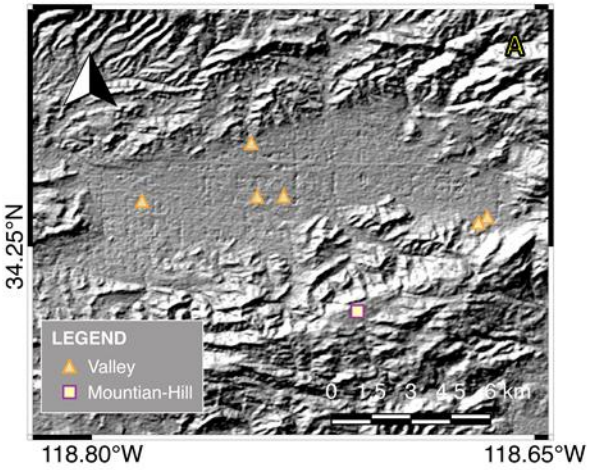

Figure 6. Simi Valley region (Box A in Figure 4)

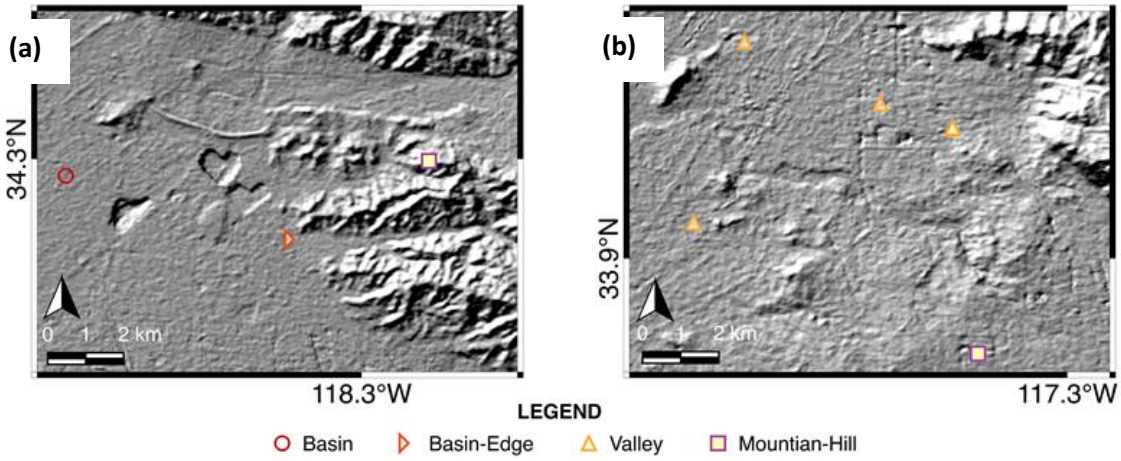

Figure 7. (a) Example location in north-eastern San Fernando Basin with relatively unambiguous site categorizations (Box B in Figure 4); (b) example location in Riverside for which the site classification was more challenging (Box C in Figure 4).

Ground Motion Analysis

Ground motion analyses were undertaken to investigate whether the site categories in Table 3 are useful, in combination with current basin effect models, for differentiating site effects in basins and other areas. This was investigated using a subset of database described previously (i.e., only the NGA-West2 data are currently considered, the newly added data is being considered in ongoing work). Our analysis uses residuals of NGA-West2 models. We focus on one such model in this paper (Boore et al. 2014), but other models are being considered in the project.

Data selection

We use a subset of the NGA-West2 database applicable to events in the Southern California region shown in Figure 2. The data added for the time period since 2011, as shown in Figure 5a, is contained without our data set but has not yet been analyzed. At this time, events in the Imperial Valley region and northern Mexico have not been considered, although that is being investigated in ongoing work.

Using this subset of events, we apply the data screening criteria of Boore et al. (2014). Particularly important elements of those criteria include (1) the use of magnitude and instrument-dependent distance cut-offs that are intended to minimize sampling bias and (2) only using recordings over a range of oscillator periods shorter than $1/\left(1.25f_{hp}\right)$, where f_{hp} is the high-pass frequency selected during component-specific data processing. This frequency is provided in the NGA-West2 flatfile, and was developed in the present work for the added recordings.

As shown in Figure 5a, the data set spans a magnitude range of about 3 to 7 and a closest distance range of about 1 to 400 km. Figure 5b shows that the range of V_{S30} is about 200-600 m/s and the range of $z_{1.0}$ is about 0 to 1000 m.

Residuals analysis

The difference between a recorded ground motion and a model prediction is referred to as a residual, *R*:

$$R_{ij} = \ln\left(Z_{ij}\right) - \mu_{ln}\left(\mathbf{M_i}, F_i, R_{ij}, V_{S30}, z_{1.0}\right) \tag{5}$$

where index i refers to an earthquake and index j refers to a recording. The quantity Z_{ij} is a ground motion observation expressed as an intensity measure. The term μ_{ln} is the mean prediction in natural log units of a ground motion model, which uses the arguments in the parenthesis in Eq. (5). We use the Boore et al. (2014) model, which has the arguments listed in Eq. (5), where *F* is a style of faulting parameter (reverse, strike-slip, etc.), *R* is the Joyner-Boore distance, and other parameters are as defined previously.

Non-zero residuals occur for a variety of reasons. A portion of the data-model differences are purely random, having no known associations. Other portions of the residuals are more systematic. For example, the ground motions for a particular event or a particular site may be systematically high or low relative to the global average. These systematic differences are referred to as event terms and site terms, η_E and η_S, respectively. As a result of these systematic effects, residuals can be partitioned as:

$$R_{ij} = \eta_{E,i} + \delta \mathrm{W}_{ij} \tag{6}$$

where δW_{ij} is the within-event residual, which can be further partitioned as,

$$\delta W_{ij} = \eta_S + \varepsilon_{ij} \tag{7}$$

where ε_{ij} is the remaining residual when the event and site terms have been removed. Recalling the standard deviation terms from the *Introduction*, the standard deviation of η_E terms is τ_{ln}, the standard deviation of δW terms is ϕ_{ln}, the standard deviation of η_S terms is ϕ_{S2S}, and the

standard deviation of ε_{ij} is $\sqrt{\phi_{P2P}^2 + \phi_{lnY}^2}$ (the P2P term appears because we are not accounting for non-ergodic path effects).

Event and site terms are computed using mixed effects analyses (Gelman et al. 2014):

$$R_{ij} = c_k + \eta_{E,i} + \eta_S + \varepsilon_{ij} \tag{8}$$

where c_k is an overall model bias for ground motion model *k*. For a given intensity measure, the mixed effects analysis provides estimates of c_k, η_E for all events, and η_S for all sites.

Our analysis of site effects from the data is based principally on the interpretation of site terms η_S. By using these results, we have removed from the residuals systematic effects associated with the earthquake events (i.e., η_E), which are expected to be unrelated to site response. Another effect that needs to be checked before interpreting site effects is path-scaling. This can be done by checking for trends of δW_{ij} with distance, which is shown in Figure 8 for the intensity measures of PGA and S_a(2.0) (pseudo-spectral acceleration at a period of 2.0 sec). The lack of trend suggests that the path scaling in the model is unbiased for the data set, and hence the model is suitable for analysis of site effects.

By removing event-related effects, and checking for path effects, we improve the likelihood that trends observed in the data are principally related to site response. These are important checks to perform when analyzing site effects using residuals, which is also known as a *non-reference site* approach (Field and Jacob, 1995).

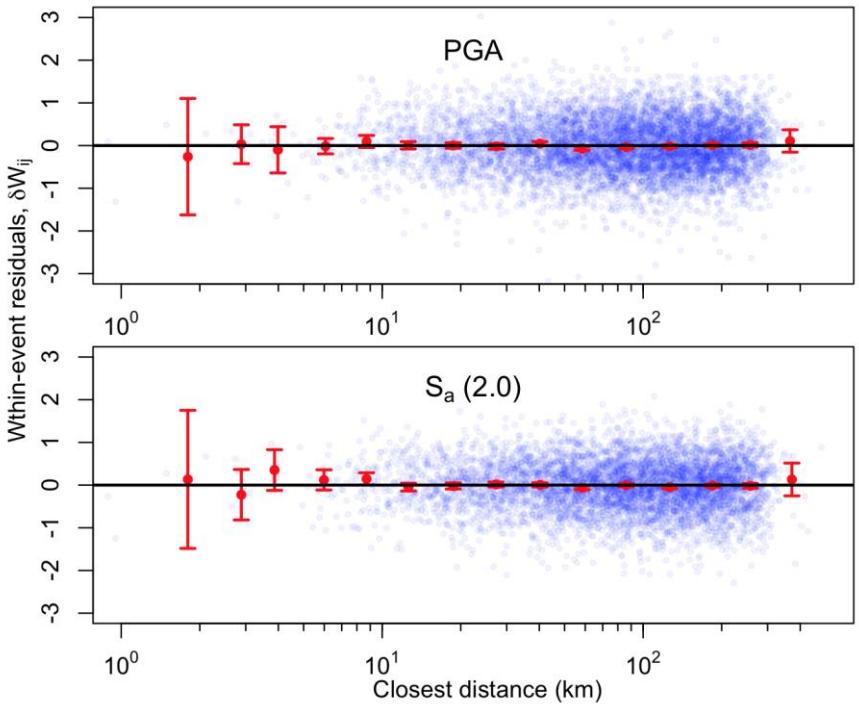

Figure 8. Within-event residuals for southern California data plotted as a function of distance. Binned means and their 95% confidence intervals are shown. There is no trends in the data with distance, indicating that the path scaling in the ground motion model is unbiased for the region.

Mean site response

For the intensity measures of PGA and $S_a(2.0)$, Figure 9 shows the trend of site terms η_S with differential depth, defined as:

$$\delta z_1 = z_{1.0} - \overline{z_{1.0}} \tag{9}$$

For the present analysis, we take $\overline{z_{1.0}}$ using the CY14 model (Eq. 3). We will investigate the impact of updates to the centering model in future work. Figure 9 shows results for all data combined (i.e., all site categories). There is no appreciable trend in the site terms, which indicates that the site terms in the ground motion model (V_{S30}-scaling term and depth term) are capturing average regional trends.

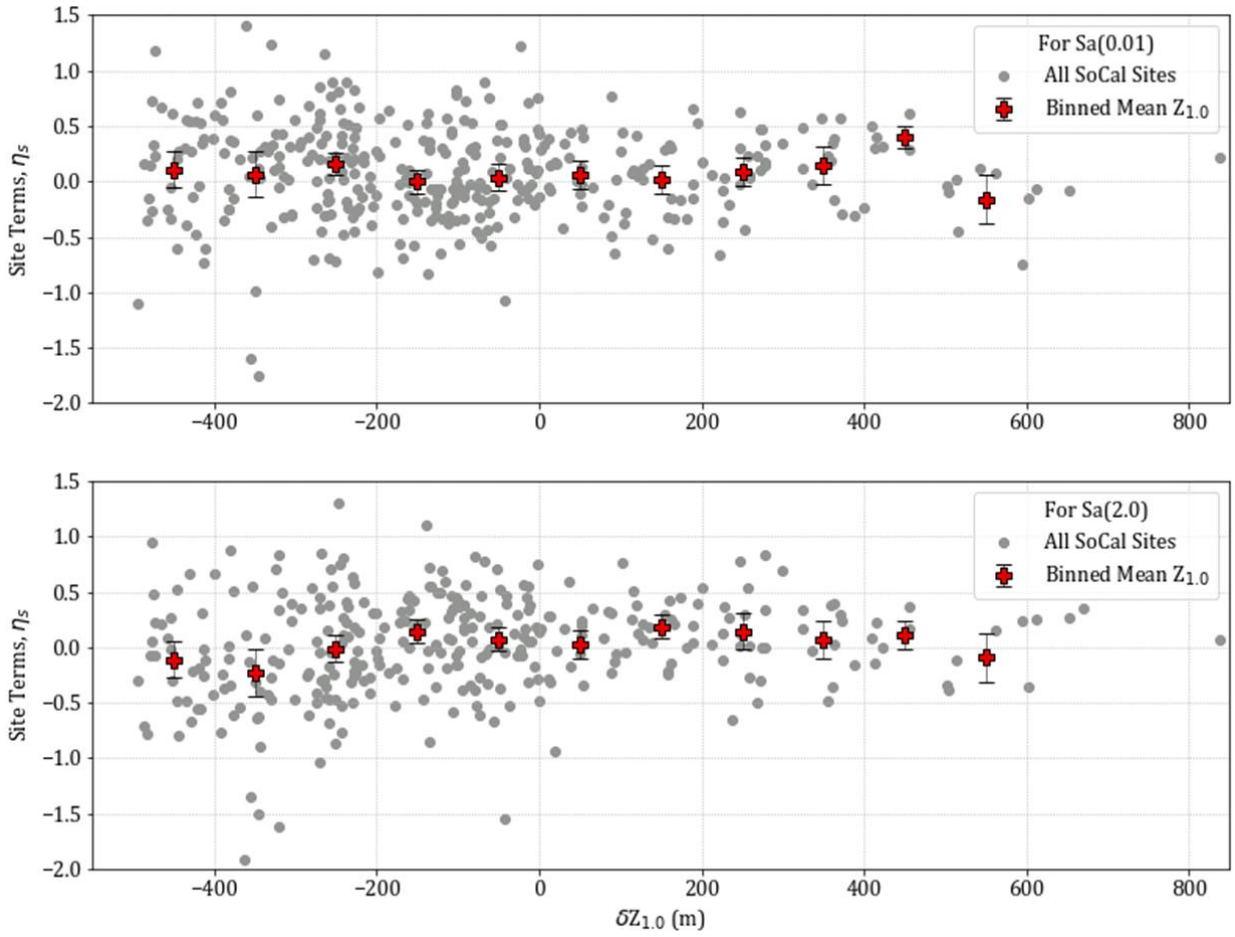

Figure 9. Variation of site terms with differential depth δz_1 for all considered sites in southern California region for intensity measures of PGA and $S_a(2.0)$.

Figure 10 shows trends of $S_a(2.0)$ data with differential depth in the site categories in Table 3. The differential depth range -300 to -100 m (for basin, valley, and mountain-hill sites) has an upward trend. The basin term in the ground motion model has a ramp in this range, so the residuals suggest this ramp could be steeper. Interestingly, the basin edge data indicate a weakly negative trend over this same depth range, indicating that the ramp in the models should be flatter for this category.

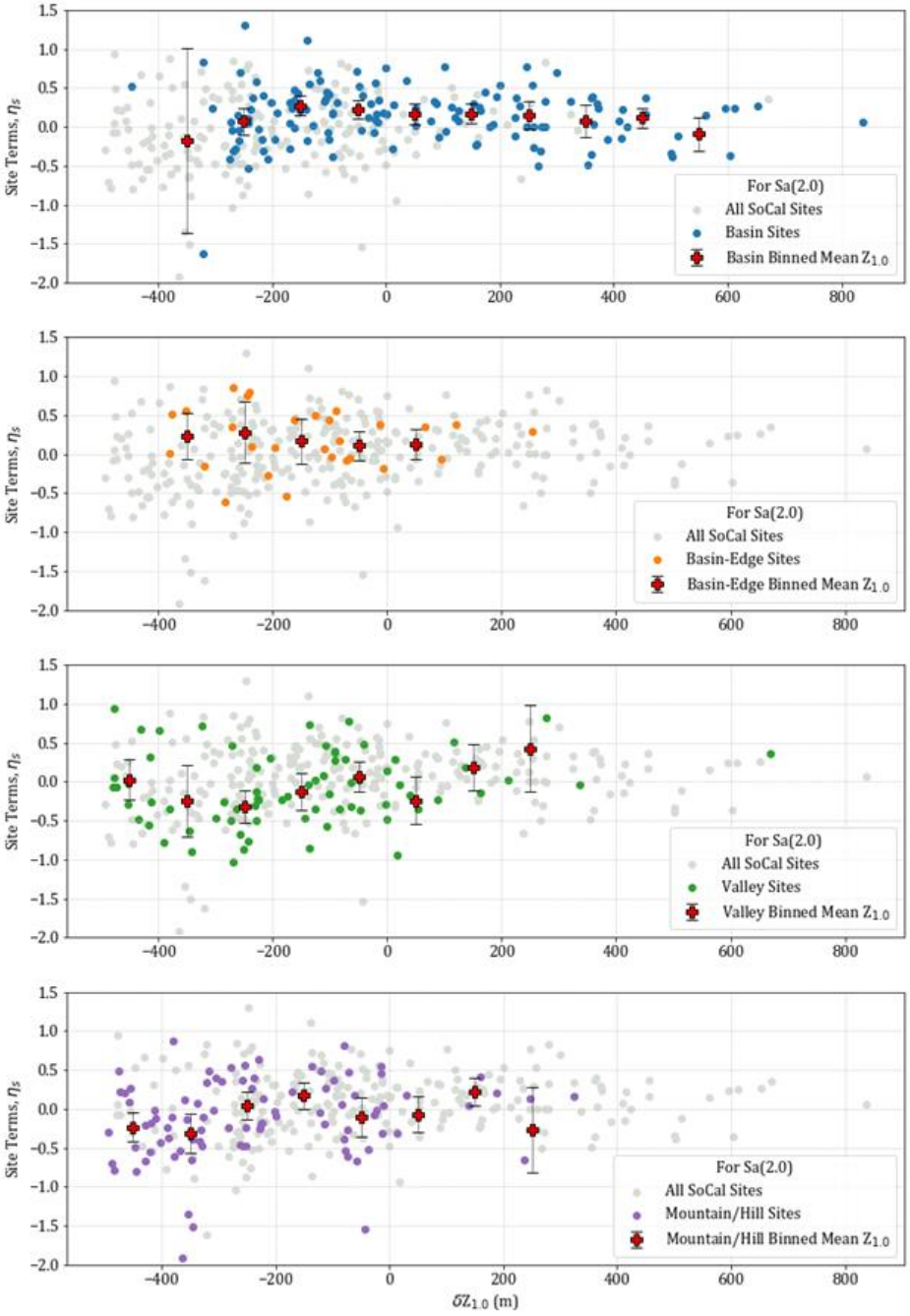

Figure 10. Variation of site terms with differential depth δz_1 for sites within the four site categories for intensity measure $S_a(2.0)$.

Mean biases are plotted as a function of period in Figure 11. The means are generally small (less than about 0.1), the main exceptions being basin sites at long periods (> 1.0 sec), valley sites at short periods (< 0.5 sec), and basin edge sites over the full period range, each of which have positive biases (ground motions under-predicted). Mountain-hills sites have negative bias (ground motions are over-predicted).

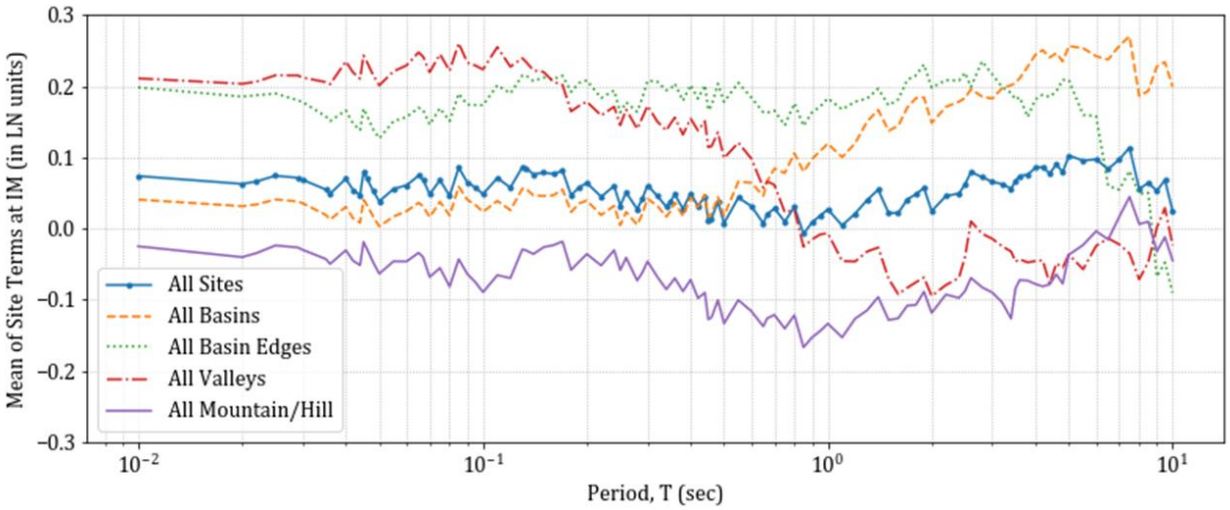

Figure 11. Period-dependence of mean of site terms the four site categories.

Figure 12 shows trends for basins (i.e., sites in the basin and basin edge categories) for four basin structures with significant information: Los Angeles, San Fernando, San Bernardino-Chino, and San Gabriel. The trends with differential depth are generally flat for the Los Angeles basin, which is not surprising because this basin dominates the data set. The San Fernando data has a weak downward trend with differential depth for negative δz_1, suggesting that the reduction of ground motion for $\delta z_1 < 0$ may produce under-prediction bias for this basin (although the data is sparse). The results for the San Gabriel and San Bernardino-Chino basins show some evidence of upward trends, suggesting that the differential scaling could be slightly stronger for these structures than the ergodic model.

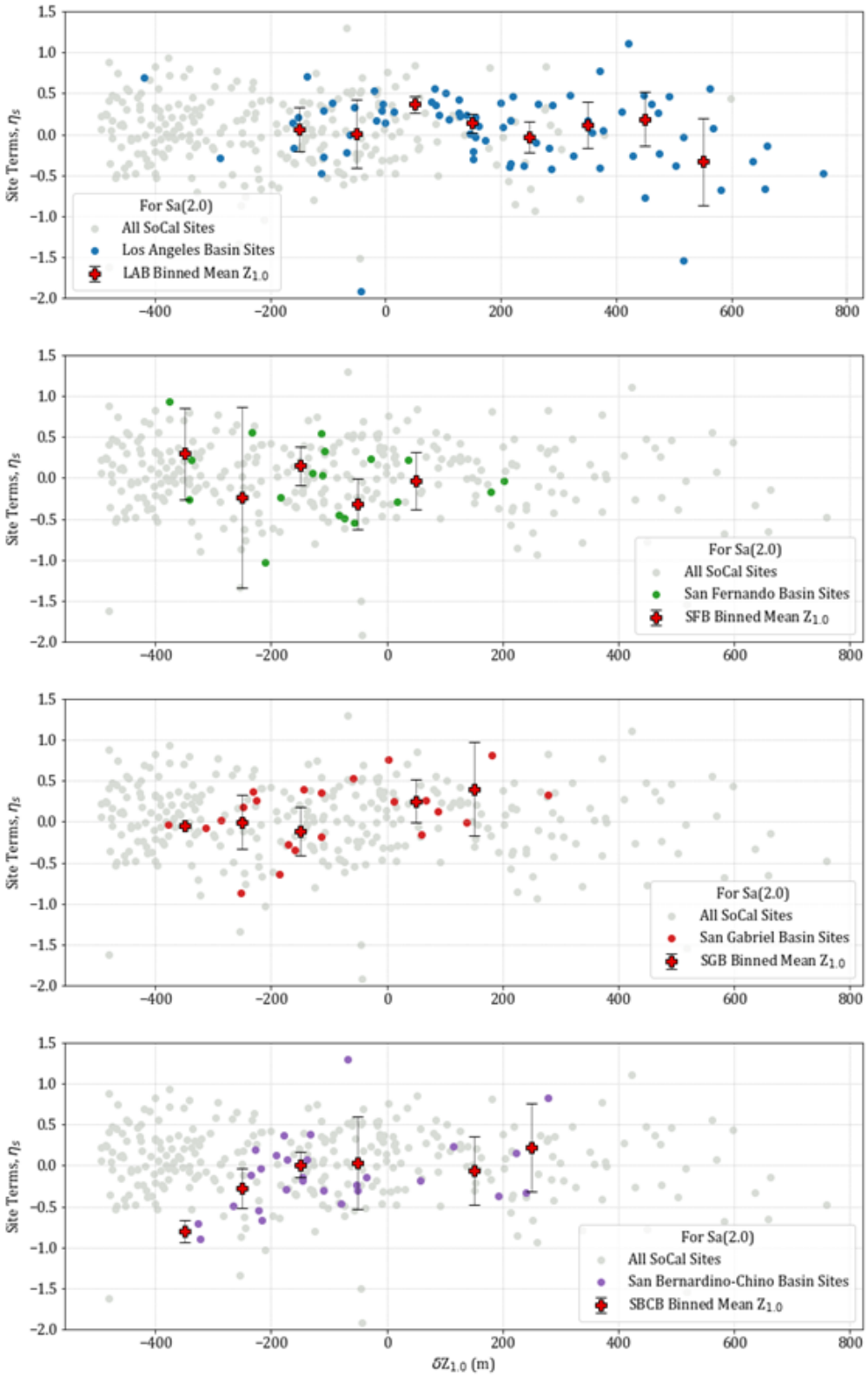

Figure 12. Variation of site terms with differential depth δz_1 for basin and basin edge sites within four basin structures, intensity measure $S_a(2.0)$.

Site-to-site variability

Al Atik (2015) performed residuals analyses similar to those presented here for the full NGA-West2 data set, and based on those analyses, proposed models for site-to-site standard deviation ϕ_{S2S}. Her analyses showed that ϕ_{S2S} is magnitude-dependent, with higher variability for oscillator periods < 1.0 sec for **M** < 5.5 events than for **M** > 5.5 events. At periods > 1.0 sec, the reverse was true (higher ϕ_{S2S} for larger **M** events). These results provide a useful baseline against which to compare our results. Here we present results for the subset of events with **M** < 5.5 in order to illustrate the effects of site condition on ϕ_{S2S}. Similar trends were observed for the larger magnitude data.

Figure 13 compares ϕ_{S2S} for the full data set with the findings of Al Atik (2015). The two sets of standard deviations are nearly identical, indicating that the Southern California data is consistent with global data regarding site-to-site standard deviations.

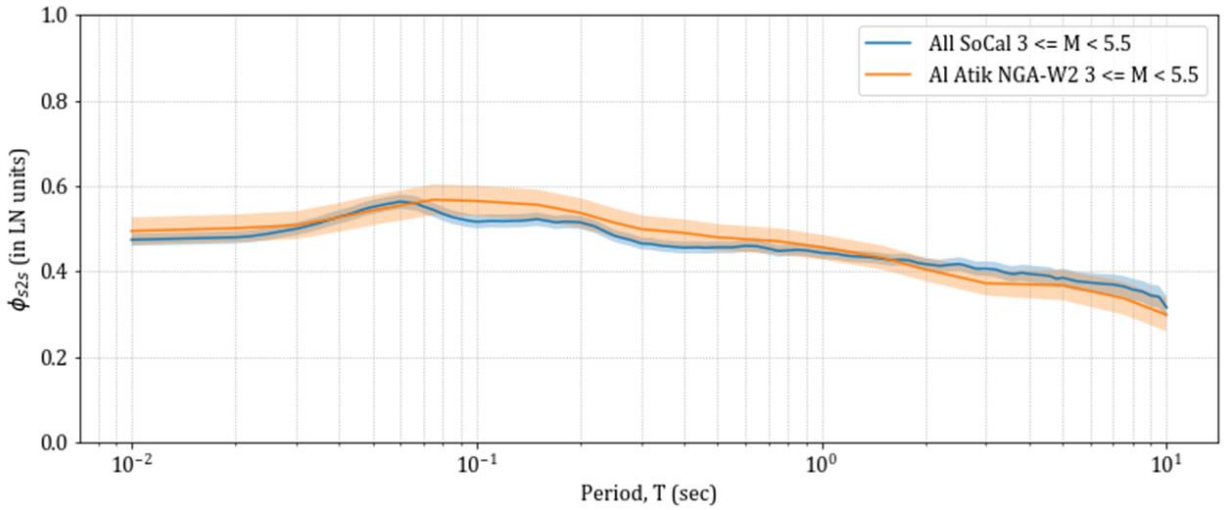

Figure 13. Site-to-site standard deviations, and their 95% confidence intervals, as a function of period for global data (Al Atik 2015) and Southern California data considered in this study. **M** < 5.5 events.

Figure 14 compares ϕ_{S2S} for sites within the proposed site categories in Table 3, with the overall ϕ_{S2S} (across all sites) shown as a baseline for comparison. The variations with site condition are appreciable. Basin sites have lower than baseline ϕ_{S2S} over nearly the full period range. In contrast, basin edge sites have higher variability at short periods and lower at period > 1 sec. Valleys have nearly the opposite trend, with low variability at short periods and high variability at long periods. Mountain-hill sites follow a similar trend to basin edge sites, although with consistently higher variability across all periods.

Figure 15 compares site-to-site standard deviations for all basin sites (as shown in Figure 14) to results for individual basins. The variations in ϕ_{S2S} between basins are small relative to the variability between site categories (Figure 14).

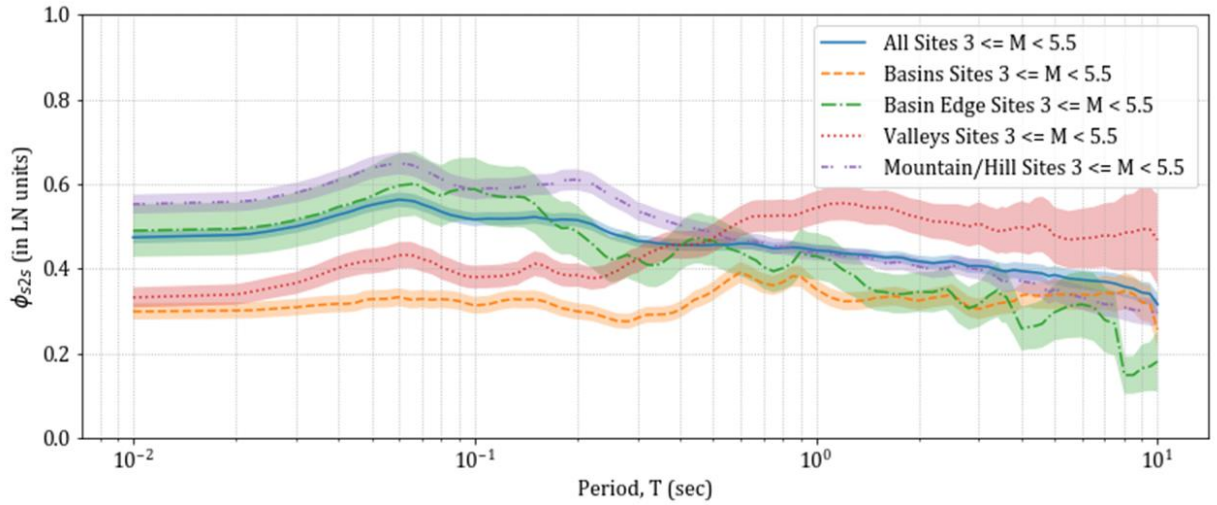

Figure 14. Site-to-site standard deviations, and their 95% confidence intervals, as a function of period for Southern California data sorted by site category. **M** < 5.5 events.

Summary and Interpretation of Results

The V_{S30}-scaling and basin differential depth-scaling relations in some of the NGA-West2 ground motion models are ergodic, meaning that they are intended to represent average site response for a large data set. While regionalization of site response was checked for V_{S30}-scaling, it has not previously been considered for basin depth. In this paper, we present preliminary results of an ongoing study investigating the performance of these global models with respect to southern California data, with particular attention placed on various sedimentary basin structures in the region.

We propose a morphology-based site categorization scheme intended to distinguish sites in large sedimentary basins from sites in smaller sedimentary structures (valleys), along basin edges, and in non-basin areas. Introducing this scheme to ground motion modeling reveals some features that to some extent might be expected. For example, relatively small sedimentary structures have stronger ground motions at short periods than provided by the ergodic models. This is expected because predominant periods for such sites would also be expected at short periods. Likewise, the ergodic models under-predict long-period ground motions in larger sedimentary structures (basins), which would be expected to have, on average, long predominant periods. When specific basin structures are investigated, we see some differences between deep coastal basins (e.g., Los Angeles) and generally shallower, graben-type interior basins (San Bernardino-Chino, San Gabriel, San Fernando). This suggests that the geologic histories of basins may have a quantifiable impact on site effects beyond their effect on V_{S30} and sediment depth. This hypothesis will be explored further in future work.

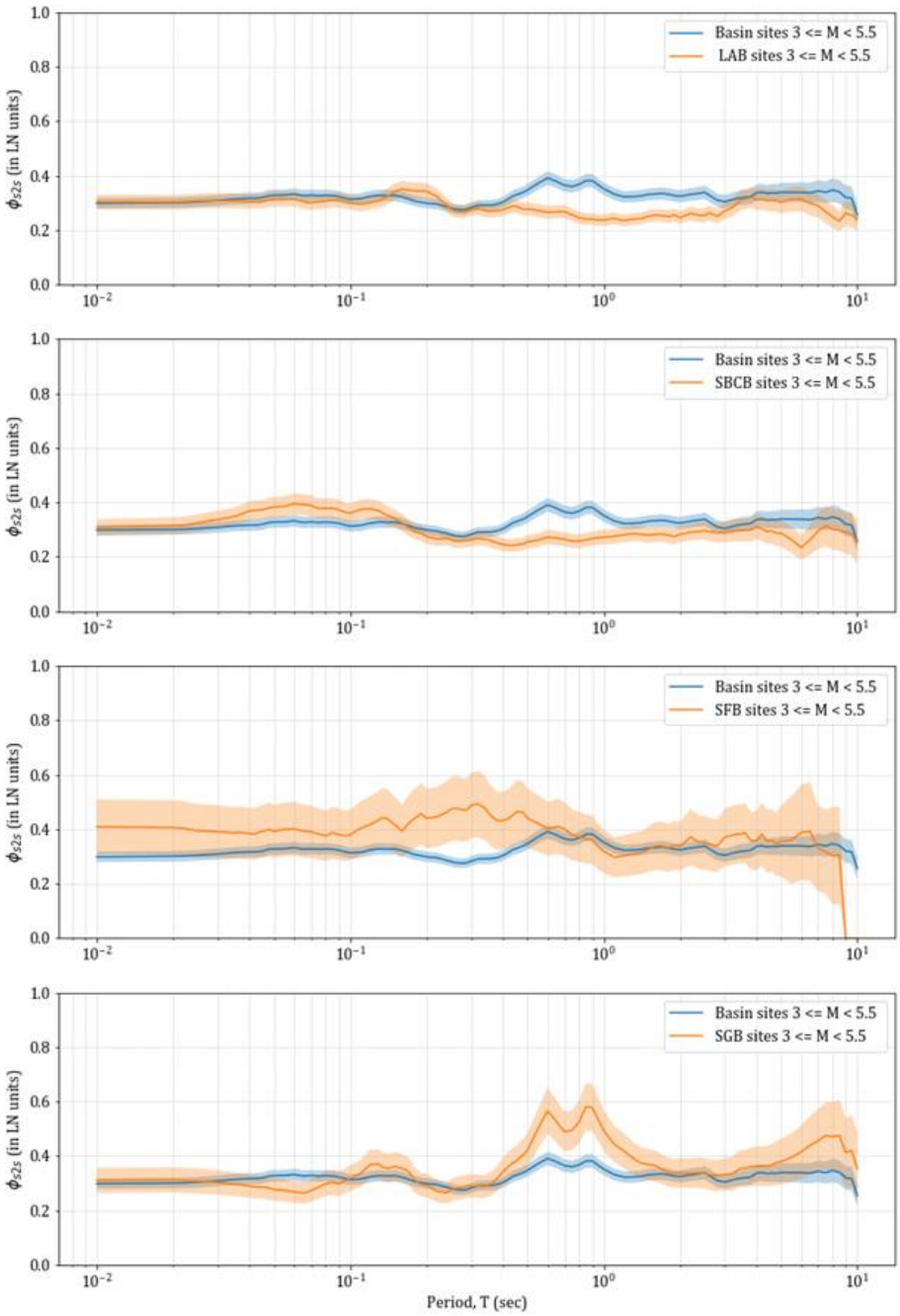

Figure 15. Variation of site-to-site standard deviations, and their 95% confidence intervals, as a function of period for four basin structures. LAB = Los Angeles basin, SBCB = San Bernardino-Chino basin, SFB = San Fernando basin, SGB = San Gabriel basin.

The morphology-based site categories have an appreciable impact on site-to-site standard deviation, which is a significant contributor to overall within-event dispersion. These effects are arguably the most impactful finding of this study. Dispersion is much lower for basin sites than for other site categories, whereas mountain-hill sites have relatively high site-to-site dispersion.

Individual basins have relatively minor variations in site-to-site variability, suggesting that a single model could be used to represent basins collectively in southern California.

Acknowledgments

Funding for this study is provided by California Strong Motion Instrumentation Program, California Geological Survey, Agreement Number 1016-985. This support is gratefully acknowledged. Partial support was also provided under award number G17AP00018 from the U.S. Geological Survey and from NSF-AGEP California Alliance Fellowship (awards 1306595, 1306683, 1306747, 1306760). The views and conclusions presented in this paper are those of the authors, and no endorsement is implied on the part of the State of California or the U.S. Federal government. We thank Yousef Bozorgnia of UCLA for providing access to data processing codes. We thank Phil Maechling, Edric Pauk, and Mei-Hui Su of the Southern California Earthquake Center for providing access to community velocity models.

References

Al Atik, L., Abrahamson, N. A., Bommer, J. J., Scherbaum, F., Cotton, F., and Kuehn, N., 2010. The variability of ground motion prediction models and its components, *Seism. Res. Lett.*, **81** 794–801.

Al Atik, L., 2015. NGA-East: Ground motion standard deviation models for Central and Eastern North America, *PEER Report No. 2015/09*, Pacific Earthquake Engineering Research Center, University of California, Berkeley, CA.

Allen, P. A., and Allen, J. R., 2013. *Basin Analysis: Principles and Application to Petroleum Play Assessment*. John Wiley & Sons.

Ancheta, T.D., Darragh, R.B., Stewart, J.P., Seyhan, E., Silva, W.J., Chiou, B.S.-J., Wooddell, K.E., Graves, R.W., Kottke, A.R., Boore, D.M., Kishida, T., and Donahue, J.L., 2014. NGA-West2 database, *Earthquake Spectra*, **30**, 989-1005.

Anderson, M., Matti, J., and Jachens, R., 2004. Structural model of the San Bernardino basin, California, from analysis of gravity, aeromagnetic, and seismicity data. *J. Geophy. Res.*: *Solid Earth*, **109**(B4).

Baher, S.A. and Davis, P.M., 2003. An application of seismic tomography to basin focusing of seismic waves and Northridge earthquake damage, *J. Geophy. Res.-Solid Earth*, **108**(B2), Art. No.2122.

Boore, D.M., 2010. Orientation-independent, nongeometric-mean measures of seismic intensity from two horizontal components of motion, *Bull. Seismol. Soc. Am.*, **100**, 1830–1835.

Brocher, T. M., Aagaard, B.T., Simpson, R.W., and Jachens, R.C., 2006. The USGS 3D seismic velocity model for northern California, presented at the 2006 Fall Meeting, AGU, San Francisco, California, 11–15 December, Abstract S51B–1266.

Campbell, K. W., and Bozorgnia, Y., 2014. NGA-West2 ground motion model for the average horizontal components of PGA, PGV, and 5% damped linear acceleration response spectra. *Earthquake Spectra*, **30**, 1087-1115.

Chen, P., and Lee, E. J., 2017. UCVM 17.3.0 Documentation. Retrieved from http://hypocenter.usc.edu

Contreras, V., 2017. Development of a Chilean ground motion database for the NGA-Subduction project, *MS Dissertation*, Univ. California, Los Angeles.

Dickinson W. R., 1974, Plate tectonics and sedimentation: Society of Economic Paleontologists and Mineralogists Special Publication 22, p. 1-27.

Dickinson, W. R., 1976, Plate tectonic evolution of sedimentary basins: American Association of Petroleum Geologists Continuing Education Course Notes Series 1, 62 p.

Ely, G., P. Small, T. Jordan, P. Maechling, and F. Wang. 2016. A V_{S30}-derived near-surface seismic velocity model. In preparation. http://elygeo.net/2016-Vs30GTL-Ely+4.html.

Ely, G. P., Jordan, T. H., Small, P., & Maechling, P. J. (2010). A V_{S30}-derived near-surface seismic velocity model. In *Abstract S51A-1907, Fall Meeting*. San Francisco, CA: AGU.

Field, E. H., and Jacob, K.H., 1995. A comparison and test of various site response estimation techniques, including three that are not reference site dependent, *Bull. Seismol. Soc. Am.* **85**, 1127–1143.

Gelman, A., Carlin, J. B., Stern, H. S., Dunson, D. B., Vehtari, A., and Rubin, D. B., 2014. *Bayesian Data Analysis*, 3rd edition, CRC Press.

Graves, R.W., 1993. Modeling three-dimensional site response effects in the Marina District, San Francisco, California, *Bull. Seism. Soc. Am.*, **83**, 1042-1063.

Graves, R.W., Pitarka, A., and Somerville, P.G., 1998. Ground motion amplification in the Santa Monica area: effects of shallow basin edge structure, *Bull. Seism. Soc. Am.*, **88**, 1224-1242.

Hauksson, E., 2010. Crustal structure and seismic distribution adjacent to the Pacific and North America plate boundary in southern California, *J. Geophys. Res.*, **105 (**B6), 13,875–13,903.

Ingersoll, R. V. and Rumelhart, P. E., 1999. Three-stage evolution of the Los Angeles basin, southern California. *Geology*, **27**, 593-596.

Langenheim, V. E., Wright, T. L., Okaya, D. A., Yeats, R. S., Fuis, G. S., Thygesen, K., & Thybo, H., 2011. Structure of the San Fernando Valley region, California: Implications for seismic hazard and tectonic history. *Geosphere*, **7**, 528-572.

Lee, E.J., Chen, P., Jordan, T.H., Maechling, P.J., Denolle, M., and Beroza, G.C., 2014. Full-3-D tomography for crustal structure in southern California based on the scattering-integral and the adjoint-wavefield methods, *J. Geophys. Res.*, **119**, 6421–6451.

Kawase, H., 1996. The cause of the damage belt in Kobe: 'The basin edge effect,' constructive interference of the direct S-wave with the basin induced diffracted/Rayleigh waves, *Seism. Res. Letters*, **67**, 25-34.

Kingston, D. R., Dishroon, C. P., & Williams, P. A., 1983. Global basin classification system. *AAPG bulletin*, **67**, 2175-2193.

Kohler, M. D., Magistrale, H., and Clayton, R.W., 2003. Mantle heterogeneities and the SCEC reference three-dimensional seismic velocity model version 3, *Bull. Seismol. Soc. Am.*, **93**, 757–774.

Magistrale, H., Day, S., Clayton, R., Graves, R.W., 2000. The SCEC southern California reference three-dimensional seismic velocity model version 2, *Bull. Seism. Soc. Am.*, **90,** S65–S76.

Parker, G.A., Stewart, J.P., Hashash, Y.M.A., Rathje, E.M., Campbell, K.W., Silva, W.J., 2019. Empirical linear seismic site amplification in Central and Eastern North America, *Earthquake Spectra*, https://doi.org/10.1193/083117EQS170M.

Petersen, M.D., Moschetti, M.P., Powers, P.M., Mueller, C.S., Haller, K.M., Frankel, A.D. Zeng, Y. Rezaeian, S., Harmsen, S.C., Boyd, O.S., Field, N., Chen, R., Rukstales, K.S., Luco, N., Wheeler, R.L., Williams, R.A., and Olsen, A.H., 2015. The 2014 United States national seismic hazard model. *Earthquake Spectra*, **31**, S1-S30.

Pitarka, A., Irikura, K., Iwata, T. and Sekiguchi, H., 1998. Three-dimensional simulation of the near-fault ground motion for the 1995 Hyogo-ken Nanbu (Kobe), Japan, earthquake, *Bull. Seism. Soc. Am*., **88**, 428-440.

Rathje, E.M., Dawson, C., Padgett, J.E., Pinelli, J.-P., Stanzione, D., Adair, A., Arduino, P., Brandenberg, S.J., Cockeril, T., Esteva, M., Haan, F.L. Jr., Hanlon, M., Kareem, A., Lowes, L., Mock, S., and Mosqueda, G., 2017. DesignSafe: A new cyberinfrastructure for natural hazards engineering. *Natural Hazards Review*. **18**.

Shaw, J. H., Plesch, A., Tape, C., Suess, M.P., Jordan, T.H., Ely, G., Hauksson, E., Tromp, J., Tanimoto, T., Graves, R.W. et al., 2015. Unified structural representation of the southern California crust and uppermantle, *Earth Planet. Sci. Lett.*, **415**, 1, doi: 10.1016/j.epsl.2015.01.016.

Small, P., Gill, D., Maechling, P. J., Taborda, R., Callaghan, S., Jordan, T. H., Olsen, K.B., Ely, G.P., and Goulet, C., 2017. The SCEC unified community velocity model software framework. *Seismological Research Letters*, **88**(6), 1539-1552.

Stafford, J.S., Rodriguez-Marek, A., Edwards, B., Kruiver, P.P., and Bommer, J.J., 2017. Scenario dependence of linear site-effect factors for short-period response spectral ordinates. *Bull. Seismol. Soc. Am.*, **107**, 2859–2872.

Stephenson, W.J., Williams, R.A., Odum, J.K., and Worley, D.M., 2000. High-resolution seismic reflection surveys and modeling across an area of high damage from the 1994 Northridge earthquake, Sherman Oaks, California, *Bull. Seism. Soc. Am.*, **90**, 643-654.

Stewart, J.P., Afshari, K., Goulet, C.A., 2017. Non-ergodic site response in seismic hazard analysis, *Earthquake Spectra*, **33**, 1385-1414.

Süss, M. P., and Shaw, J.H. 2003. P wave seismic velocity structure derived from sonic logs and industry reflection data in the Los Angeles basin, Calif. *J. Geophys. Res.*, **108**, 2170, doi: 10.1029/2001JB001628.

Thompson, E.M., 2018. An updated Vs30 Map for California with geologic and topographic constraints: U.S. Geological Survery data release. https://doi.org/10.5066/F7JQ108S.

Thompson, E.M., Wald, D.J., and Worden, C.B., 2014. A V_{S30} map for California with geologic and topographic constraints, *Bull. Seismol. Soc. Am.*, **104**, 2313-2321

Wang, P., Stewart, J.P., Bozorgnia, Y., Boore, D.M., and Kishida, T., 2017. "R" Package for computation of earthquake ground-motion response spectra, *PEER Report No. 2017/09*, Pacific Earthquake Engineering Research Center, UC Berkeley, CA.

Yeats, R.S., 2004. Tectonics of the San Gabriel Basin and surroundings, southern California. *GSA Bulletin*, **116**(9-10), 1158-1182.

Yong, A.K., 2016. Comparison of measured and proxy-based V_{S30} values in California, *Earthquake Spectra*, **32**, 171-192.

Yong, A.K., Hough, S.E., Iwahashi, J., and Braverman, A., 2012. Terrain-based site conditions map of California with implications for the contiguous United States. *Bull. Seismol. Soc. Am.* **102**, 114-128.

CRITICAL ASSESSMENT OF ACCIDENTAL TORSION IN BUILDINGS WITH SYMMETRIC PLANS USING CSMIP DATA

Yijun Xiang, Farzad Naeim, Farzin Zareian

Department of Civil & Environmental Engineering
University of California, Irvine

Abstract

This research investigated the validity of accidental torsion provisions in ASCE-7 for buildings that are regular in plan and elevation with rigid diaphragms. MDOF systems of 4-, 8-, 12- and 20-story building prototypes along with plan aspect ratio of 1:1, 1:2, 1:4 and 1:8 are modeled. The building models possess translational to rotational period ratios (Ω) ranging from 1.1 to 2.0. Uncertainty in stiffness is treated as the main source of eccentricity. Equivalent design eccentricity indicates that the 5% equivalent eccentricity rule is adequate to capture the median magnification in deformation due to accidental torsion. 11 buildings selected from CSMIP database are studied to verify the analytical results.

Introduction

Consideration of accidental torsion is required by seismic code provisions such as ASCE 7-10 (ASCE, 2010) and ASCE 7-16 (ASCE, 2017) to account for the randomness in mass location and stiffness of Vertical Lateral Load Resisting systems (VLLRs). Equivalent seismic lateral force needs to be applied at a distance which equals 5% of the plan dimension perpendicular to ground motion direction from the center of mass of floor diaphragm.

A considerable amount of research has been carried out for accidental torsional moments in symmetric-in-plan buildings (De la Llera & Chopra 1992; 1994; 1995; Lin et al., 2001; Hernandez & Lopez, 2004; De-la-Colina & Almeida, 2004; Basu et al., 2014). De la Llera and Chopra (1992) used recorded data from three buildings instrumented by California Strong Motion Instrumentation Program (CSMIP) to conclude that the 5% accidental torsional rule is adequate. They developed single-story linear analytical models in their follow up research (De la Llera & Chopra, 1994; 1995), demonstrating that 5% eccentricity is adequate for most steel and concrete special moment-resisting frames based on response spectrum analysis (RSA).

In order to quantify the level of uncertainty in stiffness of VLLRs, the variability of element cross section dimensions, second moment of inertia, and material strength is studied through literature review. For reinforced concrete material, Ramsay, Mirza and MacGregor (1979) concluded that deformation of reinforced concrete beams has a coefficient of variation (CoV) of 0.14, and the same value is applied in De la Llera and Chopra (1994) to model reinforced concrete frames. While for steel, Ellingwood and Galambos (1980) and Melechers (1987) showed that the coefficient of variation of Young's modulus is approximately 0.06. ASTM A6-05 and ASTM A992-04 provide variability of structural element dimensions and material strength, respectively. Bournonville et al. (2004) concluded that coefficient of variation

of reinforcement yield strength ranges from 0.03 to 0.09. In this research, section dimension is assumed to have a coefficient of variation ranging from 0.01 to 0.04, and material yield stress is assumed to have a coefficient of variation of 0.05. To keep consistency with reinforced concrete material, a CoV of 0.14 is set for steel material with a slight overestimate and therefore leads to slightly conservative results.

Methodology

This study aims at quantifying building torsional characteristics such as deformation magnification factors α_1 and α_2 (will be explained in the following) and the equivalent design eccentricity (represented by e(%) shown in the following) which is used to account for effect of accidental torsion during design procedures. Statistics measures of these parameters (e.g. median and 84%) are obtained through building models subject to ground motion excitations of different hazard levels.

Translational and torsional modes of vibrations simultaneously affect the general response of a building. In a parametric form, a factor denoted with Ω, that is the ratio of dominant translational period (T_{tran}) to dominant rotational period (T_{rot}), is introduced (Eq. 1). Large Ω values associated with perimeter frame buildings and small Ω values represent core-wall systems with low torsional stiffness. Building models of Ω ranging from 1.1 to 2.0 are developed, which covers most of the building cases.

$$\Omega = \frac{T_{tran}}{T_{rot}} \quad \text{Eq. (1)}$$

Parameters that characterize building torsional response

Torsional vibration in a nominally symmetric system is caused by asymmetric stiffness distribution with randomness in stiffness of VLLRs. Measurements are taken for the largest displacement amplification among four corners of each floor based on the rigid diaphragm assumption. Given this background, two torsional vibration parameters are introduced (Eq.2, and Eq.3) to study the contribution of displacement response to building torsional effects at each floor. In these equations, δ_{tran} denotes the maximum displacement of the floor due to translational vibration; δ_{rot} denotes the maximum rotated angle of the floor due to translational vibration. δ_b denotes the displacement of a symmetric base system (with no randomness in VLLRs). α_1 is the ratio of peak total displacement of an asymmetric system to peak translational response of the base system. It estimates the total displacement amplification considering stiffness eccentricity and compares it to a non-eccentric base system. α_2 is the ratio of peak total displacement to peak translational displacement within the same asymmetric system. It stands for the contribution of rotational response to the total response.

$$\alpha_1 = \frac{max(\delta_{trans} + \delta_{rot})}{max(\delta_b)} \quad \text{Eq. (2)}$$

$$\alpha_2 = \frac{max(\delta_{trans} + \delta_{rot})}{max(\delta_{trans})} \quad \text{Eq. (3)}$$

Equivalent eccentricity from static pushover

Torsional vibration characteristics represent the amplification in displacement due to stiffness uncertainty in asymmetric buildings, and those characteristics need to be transferred to a measure of a distance representing how far away the equivalent lateral force should be applied to the center of mass to capture the same amount of torsional displacement amplification during the design of the building. To analyze the displacement amplification caused by eccentric static loading, an eccentric equivalent lateral force is applied to the base system. In comparison, a non-eccentric equivalent lateral force is also applied to the base system at the center of mass. The ratio between two displacements in these two scenarios demonstrates the amplification due to eccentric push over (see Eq. 4). It can be shown that aside from Ω, the plan aspect ratio *n* affects pushover displacement amplification as well. The *n* term in Eq. 4 represents displacements measured at the edge of the diaphragm and the $(1+n^2)$ term represent amount of rotational inertia. Given time history displacement data, median and 84% of equivalent eccentricity (denoted as $e^{50\%}$ and $e^{84\%}$)can be obtained by equating median and 84% of α_1 (denoted with $\alpha_1^{50\%}$ and $\alpha_1^{84\%}$) with α_p as shown in Eq. 5 and Eq. 6, with *n* values of 1, 2, 4 and 8 applied.

$$\alpha_p = \frac{\delta_p}{\delta_{np}} = 1 + \frac{6ne}{\Omega^2(1+n^2)} \qquad \text{Eq. (4)}$$

$$e^{50\%} = \frac{\left(\alpha_1^{50\%} - 1\right)\Omega^2(1+n^2)}{6n} \qquad \text{Eq. (5)}$$

$$e^{84\%} = \frac{\left(\alpha_1^{84\%} - 1\right)\Omega^2(1+n^2)}{6n} \qquad \text{Eq. (6)}$$

Building Models and Ground Motions

4-story, 8-story, 12-story and 20-story building models are generated in OpenSees. For a 2D building model, each frame is designed as a single bay generic frame with 20’ bay width and 12’ story height. (see Figure 1). The ratio of the second moment of inertia of beams and columns in this idealized model is set to be 1.0, which leads to reasonable beam to column stiffness ratio (ρ) and strong column weak beam ratio (assuming proportional strength and stiffness).

Distribution of second moment of inertia along the building height follows the distribution of story shear using ASCE-7 Equivalent Lateral Force (ELF) method. Moment of inertia of beams and columns are computed through optimization method targeting periods of 1.6s, 2.4s, 3.0s and 4.0s for 4-story, 8-story, 12-story and 20 story building, respectively. Assuming each story yields at a drift ratio of 0.01, rotation of beams and columns are computed at story yield point, from which moment capacity of beams and columns can be obtained based on double curvature assumption. Springs with bilinear hysteretic (Ibarra et al., 2005) characteristics are placed at beam as illustrated in Figure 1. Parameters for the bilinear hysteretic springs are shown in Figure 1b. To show the validity of 2D generic model, pushover analysis is

carried out, Figure 2 shows the pushover curve of the generic frames subject to ELF lateral load from ASCE-7.

Three dimensional (3-D) systems with plan aspect ratio of 1:1, 1:2, 1:4 and 1:8 are modeled using 2-D generic frames in both directions. Figure 3 shows the plan view the 3-D models used in this study. A 3-D model with plan aspect ratio of 1:*n* is modeled as *n* numbers of 1:1 square buildings being placed in a row. This model is further simplified using four VLLRs, with each VLLR being *n* times stiffer and stronger, and with rotational stiffness K_θ, period ratio Ω. The dimension of the slab is unchanged. Each building model represents a certain case with fixed Ω and plan aspect ratio, and only those cases with two translational period (in two orthogonal directions) ratio larger than 0.5 and less than 2 are kept for ground motion time history analysis.

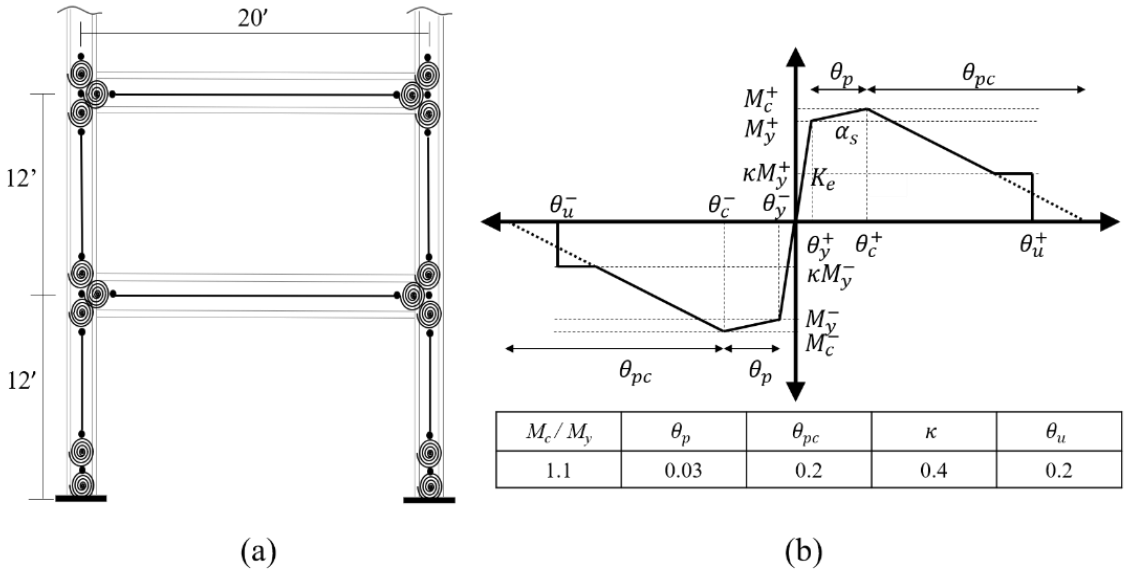

M_c / M_y	θ_p	θ_{pc}	κ	θ_u
1.1	0.03	0.2	0.4	0.2

Figure 1. Generic frame used in this study: (a) geometry, (b) spring backbone curve

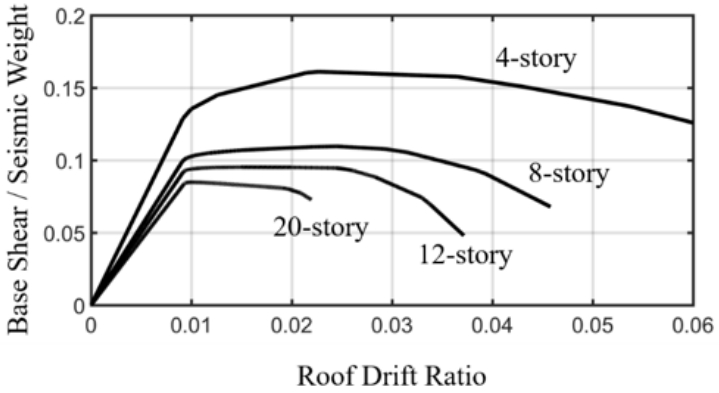

Figure 2. Pushover curves of the generic frames used in this study, (b) Modeling approach to capture plan aspect ratio

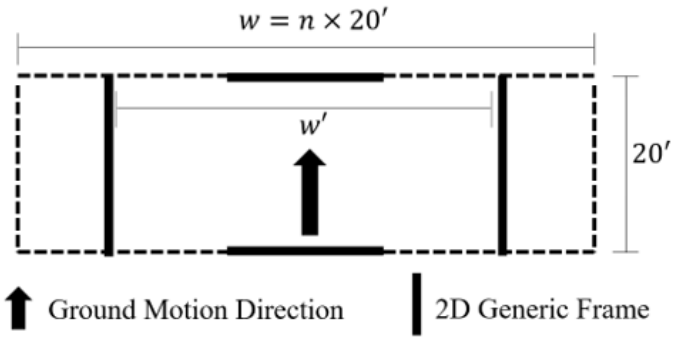

Figure 3. Modeling approach to capture plan aspect ratio

Two building locations are selected: Downtown San Francisco (37.7749°, -122.4194°) and Downtown Los Angeles (37.0416°, -118.2468°) and three design hazard levels are considered: 50% probability of exceedance in 50 years (return period of 72 years), 10% probability of exceedance in 50 years (return period of 475 years) and 2% probability of exceedance in 50 years (return period of 2475 years). Altogether six scenarios are analyzed in this study. Disaggregation using OpenSHA is first employed to obtain magnitude, distance and epsilon for each scenario. Conditional spectrum covering a period range from 0.2 times smallest first translational period to 1.5 times largest first translational period is then used for selection of 30 pairs of ground motion with scaling factor larger than 0.5 and lesser than 2.0.

General Observations and Trends

Results of the downtown Los Angeles site at 475 years average return period are illustrated in this section, similar patterns can be found at other hazard levels, and at the downtown San Francisco site. The authors suggest that the results of a 475 years average return period would be more attractive given that this hazard level is generally closer to the design basis earthquake in ASCE-7. Statistics of torsional characteristics such as α_1, α_2 and equivalent eccentricity are computed at all story levels. One may either focus on statistics of the most critical floor with the largest value of α_1 and α_2, representing the worst-case scenario, or focus on statistics of all floors. Results of *all floors* from 8-story and 12-story building models are illustrated in this section, similar results can be found for 4-story and 20-story buildings.

Figure 4 shows the variation of median and 84% of α_1 (i.e. $\alpha_1^{50\%}$ and $\alpha_1^{84\%}$) for all buildings with combinations of aspect ratio and Ω. Circle, asterisk, triangle, and square markers represent information associated with 1:1, 1:2, 1:4, and 1:8 floor plan aspect ratios, respectively. Similar trend can be observed in both median value and dispersion (difference between 50% and 84%) of α_1 as they decline with Ω becomes larger. In general, 12-story buildings have higher α_1 compared to 8-story buildings: the median of α_1 for 12-story buildings can reach up to 1.16 and the 84 percentiles up to 1.35; the median of α_1 for 8-story buildings can reach up to 1.10 and the 84 percentiles up to 1.30.

Figure 5 shows the variation of median and 84 percentiles of α_2 (i.e. $\alpha_2^{50\%}$ and $\alpha_2^{84\%}$) for all buildings with respect and Ω. It can be observed that although both acting as inversely proportional to Ω, α_2 has a much higher dependency on Ω than α_1. 8-story buildings can have α_2

values as high as 1.15 in median, and 1.37 in 84 percentiles. For tall buildings such as 12-story ones, α_2 goes up to 1.19 in median and 1.37 in 84 percentiles.

Equivalent eccentricity is even less dependent on Ω, because the mapping from α_1 to α_p offsets the Ω dependency. Figure 6 shows that the median value of equivalent eccentricity to capture accidental torsional moment is between 2% to 5% for almost all buildings and floor aspect ratios except for 1:1 floor plan aspect ratio, where median equivalent eccentricity exceeds 9%. Much of this deviation is due to the derivation of α_p (see Eq. 4). A larger equivalent eccentricity is needed for a 1:1 plan to achieve similar displacement magnification to that of a larger floor plan aspect ratio. In the same manner, for the 84 percentiles, equivalent eccentricity is between 6% and 12% for all cases except 1:1 plan aspect ratio, which can reach 28%.

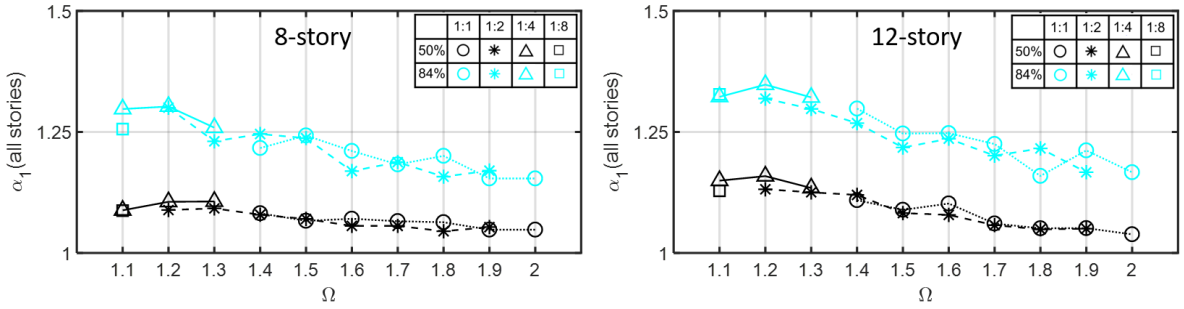

Figure 4. Variation of $\alpha_{1,all}^{50\%}$ and $\alpha_{1,all}^{84\%}$ with respect to Ω and plan aspect ratio for all buildings

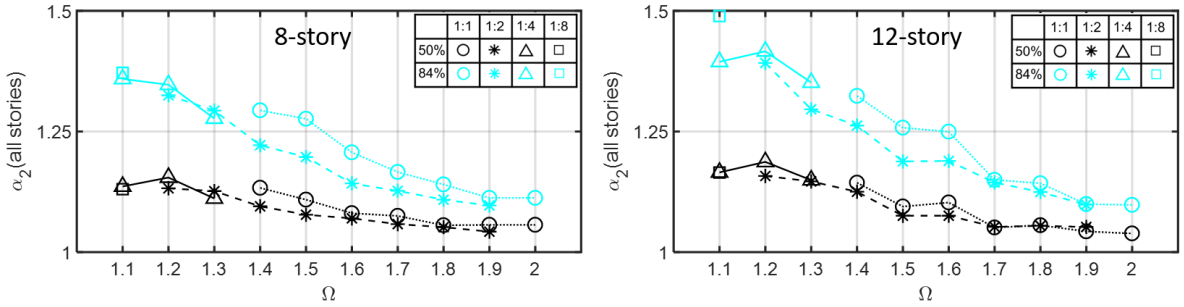

Figure 5. Variation of $\alpha_{2,all}^{50\%}$ and $\alpha_{2,all}^{84\%}$ with respect to Ω and plan aspect ratio for all buildings

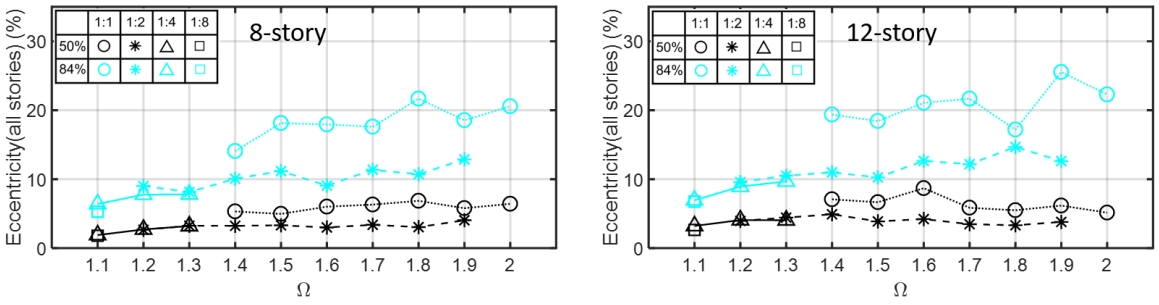

Figure 6. Variation of $e_{all}^{50\%}$ and $e_{all}^{84\%}$ with respect to Ω and plan aspect ratio for all buildings

Comparison between Analytical and CSMIP data

To validate analytical results, variation of α_2 with respect to Ω and plan aspect ratio of 11 buildings along with 12 sets of translational and rotational responses are selected from CSMIP database (Table 1). The selected buildings are nominally symmetric in plan and have more than one sensor on each floor in at least one direction (#57357 has two sensors in both directions) to enable extraction of rotational response. 4- and 5-story CSMIP buildings are categorized into the 4-story building group, 7-, 8- and 9-story CSMIP buildings are categorized into the 8-story building group and 13-story CSMIP buildings are categorized into the 12-story building group. As shown in Figure 7 and 8, α_2 is computed from every instrumented floor for each seismic event, then compared to the analytical results of $\alpha_{2,all}^{50\%}$ and $\alpha_{2,all}^{84\%}$ under hazard level of 50% probability of exceedance in 50 years (72-year average return period) at downtown Los Angeles site. The authors believe this comparison is relatively accurate since the recorded seismic events have spectral acceleration ranging from 0.0004g to 0.5g, with a median of 0.03g. In order to make comparison with analytical results, plan aspect ratio of CSMIP buildings is manually divided into two categories: larger than 1:1 and less than 1:2, larger than 1:2 and less than 1:4, denoted by red circle and blue cross respectively in Figure 7 and 8. Ω is computed using signal processing and system identification techniques, so that the Ω estimate varies for the same building subject to different ground motion excitations.

Table 1. Selected buildings from CSMIP database

Building ID	*Number of stories*	*Plan Aspect Ratio*	*Category*
12299	4	1.8	
58261	4	1.9	4-story
24463	5	1.4	
12493	4	1.7	
24571	9	2.5	
24386	7	2.8	8-story
23481	7	1.5	
24249	8	2.3	
57357, x-dir	13	1.0	
57357, y-dir	13	1.0	12-story
58354	13	1.0	
24322	13	2.6	

Analytical building models have Ω values ranging from 1.1 to 2; Ω of CSMIP buildings do not necessarily cover the same range and can reach less than 1.1 under certain circumstances. However, a declining trend in α_2 with increasing Ω can be observed both in analytical models and CSMIP buildings. Plan aspect ratio, on the other hand, is not as a significant factor as Ω for both analytical and CSMIP statistics. The 50 percentiles of the analytical results are able to capture the median of α_2 obtained from CSMIP buildings and the dispersion of CSMIP data matches well with that of analytical data: the more torsionally sensitive the system is, the higher the variance of α_2 will be.

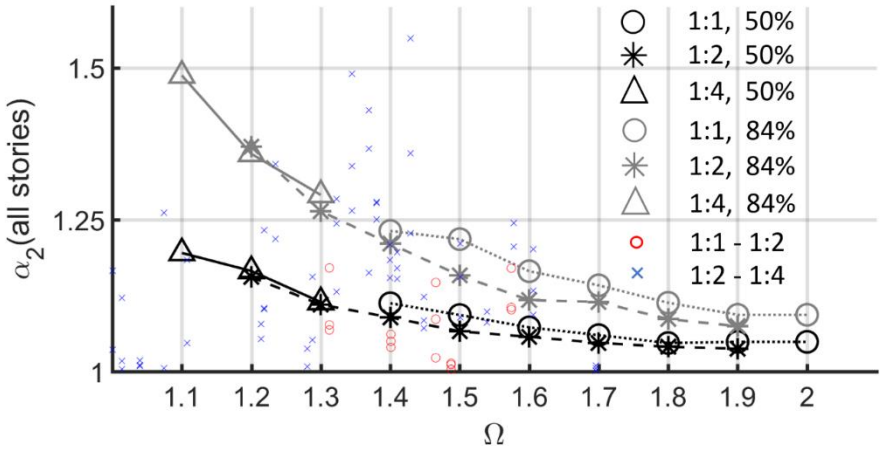

Figure 7. Analytical and CSMIP data of $\alpha_{2,all}^{50\%}$ and $\alpha_{2,all}^{84\%}$ with respect to Ω and plan aspect ratio for 4-story buildings subject to ground motions of 72-year average return period

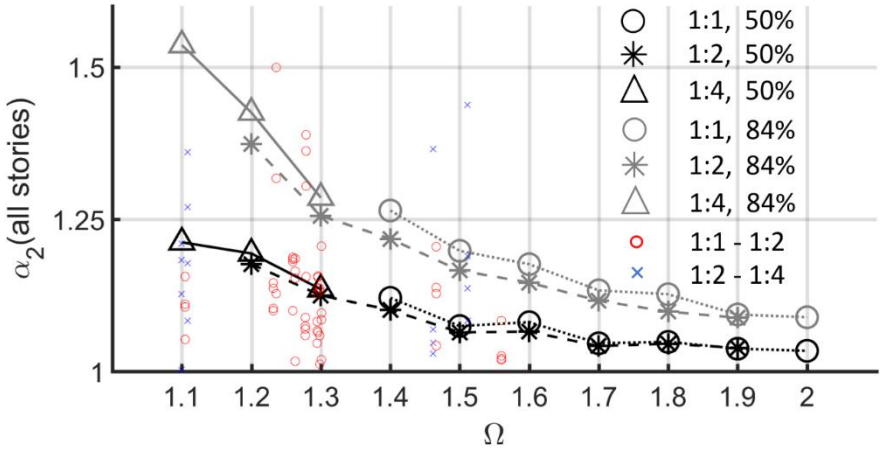

Figure 8. Analytical and CSMIP data of $\alpha_{2,all}^{50\%}$ and $\alpha_{2,all}^{84\%}$ with respect to Ω and plan aspect ratio for 4-story buildings subject to ground motions of 72-year average return period

Conclusions

The research aims at quantification of equivalent eccentricity and other torsional vibration characteristics such as displacement amplifications that captures the effects of accidental torsional moment in building structures. It is assumed that randomness in VLLRs stiffness is the source of accidental torsion. A combination of four build heights with 4, 8, 12, and 20 stories, four floor plan aspect ratios (i.e. 1:1, 1:3, 1:4, and 1:8) and period ratio Ω ranging from 1.1 to 2.0 are considered. For each combination, 3-D models are generated, and each model consists of a single-bay generic frame whose stiffness and strength are well calibrated to meet target dominant periods and reach yield moment at beam ends at 1% inter-story drift ratio.

The coefficient of variation of the stiffness of all structural elements is set to 0.14 following a comprehensive literature survey. By selecting 30 pairs of ground motions that represent seismic hazard with average 475 years return period at Downtown Los Angeles, Monte-Carlo simulation was employed to obtain statistical measures of α_1, α_2 and equivalent eccentricity *e*% due to randomness in VLLRs stiffness. Similar simulations were conducted for Downtown San Francisco, and at 72 and 2475 years return period at both locations.

The results demonstrate that the 5% equivalent eccentricity rule is adequate to capture the median value of magnification in deformation due to accidental torsion. In all cases this value is conservative other than buildings with 1:1 aspect ratio, where a 10% equivalent eccentricity may be required. This conclusion is based on preforming statistical analysis on all floor displacement magnifications and the reported value would be larger if the most critical is or a higher than median confidence (e.g. 84%) is sought to develop the estimates of equivalent eccentricity.

11 symmetric-in-plan buildings with recorded translational and rotational response are selected from CSMIP database. Selected buildings fall into 3 categories in terms of building heights: 4-, 8- and 12-story, and into 2 categories in terms of plan aspect ratio: 1:1 – 1:2 and 1:2 – 1:4. Results of CSMIP data is compared to analytical data obtained from 72-year average return period at downtown Los Angeles site. A good match in median values and dispersion of α_2 with respect to Ω verifies the validity of analytical results.

Acknowledgements

The contents of this report were developed under Agreement No. 1016-986 from the California Department of Conservation, California Geological Survey, Strong Motion Instrumentation Program. However, these contents do not necessarily represent the policy of that agency nor endorsement by the State Government.

References

ASCE-American Society of Civil Engineers (2007). *Seismic rehabilitation of existing buildings*. ASCE/SEI 41-06, Reston, VA.

ASCE-American Society of Civil Engineers (2017). *Minimum Design Loads for Buildings and Other Structures* (ASCE/SEI 7–16). American Society of Civil Engineers: Reston, VA.

ASCE-American Society of Civil Engineers (2010). *Minimum Design Loads for Buildings and Other Structures* (ASCE/SEI 7–10). American Society of Civil Engineers: Reston, VA.

ASTM A6 (2005). *Standard Specification for General Requirements for Rolled Structural Steel Bars, Plates, Shapes, and Sheet Piling*. American Standards for Testing and Materials, ASTM International, West Conshohocken, Pennsylvania.

ASTM A992 (2004). *Standard Specification for Structural Steel Shapes.* American Standards for Testing and Materials, ASTM International, West Conshohocken, Pennsylvania.

Baker, JW. (2011). Conditional Mean Spectrum: Tool for Ground-Motion Selection. ASCE Journal of Structural Engineering, 137 (3), 322-331.

Basu, D., Constantinou, M., Whittaker, A. (2014). An Equivalent Accidental Eccentricity to Account for The Effects of Torsional Ground Motion on Structures. *Engineering Structures*, 69: 1-11.

Bournonville, M., Dahnke, J. and Darwin, D. (2004). Statistical Analysis of the Mechanical Properties and Weight of Reinforcing Bars. *Structural Engineering and Engineering Materials*. Report 04-1.

De-la-Colina, J., Almeida, C. (2004). Probabilistic Study on Accidental Torsion of Low-Rise Buildings. *Earthquake Spectra*, 20(1):25-41.

De la Llera, JC., Chopra, A. (1992). Evaluation of Code-Accidental Torsion Provisions using Earthquake Records from Three Nominally Symmetric-Plan Buildings. *SMIP92 Seminar Proceedings*.

De la Llera, JC., Chopra, A. (1994). Accidental Torsion in Buildings Due to Stiffness Uncertainty. *Earthquake Engineering and Structural Dynamics*, 23:117-136.

De la Llera, JC., Chopra, A. (1995). Estimation of Accidental Torsion Effects for Seismic Design of Buildings. *Journal of Structural Engineering*, 121(1):102-114.

Ellingwood, B., Galambos, T., MacGregor, J. and Cornell, C. (1980). Development of a probability based load criterion for American National Standard. *Special Publication No.577*, National Bureau of Standards, Washington, DC.

Hernandez, JJ., Lopez, O. (2004). Dependence of Accidental Torsion on Structural System Properties. *Proceedings of the 13th World Conference on Earthquake Engineering*, Vancouver, Canada.

Juang, J. (1997). Identification of Linear Structural Systems using Earthquake Induced Vibration Data. *Journal of Guidance, Control, and Dynamics*, 20(3):492-500.

Ibarra L.F., Medina R. A., and Krawinkler H. (2005). "Hysteretic models that incorporate strength and stiffness deterioration", Earthquake Engineering and Structural Dynamics, 34(12), 1489-1511.

Lin, WH., Chopra, A., De la Llera, JC. (2001). Accidental Torsion in Buildings: Analysis versus Earthquake Motions. *Journal of Structural Engineering*, 127(5):475-481.

Melchers, R. (1987). *Structural Reliability: Analysis and Prediction*, Ellis Horwood, Chichester, 1987.

Ramsay, R., Mirza, S., and MacGregor. (1979). Monte Carlo Study of Short Time Deflections of Reinforced Concrete Beams. *ACI*, Vol.76 (897-918)

Van Overschee, P., B. De Moor. (1996). *Subspace Identification of Linear Systems: Theory, Implementation, Applications*. Springer Publishing.

Zhang, H., Paevere, P., Yang, Y., Foliente, GC., Ma, F. (2001) System identification of hysteretic structures. In *Nonlinearity and Stochastic Structural Dynamics, IUTAM Symposium*, Chennai, India, 1999 Narayanan S, IyengarRN (eds), Kluwer: Dordrecht, The Netherlands; 289–306.

SYSTEM IDENTIFICATION OF SOIL-STRUCTURE INTERACTION MECHANISMS FOR BUILDING STRUCTURES

D. S. Kusanovic, E. Esmaeilzadeh Seylabi, D. M. Asimaki

Department of Mechanical and Civil Engineering,
The California Institute of Technology, Pasadena, USA.

Abstract

We quantify the effects of dynamic soil-structure-interaction on building structures using system-identification techniques and finite element simulations. We develop analytic expressions for distributed spring and dashpot elements at the soil-foundation interface in terms of dimensionless variables. A system-identification approach based on Extended-Kalman-Filter is employed to estimate the *true* soil impedance as seen from the building-foundation system. The impedances estimated are next used to span the range of applicability of the proposed soil impedance model using nonlinear curve-fitting. We find good-agreement between the proposed flexible-based-model and the full finite element-model in period lengthening, radiation damping, time-history responses and their frequency contents.

Introduction

The accuracy of numerical models in civil engineering to predict the linear or nonlinear responses of structures depends among other phenomena on how well sources of energy dissipation and interaction processes are modeled. Energy dissipation mechanisms in the last decades has been considered through a series of simplified models: for instance, energy dissipation in buildings has been represented using mathematical models based on *viscous damping*. The basic idea is to combine all the sources of energy dissipation -- especially those which may be impractical, too complex, or not fully understood -- into a simple set of viscous parameters. Although it has been well established that some of the dissipation mechanisms do not behave in a viscous manner (Bernal 1994, Hall 2006), this inconsistency is frequently ignored in engineering practice because it simplifies the analysis (Jacobsen 1930) and produces reasonable results (Beck 1980). On the other hand, *soil-structure-interaction* (SSI) modeling is most of the time accounted in practice using *fixed-base* building models. In this approach modification of properties such as damping ratios is usually performed to account for mechanisms such as radiation damping. However, SSI effects can be considered in numerical analyses of building structures, more rigorously, using one of two methods: the *direct method* and the *substructure method*. In the *direct method*, the super-structure, the foundation, and the surrounding soil are explicitly taken into account, using for the most part the finite element method (Bathe 1996, and Hughes 2000); and since it is impossible to model the semi-infinite extent of the soil with finite number of the elements, appropriate boundary conditions have to be determined and applied to model the radiated energy (Lysmer 1969, and Basu 2003). Due to the computational time, memory constraints, and numerical modeling expertise involved in implementing the direct method, the state-of-the-practice has adopted the *substructure method*

(Wolf 1985, and NEHRP 2013). In this case, the problem is divided into two systems: *the superstructure* and the *soil-foundation* sub-systems. The soil-foundation system is first represented as force-deformation relationships in a representative frequency, known as *impedance functions*, which are then applied to the nodes along the soil-foundation interface to model the dynamic interaction between soil-foundation and superstructure. However, this approach presents two major difficulties: (i) the superposition method only works when the soil behaves elastically, and (ii) the representative frequency of the combined system at which the impedance functions respond is not clear. In order to address the issues presented in the *substructure method*, we propose an inference technique based on extended Kalman filtering (EKF) to estimate the values of the dynamic soil-spring and soil-dashpot elements to account for the dynamic response of the coupled building-foundation system. The identified soil-spring and soil-dashpot elements are employed to derive closed-form parametric expressions for the distributed soil-stiffness and soil-dashpot elements. Although the presented framework is here demonstrated to estimate the impedance functions of linear soil-structure problems, it is general enough that it can be extended to the case that both the structure and the surrounding soil are nonlinear.

The remainder of the paper is organized as follows: in §2 and §3, we use dimensional analysis to derive analytic expressions of the soil spring and dashpot coefficients as seen from the building foundation. We calibrate these expressions using a Bayesian identification approach based on Extended-Kalman-Filter (EKF) formulated to minimize the error between the *full-finite-element-model* (direct-method) and the *flexible-base-model* (substructure-method). In §4, we present analytical expressions for the period elongation and radiation damping of a flexible-base system on distributed horizontal and vertical springs, expressed as a function of an equivalent fixed-base system. We also present the equations of motion of a planar building that explicitly account for the building and foundation geometry as well as the soil-stiffness and energy radiated away from the building. Finally, in §5, we provide some discussion and concluding remarks regarding this new framework for modeling SSI problems using the *substructure method*.

The Problem Statement and Dimensional Analysis

The SSI continuum model we investigate in this study is composed of a building represented by its first-modal-height (h). The building, at the same time, is supported on a foundation system whose geometry is characterized by its half-foundation-length (B), and its foundation-depth (D). Moreover, the foundation system rests on a homogeneous soil half-space characterized by its shear-wave velocity (V_s). The response of the continuum model is approximated using the finite-element-method (Bathe 1996, and Hughes 2000). The material and elements are here considered to be isotropic linear and elastic, and no viscous damping is added so that the energy radiated away from the building comes only from radiation damping. Since, there are a large number of different SSI configurations that can be modeled, we employ *dimensional-analysis* to span the *dimensional-parameter space*, so that all possible cases or at least those in the range of applicability in civil engineering are covered. These parameters agrees with those proposed in Veletsos 1974, and they are listed below,

a) Structure-to-soil stiffness ratio:

$$\Pi_1 = \frac{h}{V_S T}$$

b) Building-aspect ratio:

$$\Pi_2 = \frac{h}{B}$$

c) Foundation-aspect ratio:

$$\Pi_3 = \frac{D}{B}$$

Three different buildings with fixed-base-fundamental period $T \approx (0.5, 1.0, 1.5)$ s, fixed-first-modal height $h \approx (15.0, 30.0, 40.0)$ m, foundation depth $D = (1.0, 2.5, 5.0)$ m, and supported on eleven distinct soils with shear wave velocities $V_s = (80, 100, 125, 150, 175, 200, 225, 250, 300, 400, 500)$ m/s are considered. These values will generate the *structure-to-soil stiffness ratio* to vary between $\Pi_1 \in [0.05 - 0.4]$, the *building-aspect ratio* to vary between $\Pi_2 \in [1.5 - 4.0]$, and the *foundation aspect ratio* to vary between $\Pi_3 \in [0.1 - 0.5]$. The range of parameters Π_1, Π_2 and Π_3, are chosen to be consistent with the range of applicability presented in Stewart 1999. The buildings employed in the dimensional analysis are schematically shown in Figure 1.

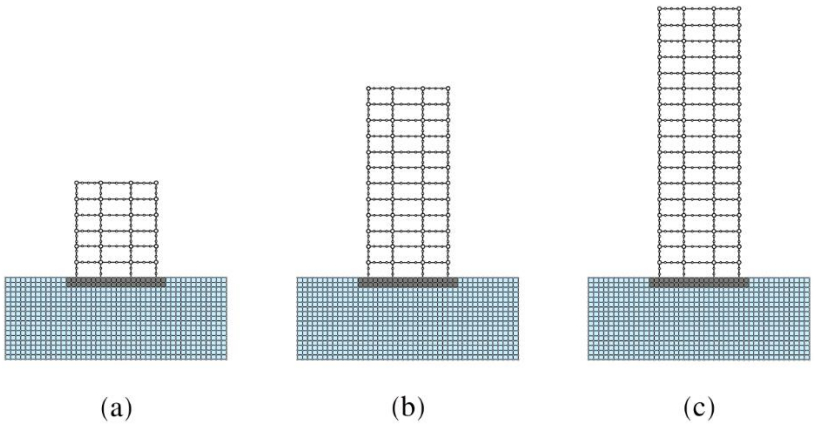

Figure 1. Building configurations employed in the dimensional analysis for the SSI problem.

Model Inversion for Soil-Structure Interaction Parameters

Once the *dimensional-parameter space* is defined, the *system-identification* can be applied to the SSI problems using the *substructure method*. The presented framework is thus performed in two stages: (i) as shown in Figure 2a, the *direct method* is employed from which a plane vertically-incident SV-wave is propagated upwards and the "true" building responses such as displacements or accelerations are recorded, then (ii) as shown in Figure 2b, the *substructure method* is employed in which the surrounding soil is replaced by a set of spring and dashpot

elements all over the foundation interface to emulate the soil inertia, stiffness and energy radiated away from the building. Such soil-spring and soil-dashpot elements are updated so that the error between the *direct-method* and the *substructure-method* is minimized. This approach ensures that information of the higher modes are implicitly considered in the estimation of the soil spring and dashpot elements. As part of this procedure, for the given set of spring and dashpot elements, we need to solve the semi-discrete Equation (1).

$$\mathbf{M}\,\ddot{\boldsymbol{u}}(\widehat{\boldsymbol{\theta}}) + \mathbf{C}(\widehat{\boldsymbol{\theta}})\,\dot{\boldsymbol{u}}(\widehat{\boldsymbol{\theta}}) + \mathbf{K}(\widehat{\boldsymbol{\theta}})\,\boldsymbol{u}(\widehat{\boldsymbol{\theta}}) = -\boldsymbol{L_g}\ddot{u}_{FFM}(t), \qquad (1)$$

where the variable $\ddot{u}_{FFM}(t)\ \epsilon\ \mathbb{R}$ represents the free-field ground motion signal at time t. The vector $\boldsymbol{L_g}\ \epsilon\ \mathbb{R}^n$ represents the earthquake influence vector that acts on the system, i.e., the vector that quantifies the inertial forces. The vectors $\boldsymbol{u}(\widehat{\boldsymbol{\theta}})\ \epsilon\ \mathbb{R}^n$, $\dot{\boldsymbol{u}}(\widehat{\boldsymbol{\theta}})\ \epsilon\ \mathbb{R}^n$ and $\ddot{\boldsymbol{u}}(\widehat{\boldsymbol{\theta}})\ \epsilon\ \mathbb{R}^n$ are the outputs of the system - here the displacement, velocity and acceleration respectively. $\mathbf{M}\ \epsilon\ \mathbb{R}^{n\times n}$, $\mathbf{C}(\widehat{\boldsymbol{\theta}})\ \epsilon\ \mathbb{R}^{n\times n}$ and $\mathbf{K}(\widehat{\boldsymbol{\theta}})\ \epsilon\ \mathbb{R}^{n\times n}$are the mass, damping, and stiffness matrices of the dynamical system, $\widehat{\boldsymbol{\theta}}\ \epsilon\ \mathbb{R}^{n_\theta}$ is the vector of system identifiable parameters, n the number of degree-of-freedom of the system, and n_θ the number of identifiable parameters.

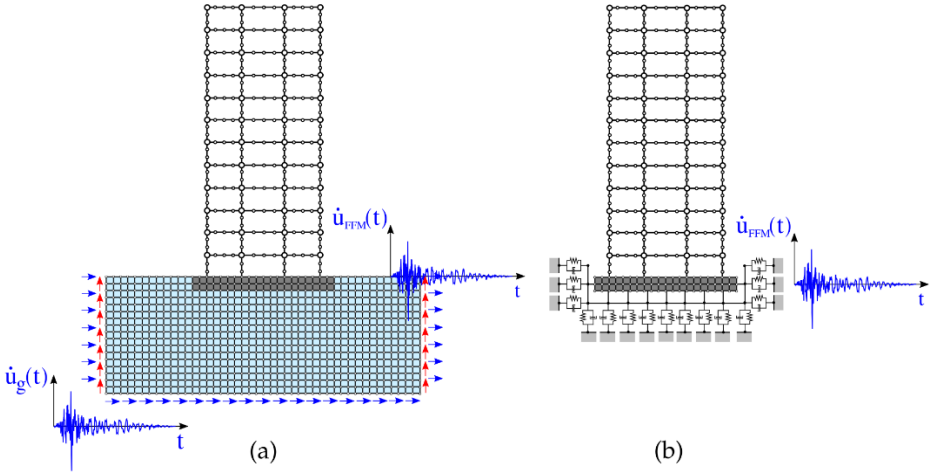

Figure 2. System-identification framework applied to SSI (a) Direct method from which the true responses are computed, and (b) Substructure method from which the spring and dashpot coefficients are estimated.

In the *direct-method*, the input-ground motion $\dot{u}_g(t)$ is prescribed as an effective force function at the base of the model at each soil node (Lysmer 1969, Asimaki 2004). For this purpose, a Ricker-wavelet (Ricker 1945) is selected and given in Equation (2),

$$\dot{u}_g(t) = (1 - 2\gamma(t - t_0)^2)e^{-\gamma(t-t_0)^2}, \qquad (2)$$

where $\gamma = (\pi f_0)^2$, $f_0 = 2$ [Hz] is the characteristic frequency, t_0 is the time position where the velocity will become maximum. On the other hand, the absorbing boundary conditions are implemented according to (Lysmer 1969, Asimaki 2004). Once the responses of the *direct-method* are obtained, an estimation method based on *Extended-Kalman-Filter* (EKF) is applied

to identify the soil-spring and soil-dashpot elements. The estimation process assumes that soil-spring and soil-dashpot coefficients are time-invariant, and therefore their evolution is modeled as a random walk process using a time invariant zero mean Gaussian noise with a known covariance matrix as it is given in Equation (5). We also assume that the error due to the misfit between the measured and predicted responses can be represented as a time invariant zero mean Gaussian noise with a known covariance matrix as it is given in Equation (6). Then, the parameter and measurement equations are given as follows:

$$\boldsymbol{\theta}_k = \boldsymbol{\theta}_{k-1} + \boldsymbol{q}_{k-1}, \quad (3)$$

$$\boldsymbol{y}_k = h_k(\boldsymbol{\theta}_k) + \boldsymbol{r}_k, \quad (4)$$

$$\boldsymbol{q}_k \sim (\boldsymbol{0}, \boldsymbol{Q}_k), \quad (5)$$

$$\boldsymbol{r}_k \sim (\boldsymbol{0}, \boldsymbol{R}_k), \quad (6)$$

where $\boldsymbol{\theta}_k \in \mathbb{R}^{n_\theta}$ is the parameter vector at the $k-$th updated stage. The variable $\boldsymbol{y}_k \in \mathbb{R}^{n_y}$ is the response vector of the system. $h_k(\boldsymbol{\theta}_k)$ is the non-linear vector-value measurement function such that, h: $\mathbb{R}^{n_\theta} \rightarrow \mathbb{R}^{n_y}$. $\boldsymbol{q}_k \in \mathbb{R}^{n_\theta}$ and $\boldsymbol{r}_k \in \mathbb{R}^{n_y}$ are the process and observation noises which are both assumed to be zero mean multivariate Gaussian noises with covariance $\boldsymbol{Q}_k \in \mathbb{R}^{n_\theta \times n_\theta}$ and $\boldsymbol{R}_k \in \mathbb{R}^{n_y \times n_y}$ respectively.

The EKF algorithm is then employed in the *substructure-method* to update the values of the soil-spring and soil-dashpot elements. A total of 99 identifications are required to modestly span the *dimensional-parameter space*. Then, a non-linear curve-fitting is performed to this set of coefficients to find a relation. In the dimensional analysis we have not considered ν as the influencing parameter, however the normalizing factor is written in terms of the Poisson's ratio such that the structure of each non-linear impedance function resembles the well-known static stiffness of homogeneous soil in half-space in the three dimensional setting. In particular, these equations take the following form

$$k_x(\hat{\boldsymbol{\pi}}, \hat{\boldsymbol{\alpha}}, \hat{\boldsymbol{\beta}}) = \frac{\rho_s {V_s}^2}{1-\nu} B \; \frac{\beta_0}{\beta_1 + \left(\frac{B}{B_r}\right)^{\beta_2}} \left[\alpha_0 + \alpha_1 \left(\frac{h}{B}\right)^{\alpha_2} \left(\frac{D}{B}\right)^{\alpha_3} \left(\frac{h}{V_S T}\right)^{\alpha_4}\right] \quad (7)$$

$$k_z(\hat{\boldsymbol{\pi}}, \hat{\boldsymbol{\alpha}}, \hat{\boldsymbol{\beta}}) = \frac{\rho_s {V_s}^2}{1-\nu} D \; \frac{\beta_0}{\beta_1 + \left(\frac{B}{B_r}\right)^{\beta_2}} \left[\alpha_0 + \alpha_1 exp\left(\alpha_2 \frac{h}{B}\right) exp\left(\alpha_2 \frac{D}{B}\right) \left(\frac{h}{V_S T}\right)^{\alpha_4}\right] \quad (8)$$

$$c_x(\hat{\boldsymbol{\pi}}, \hat{\boldsymbol{\alpha}}, \hat{\boldsymbol{\beta}}) = \frac{\rho_s {V_s}^2}{1-\nu} TD \; \frac{\beta_0}{\beta_1 + \left(\frac{B}{B_r}\right)^{\beta_2}} \left[\alpha_0 + \alpha_1 \left(\frac{h}{B}\right)^{\alpha_2} \left(\frac{D}{B}\right)^{\alpha_3} \left(\frac{h}{V_S T}\right)^{\alpha_4}\right] \quad (9)$$

$$c_z(\hat{\boldsymbol{\pi}}, \hat{\boldsymbol{\alpha}}, \hat{\boldsymbol{\beta}}) = \frac{\rho_s {V_s}^2}{1-\nu} TD \; \frac{\beta_0}{\beta_1 + \left(\frac{B}{B_r}\right)^{\beta_2}} \left[\alpha_0 + \alpha_1 \left(\frac{h}{B}\right)^{\alpha_2} \left(\frac{D}{B}\right)^{\alpha_3} \left(\frac{h}{V_S T}\right)^{\alpha_4}\right] \quad (10)$$

where $\widehat{\boldsymbol{\pi}} \epsilon \mathbb{R}^{n_p}$ is the *vector of dimensional parameters*, $\widehat{\boldsymbol{\alpha}} \epsilon \mathbb{R}^5$ is the vector of non-linear coefficient to be determined employing the data provided with the 99 analyses, and $\widehat{\boldsymbol{\beta}} \epsilon \mathbb{R}^3$ is the *influence-foundation vector*. Table I provides the estimated values that minimize the discrepancies between the data of the 99 configurations. The foundation influence coefficient vector is given as $\widehat{\boldsymbol{\beta}} = (1.16142, 0.05551, 1.93470)$, and the reference foundation length is taken as $B_r = 10\ [m]$ in the presented analysis.

Soil	Non-linear Regression Coefficients				
Impedance	α_0	α_1	α_2	α_3	α_4
k_x	0.007	0.2533	-1.6191	-0.8519	2.1399
k_z	0.0237	0.1785	0.178	-9.0619	-0.0938
c_x	0.0009	0.0205	-1.1906	-2.1511	3.1718
c_z	0.0002	0.0074	-1.0508	-1.1192	0.9116

Table I. Coefficients for the normalized soil-structure-interaction function for the soil coefficients provided in equations (7), (8), (9), and (10) respectively.

Validation of Soil-Spring and Soil-Dashpot Elements

A new set of fifteen more buildings with different topology are generated. The first-modal building parameter as well as the soil impedances for the new candidates are summarized in Table II. Figure 3 represents the configurations represented in Table II in the *dimensional-parameter space* Ω_{DS}. The blue-rectangle represents the *dimensional-analysis space* Ω_{DA} for which the inversion was carried out, and the size of these dots represents the intensity or susceptibility of the building frame to the SSI effect.

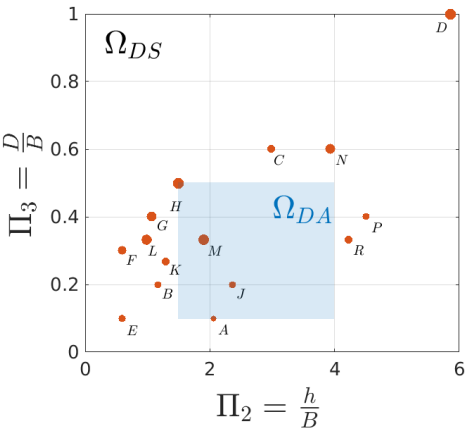

Figure 3. The validation cases represented in the dimension analysis domain.

In figures 4 - 6 the time history responses at the first-modal height for the total-horizontal displacement $\widehat{\Delta}_X^h$ and the total-vertical displacement $\widehat{\Delta}_Y^h$ are represented in solid-blue line and solid-red line for both the *direct-method* and the *substructure-method* respectively. In addition, the total-horizontal displacement of the roof $\widehat{\Delta}_X^r$ and the total-horizontal displacement of the ground level $\widehat{\Delta}_X^g$ are displayed in a similar fashion. Moreover, the frequency contents of such

signals for the total displacement are represented in the same figures, along with the normalized representation of the evaluated frame so that the different topologies considered in these three cases become much clearer. It can be seen in these figures that a good-agreement is achieved in both the total displacements at different levels, and the frequency content of the corresponding signals.

Frame Name	Fixed Period	Found. Mass	Building Dimensions			Shear Velocity	Dimensional Parameters		
			B	D	h				
	s	10^5 kg	m	m	m	V_s m/s	Π_1	Π_2	Π_3
A	0.25	0.125	5.0	0.5	10.270	250	0.162	2.05	0.10
B	0.35	0.250	5.0	1.0	5.820	80	0.208	1.16	0.20
C	0.40	0.500	5.0	3.0	14.940	150	0.248	2.99	0.60
D	0.90	0.500	5.0	5.0	29.320	120	0.272	5.86	1.00
E	0.25	0.500	10.0	1.0	5.890	130	0.181	0.59	0.10
F	0.28	0.500	10.0	3.0	5.900	100	0.214	0.59	0.30
G	0.60	0.500	10.0	4.0	10.670	75	0.237	1.07	0.40
H	0.48	0.500	10.0	5.0	14.980	115	0.274	1.50	0.50
J	1.08	0.500	15.0	3.0	35.380	190	0.172	2.36	0.20
K	0.65	0.500	15.0	4.0	19.350	150	0.198	1.29	0.27
L	0.49	0.500	15.0	5.0	14.830	120	0.253	0.99	0.33
M	0.85	0.500	15.0	5.0	28.510	125	0.268	1.90	0.33
N	0.53	0.500	5.0	3.0	19.650	150	0.247	3.93	0.60
P	1.75	0.500	10.0	4.0	45.100	150	0.172	4.51	0.40
R	2.13	0.500	15.0	5.0	63.440	150	0.198	4.23	0.33

Table II. Building parameters employed in the validation process.

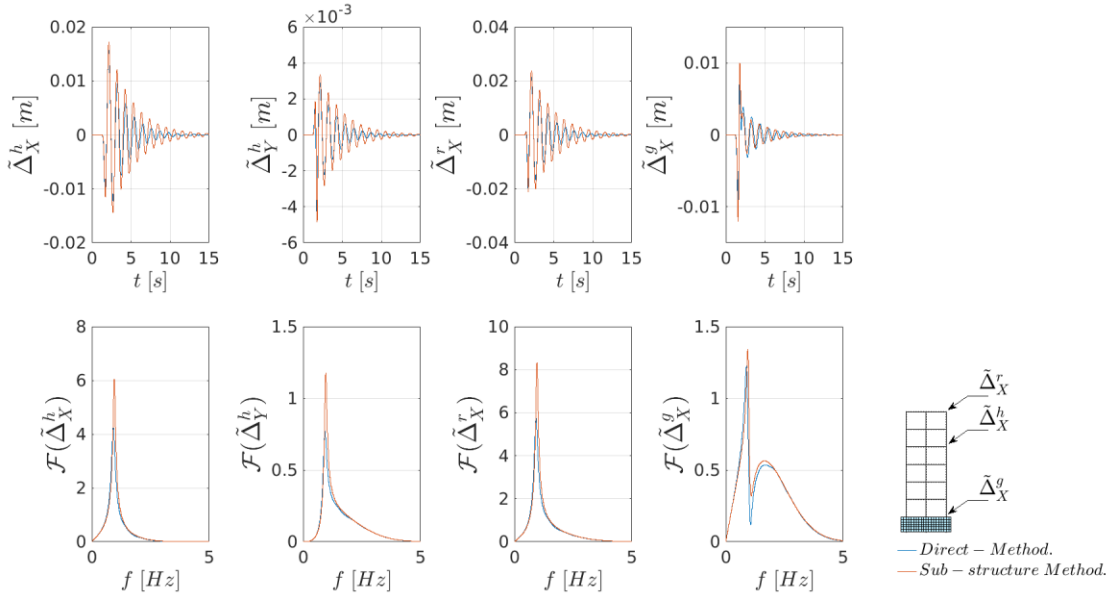

Figure 4. (Frame C): The parameters considered in the analysis are for the building a fixed-fundamental period T = 0.40 s, and a fixed-first modal height h = 14.94 m. The foundation dimensions are a half-length B = 5 m, and a foundation depth D = 3.0 m. The soil shear velocity is Vs = 150 m/s.

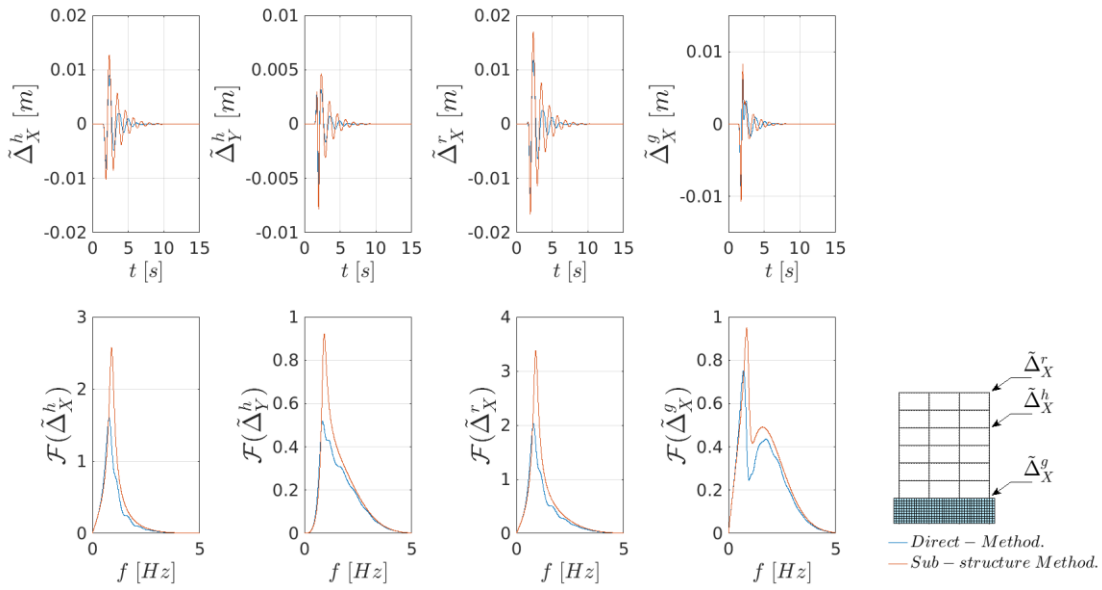

Figure 5. (Frame H): The parameters considered in the analysis are for the building a fixed-fundamental period T = 0.48 s, and a fixed-first modal height h = 14.98 m. The foundation dimensions are a half-length B = 10 m, and a foundation depth D = 5.0 m. The soil shear velocity is Vs = 115 m/s.

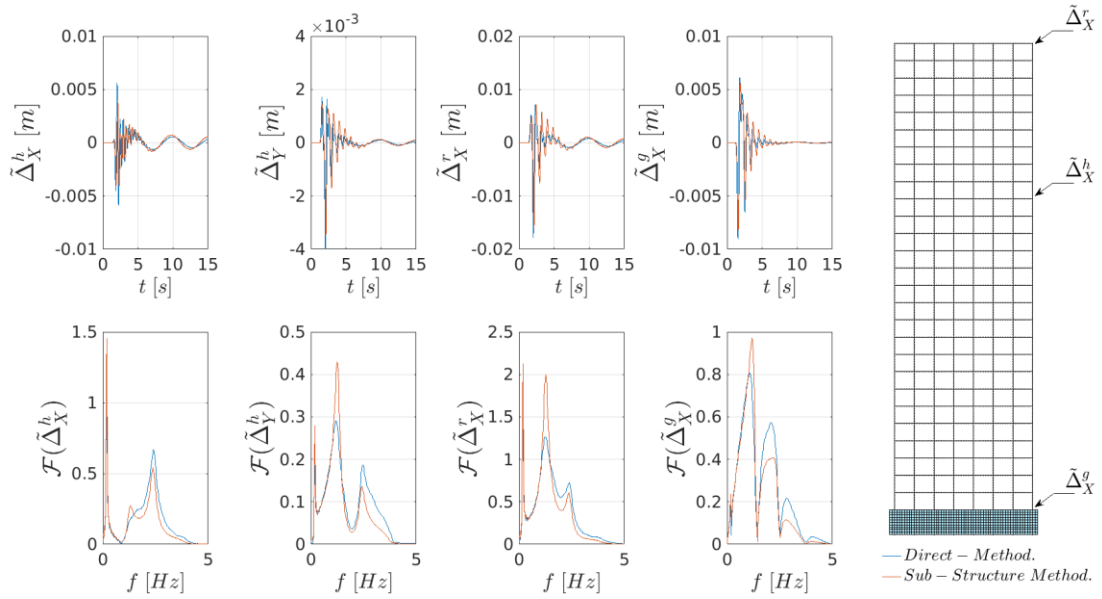

Figure 6. (Frame R): The parameters considered in the analysis are for the building a fixed-fundamental period T = 2.13 s, and a fixed-first modal height h = 63.44 m. The foundation dimensions are a half-length B = 15 m, and a foundation depth D = 5.0 m. The soil shear velocity is Vs = 150 m/s.

Table III quantifies the discrepancies between the *direct-method* and the *substructure-method*. In particular, the error associated to maximum displacement in the complete model is evaluated. The period elongation as well as the radiation damping error are also computed.

Finally the slope as well as the correlation of the time-series between the *full-finite-element model* and the *substructure-finite-element model* are computed at each node, and the maximum discrepancy between them is reported in Table III. The slope of such correlation measures how-well the simulated signal scales from the true response, and the Pearson's coefficient measures how-similar the signals are. It can be noted in Table III that the response signals of building frames M and J are very identical to the ones obtained using the *full-finite-element model*, when absolute quantities such as maximum displacement responses, period elongation, and global damping of the signal are compared. These results are consistent since these frames are inside the dimensional-design space, and we expect a good-agreement in this area. On the contrary, one should give special consideration to frame D, in which the signals, even though capture the maximum amplitude and the period elongation, fail in capturing the signal's pattern. This validation point is placed on purpose far from the *design space*, and therefore it was expected not to have a good-agreement since the extrapolation process becomes inaccurate. However, as it was pointed out earlier for all those frames that are near the dimensional-design space the results in displacements and frequency contents are quite accurate. Another important point to highlight is that for those buildings which are flexible, i.e., frame J, M, P and R, the higher mode responses are well-captured employing the *substructure-method* and the soil-spring and soil-dashpot elements presented here.

Model Reduction for Soil-Structure Interaction Parameters

We next present analytic expressions for the *period elongation* and *radiation damping* of an equivalent fixed-base system, as a function of the soil-stiffness (k_x, k_z) and soil-dashpot (c_x, c_z) elements which are distributed along the soil-foundation interface. In this analysis, we assume that the distributed soil-stiffness and soil-dashpot coefficients are known, moreover, the expressions derived hereafter can be considered as an extension of the ones proposed in Givens 2016, Stewart 1999 since we generate the coupling restoring moment term in a consistent manner by using both horizontal and vertical spring elements, as it is shown in Figure 7.

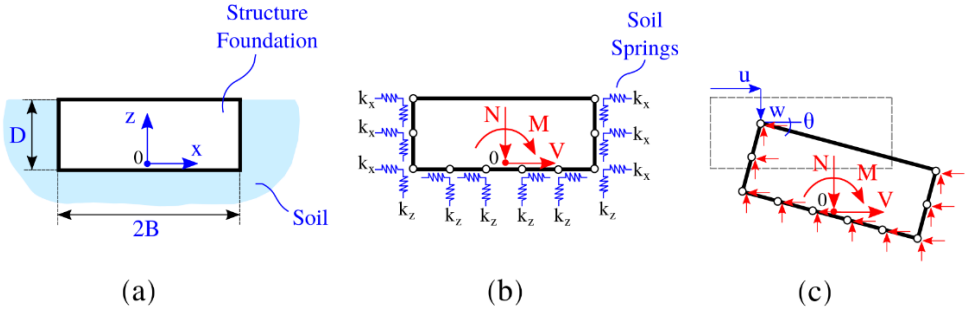

Figure 7. The soil-foundation system. (a) Geometry of the foundation system, (b) Modeling of the soil continuum as distributed springs, and (c) Free-body diagram of the foundation.

In Figure 7a, the external forces applied to the system are an axial force N, a shear force V, and a moment M. These forces are such that $N, V, M: f\left(\boldsymbol{u}(x,z)\right) \rightarrow \mathbb{R}$, where $\boldsymbol{u}(x,z)$ represents the displacement field. The restoring forces exerted by the soil are represented as springs acting over the foundation perimeter as shown in Figure 7b. Moreover, the foundation is assumed to be rigid so that the displacement field can be described with three degrees-of-

freedom as shown in Figure 7c. Next, and without loss of generality, we assume that the distributed horizontal springs k_x and vertical springs k_z are constant over the soil-foundation interface, this is basically to assume that $k_x(x,z) = k_x$, and $k_z(x,z) = k_z$. It should be noted that we used the same assumption for model inversion, as elaborated before. Satisfying equilibrium of forces and moment for the system presented in Figure 7c results in the lumped stiffness and damping matrices written in the following compact form.

$$\mathbf{\Lambda} = \begin{bmatrix} \Lambda_{zz} & 0 & 0 \\ 0 & \Lambda_{xx} & \Lambda_{x\theta} \\ 0 & \Lambda_{x\theta} & \Lambda_{\theta\theta} \end{bmatrix} = \begin{bmatrix} 2\,\lambda_z(D+B) & 0 & 0 \\ 0 & 2\,\lambda_x(D+B) & \lambda_x D^2 \\ 0 & \lambda_x D^2 & \frac{2}{3}\lambda_x D^3 + \frac{2}{3}\lambda_z B^3 + 2\,\lambda_z B^2 D \end{bmatrix}, \quad (11)$$

where the matrix $\mathbf{\Lambda}$ represents either the stiffness or damping matrix of the foundation system, and λ the distributed spring or dashpot coefficient. A dynamic analysis can now be performed to the simplified flexible-base system as the one shown in Figure 8b, in which the surrounding soil is replaced by uniform distributed horizontal and vertical springs k_x, k_z and dashpots c_x, c_z. Equation (11) allows us to compute the reduced reactive soil forces that must be added to the foundation so that the dynamic equilibrium using Dalambert's principle can be carried out.

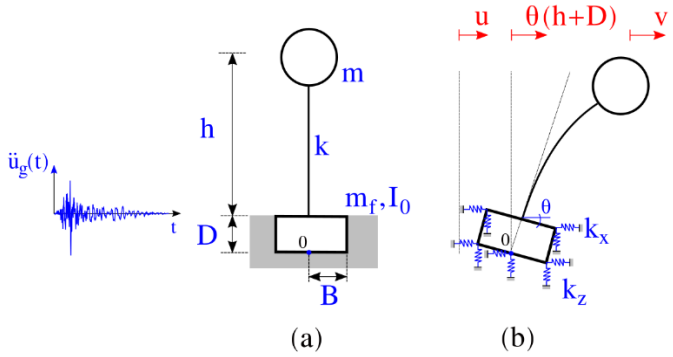

Figure 8. Reduced soil-structure-interaction model for dynamic analysis.

In this regard, the equation of motion is written as

$$\begin{bmatrix} m & m & m(h+D) \\ m & m+m_f & m(h+D)+m_f\frac{D}{2} \\ m(h+D) & m(h+D)+m_f\frac{D}{2} & m(h+D)^2+m_f\frac{D^2}{4}+I_0 \end{bmatrix} \begin{bmatrix} \ddot{u} \\ \ddot{v} \\ \ddot{\theta} \end{bmatrix} + \begin{bmatrix} c & 0 & 0 \\ 0 & c_{xx} & c_{x\theta} \\ 0 & c_{x\theta} & c_{\theta\theta} \end{bmatrix} \begin{bmatrix} \dot{u} \\ \dot{v} \\ \dot{\theta} \end{bmatrix}$$
$$+ \begin{bmatrix} k & 0 & 0 \\ 0 & k_{xx} & k_{x\theta} \\ 0 & k_{x\theta} & k_{\theta\theta} \end{bmatrix} \begin{bmatrix} u \\ v \\ \theta \end{bmatrix} = - \begin{bmatrix} m \\ m+m_f \\ m(h+D)+m_f\frac{D}{2} \end{bmatrix} \ddot{u}_g(t), \quad (12)$$

where the variables u, v, and θ are the relative displacement of the foundation, the relative displacement of the mass and the total rotation of the foundation respectively. The variables $\dot{u}, \dot{v}$, and $\dot{\theta}$ are the velocities, and $\ddot{u}, \ddot{v}$ and $\ddot{\theta}$ are the accelerations in the above mentioned degrees of

freedom. The variables k and c represent, respectively, the fixed-base stiffness and viscous damping of the building, and $k_{xx}, k_{x\theta}, k_{\theta\theta}, c_{xx}, c_{x\theta}$ and $c_{\theta\theta}$ are the soil-stiffness and soil-dashpot matrix coefficients provided in Equation (11). The variable m is the mass of the fixed-base building, m_f the mass of the foundation, and I_0 the rotational inertia of the foundation, and lastly $\ddot{u}_g(t)$ is the ground acceleration.

The stiffness and damping matrices in Equation (11) can also be employed to replace the simplified flexible-base system of modified height $\bar{h} = h + D$, stiffness $k \in \mathbb{R}^+$, structural damping $\beta \in \mathbb{R}^+$, supported by a distributed horizontal spring $k_x \in \mathbb{R}^+$and distributed vertical springs $k_z \in \mathbb{R}^+$with an equivalent fixed-base single-degree-of-freedom system with mass $m \in \mathbb{R}^+$, modified-stiffness $\tilde{k} \in \mathbb{R}^+$, modified-fundamental period $\tilde{T} \in \mathbb{R}^+$, and modified damping $\beta_0 \in \mathbb{R}^+$as it is presented in Givens 2016, Stewart 1999. This idea is depicted in Figure 9.

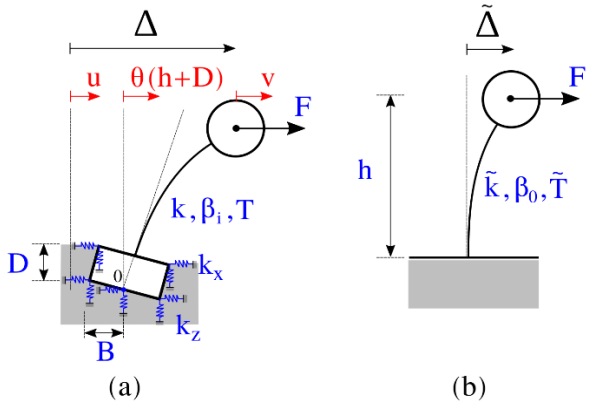

Figure 9. Model reduction from (a) the simplified flexible-base system into (b) the equivalent fixed-base system.

It can be shown that the *period elongation* is defined as follows:

$$\frac{\tilde{T}}{T} = \sqrt{1 + \frac{k}{k_{xx}\, k_{\theta\theta} - k_{x\theta}{}^2}\left(\bar{h}^2 k_{xx} - 2\,\bar{h}\, k_{x\theta} + k_{\theta\theta}\right)}, \qquad (13)$$

Note that in Equation (13) when the stiffness $k_{x\theta} = 0$, the expression reduces to the same as the one presented in Givens 2016, Stewart 1999. Following a similar procedure as presented in Givens 2016, Stewart 1999 we obtain the reduced *foundation-damping* provided in Equation (14),

$$\beta_0 = \frac{\beta_i}{\left(\frac{\tilde{T}}{\overline{T}}\right)^2} + \frac{\beta_x}{\left(\frac{\tilde{T}}{T_x}\right)^2}\left(\frac{1-\bar{h}\frac{k_{x\theta}}{k_{\theta\theta}}}{1-\frac{{k_{x\theta}}^2}{k_{xx}\,k_{\theta\theta}}}\right)^2 - \frac{2}{\left(\frac{\tilde{T}}{T_x}\right)}\frac{\beta_{x\theta}}{\left(\frac{\tilde{T}}{T_\theta}\right)}\frac{k_{x\theta}}{\sqrt{k_{xx}\,k_{\theta\theta}}}\frac{\left(1-\frac{k_{x\theta}}{\bar{h}\,k_{xx}}\right)\left(\bar{h}\frac{k_{x\theta}}{k_{\theta\theta}}-1\right)}{\left(1-\frac{{k_{x\theta}}^2}{k_{xx}\,k_{\theta\theta}}\right)^2}$$
$$+ \frac{\beta_\theta}{\left(\frac{\tilde{T}}{T_\theta}\right)^2}\left(\frac{1-\frac{k_{x\theta}}{\bar{h}\,k_{xx}}}{1-\frac{{k_{x\theta}}^2}{k_{xx}\,k_{\theta\theta}}}\right)^2, \qquad (14)$$

where we define the *translational period* as $T_x = 2\pi\sqrt{\frac{m}{k_{xx}}}$ and the *rocking period* as $T_\theta = 2\pi\sqrt{\frac{m\bar{h}^2}{k_{\theta\theta}}}$. Note once again that when the stiffness $k_{x\theta} = 0$ in Equation (14) the expression reduces to the one presented in Givens 2016, Stewart 1999 for the foundation damping.

Global Soil-Structure-Interaction effects on Buildings

In this section, equations (13) and (14) are employed to estimate the *period lengthening* and *radiation damping*. In addition, and in order to compare how much these values deviate, the so-called and well-accepted modified-Bielak-method - described in details in Jacobo 1975, Stewart 1999 - is employed. However, the modified-Bielak-method requires the impedance function of the soil to be prescribed. In order to deal with this situation, the procedure described in Seylabi 2016 is employed to compute the translational and rotational impedance functions of the half-space soil in plane strain condition assuming a rigid foundation.

Figures (10) shows the period elongation and radiation damping computed using the modified-Bielak-method and the system-identification method based on the Kalman filtering for different foundation aspect ratios. As shown, a good-agreement between the proposed expressions and the one obtained using modified-Bielak-method is achieved. On the one hand, it is evident that Equation (13) provides with more flexible models, but on the other hand, Equation (14) provides with less-dissipative values when they are compared with the modified-Bielak-method. A very close fit is however obtained for the three-buildings when the *foundation aspect ratio* is small (i.e., $\Pi_3 = 0.1$). The discrepancies must be attributed mainly to the fact that the estimated frequency of the interaction using the system-identification framework can be different from the one obtained using the modified-Bielak-method. Moreover, in the system-identification framework, we are implicitly compensating for kinematic interaction in the embedded cases as well as we are implicitly considering the spring and dashpot coupling terms. It can be seen in both equation (13) and (14) that mentioned coupling in the stiffness and damping matrices generate a slight increase in the period elongation ratio as well as a slight decrease in the radiation damping. It is indeed evident that if the term $k_{x\theta}$ is set to be zero, then the expression given in Equations (13) and (14) and the ones provided in Jacobo 1975, Stewart 1999 are totally equivalent. However, this small deviation plays an important role in the period elongation and radiation damping of the *reduced-model* when the foundation embedment becomes larger.

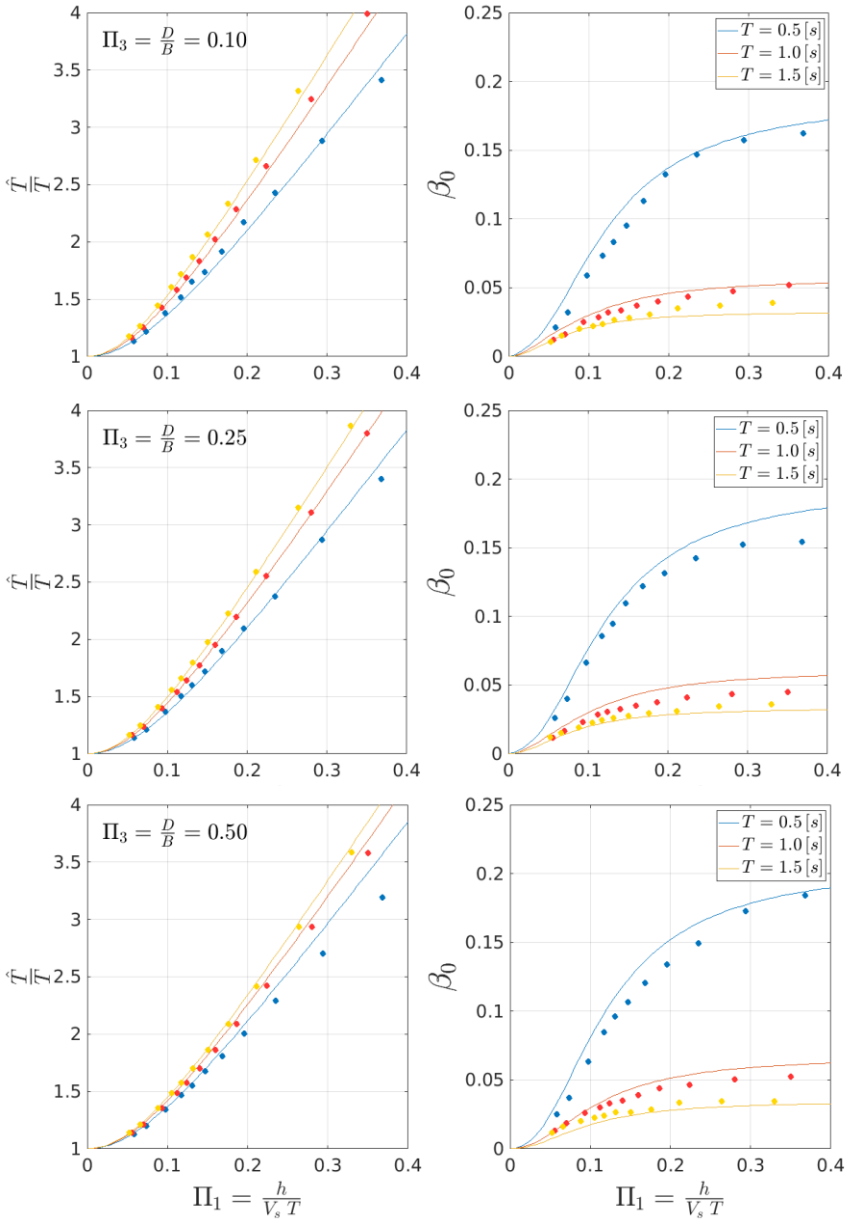

Figure 10. Period elongation ratio $\tilde{T}/T$ and radiation damping β_0 for the three buildings with $T = (0.507, 1.025, 1.531)$ s, supported on eleven homogeneous soil half-space with $V_s = (80, 100, 125, 150, 175, 200, 225, 250, 300, 400, 500)$ m/s. The solid-lines represent the modified-Bielak-method while the solid-dots represents equation (13) or (14) using the system-identification-method.

Summary and Conclusions

In this study, we first presented analytic expressions to estimate soil's impedance functions to account for inertial interaction and kinematic interaction in terms of dimensional parameters. In particular, the *structure-to-soil-stiffness ratio*, *foundation-aspect ratio*, and *building-aspect ratio* are chosen as dimensionless parameters in this framework. The distributed soil-spring and soil-dashpot elements identified using the Extended-Kalman-Filter are the one

that best represents the system interaction between the soil and the structure since it minimizes the error between the *direct-method* and the *substructure-method*. These soil-spring and soil-dashpot functions were then tested using the substructure-flexible-based-model to validate its accuracy and predictive power in several configuration systems. It is worth mentioning that the impedance expressions obtained using the EKF are assumed to be frequency independent. This assumption is not inaccurate since the frequency contents of earthquake signals in general varies between $0.2 - 10$ Hz, range in which the impedances of the homogeneous soil half-space are more-or-less constant. Another important aspect we consider is because of the building' symmetry the responses are dominated by their first-mode of vibration. However, higher-mode responses are well-captured employing the framework presented here. We second presented analytic expressions to evaluate the effects of period lengthening and radiation damping for a reduced-fixed-base system. The provided expressions can be considered as an extension to Givens 2016, Stewart 1999 since it incorporates the coupling term in the stiffness matrix as well as the damping matrix. In overall a good-agreement is reached not only for global parameters such as maximum displacements, period lengthening and radiation damping, but also for local responses such as time-history displacements at each node evaluated in terms of correlation between both the *direct-method* and the *substructure-method*.

Nevertheless, extrapolation far from the *dimensional-analysis design domain* represented in a blue rectangle in Figure 3 can produce large errors in global responses such as period elongation, and radiation damping. However, for almost all cases represented in this work, we note a good-agreement in both time history responses and their frequency content for the extrapolated values. The discrepancies are mostly attributed to the facts that (i) the extrapolation of the soil spring and dashpot elements using equations (7), (8), (9), and (10) is not exact, and (ii) the number of building frames considered in this analysis to span the whole dimensional-parameter space may not be enough—therefore a more refined sampling for *building-aspect ratio* (Π_2) and *foundation-aspect ratio* (Π_3) should be employed to provide with a much better approximation. Overall, extrapolation close to the *design domain* provides a very small error in terms of time history responses, maximum displacements, period lengthening and radiation damping when they are compared to the full-finite element model as it is presented in Table III.

Frame Name	Maximum Displacement Error	Period Elongation Error	Radiation Damping Error	Correlation Slope m	Correlation Pearson's R^2
A	0.0268	0.006	0.1017	1.0610	0.9660
B	0.1709	0.032	0.1073	1.1390	0.9677
C	0.1176	0.045	0.1073	1.1113	0.9212
D	0.2158	0.2131	0.3845	0.2394	0.2321
E	0.22	0.0874	0.1554	0.9772	0.8973
F	0.2407	0.0688	0.0096	1.1743	0.9462
G	0.2061	0.1204	0.1141	1.2246	0.8947
H	0.233	0.113	0.0893	1.2071	0.8689
J	0.1787	0.0491	0.0276	1.1088	0.8604
K	0.1787	0.0977	0.0663	1.1088	0.8604
L	0.1815	0.0794	0.0238	1.1250	0.9137
M	0.2341	0.0568	0.0164	1.1005	0.8913
N	0.013	0.0304	0.0124	0.9472	0.9252
P	0.171	0.004	0.1077	0.9070	0.7821
R	0.0895	0.0848	0.1321	0.7400	0.6713
max	0.013	0.004	0.0096	0.7400	0.6713
min	0.2407	0.1204	0.1554	1.2246	0.9677
Average	0.1615	0.0625	0.0765	1.0666	0.8833

Table III. Errors associated to response parameters employed in the validation process.

Acknowledgments

This study was supported partially by the California Geological Survey through Contract # 106-987. This support is gratefully acknowledged. Any opinions, findings, conclusions or recommendations expressed in this study are those of the authors and do not necessarily reflect the views of the sponsoring agency.

References

Bernal D., 1994. Viscous damping in inelastic structural response. Journal of Structural Engineering; 120(4):1240–1254.

Hall J., 2006. Problems encountered from the use (or misuse) of Rayleigh damping. Earthquake Engineering & Structural Dynamics.

Jacobsen L., 1930. Steady force vibration as influenced by damping, vol. 52. American Society of Mechanical Engineers.

Beck J, Jennings P., 1980. Structural identification using linear models and earthquake records, vol. 8. Earthquake Engineering Structural Dynamics.

Bathe K., 1996. Finite Element Procedures. Prentice-Hall International Series in, Prentice Hall.

Hughes T., 2000. The Finite Element Method: Linear Static and Dynamic Finite Element Analysis. Dover Civil and Mechanical Engineering, Dover Publications.

Lysmer J, Kuhlemeyer R., 1969. Finite Dynamic Model for Infinite Media. Reprint (University of California), Department of Civil Engineering, University of California, Institute of Transportation and Traffic Engineering, Soil Mechanics Laboratory.

Basu U, Chopra AK., 2003. Perfectly matched layers for time-harmonic elasto-dynamics of unbounded domains: theory and finite-element implementation. Computer Methods in Applied Mechanics and Engineering; 192(11):1337–1375.

Wolf JP., 1985. Dynamic soil-structure interaction. Upper Saddle, N.J.: Prentice-Hall. Security U, Agency FEM. Improvement of Nonlinear Static Seismic Analysis Procedures: Fema 440. Createspace Independent Publication.

Veletsos A, Meek J., 1974. Dynamic behavior of building-foundation systems. Earthquake Engineering & Structural Dynamics; 3(2):121–138.

Stewart JP, Seed RB, Fenves GL., 1999. Seismic soil-structure interaction in buildings. ii: Empirical findings. Journal of Geotechnical and Geo-environmental Engineering; 125(1):38–48.

Ricker N., 1945. The computation of output disturbances from amplifiers for true wavelet inputs. GEOPHYSICS; 10(2):207–220.

Assimaki D., 2004. Topography effects in the 1999 Athens earthquake: engineering issues in seismology. PhD Thesis, Massachusetts Institute of Technology. Dept. of Civil and Environmental Engineering.

Givens MJ, Mylonakis G, Stewart JP., 2016. Modular analytical solutions for foundation damping in soil-structure interaction applications. Earthquake Spectra; 32(3):1749–1768.

Stewart JP, Fenves GL, Seed RB., 1999. Seismic soil-structure interaction in buildings. i: Analytical methods. Journal of Geotechnical and Geo-environmental Engineering; 125(1):26–37.

Jacobo B., 1975. Dynamic behavior of structures with embedded foundations. Earthquake Engineering & Structural Dynamics; 3(3):259–274.

Seylabi EE, Jeong C, Taciroglu E., 2016. On numerical computation of impedance functions for rigid soil-structure interfaces embedded in heterogeneous half-spaces. Computers and Geotechnics; 72:15–27.

EFFICIENCY OF GROUND MOTION INTENSITY MEASURES WITH EARTHQUAKE-INDUCED EARTH DAM DEFORMATIONS

Richard J. Armstrong[1], Tadahiro Kishida[2], and DongSoon Park[3]

[1] California State University, Sacramento, United States.
[2] Khalifa University, United Arab Emirates.
[3] K-Water Convergence Research Institute, Republic of Korea.

Abstract

In a seismic hazard analysis (SHA), the earthquake loading level should be predicted for one or more ground motion intensity measures (IMs) that are expected to relate well with the engineering demand parameters (EDPs) of the site. In this particular study, the goal was to determine the IMs that best relate to embankment dam deformations based on non-linear deformation analysis (NDA) results of two embankment dams with a large suite of recorded ground motions. The measure utilized to determine the "best" IM was standard deviation in the engineering demand parameter (e.g., deformation) for a given IM—$\sigma_{\ln EDP|\ln IM}$, also termed "efficiency." Results of the study demonstrated that for the NDA model used, Arias intensity (AI) was found to be the most efficient predictor of embankment dam deformations. In terms of spectral acceleration (SA)-based IMs, the SA at short periods and then in the general range of the natural period of the dams were seen to be the most efficient IM, but was in almost all cases not as efficient as AI. In terms of total standard deviation ($\sigma_{\ln DYF|M,R,S}$) of EDP conditioned on earthquake source parameters, the poor predictability of AI relative to other IMs resulted in a higher total standard deviation given an earthquake. Within this context, CAV was deemed the best IM.

Introduction

In a seismic evaluation of an embankment dam, the earthquake loading level should be predicted for one or more ground motion intensity measures (IMs) that are expected to relate well with the engineering demand parameters (EDPs) of the site. For embankment dams, the EDP of interest is typically horizontal or vertical crest displacement, and the IMs often selected are spectral acceleration (SA), peak ground velocity (PGV), and Arias intensity (AI). The design target level for one or more of these IMs is then predicted as part of a seismic hazard analysis. In dam engineering practice in the United States, deterministic seismic hazard analyses are still very common. In conducting these deterministic seismic hazard analyses, the conventional approach for setting the design target levels is to select the target value of each intensity measure to represent a specified percentile level uniformly. An alternative to this approach is to select a single intensity measure, called the conditioning intensity measure, that relates well to embankment-dam response and then to apply this percentile level to that particular intensity measure only. The mean values of the other intensity measure targets are then selected, given (or "conditioned on") the value of the conditioning intensity measure. The second approach is

termed the conditional mean approach. A comparison of the conventional and conditional mean approaches in the context of dam-engineering practice is found in Armstrong (2017).

In a seismic hazard analysis, an important consideration is which IMs are to be used. This especially in the case with selecting the conditioning intensity measure, because the hazard level most directly relates to this IM. An optimal type of IM should relate well to the EDP of interest—in the case of dams, for example, horizontal or vertical crest displacement. Determination of such an "optimal" IM has been previously related to the so-called efficiency and sufficiency of the IM (Cornell and Luco, 2001). Efficiency is related to the variability in the random error term in the regression analysis between the $\ln IM$ and the $\ln EDP$ ($\sigma_{\ln EDP|\ln IM}$). In this context, IMs that produce less $\sigma_{\ln EDP|\ln IM}$ in predicting EDP are considered more efficient. The term sufficiency relates to the ability of an IM to predict the EDP without the need for specifying the earthquake magnitude or site-to-source distance. In this context, a sufficient IM would have a random error term from the regression analysis that did not demonstrate any bias with magnitude and site-to-source distance.

The efficiency of IMs in the context of embankment and slope deformations has been investigated in previous studies (e.g., Bray and Travasarou, 2007; Saygili and Rathje, 2007; and Beaty and Perlea, 2012). Based on these studies, it has been suggested that for stiff embankment dams in which significant strength loss is not expected, the SA at the first-mode period of the structure relates well with embankment deformations. However, for embankment dams founded on liquefiable alluvium, other non-SA intensity measures have been found to relate better to embankment deformations (Beaty and Perlea, 2012)—such as AI; cumulative absolute velocity, CAV; and $\sqrt{AI \cdot D595}$, where $D595$ is the duration between 5% and 95% AI. These studies, however, have been based on either Newmark-type sliding block analyses with large ground motion databases (e.g., Bray and Travasarou, 2007; Saygili and Rathje, 2007) or on non-linear deformation analyses shaken with significantly smaller sets of ground motions (Beaty and Perlea, 2012).

In this study—supported by the California Department of Conservation, California Geological Survey, Strong Motion Instrumentation Program, Agreement 1016-988—data from strong ground motion recordings during the 1989 Loma Prieta earthquake were used to validate non-linear deformation analysis models of Lenihan and Anderson dams that were subsequently used in assessing the efficiency of ground motion IMs with embankment-dam deformations. A suite of 342 recorded ground motions were used with these validated NDA models to assess the relationship between ground-motion characteristics and embankment-dam deformations. The paper begins with a summary of the NDA of Lenihan and Anderson dams during the 1989 Loma Prieta earthquake. Subsequently, the ground motion database used in the analysis is described, followed by presentation of the results in the context of the efficiency of each IM. The impacts of including the predictability of each IM in predicting deformations are also discussed. The paper ends with conclusions from this study.

NDA Validation Against 1989 Loma Prieta Earthquake

Description of Embankment Dams

James J. Lenihan Dam is a 207-ft-high zoned earthfill dam that was constructed in 1952 (Figure 1). Lenihan Dam impounds a reservoir that has a maximum capacity of 19,044 acre-ft at the spillway elevation of 653 ft (TGP, 2012). The zoned earthfill dam is composed of upstream and downstream shells, core, and drainage zones. The core is further divided into an upper and lower core to reflect differences in material properties. The upstream shell is composed of gravelly clayey sands to sandy clays, while the upper core is composed of gravelly clayey sand to clayey gravel. The lower core is classified as highly plastic sandy clays to highly plastic silty sands-sandy silts. The downstream shell consists of gravelly clayey sand to clayey gravels. The embankment materials were constructed on Franciscan Complex bedrock, without a foundation seepage cutoff or grout curtain. Instrumentation at this dam includes survey monuments, piezometers, inclinometers, seepage weir, and strong ground motion instruments.

A new seismic evaluation of Lenihan Dam was performed in 2011 by Terra-GeoPentech (TGP, 2012) and reviewed by Division of Safety of Dams (DSOD) (Kuhl, 2012). This new study included a site investigation, site characterization, and subsequent deformation analyses. Important outcomes were: (1) no alluvium or colluvial soils were left in place beneath the embankment; (2) no liquefiable materials were located within the dam or the dam foundation, (3) all embankment materials were well-compacted (with the exception of the internal drainage zones); and (4) for the design earthquake, no seismic remedial measures are necessary.

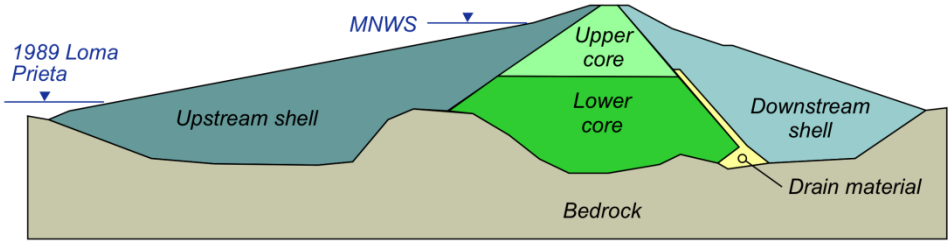

Figure 1: Design cross-section with reservoir level of 556 ft during the 1989 Loma Prieta Earthquake and at the maximum normal water surface elevation of 653 ft.

Anderson Dam is a 240-ft-high zoned rockfill and earthfill embankment (Figure 2). The dam was originally constructed to an elevation of 641 ft in 1950; it was subsequently raised to an elevation of 647.2 ft in 1987. Anderson Dam impounds a reservoir that has a maximum capacity of 90,000 acre-ft at the spillway elevation of 627.8 ft (Ryan et al., 2013). The zoned dam includes upstream and downstream rockfill shells, a compacted clay core, and a graded transition between the rockfill and clay core (Ryan et al., 2013). The rockfill shells are composed of cobbles and gravel with varying amounts of sand and clay, and the clay core is composed of clayey sand with gravel and sandy clay with gravel. The finer rockfill found within the lower portions of the shells (named lower finer fill, or LFF) is composed of clayey sand with gravel. The foundation alluvium ranges from clayey gravel with sand to clayey sand with gravel.

Bedrock is composed of Franciscan Melange. Instrumentation includes survey monuments, piezometers, inclinometers, and strong ground motion instruments.

A new seismic evaluation study of Anderson Dam occurred in 2011 by AMEC Geomatrix (AMEC, 2011) and review by DSOD (Dorsey, 2011). This new study included a detailed site investigation program, site characterization, and subsequent deformation analyses. Important outcomes of this study were: (1) the alluvium, primarily clayey sand with gravel; was susceptible to liquefaction; (2) the lower finer fill (LFF) was also susceptible to liquefaction, and (3) the cyclic resistance estimated from Becker Hammer Penetration testing (BPT) was less than the anticipated cyclic stress demand, so liquefaction triggering and shear strength loss were expected to occur. As a result of liquefaction in the lower finer fill and alluvium, large earthquake-induced deformations were expected by both AMEC and DSOD (Dorsey, 2011). As a result, a significant reservoir restriction was imposed, and a seismic remediation is currently planned.

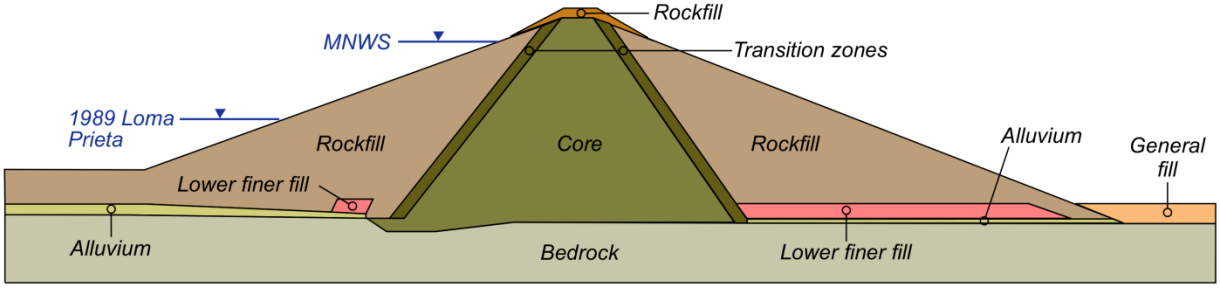

Figure 2: Design cross-section of Anderson Dam with reservoir level of 513 ft during the 1989 Loma Prieta Earthquake and at the MNWS elevation of 628 ft.

Numerical Analysis Details

The response of each dam in the 1989 Loma Prieta earthquake was modeled with non-linear deformation analyses (NDA) using the program FLAC (Itasca Consulting Group, 2016). This program uses an explicit solution scheme and is well suited for performing deformation analyses with non-linear material response, large geometry changes, and instability. The numerical meshes used in the NDA of Lenihan and Anderson Dams are shown in Figures 3 and 4, respectively. The element sizes of each model ranged from around 2 ft to 10 ft and were able to transmit motion frequencies accurately up to at least 10 hertz.

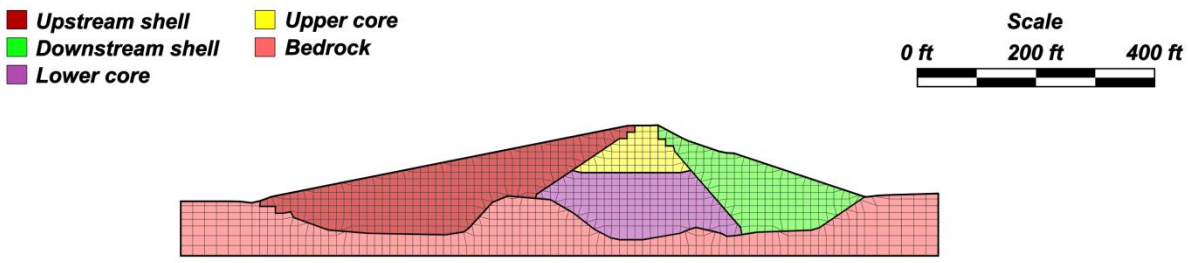

Figure 3: Numerical mesh for Lenihan Dam.

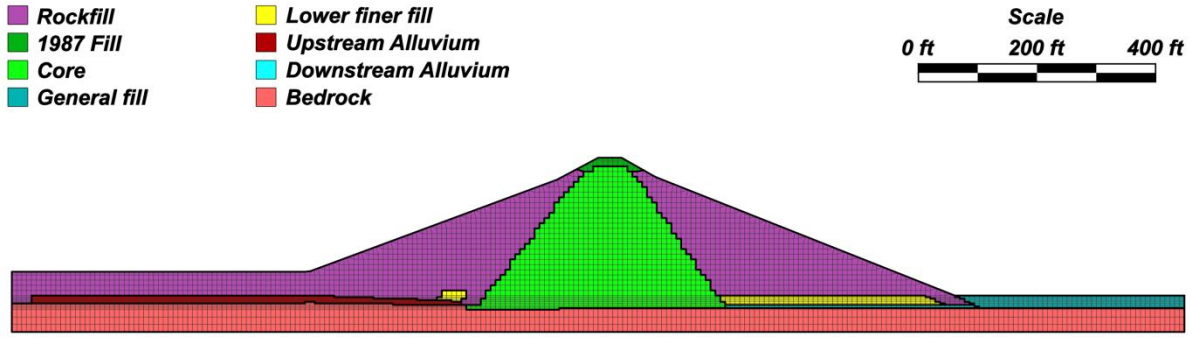

Figure 4: Numerical mesh for Anderson Dam.

Characterization of Material Properties

The expected non-linear soil response in the embankment and soil foundation was modeled in FLAC using either the UBCHYST or PM4Sand constitutive models. The UBCHYST constitutive model (Byrne and Naesgaard, 2015) was utilized for all soils in which the dynamic response could be modeled either as fully-drained or undrained and without significant strength-loss during shaking. For coarse-grained soils in which changes in excess porewater pressure during shaking were deemed critical to capture, the PM4Sand model (Boulanger and Ziotopoulou, 2017) was utilized. The calibration protocol utilized for UBHYST is described in Armstrong (2018a) and the calibration protocol for PM4Sand in Armstrong (2018b). The material properties recommended from recent studies (AMEC, 2011 and TGP, 2012) were either used directly in the NDA or modified based on alternative assumptions. All material properties used in these analyses are provided in Armstrong (2008c).

Establishment of Pre-Earthquake Stresses and Boundary Conditions

The state of stress was modeled prior to the earthquake, because these stresses affect both the initial conditions for the dynamic analysis and the values of shear strength. Total stresses for the embankment were estimated by sequentially adding rows of elements of the mesh and solving for static equilibrium with each new row of elements. This process was continued for the entire embankment. The goal of this process was to mimic roughly the actual construction process. Porewater pressures were based on a seepage analysis of each dam prior to the 1989 Loma Prieta earthquake. Note that prior to the 1989 Loma Prieta earthquake, less-than-average rainfall had occurred for several years, and both reservoirs were low relative to the normal. For Lenihan Dam, the reservoir was at 556 ft, significantly below the maximum normal water surface (MNWS) elevation of 653 ft; and for Anderson Dam, the reservoir was 513 ft, also significantly below the MNWS elevation of 628 ft. For these non-steady state seepage conditions, the approach used for modeling was threefold: (1) to capture first the steady-state seepage conditions corresponding to the MNWS, (2) to change the boundary conditions to model the lower reservoir level during the earthquake, (3) to rerun the analysis until the porewater pressure in the embankment was lowered to the values similar to those measured prior to the 1989 Loma Prieta earthquake. For the initial steady-state seepage conditions corresponding to the reservoir at the MNWS, the horizontal and vertical permeabilities were adjusted until the

calculated total head reasonably corresponded to piezometer recordings when the reservoir was near the same elevation.

Dynamic Analysis Results

Strong ground motion recordings from the 1989 Loma Prieta earthquake were utilized in the NDAs in two ways: (1) as a direct input at the base of each NDA, and (2) as a comparison to the calculated time histories from the NDAs. Three strong ground motion instruments were available at Lenihan Dam: a strong ground motion instrument located on the left abutment and two instruments located along the embankment crest. Eight strong ground motion instruments were available at Anderson Dam: a strong ground motion instrument located at the left abutment, two instruments at the toe and downstream of the embankment, three instruments located along the crest, and two instruments along the downstream slope.

The ground motion used as the input at the base of the NDA for Lenihan Dam corresponded to the abutment strong ground motion recording in the transverse direction. For Anderson Dam, the ground motion input at the base of the NDA was the toe strong ground motion recording in the transverse direction. The toe recording at Anderson Dam was used because it resulted in the calculated crest response in the NDA much more similar to that observed than when the abutment recording was used as the input at the base of the NDA. The velocity time histories of the strong ground motion recordings (i.e., abutment recording for Lenihan Dam and toe recording for Anderson Dam) were converted to shear stress time histories and applied to the base of the numerical model. The "field-field" condition used in FLAC was applied along the vertical boundary of the foundation soil and rock, and numerical dashpots were applied along the vertical foundation soil and rock and along the base of the numerical model.

As an initial evaluation of the NDA results, the IMs calculated from the NDA are compared to those measured from similarly located strong motion recordings (Figures 5 and 6). In particular, for Lenihan Dam, SA calculated from the crest is compared to the SA measured from the two strong motion recordings located along the crest. For Anderson Dam, SA calculated at the crest is compared to the SA measured from a strong ground motion recording located along the approximate maximum section of the dam. The calculated ratio of the SA from the crest to the SA from the base (termed RSA) of the NDA is also compared to that measured in Figures 5 and 6. For Lenihan Dam, the measured values of RSA correspond to the ratio of the SA from the crest at either of the two strong motion recordings at the crest (i.e., SA_i with i = Lt. crest or Rt. crest) to the SA from the strong ground motion recording at the rock abutment. For Anderson Dam, the measured values of RSA correspond to the ratio of the SA from the crest at the strong ground motion recording located along the approximate maximum section of the dam to the SA from the strong ground motion recording at the toe or abutment (e.g., SA_i with i = Toe or Abutment). Finally, in Figures 5 and 6, PGV, AI, and $D595$ are computed at the crest from the NDA and compared to those measured from the same strong ground motion recordings at the crest as used in determining the crest SA.

As seen in Figures 5 and 6, the general trends and magnitude of IMs were captured reasonably well with the NDA. For Lenihan Dam, computed crest PGA, PGV, and AI were 17.6%, 2.5%, and 19.2% smaller, respectively, than measured from the left crest strong ground motion recording. PGA, PGV, and AI were 30.0%, 13.8%, and 52.2% smaller, respectively, than

measured from the right crest strong ground motion recording. $D595$ was computed 61.8% (left crest instrument) and 43.2% (right crest instrument) larger than that measured. For Anderson Dam, the computed crest PGA, PGV, and AI were 35.2%, 24.3%, and 37.9% smaller than the measured values, respectively, with $D595$ computed 1.9% larger than that measured.

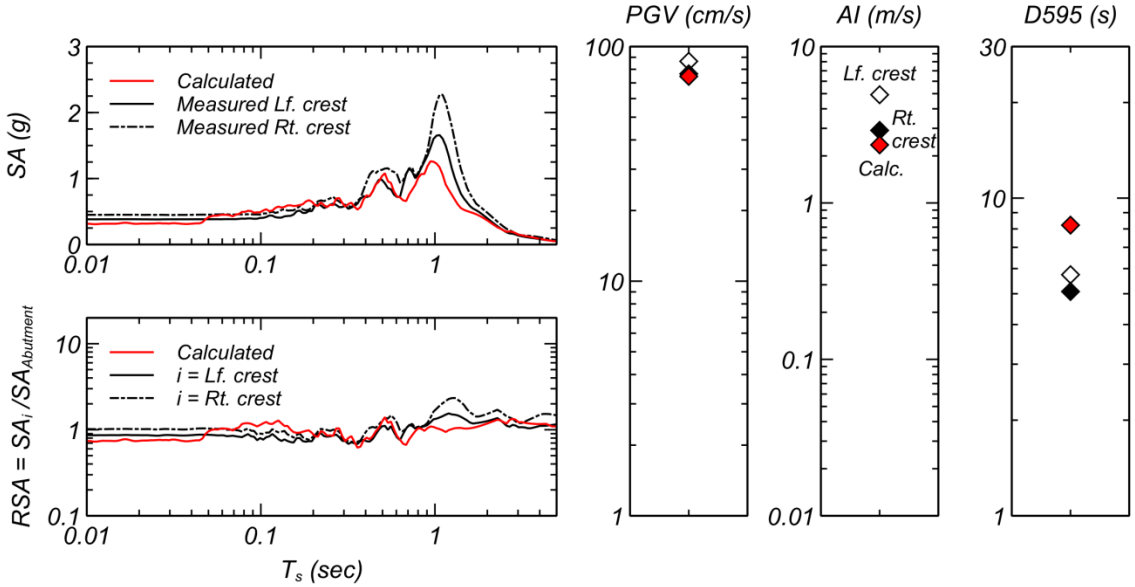

Figure 5: Summary of the calculated and measured dynamic responses for Lenihan Dam.

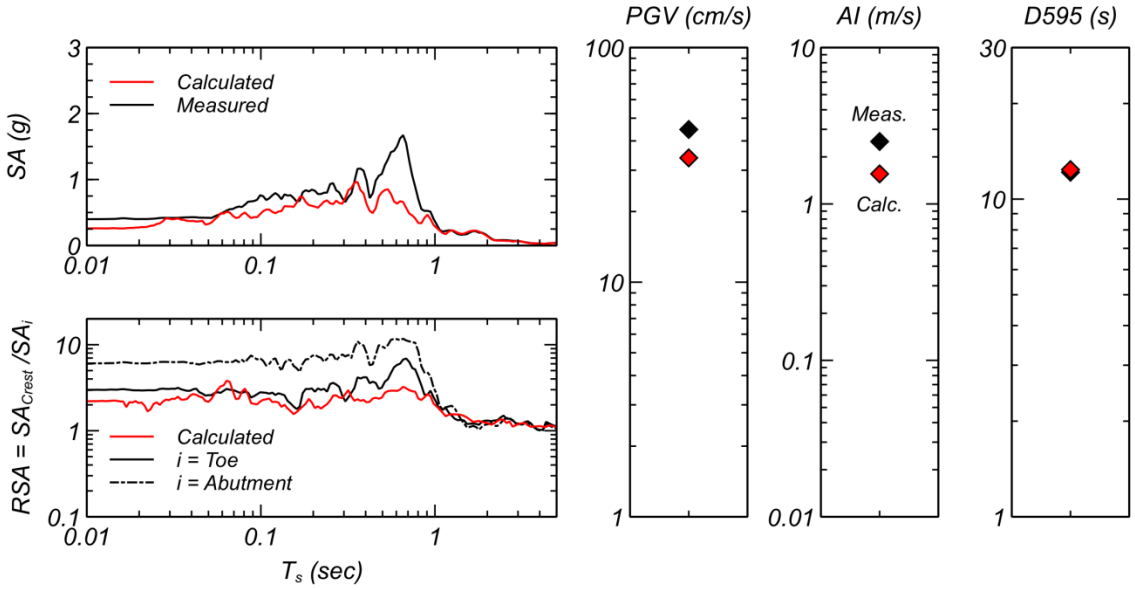

Figure 6: Summary of the calculated and measured dynamic responses for Anderson Dam.

In terms of SA, the periods in which the largest amplifications were observed (i.e., local maximums in RSA) were generally captured, but these magnitudes were less than those observed. For Lenihan Dam, the local maximum of RSA at T_s = 0.52 sec was observed at both

crest strong ground motion records, and was well captured by the NDA. However, the other local maximums of RSA at 1.2 sec or 1.3 sec were underpredicted by this NDA. For Anderson Dam, RSA was significantly underpredicted for T_s = 0.66 s, regardless if RSA was computed from the abutment or toe recording.

Computed final crest displacement in the horizontal direction (DXF, positive downstream) and vertical direction (DYF, positive downward) are summarized in Table 1 with comparison to those measured. As highlighted in Table 1, the displacements computed were in the general range of those measured.

Table 1. Comparison of computed and measured crest deformations.

	DXF	DYF
Lenihan Dam		
Measured	0.10 – 0.25 ft	0.61 – 0.85 ft
Calculated	0.42 ft	0.75 ft
Anderson Dam		
Measured	Negligible	0.04 – 0.13 ft
Calculated	-0.02 ft	0.34 ft

Numerical Analysis Ground Motion Study

Characteristics of Ground Motion Database

The ground motion database used in this study was composed of recordings with: (1) distance R_{rup} less than 30 km, similar to many dams in California; (2) magnitude $M_w \geq 5$, because it was expected that ground motions would produce appreciable deformations; and (3) $AI \geq 1$ m/s to further reduce the ground motion considered and ensure appreciable deformations. Initially, the ground motion database used in this study was composed of a subset similar to the NGA West 1 ground motion recordings (Chiou et al., 2008) as used by Armstrong (2016). The database used in the ground motion study was later augmented with new ground motion recordings from the NGA West 2 database (Ancheta et al., 2014), as well as those from the NGA West 1 database that had not been included in the initial ground motion study but that satisfied the selection criteria. In total, 342 single-component ground motions were used in the ground motion study; for those ground motions, the distribution of M_w, R_{rup}, and fault mechanisms are shown in Figure 7.

The 342 single-component ground motions represent 48 different earthquake events. The list of event names and the number of single-component ground motions utilized are summarized in Table 2. The five most frequent events in which ground motions were used are (in descending order, with percent of total included): (1) 1999 Chi-Chi Taiwan, 23.1%; (2) 1994 Northridge-01, 17.5%; (3 and 4) 1970 Imperial Valley-06 and 1989 Loma Prieta, 7.9%; and (5) 1995 Kobe Japan, 2.9%. The other 43 events account for the remaining 40.6% of ground motions.

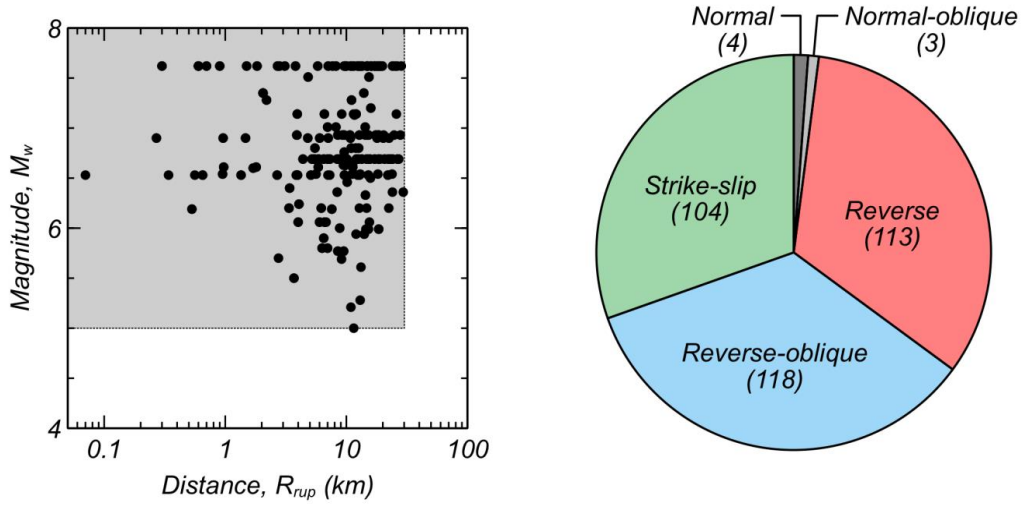

Figure 7: Range of M_w, R_{rup}, and fault mechanisms used in ground motion study.

Table 2. Distribution of earthquake events of ground motion study.

Event	Ground motions	Event	Ground motions
1970 Imperial Valley-06	27	1990 Mammoth Lakes-04	1
1971 San Fernando	2	1991 Sierra Madre	1
1972 Managua Nicaragua-01	2	1992 Big Bear-01	2
1976 Friuli Italy-01	1	1992 Cape Mendocino	6
1976 Gazi USSR	2	1992 Landers	4
1978 Tabas, Iran	4	1994 Northridge-01	60
1980 Irpinia, Italy-01	2	1994 Northridge-06	1
1980 Mammoth Lake-01	4	1995 Dinar Turkey	2
1980 Mammoth Lakes-02	1	1995 Kobe, Japan	10
1980 Mammoth Lakes-06	3	1999 Chi-Chi, Taiwan	79
1980 Victoria, Mexico	2	1999 Chi-Chi, Taiwan-03	3
1981 Wetmorland	2	1999 Chi-Chi, Taiwan-04	2
1983 Coalinga-01	4	1999 Duzce, Turkey	9
1983 Coalinga-05	4	1999 Hector Mine	1
1983 Coalinga-07	1	1999 Kocaeli, Turkey	4
1984 Morgan Hill	2	2000 Tottori, Japan	6
1985 Nahanni, Canada	2	2000 Yountville	1
1986 Chalfant Valley	2	2003 Bam, Iran	2
1986 N. Palm Springs	4	2004 Niigata, Japan	8
1986 San Salvador	4	2004 Parkfield-02	2
1987 Baja California	2	2007 Chuetsu-oki, Japan	8
1987 Supersition Hills-02	9	2008 Iwate, Japan	8
1987 Whittier Narrows-01	5	2010 El Mayor-Cucapah, MX	2
1989 Loma Prieta	27	2011 Christchurch	2

Similar to the 1989 Loma Prieta earthquake analysis, the velocity time histories of the 342 ground motion recordings were converted to shear stress time histories, which were then inputted at the base of the NDAs. The IMs for the resulting time histories at the base of the NDAs are shown in Figure 8 in terms of PGA, PGV, AI, CAV, and $D595$. Differences between IMs calculated from Lenihan and Anderson dams are due to ground motions being inputted as shear stress time histories; therefore, the calculated acceleration time history is a function of the shear stress time history as well as the overall response of the NDA model.

Referencing the base motion from the NDA from the 1989 Loma Prieta earthquake, it is seen that for Lenihan Dam, ground motions in this database have IMs that extend from less than to greater than the IMs from the 1989 Loma Prieta earthquake. For Anderson Dam, the ground motions in the database had IMs much greater than the 1989 Loma Prieta earthquake. For both dam NDA models, therefore, it is expected that the resulting deformations will go from negligible to values greater than those calculated with the 1989 Loma Prieta earthquake.

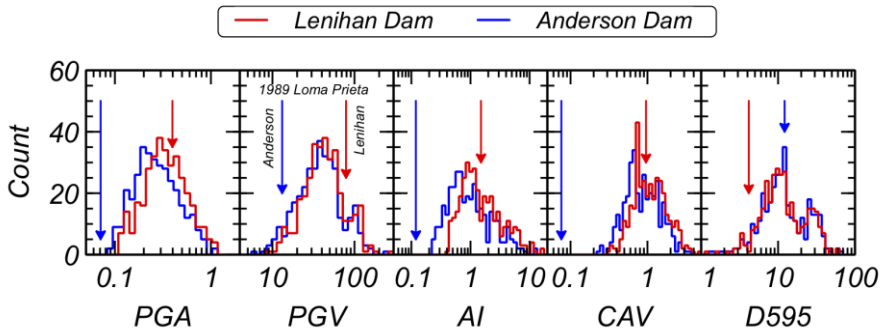

Figure 8: Distribution of IMs of ground motion recordings in study. Red and blue arrows correspond to the IM levels for Lenihan and Anderson dams, respectively, during the 1989 Loma Prieta earthquake.

Numerical Analysis Results

Overview

Analyses of the NDA models of Lenihan and Anderson dams were conducted with the 342 ground motion time histories described above. The NDA models used were identical to those used in the 1989 Loma Prieta analyses, except that the reservoir level used now corresponded to the MNWS elevations. For each analysis, time histories at key locations were stored, as well as the final solved state of the NDA model. Summary of key statistical metrics are provided in Table 3 for $IM = PGA$, PGV, AI, CAV, and $D595$ at the base and crest of the NDA models, as well as DXF and DYF (i.e., horizontal and vertical crest displacements). Ranges of IMs are significant, as are the displacements. Displacements ranged from negligible to values comparable to or greater than those computed in recent seismic evaluation studies by AMEC (2011), Dorsey (2011), TGP (2011), and Kuhl (2012).

Regression Analysis

Utilizing the results from the NDA ground motion study, the relationship between ground motion characteristics and embankment dam deformations of the two NDA models was assessed through single-variate, least-squares regression analyses between ln IMs and ln EDPs. The IMs considered were the base and crest PGA, PGV, AI, CAV, and $D595$, and the SA and RSA at 200 equal logarithmic increments of spectral period (T_s) between 0.01 and 10 seconds. PGA is taken as SA at T_s = 0.01 s. The EDPs considered were the peak and final horizontal displacements (DXP and DXF) and the peak and final vertical displacements (DYP and DYF). With the 204 IMs at the crest and base and 4 EDPs, a total of 1,632 least-squares linear regression analyses were conducted. In evaluating the regression analyses, the efficiency in EDP given each IM (i.e., $\sigma_{\ln EDP|\ln IM}$) was computed from the 1,632 least-squares linear regression analyses.

Table 3. Summary statistics from NDA study.

Item		Lenihan Dam			Anderson Dam		
		Geometric mean	MIN	MAX	Geometric mean	MIN	MAX
Base	PGA (g)	0.33	0.11	1.13	0.27	0.09	1.16
	PGV (cm/s)	42.57	9.78	263.66	37.31	6.18	259.05
	AI (m/s)	1.52	0.42	17.07	0.97	0.24	12.35
	CAV (g·sec)	1.07	0.31	4.57	0.86	0.24	3.58
	$D595$ (sec)	11.66	0.88	62.10	11.75	1.24	67.16
Crest	PGA (g)	0.33	0.17	0.50	0.33	0.18	0.61
	PGV (cm/s)	51.87	18.03	277.40	54.46	21.54	283.32
	AI (m/s)	3.35	0.74	13.38	4.10	0.89	13.66
	CAV (g·sec)	1.99	0.51	7.69	2.20	0.66	7.49
	$D595$ (sec)	19.37	3.70	249.02	18.30	3.36	249.76
	DXF (ft)	0.87	0.03	8.89	0.45	0.004	5.29
	DYF (ft)	0.63	0.06	5.31	3.14	0.53	26.10

Scatter plots of $EDP = DXP$, DXF, DYP, and DYF versus $IM = PGA$, PGV, AI, CAV, and $D595$ are shown in Figure 9 for the NDA model of Lenihan Dam and in Figure 10 for the NDA model of Anderson Dam. Note that for each plot, the horizontal and vertical axes are logarithmic, with the range equal to the minimum and maximum values in Table 3. The least-squares linear regression lines (solid red line) and 1 standard deviation ($\sigma_{\ln EDP|\ln IM}$) above and below the regression lines (dotted red lines) are also included for reference. IMs in the figures were calculated at the base of numerical models. The standard deviation computed from each of the regression analyses in Figures 9 and 10 are provided in Table 4.

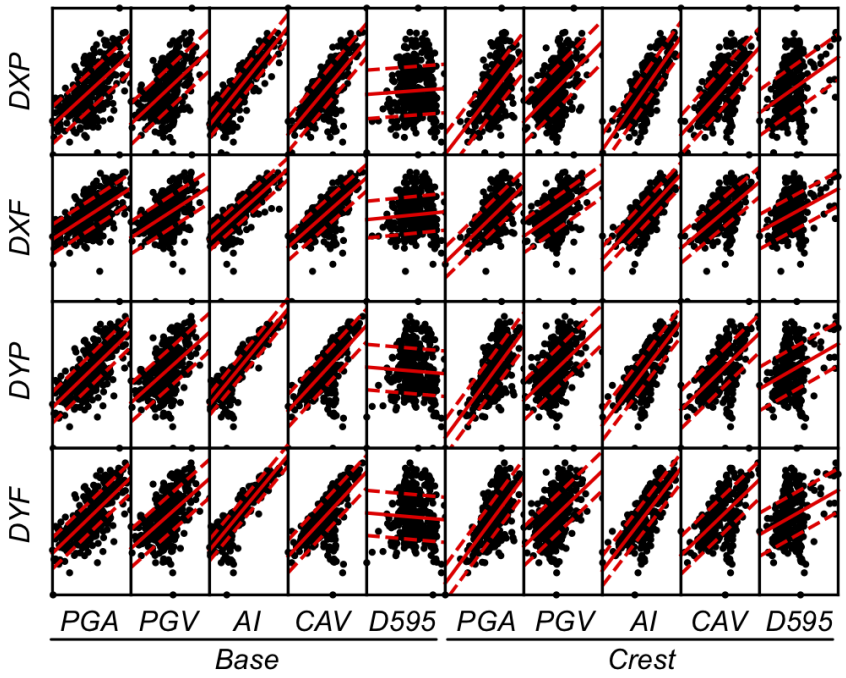

Figure 9: Comparison of IMs and EDPs for model of Lenihan Dam (all axes are logarithmic).

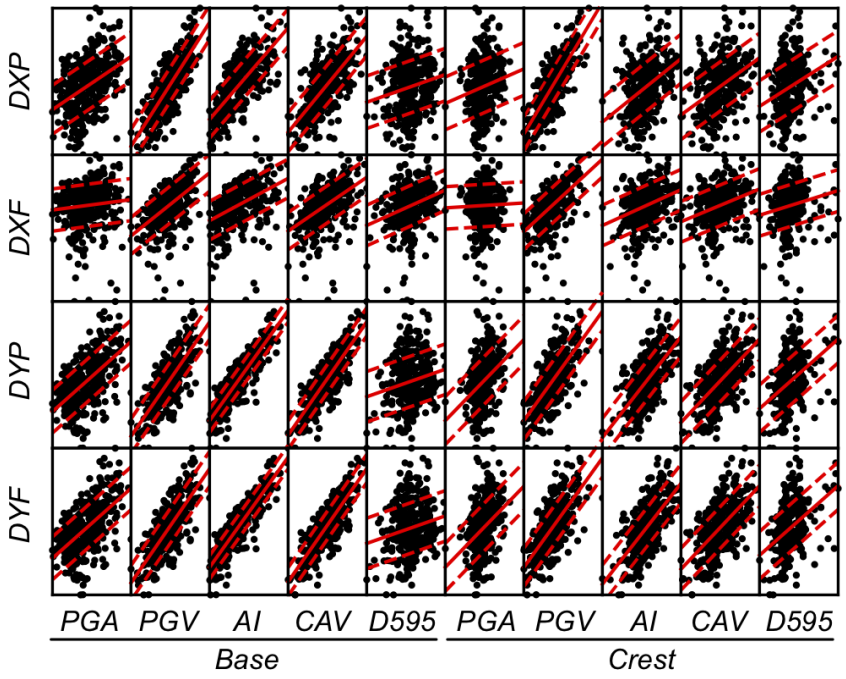

Figure 10: Comparison of IMs and EDPs for model of Anderson Dam (all axes are logarithmic).

Table 4. $\sigma_{\ln EDP|\ln IM}$ from regression analysis for models of Lenihan and Anderson dams.

IM	Lenihan Dam				Anderson Dam			
	DXP	DXF	DYP	DYF	DXP	DXF	DYP	DYF
Base								
PGA	0.517	0.572	0.478	0.480	0.653	1.026	0.568	0.569
PGV	0.574	0.629	0.588	0.592	0.454	0.897	0.461	0.461
AI	0.359	0.424	0.324	0.328	0.501	0.939	0.312	0.312
CAV	0.474	0.515	0.503	0.507	0.522	0.904	0.375	0.375
$D595$	0.674	0.714	0.695	0.699	0.703	0.988	0.671	0.672
Crest								
PGA	0.562	0.599	0.546	0.549	0.706	1.031	0.635	0.635
PGV	0.586	0.639	0.603	0.607	0.450	0.870	0.508	0.508
AI	0.434	0.469	0.458	0.462	0.655	0.989	0.512	0.512
CAV	0.543	0.576	0.579	0.584	0.660	0.991	0.556	0.556
$D595$	0.635	0.671	0.665	0.670	0.688	1.017	0.630	0.630

In evaluating the results of Figures 9 and 10 and Table 4, it can be seen that AI at the base of the model was in almost all cases the most efficient predictor (i.e., lowest $\sigma_{\ln EDP|\ln IM}$). Following AI, CAV was typically the most efficient predictor. Note that the one exception in the previous ranking was DXF for the NDA model of Anderson Dam in which PGV was actually slightly more efficient, with $\sigma_{\ln DXF|\ln PGV}$ = 0.897. In fact, for Anderson Dam, the IMs considered were not able to predict DXF as efficiently with DYF.

In terms of SA-based IMs, $\sigma_{\ln EDP|\ln IM}$ was also computed for $EDP = DXF$ and DYF against SA at the base of the numerical models. Figures 11 and 12 show the distribution of $\sigma_{\ln EDP|\ln IM}$ with spectral period for both dams. These figures also show for comparison $\sigma_{\ln EDP|\ln IM}$ for $IM = PGV$, AI, and CAV at the base of the numerical models. Note that the trends observed in $\sigma_{\ln EDP|\ln IM}$ for SA at the base of the NDA models were similar to $\sigma_{\ln EDP|\ln IM}$ with SA corresponding to the crest and with the ratio of the SA at the crest to SA at the base SA (i.e., RSA).

The efficiency of SA at the base of the numerical model was strongly dependent on the spectral period, T_s. Also, two local minima with the lowest $\sigma_{\ln EDP|\ln IM}$ (highest efficiency) were observed: (1) very low T_s (e.g., the PGA) and (2) T_s in the range of 0.3 to 0.6 seconds for Lenihan Dam and $T_s \approx 1$ second for Anderson Dam. The second local minimum represents roughly the natural period of the dam. The natural period of the dam would differ depending on the degree of soil non-linearity exhibited, but it is noted that the natural periods in which these minimums are observed are similar to the same models shaken with the 1989 Loma Prieta earthquake (i.e., Figures 5 and 6).

In this study, although SA at a T_s near the natural period of the dam demonstrated the highest efficiency for SA-based IMs, a non-SA based IM, AI at the base (i.e., the rock foundation

condition), was in fact the most efficient IM considered with the only exception being DXF for the NDA model of Anderson Dam. It is important to note that this observation is true for two dams with differing responses: one with liquefaction (Anderson Dam), and the other without liquefaction (Lenihan Dam). In the latter case, with an embankment without liquefaction, conventional understanding (e.g., Bray and Travasarou, 2007) would suggest that SA at the natural period of the dam should relate best to deformations; however, for these two dam models analyzed with NDAs, this is not the case.

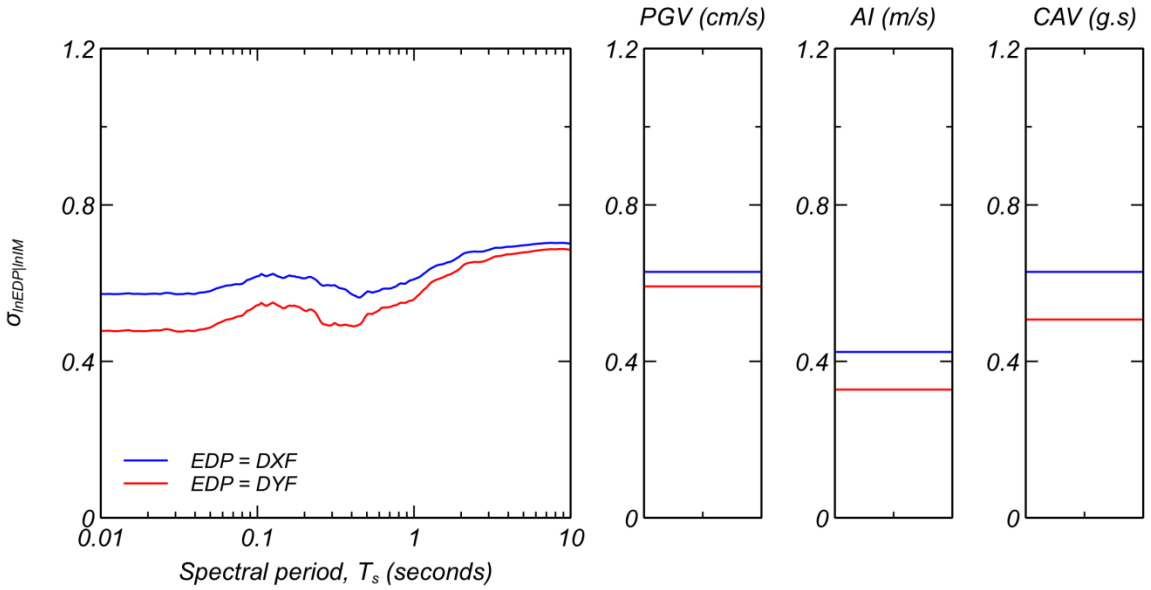

Figure 11: $\sigma_{\ln EDP|\ln IM}$ for SA, PGV, AI, and CAV for the NDA model of Lenihan Dam.

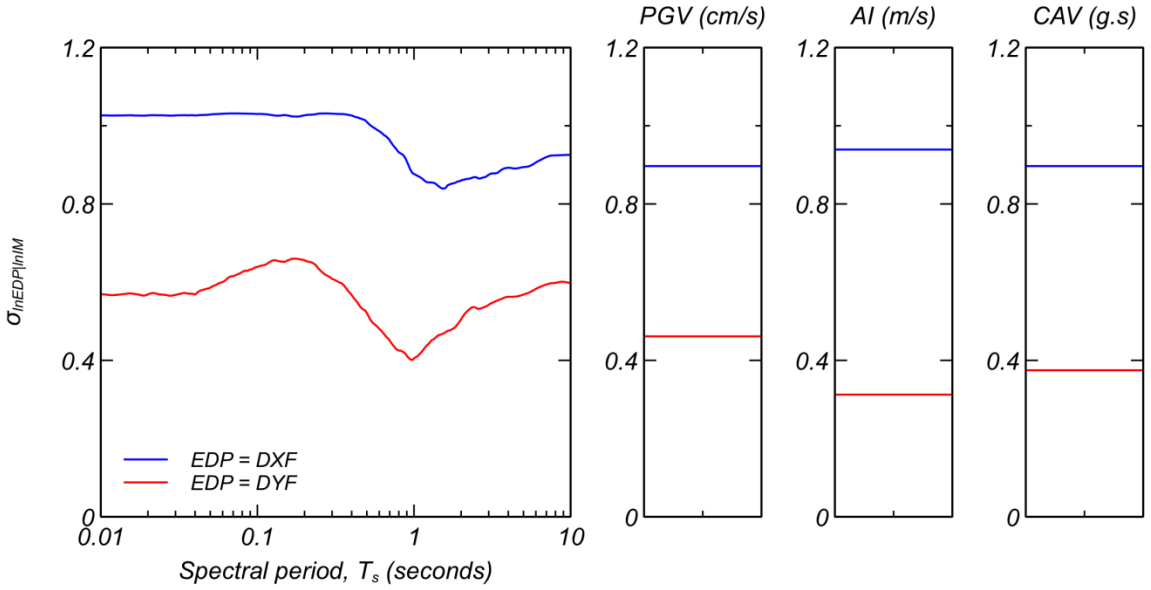

Figure 12: $\sigma_{\ln EDP|\ln IM}$ for SA, PGV, AI, and CAV for the NDA model of Anderson Dam.

Discussion

Although the efficiency accounts for the uncertainty in EDP for a given IM, it does not account for the uncertainty in the IM when predicted for a specific earthquake scenario. This uncertainty—termed predictability ($\sigma_{\ln IM|M,R,S}$)—is estimated through common ground motion prediction equations (GMPE) and is a function of the earthquake magnitude (M), the source-to-site distance (R), and other site conditions (S). The predictability defers for each IM considered. For example, consider a hypothetical site with M = 7.5, R = 10 km, $Z_{2.5}$ = 1.5 km, fault-type = strike-slip, and V_{s30} = 500 m/s. In Figure 13, the predictability of most of the IMs considered in this study are provided for this hypothetical site using Campbell and Bozorgnia (2008) to calculate $\sigma_{\ln IM|M,R,S}$ for $IM = SA$ and $IM = PGV$, Campbell and Borzorngia (2010) to predict $\sigma_{\ln IM|M,R,S}$ for $IM = CAV$, and Campbell and Bozorgnia (2012) to predict $\sigma_{\ln IM|M,R,S}$ for $IM = AI$. Note that although AI is the most efficient IM, it is, however, for the hypothetical site considered, not the most predictable IM.

The total uncertainty, which considers both the effects of the efficiency and predictability, may be computed according to $\sigma_{\ln EDP|M,R,S} = \left(\sigma^2_{\ln EDP|\ln IM} + b^2\sigma^2_{\ln IM|M,R,S}\right)^{1/2}$, where $\sigma_{\ln EDP|M,R,S}$ represents the total uncertainty and b is the coefficient in the least-squares linear regression equation $\mu_{\ln EDP|\ln IM} = a + b \ln IM$ (e.g., slope in regression lines in Figures 9 and 10), with the assumption that the residuals of $\ln IM|M,R,S$ and $\ln EDP|IM|M,R,S$ are independent. Computation of the total uncertainty for $IM = SA$, PGV, AI, and CAV at the base is provided in Figure 14 with $EDP = DYF$. As seen in Figure 14, the lower predictability in AI (i.e., high $\sigma_{\ln IM|M,R,S}$) results in a total uncertainty that is no longer the lowest for the IMs considered. Now, instead of AI, CAV at the base has the lowest total uncertainty.

The fact that CAV has the lowest total uncertainty suggests that in the common case in which IMs are predicted from a seismic hazard analysis, CAV may be the preferred IM to set the target loading level either probabilistically (e.g., return period of 2,475 years) or deterministically (e.g., 84th percentile). The mean values of the other IMs would then be selected, given (or "conditioned on") the value of CAV as the conditioning intensity measure. In the case in which the IMs at the abutment or toe of the dam are measured directly from a strong ground motion instrument during an earthquake, IM is now known and not predicted (i.e., $\sigma_{\ln IM|M,R,S}$ = 0), and the preferred IM to predict deformation would be the most efficient IM, which in the case of this work is AI. Thus, in the context of predicting damage to a dam following an earthquake in which measured abutment or toe recordings at a dam site are available, AI may be the optimal IM.

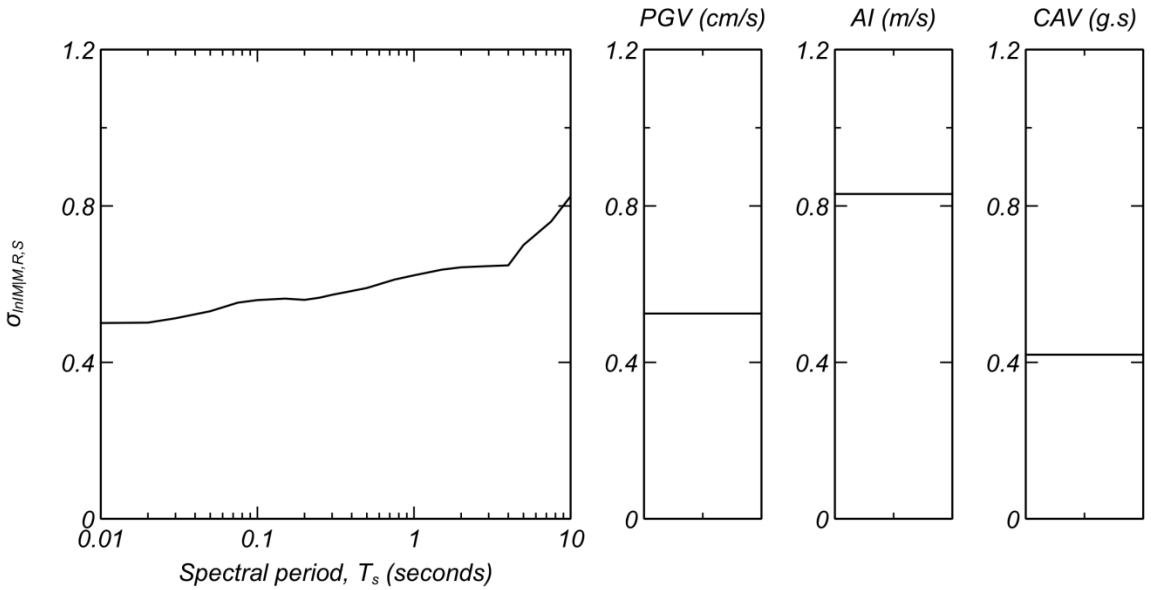

Figure 13: $\sigma_{\ln IM|M,R,S}$ for SA, PGV, AI, and CAV for the hypothetical site considered.

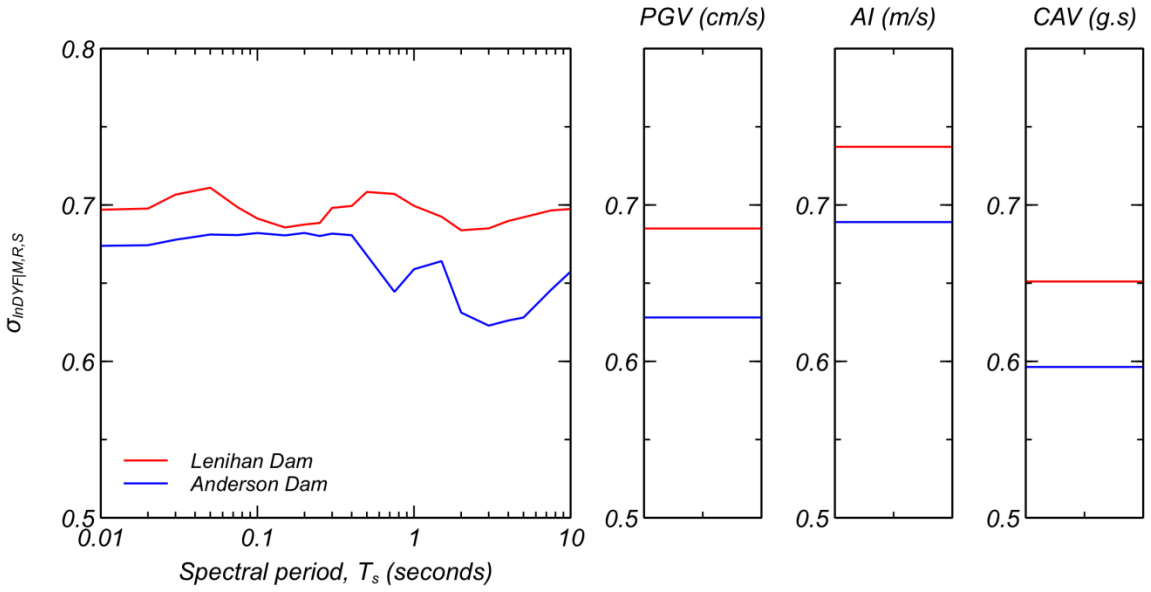

Figure 14: $\sigma_{\ln DYF|M,R,S}$ for SA, PGV, AI, and CAV for the hypothetical site considered.

Conclusions

The measured strong ground motion data at Lenihan and Anderson dams during the 1989 Loma Prieta earthquake provided a useful case-history to assess the capabilities of current NDAs. With the analysis approach described, the NDAs were able to capture reasonably well key dynamic characteristics, such as the surface acceleration response spectra and the magnitude of permanent deformations.

Using the NDA models for both dams, additional analyses with the 342 ground motions provided insight into the relationship between ground motion intensity measures and embankment dam deformation. For the NDA model of the two dams used, AI was the most efficient IM. In terms of SA-based IMs, T_s at short periods and T_s in the general range of the natural period of the dams were seen to be the most efficient SA-based IMs, but were in almost all cases not as efficient as AI. In terms of total standard deviation ($\sigma_{\ln DYF|M,R,S}$) of EDP conditioned on source parameters such as M, R, and S, the poor predictability of AI relative to other IMs resulted in a higher total uncertainty given an earthquake. Within this context, CAV was deemed the best IM.

In conducting a seismic hazard analysis with a dam similar to those modeled, this work suggests that CAV may be the preferred IM to set the target loading level either probabilistically (e.g., return period of 2,475 years) or deterministically (e.g., 84th percentile). In the case in which the IMs at the abutment or toe of the dam are measured directly from a strong ground motion instrument during an earthquake, IM is now known and not predicted (i.e., $\sigma_{\ln IM|M,R,S} = 0$), and the preferred IM to predict deformation would be the most efficient IM, which in the case of this work is AI. Thus, in the context of damage prediction of a dam following an earthquake in which measured abutment or toe recordings at a dam site are available, AI may be the optimal IM.

Acknowledgements

This work was supported by the California Department of Conservation, California Geological Survey, Strong Motion Instrumentation Program, Agreement 1016-988. The funding provided is greatly appreciated.

References

AMEC Geomatrix (2011). Anderson Dam seismic stability evaluation report (SSE-1A), Prepared for Santa Clara Valley Water District.

Ancheta T.D., Darragh R.B., Stewart J.P., Seyhan E., Silva W.J., Chiou B.S., Wooddell K.E., Graves R.W., Kottke A.R., Boore D.M., Kishida T., and Donahue J.L. (2014). NGA-West2 database. *Earthquake Spectra*, 30(3), 989 – 1005.

Armstrong, R.J. (2016). Procedure for selecting and modifying earthquake motions to multiple intensity measures. *Soil Dynamics and Earthquake Engineering*, 89, 91 – 99.

Armstrong, R.J. (2017). Use of the conditional mean for improved prediction of ground motion intensity measures for embankment dams. Proceedings, *2017 Annual United States Society of Dams Conference*.

Armstrong, R.J. (2018a). Cyclic soil behavior of common constitutive models used in non-linear deformation analyses of embankment dams. Proceedings, *2018 Annual United States Society of Dams Conference*.

Armstrong, R.J. (2018b). Numerical analysis of LEAP centrifuge experiments using a practice-based approach. *Soil Dynamics and Earthquake Engineering*., 113, 793 – 803.

Armstrong, R.J. (2018c). Relationship Between Earthquake Ground Motion Intensity Measures and Embankment Dam Deformations. Final Report submitted to California Strong Motion Instrumentation Program, California Geological Survey, Department of Conservation, June 2018.

Beaty, M.H. and Perlea, V.G. (2012). Effect of ground motion characteristics on liquefaction modeling of dams. *ASCE GeoCongress*.

Boulanger ,R. W. and Ziotopoulou, K. (2017). "PM4Sand (version 3.1): A sand plasticity model for earthquake engineering applications." Report No. UCD/CGM-17/01, Center for Geotechnical Modeling, Department of Civil and Environmental Engineering, University of California, Davis, CA, 112 pp.

Bray, J.D. and Travasarou, T. (2007). Simplified procedure for estimating earthquake-induced deviatoric slope displacement. *Journal of Geotechnical and Geoenvironmental Engineering*, 133(4), 381–92.

Byrne, P.M. and Naesgaard, E. (2015). Personal Communications. UDM Version: 5d. https://www.itascacg.com/udms/ubchyst (Accessed 05/30/18).

Campbell, K.W. and Bozorgnia, Y. (2008). NGA ground motion model for the geometric mean horizontal component of PGA, PGV, PGD and 5% damped linear elastic response spectra for periods ranging from 0.01 to 10 s. *Earthquake Spectra*, 24(1), 139-171.

Campbell, K.W. and Bozorgnia, Y. (2010). A ground motion prediction equation for the horizontal component of cumulative absolute velocity (CAV) based on the PEER-NGA strong motion database. *Earthquake Spectra*, 26(3), 634-650.

Campbell, K.W. and Bozorgnia, Y. (2012). A comparison of ground motion prediction equations for Arias intensity and cumulative absolute velocity developed using a consistent database and functional form. *Earthquake Spectra*, 28(3), 931-941.

Chiou, R., Darragh, R., Gregor, N., and Silva, W. (2008). NGA project strong-motion database. *Earthquake Spectra*, 24(1), 23-44.

Cornell, C. A., and Luco, N. (2001). Ground motion intensity measures for structural performance assessment at near-fault sites. *Proc., U.S.– Japan Joint Workshop and Third Grantees Meeting*, U.S.–Japan Cooperative Research on Urban EQ. Disaster Mitigation, Seattle.

Dorsey, C. (2011). Memorandum of design review Leroy Anderson Dam No. 72-9 Santa Clara County. California Division of Safety of Dams.

Itasca Consulting Group. (2016). FLAC, fast lagrangian analysis of continua, user's guide, version 8.0, Itasca Consulting Group, Minneapolis.

Kuhl, J. (2011). Memorandum of design review James J. Lenihan Dam No. 72-8 Santa Clara County. California Division of Safety of Dams.

Ryan, M.J., Mooers, M., Makdisi, F.I., Nelson, J., and Slack, C. (2013). Seismic stability evaluation of Anderson Dam, Santa Clara County, California. Proceedings, *2013 Annual United States Society of Dams Conference*.

Saygili, G. and Rathje, E.M. (2007). Empirical predictive models for earthquake-induced sliding displacements of slopes. *Journal of Geotechnical and Geoenvironmental Engineering*, 134(6), 790–803.

Terra GeoPentech. (2012). Lenihan Dam, site characterization, material properties, and ground motion (Report No. LN-3). Prepared for Santa Clara Valley Water District.

SYSTEM IDENTIFICATION OF BRIDGE-GROUND SYSTEMS FROM RECORDED SEISMIC RESPONSE

Ahmed Elgamal[1], Ning Wang[2], and John Li[1]

[1] University of California, San Diego, Dept. of Structural Engineering, La Jolla, CA 92093-0085
[2] Institute of Geophysics, China Earthquake Administration, Beijing, 100081, China

Abstract

A unique opportunity for gaining knowledge and insights is facilitated by the CSMIP Eureka Bridge and Samoa Bridge seismic records, along with those of the nearby Geotechnical ground downhole array. Of special interest is the response of a bridge pier in each bridge with records at the deck level, pile cap and within the underlying pile foundation. This valuable data set is employed to evaluate the ground, pile foundation, and overall bridge seismic response. Spatial variation of the recorded motions is examined. Linear and nonlinear response of the ground and the bridge are assessed using system identification techniques. During the strong shaking phase of the 2010 Ferndale Earthquake, a clear and significant stiffness reduction was observed in the response of the columns and foundations. After the strong shaking phase, flexural rigidity was seen to increase back to its original value (i.e., no perceptible permanent reduction).

Introduction

A large set of earthquake records from the highly instrumented Samoa and Eureka Channel bridge-ground systems (Figure 1) has been compiled and made available by the California Geological Survey (http://www.strongmotioncenter.org). During a large number of seismic events, more than 20 data channels for each bridge have been documenting the seismic response of the deck, foundation, abutments, and adjacent ground surface. Of special interest is the response of a pier in each bridge, instrumented at the deck, pile cap, and below ground in the foundation. Response within the pile foundations may be compared to that of the ground as documented by the nearby Eureka geotechnical downhole array.

Bridge Configurations and Instrumentation

The Samoa Channel and Eureka Channel bridge configurations are shown in Figures 2 and 3 respectively. In these figures, dense instrumentation is seen along the deck, at the abutments, and the nearby ground surface. In addition, a Pier in each bridge (S8 in Samoa and E7 in Eureka) is instrumented at the pile cap and within the underlying pile foundation.

Significant variability in the ground stratification and soil properties may be observed in the soil profiles of both bridges (Figures 2 and 3). In addition, the Eureka Channel bridge includes a substantial horizontal curve, which results in significant coupling in its longitudinal and transverse response.

(a)

(b)

(c)

Figure 1. Bridge Configuration: (a) Samoa Channel Bridge, Eureka Geotechnical Array, Middle Channel Bridge and Eureka Channel Bridge (Map Data @ 2015 Google), (b) Close-up of the Eureka Channel Bridge (http://www.strongmotioncenter.org), and (c) photo of the Samoa Channel Bridge (http://www.strongmotioncenter.org)

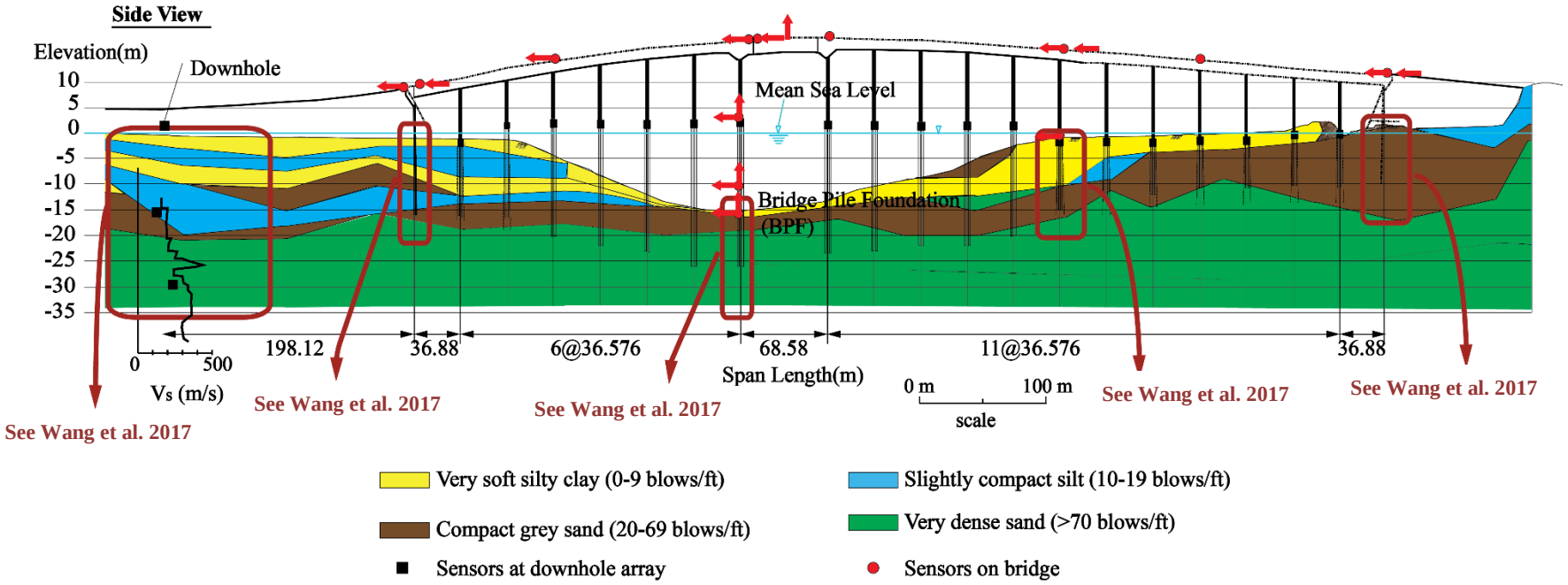

(a)

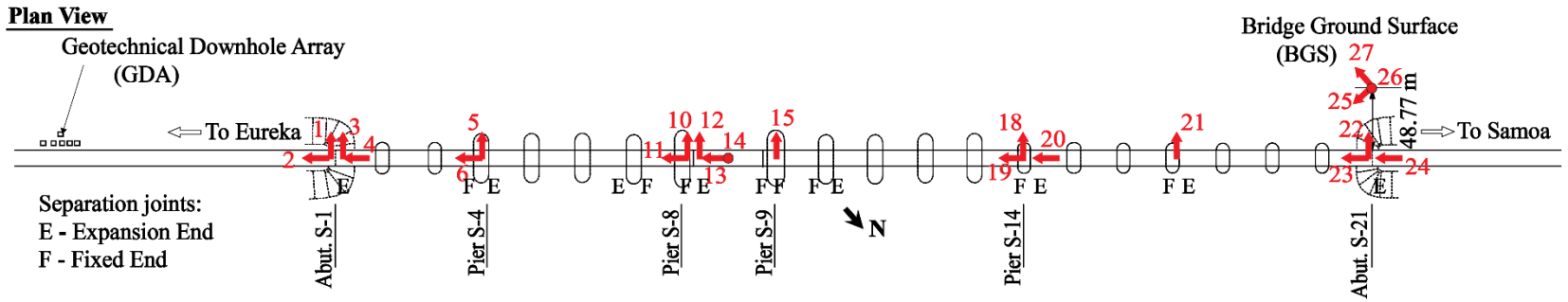

(b)

Figure 2. Layout of instrumentation at the Samoa Channel Bridge: a) bridge-ground side view (Caltrans 2002), and b) Plan view (http://www.strongmotioncenter.org)

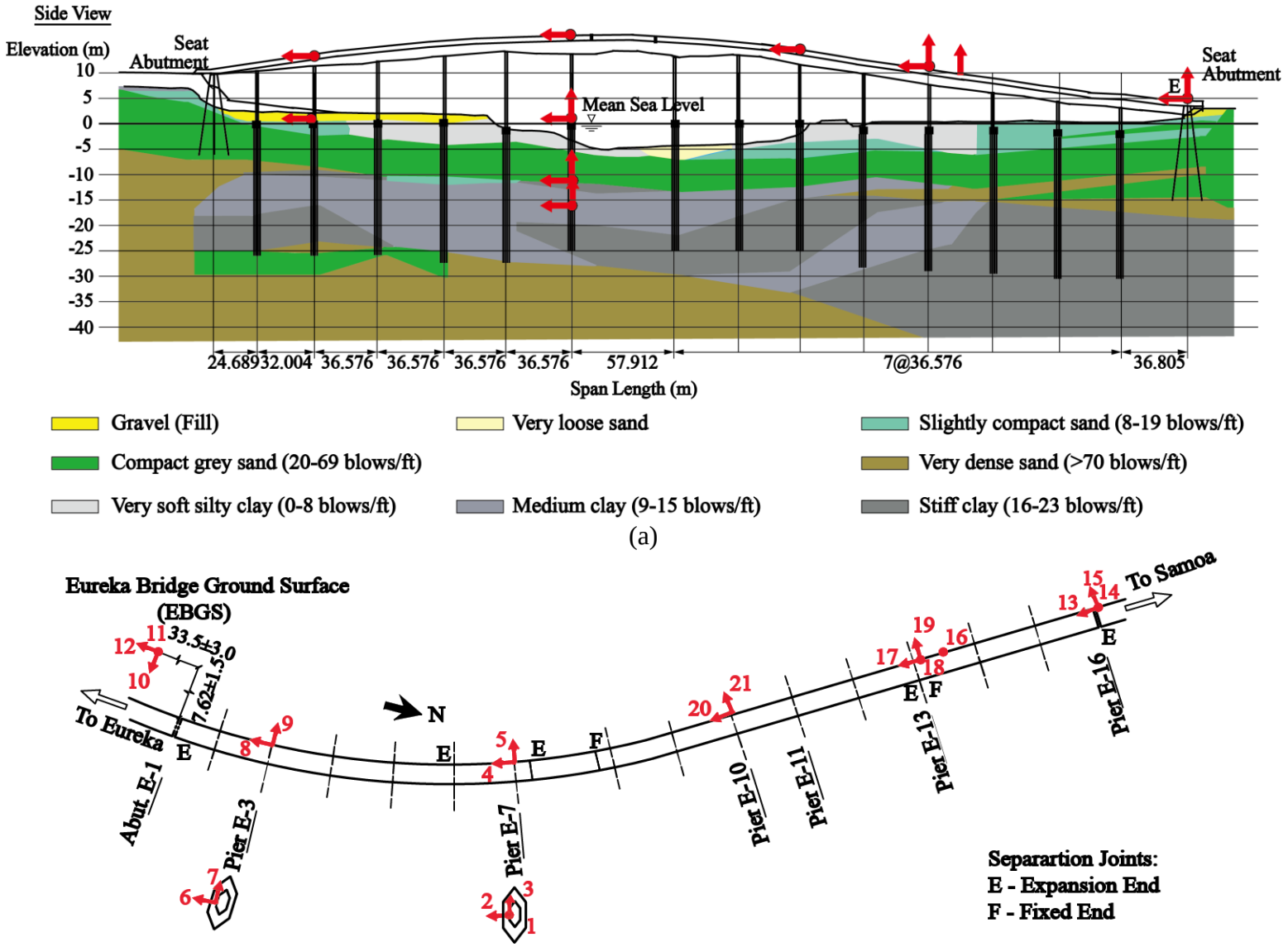

Figure 3. Layout of Instrumentation at the Eureka Channel Bridge: (a) Bridge-ground side view (Caltrans 2002), and (b) Plan view (http://www.strongmotioncenter.org)

Earthquake Motions

Records from a large number of earthquakes (e.g., Table 1) during the period of June 2007 through March 2014 are currently available with Magnitudes in the range of 4.5 M_L (local magnitude) to 6.9 M_w (moment magnitude). To date, the highest levels of recorded acceleration are due to the 2010 M_w = 6.5 Ferndale Earthquake approximately 35 km away from Ferndale, CA in a deformation zone of the southernmost Gorda Plate (http://earthquake.usgs.gov, Storesund et al. 2010).

Table 1 Recorded earthquakes at the Eureka bridge site (arranged by order of peak acceleration)

Earthquake	Epicentral Distance (km)	Horizontal Peak Acceleration (g)		
		Ground	**Bridge**	
			TRAN	LONG
Ferndale 2010 (M_w=6.5)	54.5	0.253	0.510	0.955* 0.540**
Ferndale 2014 (M_w=6.9)	82.7	0.026	0.072	0.048
Trinidad 2008 (M_w=4.6)	41.7	0.022	0.060	0.047
Humboldt Hill 2013 (M_L=4.5)	20.8	0.022	0.019	0.014
Trinidad 2007 (M_L=5.1)	65.6	0.020	0.081	0.031
Ferndale 2010 Feb (M_w=5.9)	77.8	0.018	0.046	0.022
Willow Creek 2008 (M_w=5.4)	55.4	0.012	0.026	0.017
Ferndale 2007 (M_L=5.4)	63.3	0.011	0.021	0.014

*Large peak acceleration due to spikes emanating from interaction at the separation joints (Huang and Shakal 1995, Malhotra et al. 1995)
**Estimated after removing spikes using a band-pass filter

Samoa Bridge and downhole array

Response of the soil profile at the downhole array, along the ground surface and the bridge deck was studied (Wang et al. 2017). In addition, a pattern recognition and system identification effort was undertaken to define the bridge and foundation stiffness characteristics (Wang et al. 2018). A number of main findings based on this work are included below.

The downhole array motions revealed (Wang et al. 2017):

i) a shear wave velocity profile that is consistent with that documented earlier through in-situ investigations,
ii) with peak ground acceleration of about 0.16g, G/G_{max} in the upper 17 m zone reached as low as 36%, in agreement with the widely used such relationships, and
iii) below the depth of about 16 m, lower shaking amplitudes and higher soil stiffness precluded the appearance of detectable nonlinear response.

Motions along the Samoa Bridge and Instrumented Pier S8 (deck, pile cap, and pile near mudline) revealed (Wang et al. 2017):

i) significant variability in the bridge deck motion mainly in the transverse direction along with noticeable elongation of the bridge natural period (Figure 4),
ii) in the transverse direction, with high column Moment of Inertia, deformation was mainly occurring below the pile cap within the pile group 16 m long free span (Figure 2),
iii) conversely, in the longitudinal direction (with a lower column Moment of Inertia), deformation was more evenly distributed between the column and the pile group below the pile cap, and
iv) by studying the earthquake events chronologically, no clear evidence of permanent change in stiffness was identified.

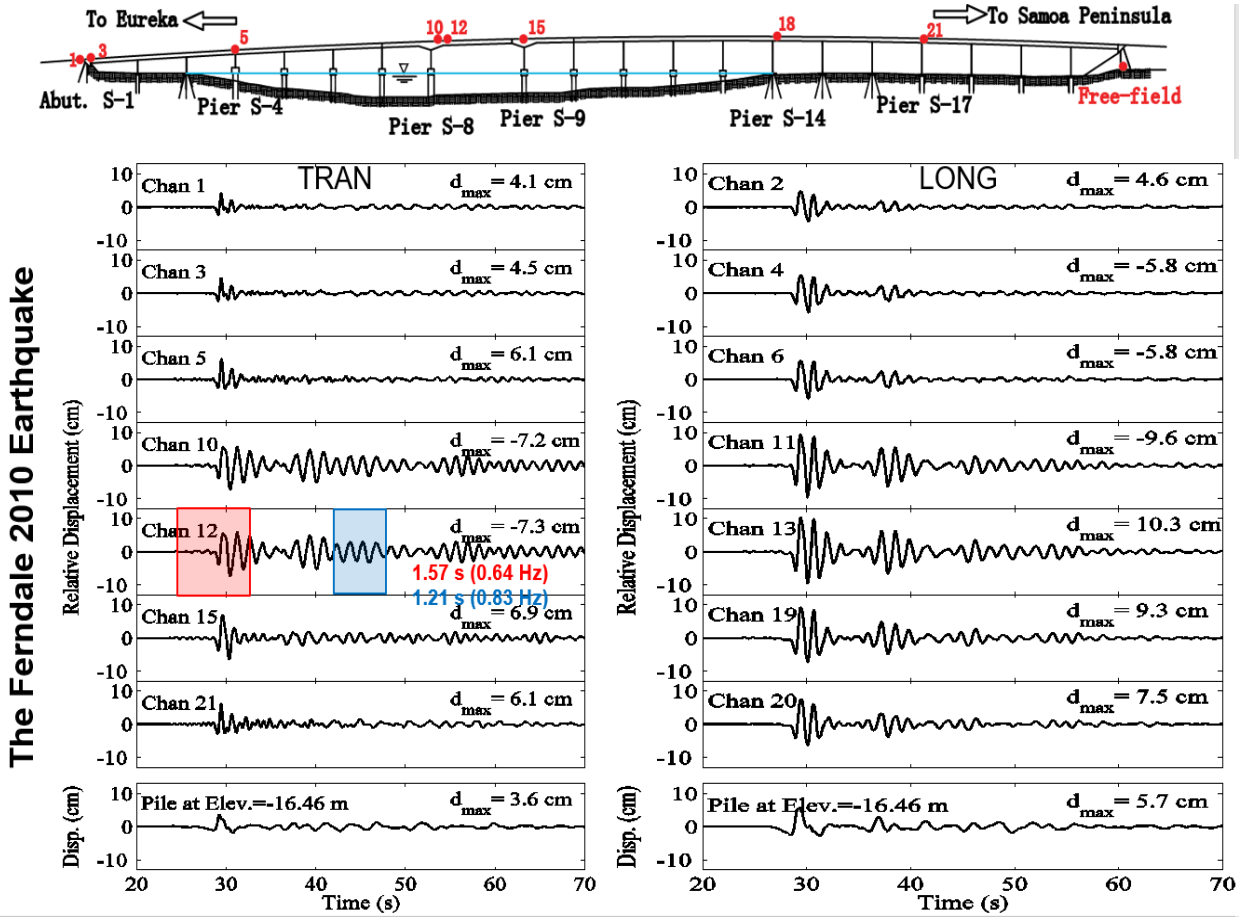

Figure 4. Motion along the Samoa Channel Bridge Deck showing variability (Wang et al. 2017) particularly as relates to the abutment (mainly in the transverse direction), and change compared to the motion at depth (reflecting resonant period of the bridge and elongation due to nonlinear response).

System Identification of the Samoa Channel Bridge Transverse motion response (Figure 5) revealed that (Wang et al. 2018):

i) Available practical guidelines concerning flexural rigidity estimates appear to be substantiated by the identified counterparts.
ii) While nonlinear response has been clearly displayed, no signs of permanent reduction in stiffness were identified to date, neither for the columns, nor for the supporting foundations.

iii) For the fully embedded pile groups, appreciable reduction in lateral stiffness was observed during the strong shaking phase of the 0.16 g PGA earthquake. The reduced stiffness was about 25 % of that during the low PGA events (Figure 5).
iv) Overall, this case history highlighted the value of strong motion instrumentation, with emphasis on the integrated monitoring of ground, foundation, and supported super-structure.

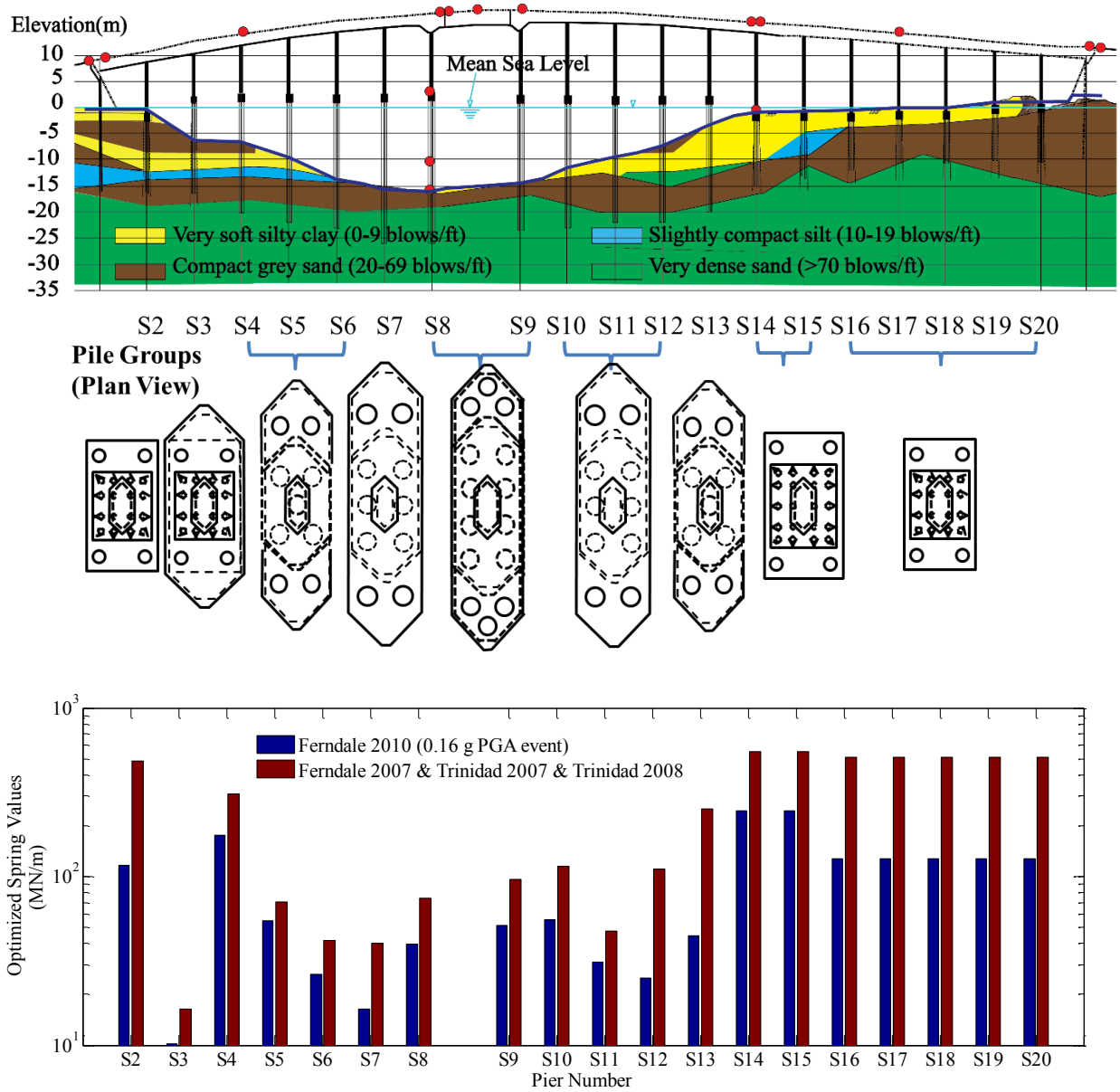

Figure 5. Samoa Channel Bridge, soil profile, pile group configurations, and identified transverse foundation stiffness (Wang et al. 2018).

Eureka Channel Bridge and Pier E7

Transverse displacement along Pier E-7 at the four instrumented elevations (Figure 3) is shown in Figure 6. In-phase response with a dominant fundamental period is evident (about 0.65

seconds). It can be seen (Figure 6) that the pile cap as well as the bridge deck displacements display a significant level of amplification. In general, the pier deformation is evenly accounted for by the column and the pile group deformations in both the transverse and longitudinal directions. This might be indicative of a less pronounced stiffness contrast between the column and pile group compared to the Samoa Channel Bridge pier S8 situation (Wang et al 2018).

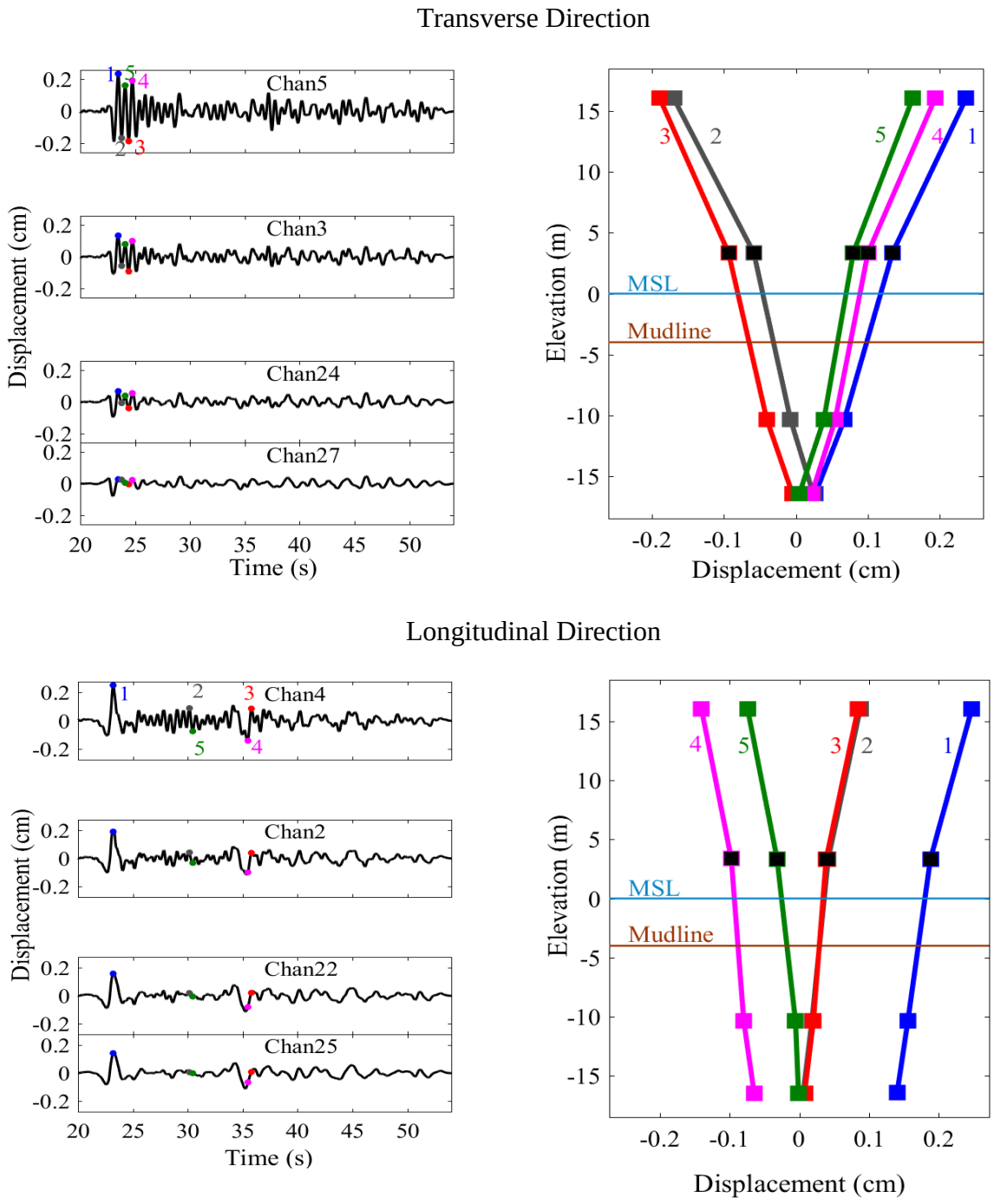

Figure 6. Time history of displacement and displaced configuration of Pier E7 at selected time instants during the 2007 Ferndale Earthquake

Eureka Channel Bridge Lateral Foundation Stiffness

A beam-column model (202 elements) representing the entire Eureka Channel Bridge with its different column heights was developed (Wang et al. 2019). The recently developed software MSBridge (Elgamal et al. 2014) was employed to generate the mesh for this curved bridge.

Focus was placed on the transverse response. Lateral springs were included at the base of the pier columns to account for stiffness of the underlying pile foundations and the associated soil-foundation-structure interaction (Lam and Martin 1986; Zafir 2002). These springs represent stiffness of the foundation down to an assumed uniform-excitation depth as defined by the recorded motion at -16.46 m. Stiffness of the lateral springs was optimized so that the computed response is compatible with the recorded motions along the bridge super-structure (Wang et al. 2019). The results shown in Figure 7 suggest (compared to the Samoa Channel bridge scenario):

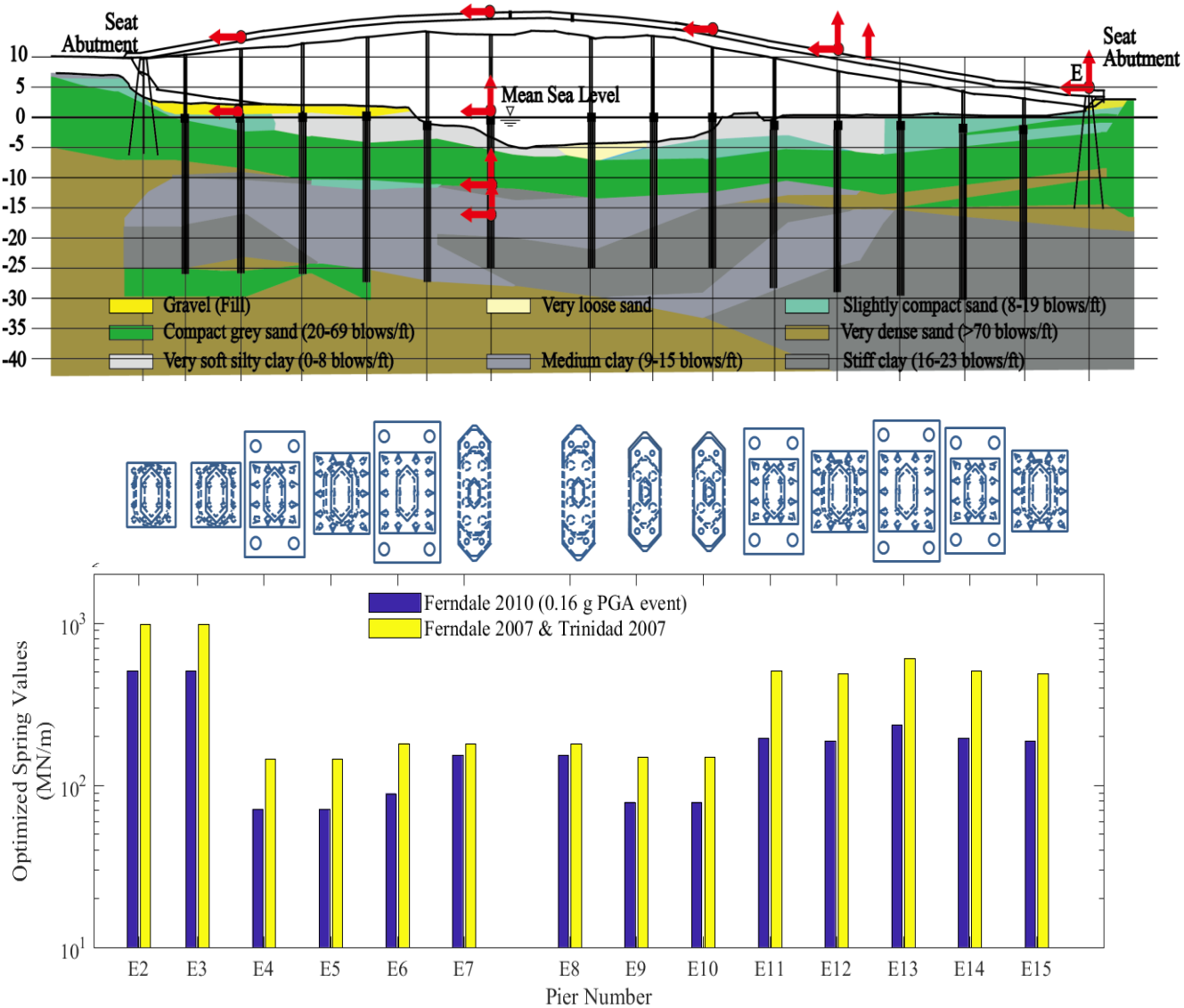

Figure 7. Identified Transverse direction base spring values along the Eureka Channel bridge

i) Foundation stiffness overall is higher,
ii) Reduction in stiffness during the strong shaking phase is pronounced, but to a lesser degree.
iii) Variability in stiffness along the bridge length is less pronounced.

Summary and Conclusions

The Eureka CSMIP seismic records (3 bridges and downhole array) constitute a unique invaluable resource for documentation of bridge and foundation response over a wide range of ground shaking scenarios. Inferred lateral stiffness of the involved pile-groups provides new insights about the actual foundation resistance at low and moderate levels of seismic excitation. These insights increase our confidence in current design/modeling assumptions, and allow for better understandings as relates to bridge response during strong earthquakes.

Acknowledgements

The research presented in this paper was funded by CSMIP, the U.S. Geological Survey, and partially by the China Earthquake Administration Grant (No. DQJB15B12). This support is gratefully acknowledged.

References

Caltrans (2002). As-built Plans, earthquake retrofit project for Samoa Channel and Eureka Channel Bridges. California Department of Transportation, Sacramento, CA, personal communication.

Elgamal, A., Lu, J., and Mackie, K. (2014). "MSBridge: OpenSees Pushover and Earthquake Analysis of Multi-span Bridges - User Manual." Department of Structural Engineering, University of California, San Diego.

Huang, M. J., & Shakal, A. F. (1995). CSMIP strong-motion instrumentation and records from the I10/215 interchange bridge near San Bernardino. Earthquake spectra, 11(2), 193-215.

Lam, I. P., and Martin, G. R. (1986). "Sesimic Design of Highway Bridge Foundations." Federal Highway Administration, Washington D.C.

Malhotra, P. K., Huang, M. J., & Shakal, A. F. (1995). Seismic interaction at separation joints of an instrumented concrete bridge. Earthquake eng & structural dyn, 24(8), 1055-1067.

Storesund, R., Dengler, L., Mahin, S., Collins, B. D., Hanshaw, M., Turner, F., and Welsh, K. (2010). M6.5 Earthquake Offshore Northern California January 9, 2010. GEER Field Reconnaissance Summary.

Wang, N., Elgamal, A., & Shantz, T. (2017). Recorded seismic response of the Samoa Channel Bridge-foundation system and adjacent downhole array. Soil Dynamics and Earthquake Engineering, 92, 358-376.

Wang, N., Elgamal, A., & Lu, J. (2018). Assessment of the Samoa Channel Bridge-foundation seismic response. Soil Dynamics and Earthquake Engineering, 108, 150-159.

Wang, N., Elgamal, A., & Li, J. (2019) Assessment of the Eureka Channel Bridge-foundation seismic response. (in preparation).

Zafir, Z. (2002). "Seismic Foundation Stiffness for Bridges." Proc., Deep Foundations 2002: An International Perspective on Theory, Design, Construction, and Performance, ASCE, GSP 116, Orlando, Florida, 1421-1437.

LOCALIZED DAMAGE DETECTION OF CSMIP INSTRUMENTED BUILDINGS USING CUMULATIVE ABSOLUTE VELOCITY: A MACHINE LEARNING APPROACH

Sifat Muin[1] and Khalid M. Mosalam[1,2]

[1.] Department of Civil and Environmental Engineering, University of California, Berkeley
[2.] Pacific Earthquake Engineering Research (PEER) Center

Abstract

Post-earthquake damage assessment can be significantly expedited when machine learning (ML) algorithms are used. Recent earthquakes showed that even when a structure is operational and safe for occupancy, people chose to evacuate and not reoccupy it immediately. Such a behavior can be attributed to lack of knowledge about the structural conditions immediately following the event and the fear of being trapped in the building if aftershocks hit. Currently, there is a lack of rapid quantifiable methods to determine if buildings are safe for reoccupation after an extreme event. However, advances in remote sensing, computing technologies, and data science in the past few years paved the way to develop ML methods that can assess and quantify the conditions of structures in near-real time. This paper introduces a methodology to assess the severity of earthquake-induced damage using low dimensional, cumulative absolute velocity (CAV)-based feature and ML tools. The appropriate features and the ML tool are identified by analyzing a single degree of freedom (SDOF) model. The identified features are then applied to assess the severity and location of damage of two multi-degree of freedom (MDOF) systems and real structures instrumented by the California Strong Motion Instrumentation Program (CSMIP). Results show that the damage detection capability of the features is high.

Introduction

Structural Health Monitoring (SHM) is the process of developing automated and online damage detection and/or assessment capability for all types of engineered systems (aerospace, civil, mechanical, etc.). It has become an important field of engineering in the US as the civil infrastructure systems of the country are aging. According to ASCE infrastructure reports (ASCE 2017), most US infrastructures are rated between mediocre or poor. Many of them are nearing the end of their design life and show signs of deteriorations. Since replacing all these structures is not feasible, SHM is necessary to monitor the structural integrity and assess deterioration for the safe and continuous operation of these infrastructures and also for prioritizing to the decision makers their retrofit or replacement actions. Advances in remote sensing, computing technologies, and data science in the past few years paved the way to develop SHM techniques that can assess and quantify the conditions of structures in near-real time utilizing machine learning (ML) techniques.

Applications of ML in damage detection have been studied for a long time. One class classifier or novelty detection analysis is one of the most popular damage detection techniques among SHM researchers. Worden et al. (2000) applied such a technique to detect damage in a

three-degree of freedom spring system. They used Mahalanobis squared distance as the discordancy measure and detected outliers if the measure is greater than a threshold. Other researchers implemented auto-associative neural network (AANN) successfully to detect damage (Dua et al. 2001; Sohn et al. 2002). Cluster analysis has also been applied to detect damage in recent years (Kesavan and Kiremidjian 2012; Santos et al. 2014). However, this analysis technique is more frequently used by researchers to classify (rather than detect) damage (Tibaduiza et al. 2012; Palomino et al. 2012).

The studies mentioned above were conducted with simulated or experimental data. The damage features used to detect or classify damage are high dimensional which require a large amount of training data that were available from the simulations or the experiments. However, existing structures have limited data when it comes to earthquake response and particularly damage under extreme events. In this paper, low dimensional, cumulative absolute velocity (CAV)-based features are proposed that can be used with a limited dataset for seismic SHM.

Development of Single Dimensional Features

The CAV has been used as an earthquake intensity measure since a study conducted by the Electric Power Research Institute (EPRI) that dates back to 1990 (Reed and Kassawara 1990). In that study, it was found that ground motion CAV has a better correlation to damage than other intensity measures such as peak ground acceleration (PGA), spectral acceleration, effective durations, etc. However, CAV of floor accelerations has never been applied in SHM to assess damage. In a recent study by Muin and Mosalam (2017), CAV is introduced as a damage feature. CAV time series, its normalized version (NCAV), and other features extracted from it show distinct patterns in damaged structures which can be used to identify and locate damage. Since it is a waveform-based feature, this method does not contain any assumptions regarding the linear or nonlinear nature of the system that generates the waveform data. However, waveform-based damage features are high dimensional where the dimension is the number of scalar quantities that are necessary to describe the feature. The amount of training data required for accurate diagnostic grows explosively with the dimension of the feature (Farrar and Worden 2012). This is a challenge for damage classification problems as the amount of available data from damaged cases is low. In this paper, several CAV-based damage features are further studied where these features are low dimensional and therefore appropriate to be used in a ML computing environment with a limited dataset. Four proposed damage features are discussed below.

Proposed Features

The CAV is mathematically defined as follows:

$$CAV = \int_0^T |\ddot{u}(t)|dt \tag{1}$$

where $|\ddot{u}(t)|$ is the absolute value of acceleration at time t and T is the total duration of the recorded acceleration time history. For the CAV calculation, the considered acceleration is the floor accelerations of a building. Higher CAV value is expected in damaging events than in undamaged cases as damaging events are correlated to high amplitude motions (Wald et al. 1999; Hancock and Bommer 2006).

The R_{CAV} is mathematically defined as follows:

$$R_{CAV} = \frac{CAV_s}{CAV_l} \tag{2}$$

where CAV_s is the CAV of the floor acceleration representing the structural response and CAV_l is the CAV of the corresponding linear system excited by the same ground acceleration. For an undamaged case and accurate linear model, this value will be 1. With damage, acceleration amplitude will typically decrease compared to the linear case due to lengthening of the natural period. Therefore, R_{CAV} is expected to decrease with increasing damage states.

The definition of S_{CAV} is as follows:

$$S_{CAV} = \frac{D_{5-75,s} - D_{5-75,l}}{D_{5-75,l}} \times 100\% \tag{3}$$

It highlights the relative wave travel times between the actual structure (subscript *s*) and its linear counterpart (subscript *l*) providing insight into the change in the wave propagation behavior caused by damage. Higher S_{CAV} means a slower rate of change due to damage. The parameter D_{5-75} in Equation 3 is the effective duration of an earthquake defined by the time to achieve 75% of the final CAV value starting from the 5% of that value (Bommer and Martinez-Pereira 1999). For an undamaged case, this value will be zero. With damage, S_{CAV} is expected to increase.

The Δ_{CAV} is calculated by taking the absolute value of the difference between the area under the CAV plots of an actual event and the corresponding linear state. The change of pattern in CAV time series and its linear counterpart provides useful information about the damage. However, comparison at each point of observation makes it a very high dimensional feature. Hence, the area is calculated as a compact (low dimension) feature.

$$\Delta_{CAV} = \left(\frac{|A_s - A_l|}{A_l}\right) \times 100 \tag{4}$$

where A_s is the area under the CAV plot of structure and A_l is the area under the CAV plot of the corresponding linear system. This value is expected to increase with damage, while for an undamaged case, it will be zero.

Methodology

A single degree of freedom (SDOF) system is utilized in this study. This model is used to select appropriate features and ML technique for the problem at hand. The SDOF model is developed in OpenSEES (McKenna 2010) using Steel01 material which has a bilinear behavior with strain hardening of 1% as shown in Figure 1. The base shear coefficient (η), which is defined by the ratio of yield base shear (*Vy*) to the weight of the building (*W*), is assumed to be 0.2.

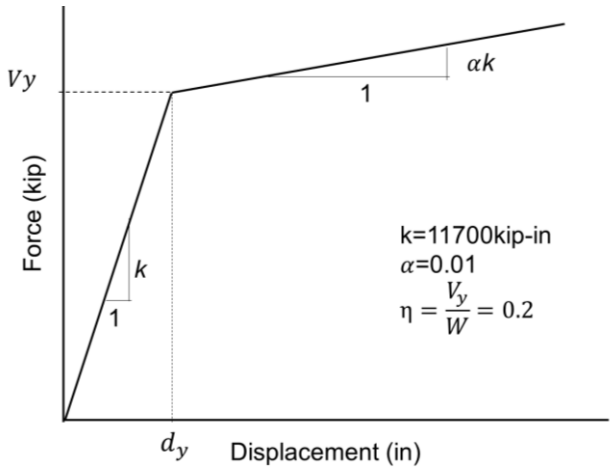

Figure 1 Story force-displacement relationship.

Two different sets of data have been used in this study. Set-1 includes responses of ground motions from the PEER NGA-West2 (Bozorgnia et al. 2014) database. This database has 21,539 records of shallow crustal earthquakes in active tectonic regions. Due to the possibility of anomalies from older data collection systems, only records from past 30 years have been selected. Moreover, records with PGA less than 1% g will not produce enough excitation useful for this study. Therefore, only records with PGA more than 1% g are considered. Lastly, to avoid homogeneity in response, not more than 20 records from a single event are selected. A total of 1,710 records matched these criteria. Set-2 comprises responses to site-specific ground motions that are used by Baker et al. (2011). These ground motions are selected by matching the uniform hazard spectrum and associated causal events for a site in Oakland, California. Set-2 consists of 120 ground motions representing three hazard levels, namely 2%, 10% and 50% probabilities of exceedance in 50 years. For the purpose of this study, damage states are defined based on displacement ductility, which is the most commonly used index to quantify structural damage. It is defined as the ratio of the maximum displacement sustained by the structure to its yield displacement as follows.

$$\mu = \frac{d_s}{d_y} \tag{5}$$

where d_s is the maximum absolute displacement of the structure and d_y is the yield displacement. If the displacement does not exceed this yield displacement, i.e. $\mu \leq 1$, then the structure is considered undamaged. The damage states are divided into three categories according to guidelines from FEMA P-58 (FEMA 2012) with $1 < \mu \leq 2$ as minor damage, $2 < \mu \leq 6$ as moderate damage, and $\mu > 6$ as major damage.

Nonlinear time history analysis (NTHA) is performed on the SDOF model with set-1 and set-2 ground motions. In the analysis, acceleration of the model is computed and the force-displacement of the spring is documented. Damage state is assigned by determining the maximum absolute displacement and consequently calculating μ according to Equation 5. For set-1, the structure remains undamaged for 1,215 (71%) records while 308 (18%) records cause minor damage, 143 (8%) records cause moderate damage, and 45 (3%) records cause major damage. This is representative of a database that collects data from real instrumented structures

where the majority of the collected data will be coming from undamaged structures and very few from severely damaged structures. For set-2, 5% causes minor damage, 29% moderate damage, and 66% major damage.

Results

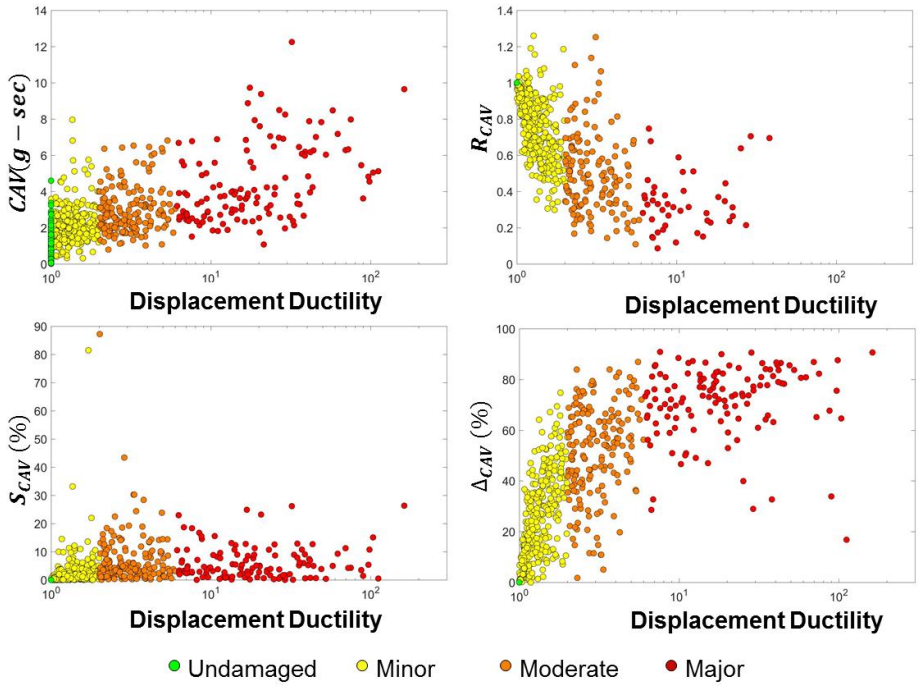

Figure 2 Plots showing relationship of proposed features and displacement ductility for four different damage states.

To identify suitable features, the relationship between each feature and the different damage states are observed. A good feature will demonstrate a certain pattern with increasing damage. Figure 2 shows the relationship of each of the four considered features with that of displacement ductility for the entire datasets (i.e. set-1 and set-2). Three of these features show trends with damage. The CAV value shows an increasing trend with the increase of displacement ductility. The R_{CAV} can distinguish minor damaged and undamaged cases as the R_{CAV} values other than 1 are damaged cases. Although for significant damage, acceleration of the structure and subsequently R_{CAV} will decrease, for certain ground motions, small damage may lead to an increase in acceleration and subsequently increase in the R_{CAV}. These are the motions for which the undamaged structure lies on the initial ascending part of the spectra.The Δ_{CAV} also shows a trend with displacement ductility. The S_{CAV} does not show any specific trend with displacement ductility. Therefore, S_{CAV} is not suitable as a damage feature.

A comparative analysis of four ML tools is performed using the three CAV-based features, namely CAV, R_{CAV}, and Δ_{CAV}, to determine the ideal feature and ML tool. The considered ML tools are logistic regression (LR), ordinal logistic regression (OLR), artificial neural network (ANN) with 10 (ANN_{10}) and 100 (ANN_{100}) neurons, and support vector machine (SVM). Two different training set and test set combinations are used for this purpose. The first

training set (TR-1) comprises of randomly sampled 85% of set-1 data as training set and the remaining 15% as the first test set (TE-1), i.e. both training and testing are performed with data from the same distribution. This is the usual practice in the ML field. The second training set (TR-2) comprises of the entire set-1 and second test set (TE-2) is set-2. The second combination is chosen in order to test the robustness of the features when tested against extreme values.

Table 1 Accuracy (%) achieved by ML models with different feature combinations with training and test sets from set-1.

Input Feature	OLR	LR	ANN_{10}	ANN_{100}	SVM
CAV	80.54	82.88	80.54	81.71	79.38
R_{CAV}	87.16	86.72	88.72	89.49	88.33
Δ_{CAV}	75.10	75.10	75.10	77.04	75.10
CAV, R_{CAV}	90.27	89.44	88.72	90.66	**91.05**
R_{CAV}, Δ_{CAV}	86.77	84.72	89.11	87.94	87.94
CAV, Δ_{CAV}	80.54	83.27	80.54	81.32	79.38
$CAV, R_{CAV}, \Delta_{CAV}$	90.27	89.05	90.27	90.66	89.88

Table 2 Accuracy (%) achieved by ML models with different feature combinations for set-1 as training set and set-2 as test set.

Input Feature	OLR	LR	ANN_{10}	ANN_{100}	SVM
CAV	36.67	12.50	18.33	15.83	8.33
R_{CAV}	60.00	42.50	30.83	37.50	20.83
Δ_{CAV}	61.67	45.00	42.50	40.00	21.67
CAV, R_{CAV}	**74.14**	61.67	18.33	40.00	25.00
R_{CAV}, Δ_{CAV}	65.83	45.00	60.00	40.00	22.50
CAV, Δ_{CAV}	70.00	60.00	51.67	36.67	24.17
$CAV, R_{CAV}, \Delta_{CAV}$	70.00	61.67	38.33	54.17	25.00

Tables 1 and 2 report the accuracy achieved by each model for the two combinations, respectively. Table 1 shows that the highest accuracy of 91.05% is achieved by the SVM model with CAV and R_{CAV} as features. ANN_{100} and OLR achieve comparable accuracies of 90.66% and 90.27%, respectively, with the same features. As expected, when the dataset is big enough in size and the data are representative of the population (i.e. training and test sets come from the same target unknown distribution), the results are not affected significantly by the choice of the ML algorithm. On the other hand, when the ML algorithms are tested over a different set of data, their predictive capabilities are significantly reduced (Table 2). For this case, the accuracy reduces for each model, where OLR achieves the highest accuracy of 74.14%, also with CAV and R_{CAV} features. This is due to the fact that ANN and SVM overfit the data of the training set and have poor generalization capabilities over the response of completely different ground motions. On the other hand, the simpler models LR and OLR have better generalization capabilities. From Table 2, it is seen that the OLR appears to be the most robust algorithm for making predictions

about events not available in the training set. For this reason, along with the fact that the computational demand of OLR is significantly smaller than ANN or SVM, OLR is used as the ML tool for the multi-degree of freedom (MDOF) analysis, as described in the next section. Moreover, it is seen that satisfactory performances are obtained using R_{CAV}, while the best ones are achieved using both CAV and R_{CAV} as features.

Damage Assessment of a MDOF Structure

Methodology

The identified features and the ML tool in the previous section are applied to MDOF systems representing a 5 story structure to evaluate the damage assessment performance. These models are also developed in OpenSEES (McKenna 2010) using the same bilinear steel model as the previously discussed SDOF system. The mass, stiffness, and damping of each story of the MDOF system are based on pushover and eigenvalue analyses reported by Mahin et al. (2015) and Günay and Mosalam (2017). The base shear coefficient (Figure 1) is taken as $\eta = 0.2$ which is representative of the value recommended by the code (ICC 2012) for regular structures designed for seismic risk category D.

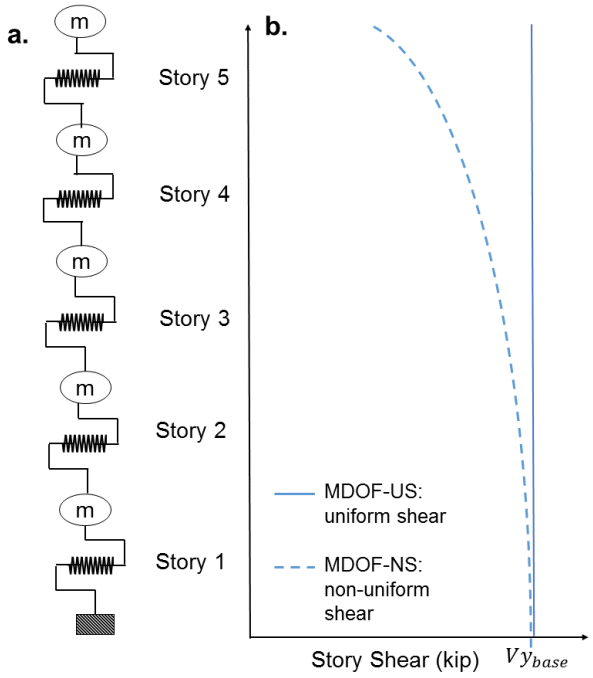

Figure 3: (a) MDOF model used in the study, (b) Story shear distribution along the height for the two models.

Figure 3a shows the MDOF representation of the 5 story structure and Figure 3b shows the story shear distribution of two different systems. One of the MDOF systems (MDOF-US) has uniform shear capacity along the height of the system which is equal to the calculated base shear (Vy_{base}). The other MDOF system (MDOF-NS) is designed to have non-uniform shear capacity distribution along the height of the structure. Designs of both systems are code conforming. However, MDOF-NS marginally meets the code and may be considered as the code minimum

design. Whereas MDOF-US has significantly higher value throughout the height and can be considered as the more conservative design which is often observed in low to medium rise structures. NTHA is performed on the models using both set-1 and set-2 ground motions, previously discussed. The acceleration is recorded at each degree of freedom along with force and displacement for each spring element. The worst damage states among the five stories are assigned as the damage state of the entire structure and its location as the worst damage location. However, for the cases when the worst damage state occurs simultaneously at several locations, the lowest story is identified as the damage location.

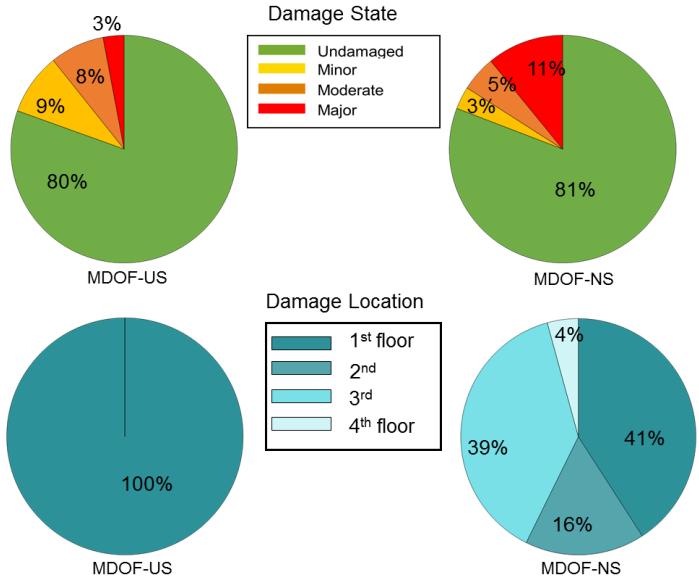

Figure 4: Worst damage state and its location distributions of the MDOF-US and MDOF-NS models.

For the MDOF-US model, out of the 1,710 cases of set-1, 1,376 (80%), 150 (9%), 133 (8%), and 51 (3%) cases are respectively undamaged, minor damaged, moderate damaged, and major damaged (Figure 4). For the MDOF-NS model, 1,382 (81%), 55 (3%), 86 (5%), and 187 (11%) cases are respectively undamaged, minor damaged, moderate damaged, and major damaged. For MDOF-US model, the worst damaged state of all 334 damage cases occurred at the first story. For MDOF-NS, 328 damaged incidents are distributed primarily between the first and third stories mainly due to the increased demand in the first story and reduced capacity of the third story.

The CAV of the first floor and the R_{CAV} of the top floor are used in this study. OLR is trained with set-1 and tested against TE-1 and TE-2 for both MDOF-US and MDOF-NS with damage categories defined similar to the case of the SDOF system. Using the damage state and location information obtained from the training set, the probability of the location of damage for a given damage state $P(n|y)$ is calculated where n is the story number, i.e. n =1 to 5 and y is the damage state, i.e. y =1, 2, and 3 for minor, moderate, and major, respectively. The probability of the worst damage location is subsequently determined using Equation 6 where the location with the highest probability is selected as that for the worst damage occurrence.

$$P(n) = P(n|y) \times P(y) \quad (6)$$

Results

Results reveal that MODF-US achieves damage state detection accuracy of 90.67% when tested with TE-1 and 84.00% when tested with TE-2. The higher accuracy with TE-1 is expected since the test set comes from the same distribution as the training set. Detection accuracy of damaged states for MDOF-NS (90.67%) is the same as that of the MDOF-US (90.67%) when tested with TE-1. However, the accuracy improves significantly to 96.67% when tested with TE-2. Table 3 presents the class-specific recall (i.e. fraction of relevant instances that have been retrieved over the total amount of relevant instances) values for the two MDOF systems for the two test sets TE-1 and TE-2. From this table, it is evident that for MDOF-US, the model predicts very well the undamaged class (99.3%) and the major damage class (92.2%). For moderate damage, it does fairly with 78.1% recall values. However, minor damage is mostly misclassified (28.6%). This is mainly due to the definition of the damage states. Since minor damage is defined as $1 \leq \mu \leq 2$, with this narrow range, the model performed poorly in detecting minor damages which was further worsened by the lack of data from minor damage states. Similar performance of the model is also observed for MDOF-NS where major damage class has high recall value (96.6%) together with the undamaged cases (99.3%). As the test cases for MDOF-NS has more data coming from the major damage and undamaged states, the results showed better overall accuracy for MDOF-NS than that of the MDOF-US.

Table 3: Class-specific recall values for the two MDOF models.

Class	MDOF-US	MDOF-NS
Undamaged	99.3	99.3
Minor	28.6	00.0
Moderate	78.1	46.3
Major	92.2	96.6

Damage locations are detected with 97.5% accuracy for MDOF-US with both TE-1 and TE-2. It is noted that three inaccurate cases are detected where the worst damage took place in both first and second stories, i.e. first story is labeled as the correct location per the definition stated above, but the model only identified second story as the worst damage location. The damage locations are detected with 93.0% accuracy and 95.0% accuracy with TE-1 and TE-2 for MDOF-NS. Damage location detection for this model is more critical since the non-uniformity of strength introduces significant uncertainty on the damage location. Thus, the results show that the location of damage can be identified with high confidence even for non-uniform structural properties by using this approach, i.e. using CAV and R_{CAV} as features with the OLR method.

Damage Detection of CSMIP Instrumented Buildings

In this section, damage assessment is conducted for real structures that are instrumented under the California Strong Motion Instrumentation Program (CSMIP). CSMIP was established in 1972 by California Legislation to obtain vital earthquake data for the scientific and the engineering communities through a statewide network of strong motion instruments. Although

the majority of instrumentations are installed at ground response stations, CSMIP also instrumented structures such as buildings, hospitals, bridges, dams, utilities, and industrial facilities. This study is focused primarily on buildings.

Building Portfolio

There is a significant number of CSMIP instrumented buildings studied in the literature, e.g. 151 instrumented CSMIP buildings studied by Fathali and Lizundia (2011), 64 instrumented CSMIP steel and reinforced concrete (RC) buildings in (Harris et al. 2015) and more than 40 CSMIP instrumented buildings in (Naeim et al. 2006), where data were collected from a significant number of earthquakes. Some of the previously studied buildings and the corresponding recorded strong motions are considered in this study. Moreover, buildings that captured responses of multiple earthquakes are ideal for this study. Several buildings selected from this large pool are investigated for the modeling of undamaged conditions. Table 4 provides a list of buildings selected in this study covering a wide range of primary lateral force resisting systems (PLFRS) and a variety of heights. The selection is influenced by having a reasonable number of earthquake data sets for each building.

Table 4 List of studied CSMIP instrumented buildings.

Index	**Station**		**PLFRS**	**Condition**	**# of EQs**	**# of sensors**
	Number	Name				
1	12267	Hemet – 4 story hospital	RCSW	U	10	10
2	58483	Oakland – 24 story residential building	RCSW	U	12	16
3	24579	Los Angeles – 9 story office building	RCMRF	U	4	18
4	24463	Los Angeles – 5 story warehouse	RCMRF	U	6	13
5	24322	Sherman Oaks – 13 story commercial building	RCMRF	U(R)	6	15
6	23634	San Bernardino – 5 story hospital	SMRF	U	5	12
7	57357	San Jose – 13 story government office building	SMRF	U(R)	3	22
8	24629	Los Angeles – 54 story office building	SMRF	U	7	20
9	3603	San Diego – 19 story commercial building	SEBF	U	3	16
10	58019	Stanford – 4 story residential building	WF	U	3	10
11	89494	Eureka – 5 story residential building	RM	U	7	13
12	58196	Berkeley- 5 Story parking structure	SCBF	U(R)	8	16
13	24386	Van Nuys- 7story hotel	RCMRF	D(R)	8	16
14	58354	Hayward - 13-story CSUH Admin Bld	RCMRF	Demo	2	16
15	01260	El Centro - Imperial Co Srvcs Bld	RCMRF	Demo	1	13

Among the selected fifteen buildings, nine of them are undamaged (U) and in operation at present, four are retrofitted (R) and currently in operation, and two have been demolished (Demo). One of the four retrofitted structures (station 24386) suffered severe damage during the 1994 Northridge earthquake while the other three were voluntarily retrofitted to seismically strengthen them. Out of the two demolished structures, one suffered from damage beyond repair (station 01260) and the other was found to be seismically unsafe (station 58354) by the California State University Seismic Review Board. The buildings have different occupancy types and PLFRS. Six of these structures have RC moment resisting frames (RCMRF), two have RC shear walls (RCSW), three have steel moment resisting frames (SMRF), two have steel braced frames (SBF), one has a wood frame (WF), and one has a reinforced masonry (RM) as the PLFRS. Each of these structures has at least 10 sensors installed at multiple floors.

H-MC framework for damage detection

The conventional post-earthquake damage assessment is a time consuming process. When relying on qualified inspectors alone, inspecting structures at the scale of a city can take weeks, if not months (Goulet et al. 2015). An alternative to using inspections alone is to use response data of the structure and ML tools to expedite the assessment process. However, a typical ML tool has some limitations when it comes to seismic damage detection due to the lack of data from damaged classes which may result in uncertainty in the detection. Human knowledge, domain expertise, and analytical skills can help to minimize these uncertainties. Therefore, an SHM framework called the human-machine collaboration (H-MC) is proposed herein which attempts to use advantages provided by ML in conjunction with the knowledge of humans. According to the National Research Council (2012), the H-MC is a framework in which humans co-work with artificial intelligence to complete specific tasks. The purpose of this framework is to use the particular strengths of both types of intelligence, and even physical capabilities, to fill in the weakness of one (e.g. the machine) by the intelligence of the other (e.g. the human).

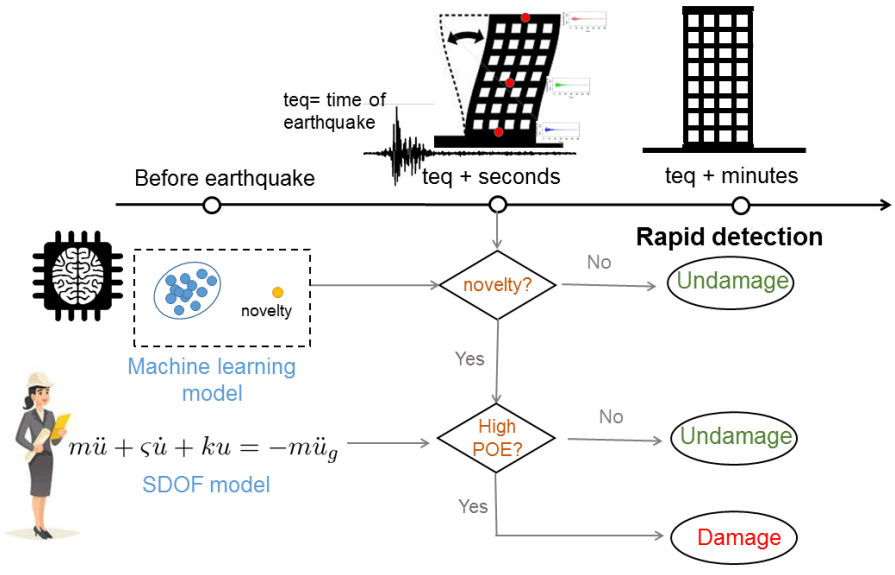

Figure 5 Human-machine collaboration (H-MC) framework for damage detection used in this study.

Figure 5 presents the H-MC framework for damage detection, which uses the responses from an undamaged structure and applies novelty detection as the ML tool for new data. Novelty detection is the identification of new or unknown data that a ML system is not aware of during training. It is similar to outlier detection, however, in the case of outlier detection the training dataset consists of outlier observations. The novelty model in this study develops non-parametric distribution using the training data and a distance measure of 1.5 times the interquartile range (IQR) to identify novelty, i.e. the new data is a novelty if it exists more than 1.5 interquartile range above the upper quartile or below the lower quartile. In the ideal case, where a large amount of data from the undamaged structure is available, considering data from low, moderate, and strong earthquakes, novelty detection alone could have indicated damage. However, for the buildings under considerations, data from strong but undamaging earthquakes are not available. Therefore, for these buildings, novelty detection may result in false positive detection for strong but undamaging events.

To overcome this limitation, the human aspect of this framework is introduced. A response envelope is developed by a domain expert representing the probability of exceedance (POE) of damage. This is performed by using a structure-specific SDOF model. NTHA is conducted using the 1,710 ground motions specified in set-1, and discussed above, having base shear coefficient recommended for the site of the building. Subsequently, the CAV and R_{CAV} of the damaging events are used to develop a joint cumulative distribution representing the POE of damage which is analogous to fragility curves but with two variables. Damage is identified when novelty is detected by the ML tool and the POE shows high probability values, as shown in Figure 5.

Results

Figures 6 to 8 show the damage detection results by the H-MC algorithm. In these figures, the colored contour plot is the POE envelope with higher probability shown with darker color. The dots are responses from all sensors installed at the roof level. When the dot is blue in color, it is detected as an undamaged event. When the dot consists of a red cross mark, it indicates damage has been identified. The damaged events will have a POE value greater than 0.5, i.e. they will be located in the darker region of the envelope. Figures 6 and 7 show that the undamaged buildings are correctly detected by the algorithm where all the responses are blue dots for these buildings. In some cases (such as station 58483, 24322, 58354, 57357, and 89494), novelty detection or POE envelope alone will result in false positive detection but when used together in the H-MC framework, the false positive results are successfully eliminated. Figure 8 shows the algorithm accurately detecting damage for station 24386 after the damaging event occurred. For station 01260, records are available from only the damaging earthquake. Therefore, the ML part of the framework is not possible to be applied for this building. However, by using the POE envelope alone, damage is detected for this case. In summary, the results show that the proposed H-MC framework uses two simple features, i.e. CAV and R_{CAV}, and able to obtain accurate detection although very limited dataset is used. This opens up the opportunity of rapid screening of existing structures after earthquakes with minimal computing time.

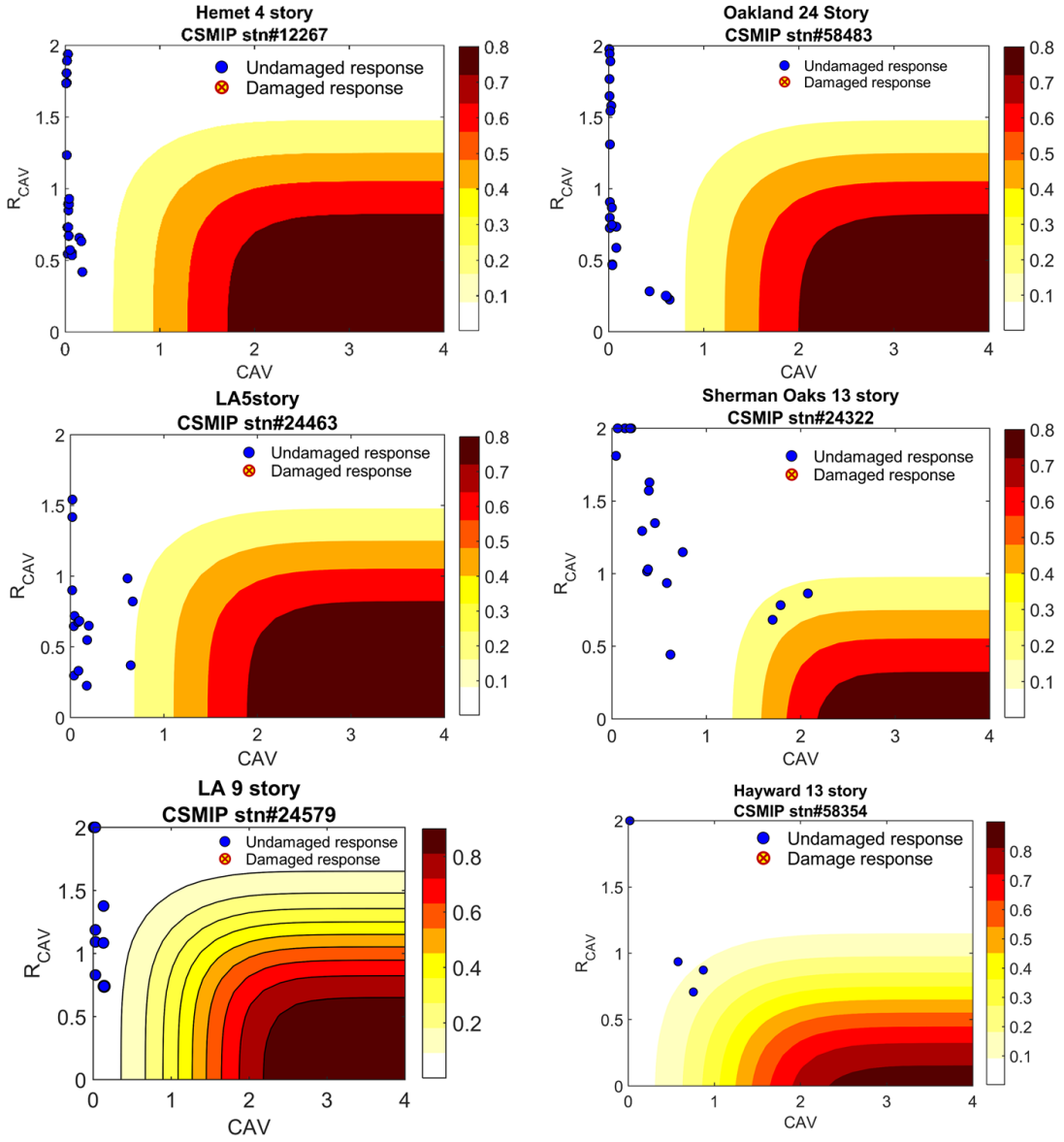

Figure 6 Plots generated by the damage detection algorithm showing accurate undamaged condition detection of the RC buildings.

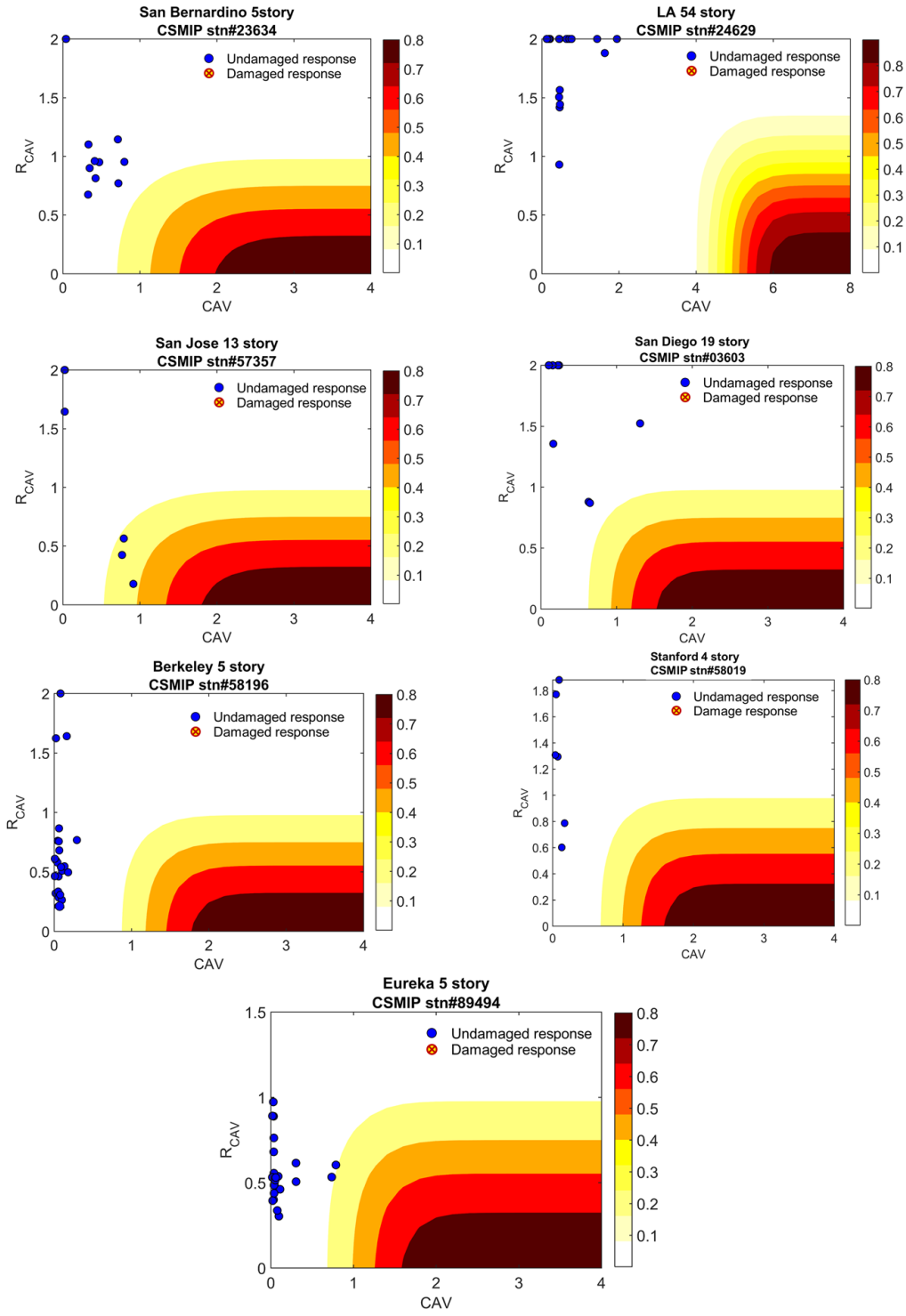

Figure 7 Plots generated by the damage detection algorithm showing accurate undamaged condition detection of steel, wood frame, and masonry buildings.

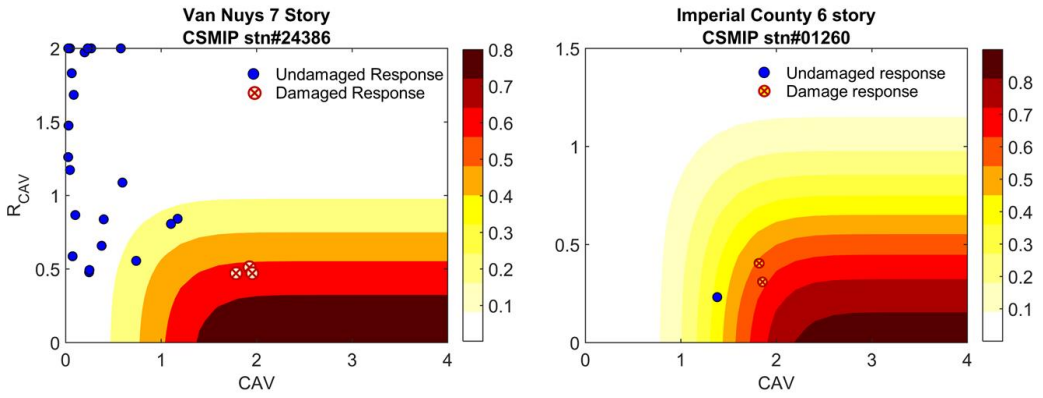

Figure 8 Plots generated by the damage detection algorithm showing accurate damaged condition detection of the two damaged buildings.

Conclusions

In this paper, a machine learning approach with single dimension features is presented to assess earthquake-induced damage in structures. Four cumulative absolute velocity (CAV)-based features are considered. A comparative study on a single degree of freedom (SDOF) system using these features and four separate machine learning tools reveals that CAV and R_{CAV} are the ideal features. These identified features are applied to assess the severity of damage of two multi-degree of freedom (MDOF) systems representing a five-story building with uniform (MDOF-US) and non-uniform (MDOF-NS) story shear capacity. Results show that this approach correctly detects the worst damage state with about 90.0% accuracy for both MDOF models when tested with NGA-West2 data. Moreover, this approach achieves damage state and location accuracies of 84.0% and 97.5%, respectively, for MDOF-US and damage state and location accuracies of 96.0% and 95.0%, respectively, for MDOF-NS for a test set significantly different from the training set.

Subsequently, the features are used in a human-machine collaboration (H-MC) framework to detect damage in selected fifteen California Strong Motion Instrumentation Program (CSMIP) instrumented buildings. The results showed that the H-MC algorithm correctly labeled the undamaged and damaged cases. This simple, low dimensional, and computationally efficient model can be reliably applied in structural health monitoring (SHM) scenarios with limited data. It opens up the opportunity to automate the process of damage detection and assess and notify the risk associated with each structure immediately after an earthquake. This is especially important for the residents of buildings in terms of having an idea about the condition of structures before conducting a formal tagging process which may take up to several weeks. Furthermore, such rapid damage assessment can be helpful for the immediate actions that need to be taken, such as deciding between leaving the building or staying in place and following the drop, cover and hold procedure. Overall, the model and corresponding results of the study can facilitate an efficient decision-making process regarding re-occupancy, emergency response, and future use of the structures following an earthquake event. This will, in turn, highlight the importance of building monitoring and encourage future building instrumentation efforts.

Acknowledgements

This research is mainly supported by the California Department of Conservation, California Geological Survey, Strong Motion Instrumentation Program agreement 1017-562. The authors would like to thank Dr. Selim Günay for his valuable inputs.

References

ASCE. 2017. “Infrastructure Report Card”. https://www.infrastructurereportcard.org/. Accessed 12 October 2017.

Baker, J.W., Lin, T., Shahi, S.K., Jayaram N. (2011) New ground motion selection procedures and selected motions for the PEER transportation research program. PEER Report 2011-3, Pacific Earthquake Engineering Research Center, UC Berkeley, CA.

Bommer, J. J. and Martinez-Pereira, A. (1999). The effective duration of earthquake strong motion. Journal of earthquake engineering, 3(02):127–172.

Bozorgnia, Y., Abrahamson, N.A., Atik, L.A., Ancheta, T.D., Atkinson, G.M., Baker, J.W., Baltay, A., Boore, D.M., Campbell, K.W., Chiou, B.S., Darragh, R., NGA-West2 research project. Earthquake Spectra, 2014, 30(3):973-987

Dua, R., Watkins, S. E., Wunsch, D. C., Chandrashekhara, K., and Akhavan, F. (2001). Detection and classification of impact-induced damage in composite plates using neural networks. In Proceedings, IJCNN’01. International Joint Conference on Neural Network. 1. 681–686.

Farrar, C. R. and Worden, K. (2012). Structural health monitoring: a machine learning perspective. Wiley, John & Sons.

Fathali, S. and Lizundia, B. (2011). Evaluation of current seismic design equations for nonstructural components in tall buildings using strong motion records. The Structural Design of Tall and Special Buildings, 20:30–46.

Günay, S. and Mosalam, K. M. (2017). Acceleration response spectrum: Revisited for higher mode effects.In 16th World Conference on Earthquake, Santiago Chile. January 9th to 13th 2017.

Goulet, J.A., Michel, C., and Kiureghian, A. D. (2015). Data-driven post-earthquake rapid structural safety assessment. Earthquake Engineering & Structural Dynamics, 44(4):549–562.

Hancock, J. and Bommer, J. J. (2006). A state-of-knowledge review of the influence of strong-motion duration on structural damage. Earthquake Spectra, 22(3):827–845.

Harris, A., Xiang, Y., Naeim, F., and Zareian, F. (2015). Identification and validation of natural periods and modal damping ratios for steel and reinforced concrete buildings in California. In SMIP15 Seminar on Utilization of Strong-Motion Data, pages 121–134.

IBC,(2012). International Code Council. International Building Code. International Code Council: Washington DC, United States.Kesavan, K. N. and Kiremidjian, A. S. (2012). A wavelet-based damage diagnosis algorithm using principal component analysis. Structural Control and Health Monitoring, 19(8):672–685.

Mahin, S., Lai, J. W., Wang, S., and Schoettler, M. (2015). Evaluating and improving the seismic performance of older tall buildings. In the second international conference on performance-based and life-cycle structural engineering. pages 25–37. School of Civil Engineering, The University of Queensland.

McKenna, F. (2010). OpenSees User's Manual.

Muin, S. and Mosalam, K. M. (2017). Cumulative absolute velocity as a local damage indicator of instrumented structures. Earthquake Spectra, 33(2):641–664.

Naeim, F., Hagie, S., Alimoradi, A., and Miranda, E. (2006). Automated post-earthquake damage assessment of instrumented buildings. In Advances in Earthquake Engineering for Urban Risk Reduction, pages 117–134. Springer.

National Research Council (NRC). 2012. Intelligent Human-Machine Collaboration: Summary of a Workshop. Edited by Ethan N. Chiang and Patricia S. Wrightson. Washington, DC: The National Academies Press. doi:10.17226/13479.

Palomino, L. V., Steffen, V., and Finzi, R. M. (2012). Fuzzy cluster analysis methods applied to impedance-based structural health monitoring for damage classification. In Topics in Modal Analysis II, Volume 6, pages 205–212. Springer.

Reed, J. W. and Kassawara, R. P. (1990). A criterion for determining exceedance of the operating basis earthquake. Nuclear Engineering Design, 123:387–396.

Santos, J., Calado, L., Orcesi, A., and Crémona, C. (2014). Adaptive detection of structural changes based on unsupervised learning and moving time-windows. In EWSHM-7th European Workshop on Structural Health Monitoring. Nantes, France.

Sohn, H., Worden, K., and Farrar, C. R. (2002). Statistical damage classification under changing environmental and operational conditions. Journal of Intelligent Material Systems and Structures, 13(9):561–574.

Tibaduiza, D., Mujica, L., Anaya, M., Rodellar, J., and Güemes, A. (2012). Independent component analysis for detecting damages on aircraft wing skeleton. In Proceedings of the 5th European Conference on Structural Control (EACS 2012), Genoa, Italy, pages 18–20.

Wald, D. J., Quitoriano, V., Heaton, T. H., and Kanamori, H. (1999). Relationships between peak ground acceleration, peak ground velocity, and modified Mercalli intensity in California. Earthquake Spectra, 15(3):557–564.

Worden, K., Manson, G., and Fieller, N. R. (2000). Damage detection using outlier analysis. Journal of Sound and Vibration, 229(3):647–667.

STRONG MOTION INSTRUMENTATION OF TWO NEW SUPER TALL BUILDINGS IN CALIFORNIA AND RESULTS FROM AMBIENT AND EARTHQUAKE RESPONSE DATA

Moh Huang, Daniel Swensen, Hamid Haddadi and Troy Reitz

Strong Motion Instrumentation Program, California Geological Survey,
Department of Conservation, Sacramento, California

Abstract

The Wilshire Grand Tower in Los Angeles and the Salesforce Tower in San Francisco are two new super tall buildings in California. Both buildings use concrete core shear walls to resist earthquake forces and were designed using a performance-based seismic design approach. During construction, the Wilshire Grand Tower and the Salesforce Tower were extensively instrumented with 36 and 32 sensors, respectively, in a joint effort by the owners and the California Strong Motion Instrumentation Program. This paper describes the sensor locations in the buildings and the instrumentation objectives. Data recorded at the Salesforce Tower during the M4.4 Berkeley earthquake of January 4, 2018, and the ambient vibration data obtained by the instrumentation systems in both buildings are presented. Results from some preliminary analyses of the data are also discussed.

Introduction

The Wilshire Grand Tower in downtown Los Angeles, shown in Figure 1, is a 73-story mixed-use office and hotel building with a surrounding podium. The main tower has 900 hotel rooms on the upper 40 floors, 400,000 square feet of office space, and various restaurants and retail spaces. The height of a typical story is 11.5 feet for hotels and 14 feet for offices. The top of the structure features restaurants, an architectural roof top sail and an architectural spire. The rooftop sail is a steel structure standing 97 feet above the main roof. A tubular steel cantilever spire is attached to the east side of the sail and extends 176 feet above the sail. With the spire, this is the tallest building west of the Mississippi River with a height of approximately 1,100 feet. The building was designed in accordance with the 2011 City of Los Angeles Building Code and performance-based seismic design procedures which were reviewed by a peer review panel (Joseph, et al., 2014; Joseph, et al., 2015). Construction began in 2014 and the building opened on June 23, 2017. The building was required by the City to be extensively instrumented by the owner. CSMIP reviewed the proposed sensor locations from the structural engineer of record, developed specifications and provided technical assistance in instrumentation. The instrumentation system with 36 sensors in the building was completed in June 2017.

The Salesforce Tower in downtown San Francisco, shown in Figure 1, is a 61-story office building. The tower is next to the new Transbay Transit Center. The top occupied floor is 901 feet above the street level. With the crown structure at the top, the building is 1,070 feet in

height and is the tallest building in San Francisco. The height of a typical story is 14.75 feet. The crown structure comprises 152.5 feet tall steel concentrically braced steel frames, supported at the top of concrete walls at Level 64 and steel columns at Level 62. The building was designed according to the 2010 San Francisco Building Code and performance-based seismic design procedures which were reviewed by a peer review panel (Valley, et al., 2014; Klemencic, 2017). Construction began in 2013 and the building opened on May 22, 2018. The owner was required by the City to instrumented the building at three levels. However, more extensive instrumentation was suggested. CSMIP developed the sensor locations and instrumentation plans, and worked with the contractor to install the instrumentation system in the building. The instrumentation system with 32 sensors in the building was completed in February 2018.

Figure 1. Views of the Wilshire Grand Tower in Los Angeles (left) and the Salesforce Tower in San Francisco (right).

Wilshire Grand Tower in Los Angeles

Building Structural System

The Wilshire Grand Tower has a roughly rectangular floor plan with dimensions of up to 244 by 112 feet. The core wall is also roughly rectangular, with dimensions of up to 128 by 38 feet. The vertical load carrying system inside the concrete core wall consists of concrete beams and slabs. Outside the core wall, the system consists of lightweight concrete over metal decks supported by steel beams, steel box columns filled with concrete, and concrete core walls. The floor slabs comprise 3.25" concrete fill over 3" metal deck from Floors 2 to 30, and 4.25" concrete fill over 2" metal deck from Floors 31 to the Roof. Concrete flat slabs are the floor

system used at the First Floor and below. As shown in Figures 2 and 3, the sail at the tower top is a glazed steel braced frame structure standing 97 feet about the main roof at Level 73. There are no floor slabs in the sail structure. A tubular steel cantilever spire is attached to the east side of the sail and extends to 176 feet above the sail. A large glass skylight separates the tower from the adjacent podium structure.

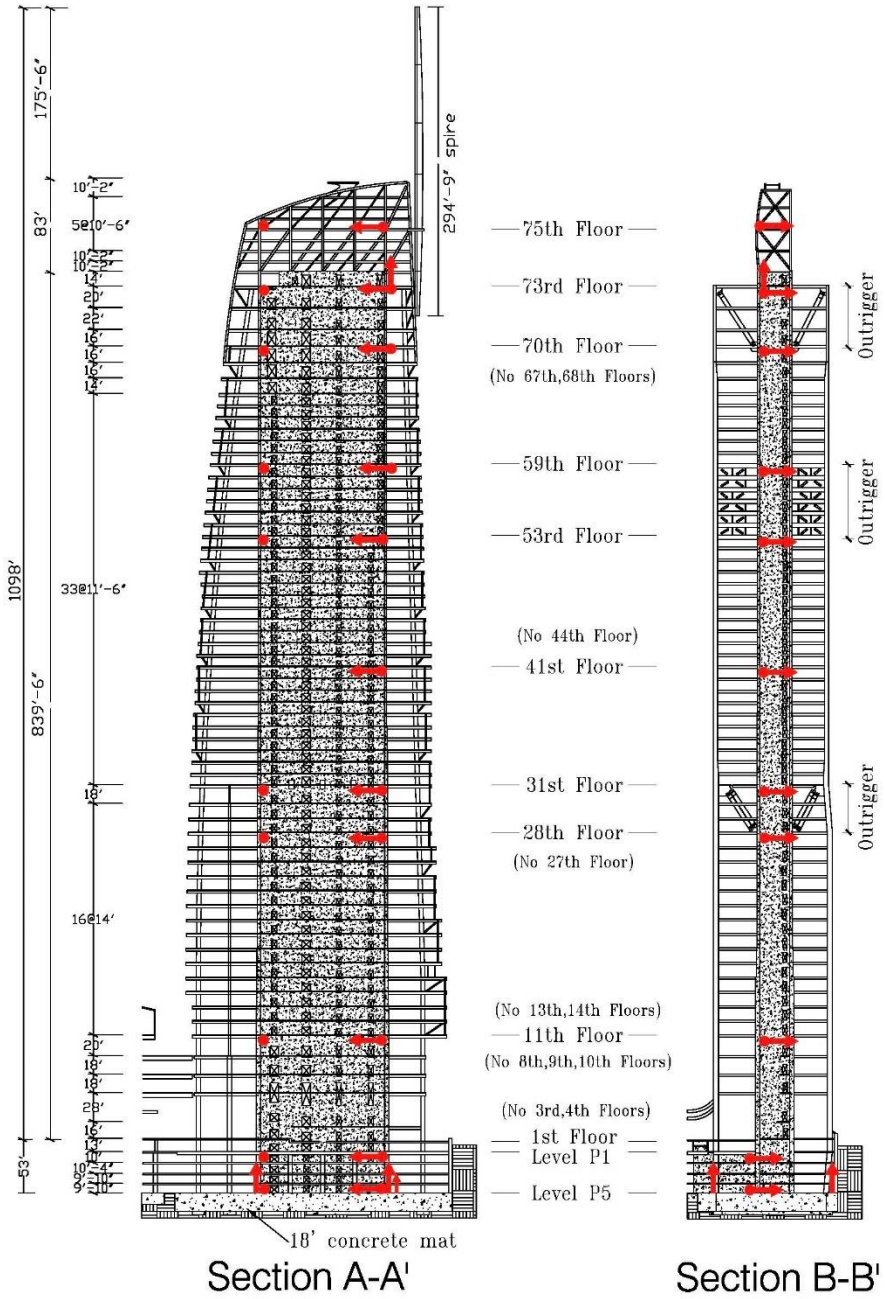

Figure 2. Section views showing the lateral force resisting system of Wilshire Grand Tower with concrete core walls and outriggers at three levels. The locations of the 36 sensors installed in the building are also shown. (Arrows indicate sensing direction; solid circles indicated out of the page.)

Figure 3. View of the concrete core wall and steel gravity system for Wilshire Grand Tower (left), and the rooftop sail structure and spire (right).

The lateral force resisting system of the building comprises concrete core shear walls with steel buckling restrained brace (BRB) outriggers and belt trusses. Concrete walls are 48" thick at the base of the structure and 24" thick near the top of the building. In the transverse direction, the core wall is about 38 feet wide and 895 feet tall, which results in a very large slenderness ratio of about 23.5. Three outriggers, as shown in Figure 2, consisting of steel BRBs extending between the core walls and concrete-filled steel box columns, are used to resist the overturning moments. A total of 170 braces are placed at three locations along the height of the structure: (1) lower outriggers between 28th and 31st Floor with ten double-double 2,200-kip BRBs (40 total); (2) middle outriggers between 53rd and 59th Floor with ten BRB frames, each frame having twelve 800-kips BRBs (120 total); and (3) upper outriggers between 70th and 73rd Floor with ten single 2,200-kip BRBs (Nieblas & Tran, 2015; Joseph et al, 2014; Joseph et al., 2016). Three-story tall steel belt trusses wrap the building at two levels to improve torsional behavior and minimize the effects of differential shortening, as shown in Figure 4.

The tower is supported on an 18 feet thick concrete mat foundation which bears on bedrock. The site is underlain by siltstone and sandstone of the Fernando Formation. The footprint of the mat foundation extends beyond the perimeter of the tower in order to reduce the bearing pressure beneath the mat and provide greater stability for the foundation. The foundation was poured continuously in mid-February of 2014; a total of 21,200 cubic yards of concrete were poured in 18.5 hours (Nieblas, 2014).

The seismic design for the podium and basement was based on the prescriptive procedures in the 2010 California Building Code and the ASCE7-05. However, the seismic design of the tower was based on performance-based procedures. In the performance-based seismic design, the building responses are checked to meet stated performance objectives at two

different shaking levels: Maximum Considered Earthquake (MCE) with a 2,475-year return period, and Service Level Design Earthquake (SLDE) with a 43-year return period. First, the design was performed using a linear elastic building model subjected to the wind loads and the SLDE level earthquake forces. Response history analyses were then performed using a nonlinear building model subjected to 11 pairs of ground motion records at the MCE shaking level. Records from two main earthquake sources were used for the analyses: magnitude 7.8 from the distant San Andreas fault and magnitude 6.6 from the local Puente Hills blind thrust fault (Joseph et al. 2015).

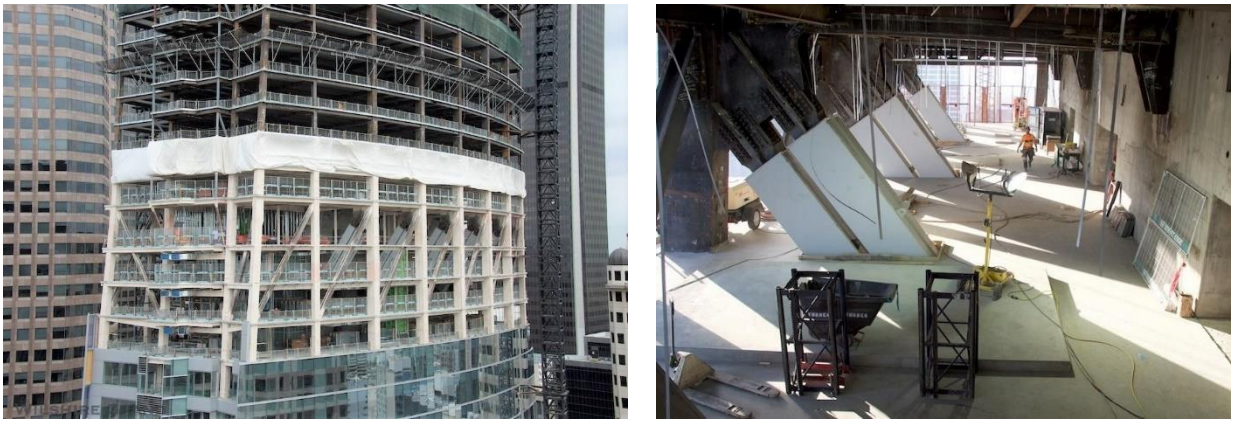

Figure 4. Steel belt trusses and BRBs between the 28th and 31st Floor of Wilshire Grand Tower.

Strong-Motion Instrumentation

The Wilshire Grand Tower was required by the City of Los Angeles to be extensively instrumented with a minimum of 32 sensors (LATBSDC, 2011). Starting in 2011, high-rise buildings with performance-based design were required to be instrumented with a minimum number of sensors dependent on the number of stories (Naeim, 2013). CSMIP contacted the owner's representative in December 2014, and offered to provide technical assistance in instrumentation as well as maintain the instrumentation system after it was installed. An agreement was reached between CSMIP and the building owner in February 2015. The structural engineer of record and the peer review panel proposed the locations of 36 sensors in the building. CSMIP engineering staff reviewed the proposed sensor locations and recommended changes to optimize placements of these 36 sensors. The locations of these 36 sensors were finalized and approved by the peer review panel. CSMIP then developed the technical specifications for the instrumentation system in June 2015. During construction, CSMIP visited and marked the sensor locations in the building with the contractor and the equipment manufacturer. The sensor cables were run by the contractor, and the sensors and recorder were installed by the equipment manufacturer. CSMIP staff performed the acceptance test for the system on June 29, 2017.

The locations of the 36 accelerometers in the Wilshire Grand Tower are shown in Figure 2. Each of the 36 sensors is connected via cabling to the central recorders. The digital recorders coupled with a communication system allow the recording system to immediately send the data to the CSMIP office in Sacramento after the system is triggered by an earthquake. Due to the

congested built environment around the building, no instrument has been installed at a nearby site to measure the reference ground motion for the building.

The primary objective of instrumentation for this building was to install a sufficient number of sensors to measure the response of the building to earthquake ground shaking. Although there are limitations on the locations for the sensors, in general, the more sensors that are installed, the more information that can be obtained. The recorded data should be adequate to characterize the seismic response of the building.

The motions of the rigid concrete mat foundation are measured by six sensors including three horizontal and three vertical sensors. As shown in Figure 5, these six sensors were installed at strategic locations at Level P5 so the six components of rigid body motion could be determined from the records from these sensors. These six components include three translational motions and three rotational motions (i.e., two rocking and one torsional) of the building base. Three horizontal sensors were repeated at Level P1, the highest level where the tower floor slab is still tied to the adjacent podium structure.

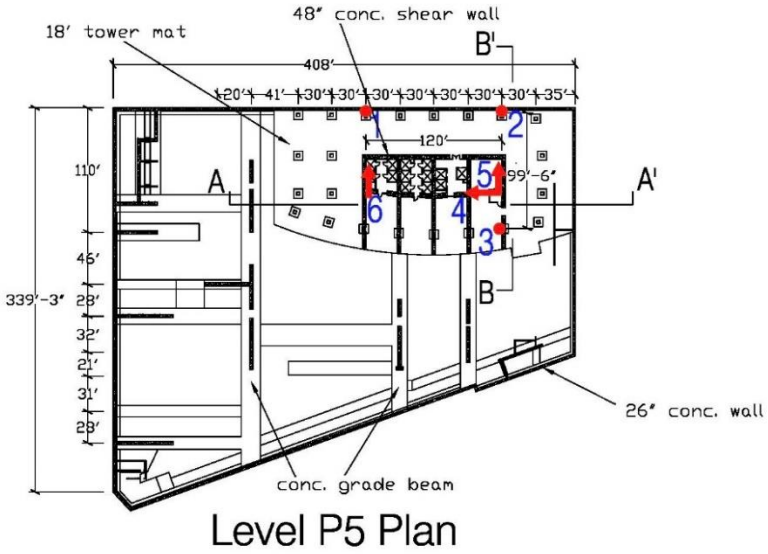

Figure 5. Locations of six sensors at Level P5, base of Wilshire Grand Tower, which measure translational and rotational motions of the concrete mat foundation.

The remaining 27 sensors were installed in the upper stories of the tower. The levels where the outrigger brace connections occur were selected to be installed with sensors. Specifically, these floors are 28th, 31st, 53rd, 59th, 70th and 73rd, as shown in Figure 2. Each of these levels was instrumented with three sensors (see Figure 6) to measure the translational and torsional motions of the floor. The 11th and 41st Floors, which are in between the outriggers, were instrumented with three and two sensors, respectively, to allow better determination of the vibration mode shapes. A vertical sensor was added at the top of the core shear wall at the 73rd Floor to measure how the building motion is amplified in the vertical direction. Finally, the sail structure on the tower top was instrumented with three sensors at the 75th Floor.

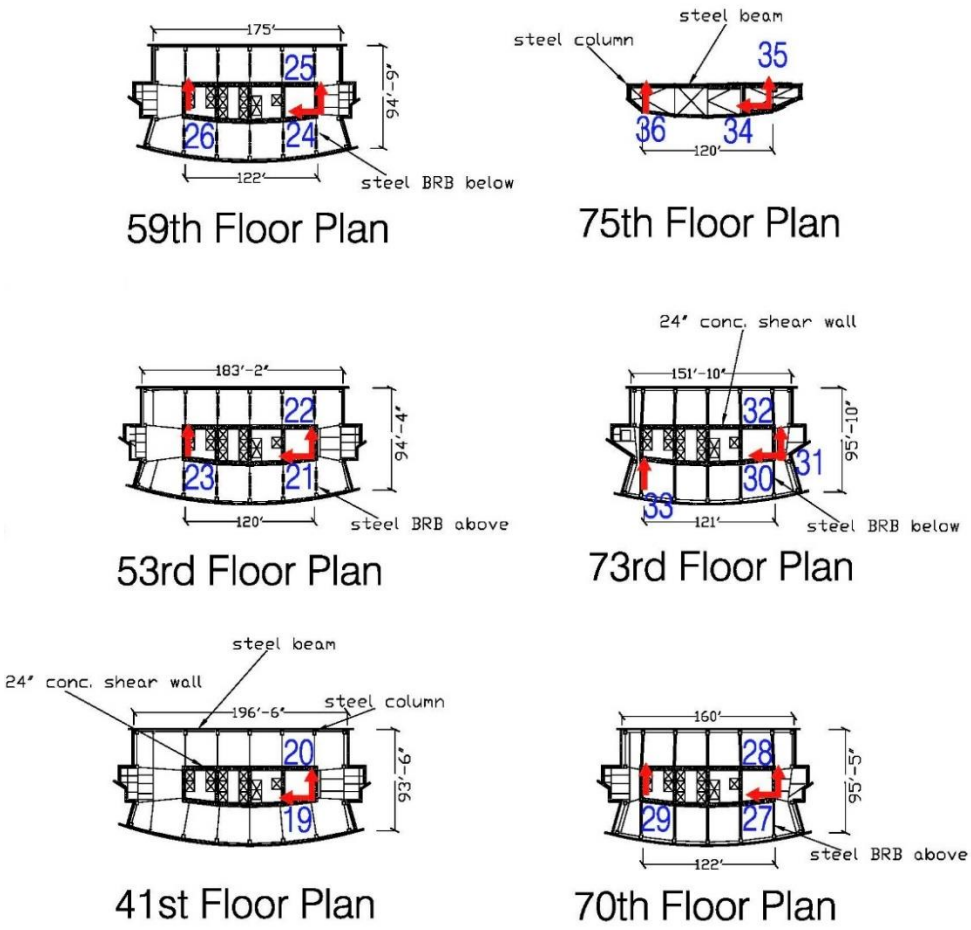

Figure 6. Sensor locations at the 41st Floor and above at Wilshire Grand Tower.

Ambient Vibration Data

After instrumentation of the building was completed, ambient vibration data were taken by manually triggering the system on September 21, 2017. The ambient data has a duration of 2.5 minutes. The sampling rate is 200 samples per second. More rigorous analyses of the ambient data can be performed by using detailed system identification methods to obtain modal frequencies and mode shapes (Celebi, et al. 2013). However, the building fundamental periods can be easily obtained from the ambient data. Figure 7 shows the ambient velocities integrated from the ambient acceleration records from sensors in the transverse (NS) direction at the eleven instrumented levels along the height of the building. A frequency band pass filter of 46 Hz to 10 seconds was applied in the data processing. Similarly, Figure 8 shows the ambient velocities from sensors in the longitudinal (EW) direction. It can be observed from Figures 7 and 8 that the ambient motions in the transverse direction were about six times larger than those in the longitudinal direction. This is due to the fact that the area exposed to wind loading is larger in the transverse direction and also that the building is stiffer in the longitudinal direction. The ambient data clearly show that the building fundamental period at the ambient shaking level is about 6.0 seconds in the transverse direction and about 3.4 seconds in the longitudinal direction. These periods can be obtained from either the time history plots in Figures 7 and 8 or the velocity response spectra shown in Figure 9.

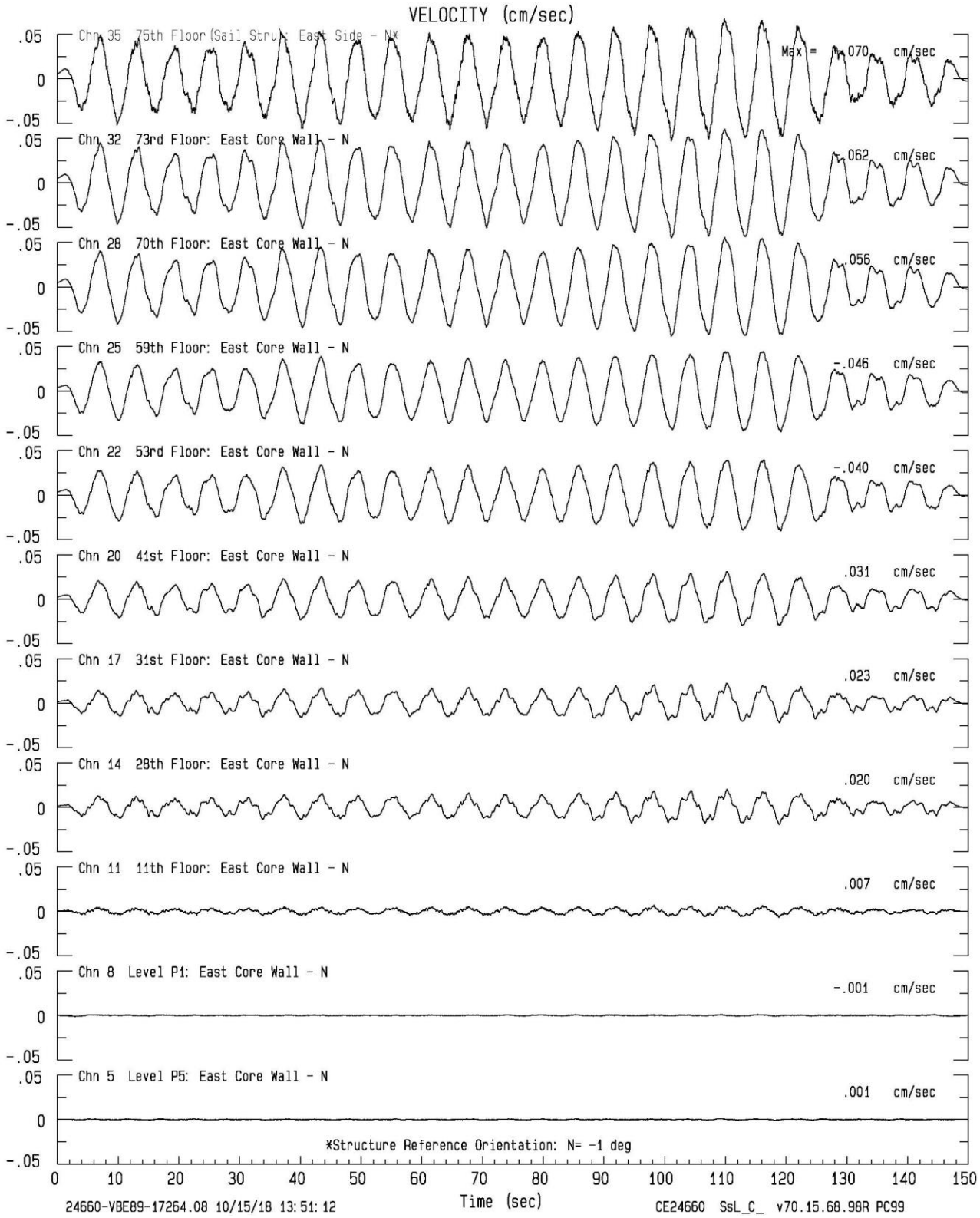

Figure 7. Velocities integrated from the ambient acceleration data from sensors in the transverse (NS) direction at 11 instrumented levels of the Wilshire Grand Tower.

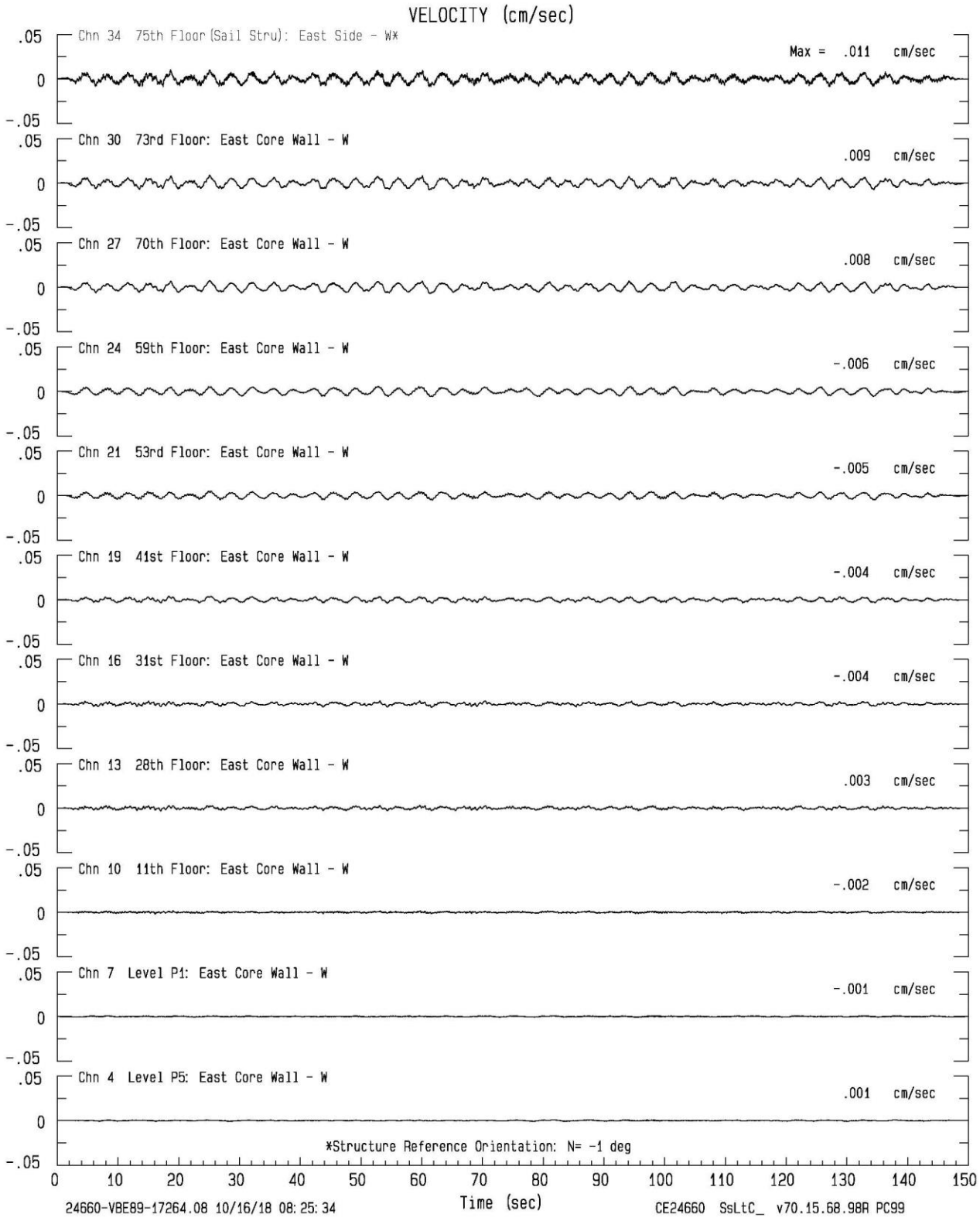

Figure 8. Velocities integrated from the ambient acceleration data from sensors in the longitudinal direction (EW) at 11 instrumented levels of the Wilshire Grand Tower.

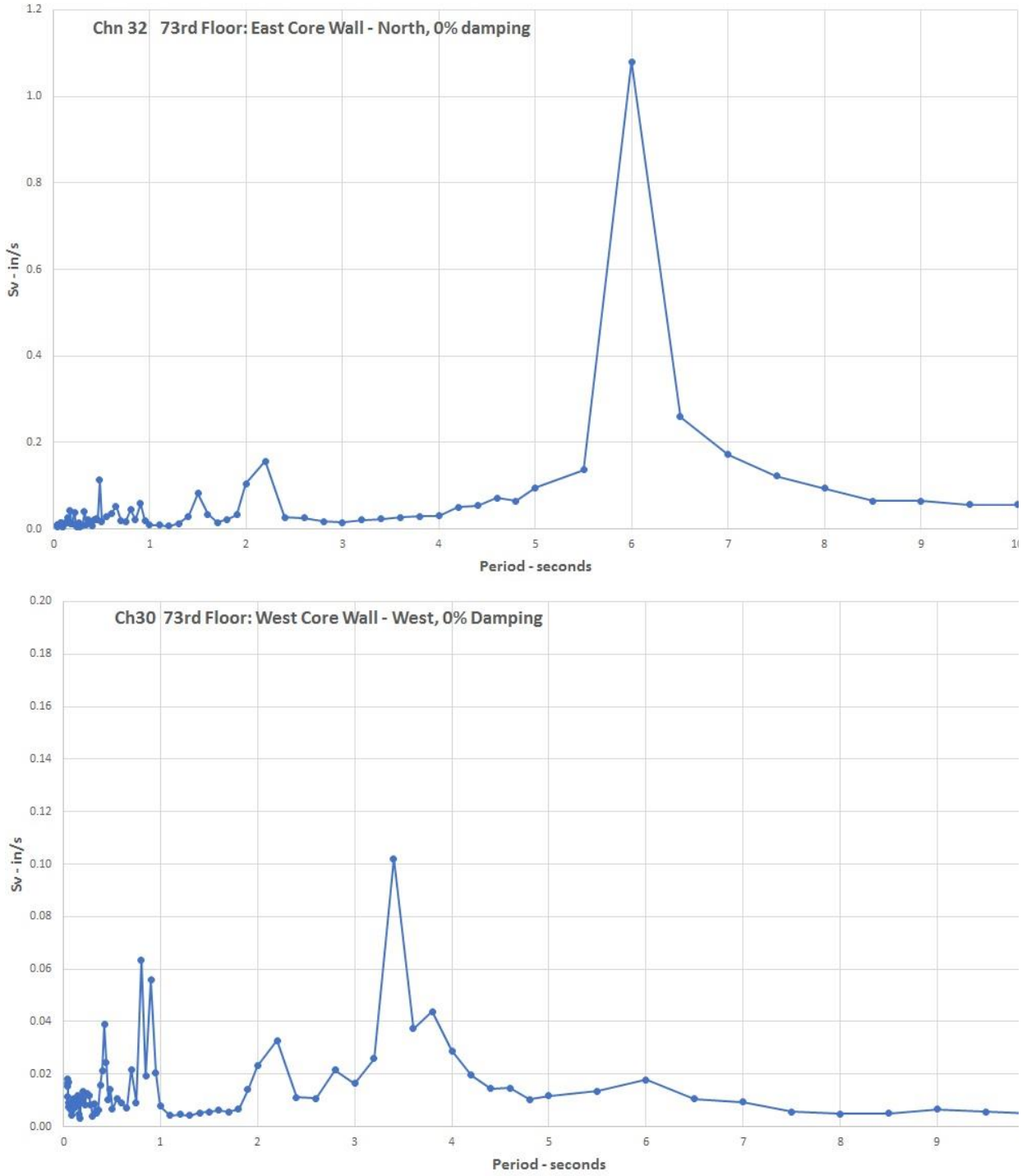

Figure 9. Zero percent damping velocity response spectra (Sv) of the ambient data from Sensor 32 (transverse direction) and Sensor 30 (longitudinal direction) on the 73rd Floor of the Wilshire Grand Tower.

Salesforce Tower in San Francisco

Building Structural System

The Salesforce Tower has a roughly square floor plan with dimensions of up to 167 by 167 feet and rounded corners. The core wall is roughly square, with dimensions of up to 89 by 83 feet. The building includes three stories below grade for parking and 61 stories above grade for offices. The basement footprint is slightly larger than the tower, with dimensions of 198 by 184 feet. The typical story height is 14′-9". The vertical load carrying system inside the concrete core wall consists of concrete beams and slabs. Outside the core wall, the system consists of lightweight concrete over metal decks supported by steel beams and columns, and concrete core walls. The exterior walls of the building are vertically straight between Levels 1 and 27. Beyond Level 27, the exterior walls gradually taper in. The top occupied floor (Level 61) is 901 feet above street level. With the steel crown structure, the top of the tower reaches a height of 1,070 feet, as shown in Figure 10. The Salesforce Tower is the tallest building in San Francisco.

The lateral force resisting system of the building comprises special concrete shear walls at the central elevator and stair core. The northern cell of the core shear wall terminates at Level 50, as shown in Figure 11. The southern cell of the core shear wall tops out at Level 64 (961 feet above the street level). The concrete wall thickness varies from 48" at the base of the structure to 24" near the top. The slenderness ratio of the concrete core is about 12.9 in the east-west direction and 12.0 in the north-south direction. The tower is crowned with a 152.5 feet tall ordinary steel concentrically braced frame structure supported at the top of concrete walls (Level 64) and steel columns at Level 62, as shown in Figure 12. There are no floor slabs on the steel crown structure.

The tower foundation is a concrete mat supported by 42 rectangular deep foundation elements (barrettes). The concrete mat varies in thickness from 14 feet at the core to 5 feet at the perimeter. The barrettes are 5 by 10.5 feet in plan and 185 to 230 feet long and are socketed into the bedrock below. The site is underlain by fill, sand and old bay mud. The depth to the bedrock from the street level is about 250 feet.

The Salesforce Tower was designed in accordance with the 2010 San Francisco Building Code. A performance-based seismic design approach was used for the building (Klemencic, et al., 2017). Response history analyses were performed using a nonlinear building model subjected to two suites of 11 pairs of ground motion records at the MCE shaking level (Valley, et al., 2014). One suite represented long period ground motions, while the other suite represented shorter period ground motions. Nonlinear soil-structure-foundation interaction analyses were performed to assess the effects from the adjacent Transbay Transit Center. The crown structure was designed as a non-structural component (Valley, et al., 2014).

Strong-Motion Instrumentation

The Salesforce Tower was required by the City of San Francisco to be instrumented at three levels (code-type instrumentation). CSMIP contacted the structural engineer of record (SEOR) and suggested extensive instrumentation of the building. CSMIP obtained permission

from the owner in February 2016 to extensively instrument the building as part of the CSMIP network. CSMIP staff developed and proposed the locations for 32 accelerometers in the building after studying the structural and architectural floor plans of the building. The sensor locations were then reviewed and commented on by the SEOR, the owner and a representative member of the Strong Motion Instrumentation Advisory Committee. During construction, CSMIP visited and marked the sensor locations in the building with the electrical contractor. The electrical contractor installed the sensor cables and received funding from the owner and CSMIP. CSMIP staff installed most of the sensors and the recorder in the building in December 2017 and completed the installation of the remaining sensors in the crown structure on February 21, 2018.

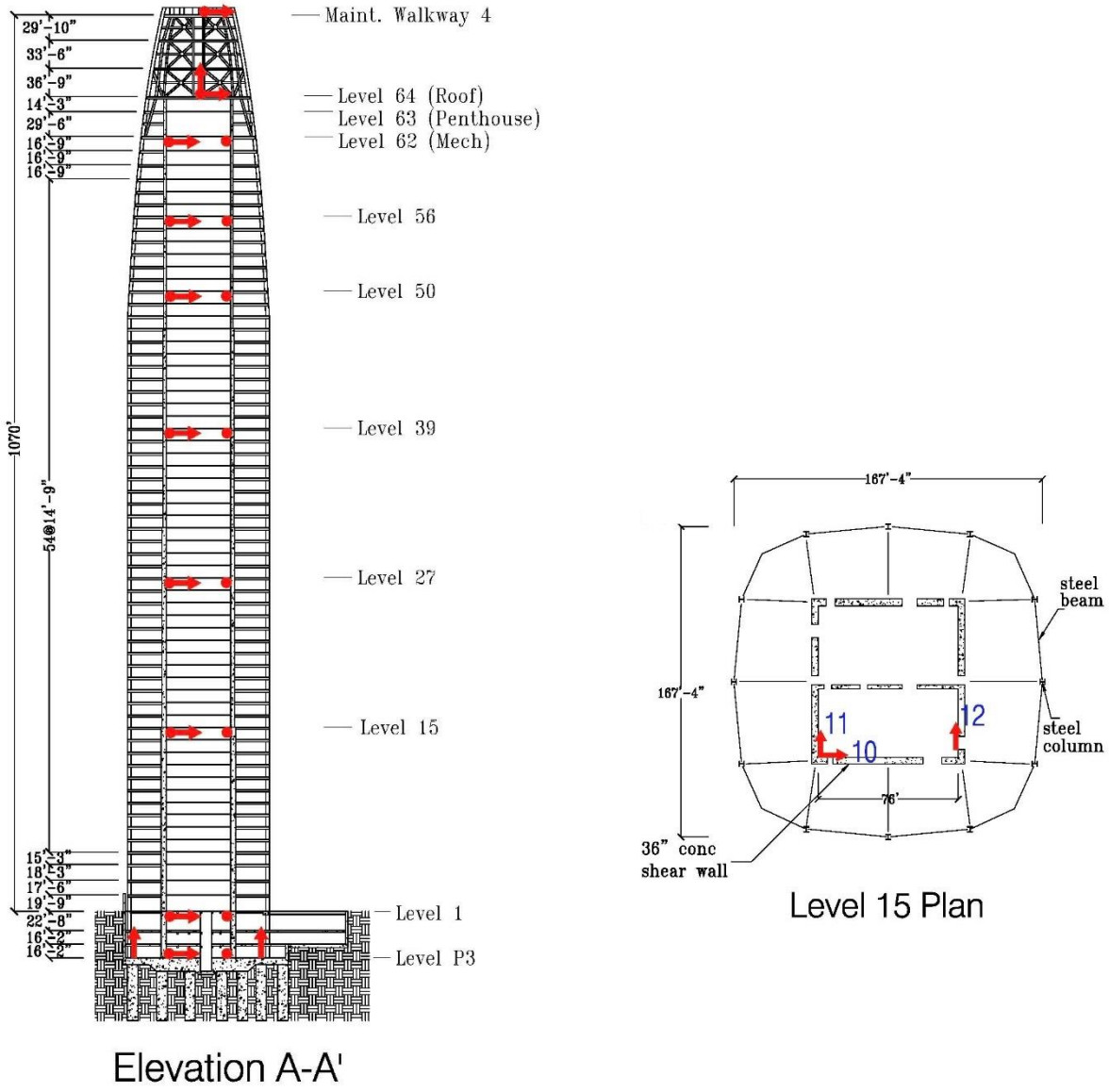

Figure 10. Elevation view showing the locations of the 32 sensors installed in the Salesforce Tower, and a typical framing plan for lower floors (Level 15 is shown).

The locations of the 32 accelerometers in the Salesforce Tower are shown in Figure 10. Each of the 32 sensors is connected via cabling to the central recorder. The digital recorder coupled with a communication system allow the recording system to immediately send the data to the CSMIP office in Sacramento after the system is triggered by an earthquake. Due to the congested built environment around the building, no instrument has been installed at a nearby site to measure the reference ground motion for the building.

Figure 11. Views of Salesforce Tower after (left) and during (right) construction. The reduction of the concrete shear wall core at Level 50 can be seen in the right photo.

Figure 12. Views of concrete core wall and steel gravity system of Salesforce Tower during construction (left) and the steel crown structure on the top of the building (right).

The building foundation is a concrete mat. The motions of this rigid concrete mat are measured by six sensors including three horizontal and three vertical sensors. As shown in Figure 13, these six sensors were installed at strategic locations at Level P3 so the six components of rigid body motion could be determined from records from these sensors. These six components include three translational motions and three rotational motions (i.e., two rocking and one torsional) of the building base. Three horizontal sensors were repeated at Level 1 where the floor slab is tied to the 24" perimeter concrete walls at street level.

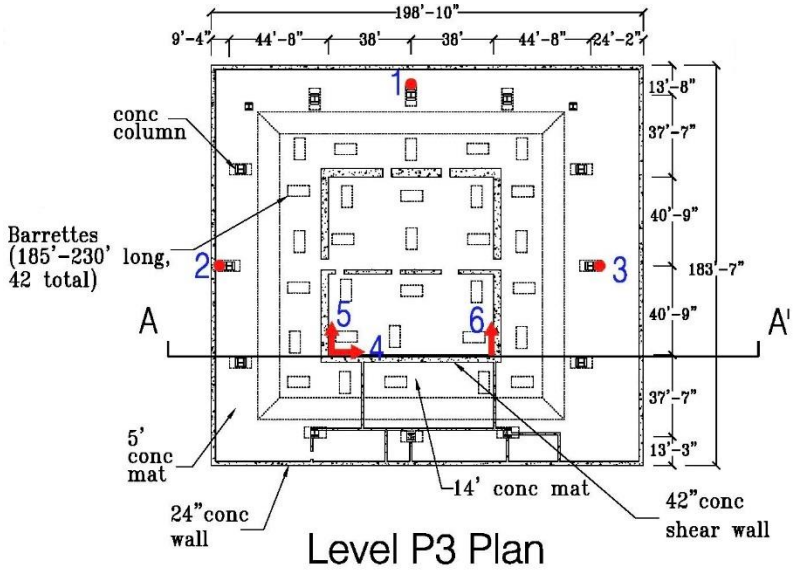

Figure 13. Locations of six sensors at Level P3, base of the Salesforce Tower, which measure translational and rotational motions of the concrete mat foundation.

The remaining 23 sensors were installed in the upper stories of the tower. The levels selected to be installed with sensors are spaced evenly along the height of the building. Specifically, these floors are Levels 15, 27, 39, 50, 56 and 62, as shown in Figure 10. In particular, Level 50 was selected because the core concrete shear walls are reduced at this level. Each of these levels was instrumented with three sensors to measure the translational and torsional motions of the floor. At the request of the owner, these sensors could not be installed in any office space. Therefore, they could only be installed inside the central core, as shown in Figure 14. The sensors were installed in the southern cell of the core wall because it goes all the way to Level 64. The sensor locations inside the core are repeated at each level except at Level 64. For the crown structure, three sensors including one vertical sensor and two horizontal sensors were installed at Level 64, which is the top of the core shear wall and the base of the steel crown structure. Finally, two horizontal sensors were installed at the top of the steel crown structure to measure its response.

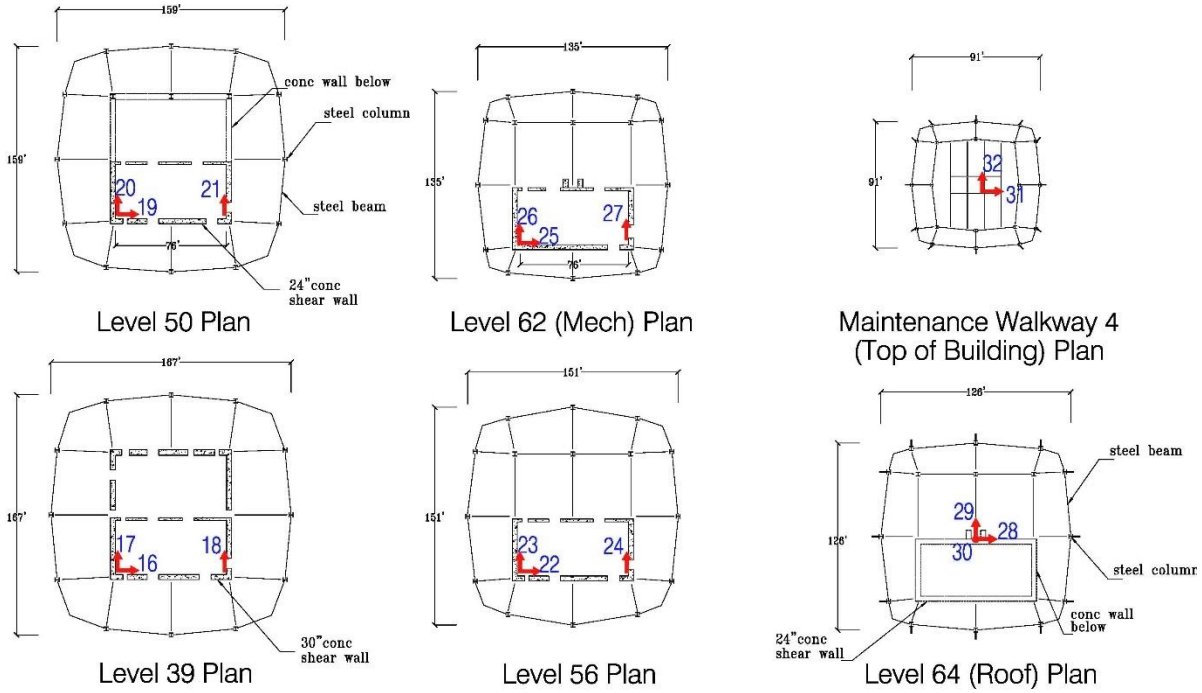

Figure 14. Sensor locations at the 41st Floor and above at Wilshire Grand Tower.

Record from M4.4 Berkeley Earthquake of January 4, 2018

The M4.4 Berkeley earthquake occurred on January 4, 2018 at a distance of about 10 miles from the Salesforce Tower. At the time of the earthquake, most of the sensors in the building had been installed. The sensors at the crown structure were not installed because the area was not accessible yet. The instrumentation system with 26 installed sensors recorded the Berkeley earthquake even though the system was not fully installed. The recorded motions from the Berkeley earthquake were small amplitude responses of the building. Recorded peak accelerations were 1.3% g at Level P3 and 3.0% g at Level 62. The acceleration records are shown in Figure 15 for the north-south direction and in Figure 16 for the east-west direction. The first vibrational mode of the building in each direction was hardly excited by this small earthquake which did not generate any significant long period ground motions. Motions of higher modes dominated in the acceleration, velocity and displacement time histories. However, we could find the first mode in the tripartite response spectra plots, such as those from the sensors at Level 62 shown in Figure 17. The first mode period is about 5.0 seconds in each direction. In addition, the floor torsional motion could be seen in the records of a pair of sensors in the north-south direction at the upper levels, such as the records shown in Figure 15 from Sensors 26 and 27 at Level 62.

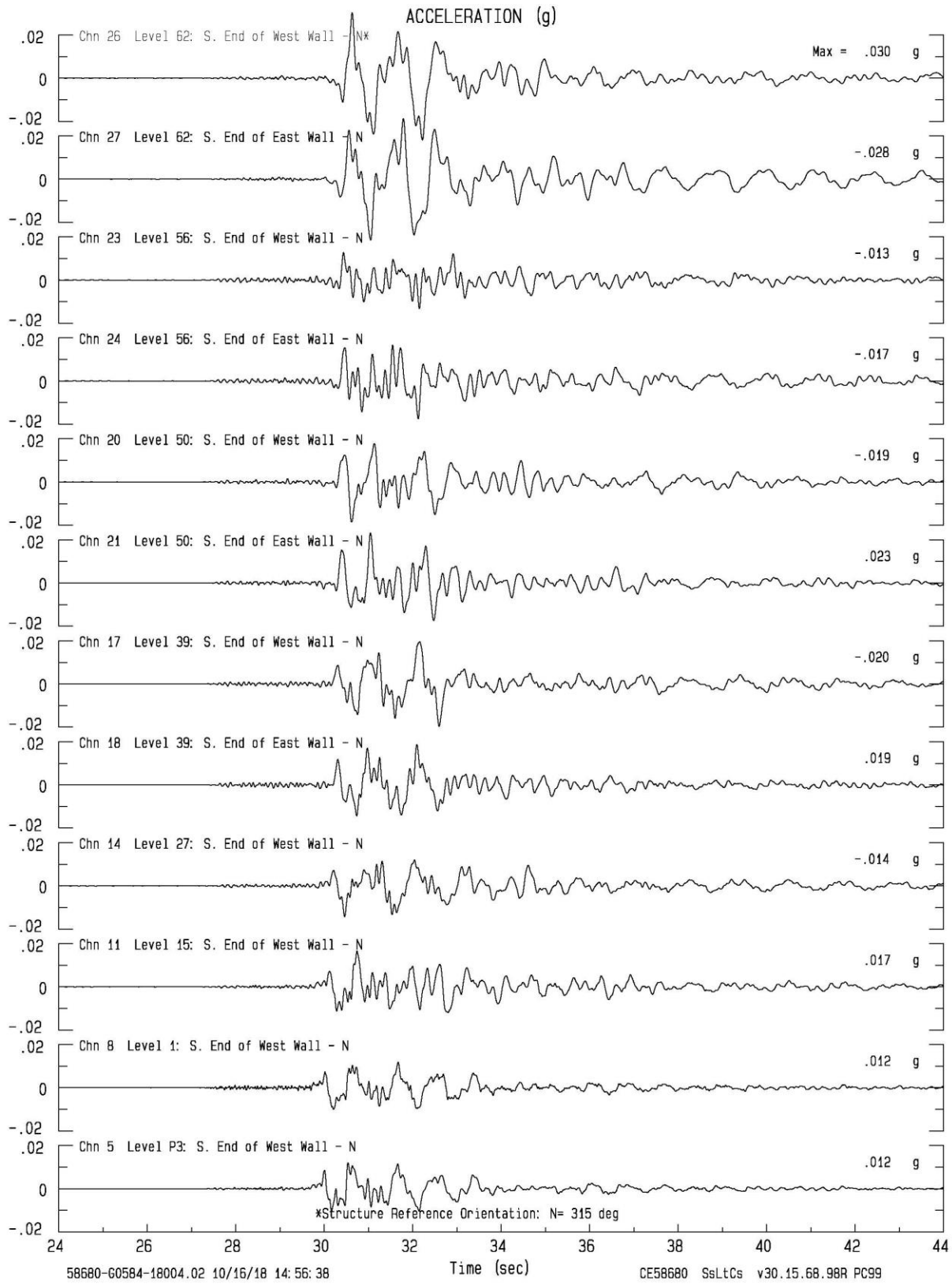

Figure 15. Acceleration records from selected sensors in the NS direction obtained from Salesforce Tower during the M4.4 Berkeley earthquake of January 4, 2018.

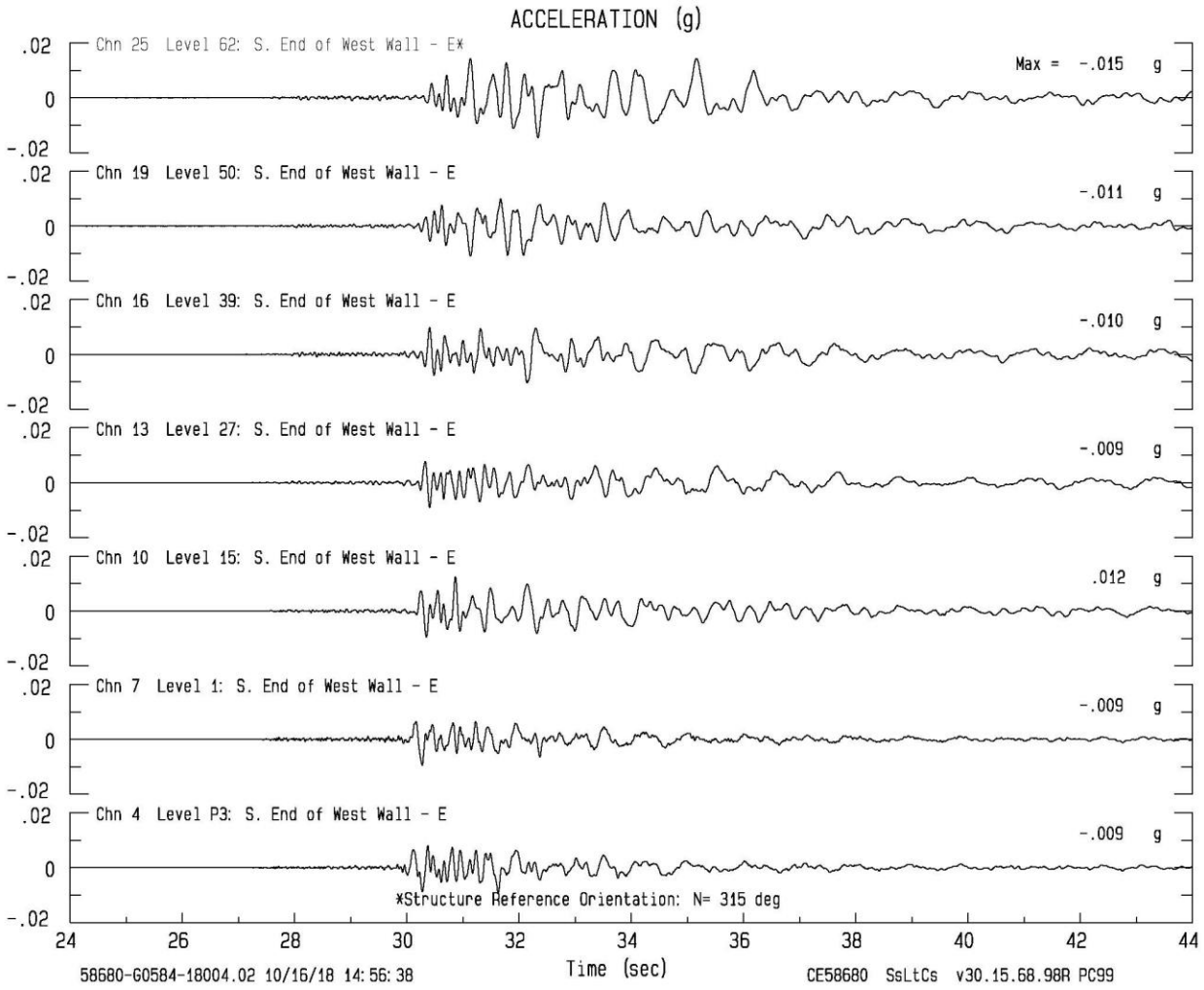

Figure 16. Acceleration records from selected sensors in the EW direction obtained from Salesforce Tower during the M4.4 Berkeley earthquake of January 4, 2018.

Ambient Vibration Data

After the instrumentation in the building was completed, ambient vibration data were taken by manually triggering the system on March 1, 2018. The ambient data has a duration of 2.5 minutes. The velocities integrated from the ambient acceleration records from selected sensors at the ten instrumented levels along the height of the building are shown in Figures 18 and 19 for the north-south and east-west directions, respectively. A frequency band pass filter of 46 Hz to 10 seconds was used in data processing. The record at the top of the crown structure contains some high-frequency motions which are probably associated with local vibration of the steel members. The zero damping velocity response spectra for the ambient motions measured at Level 64 are shown in Figure 20. The time history plots and the response spectra clearly show that the building fundamental period at the ambient shaking level is about 5.0 seconds in both directions.

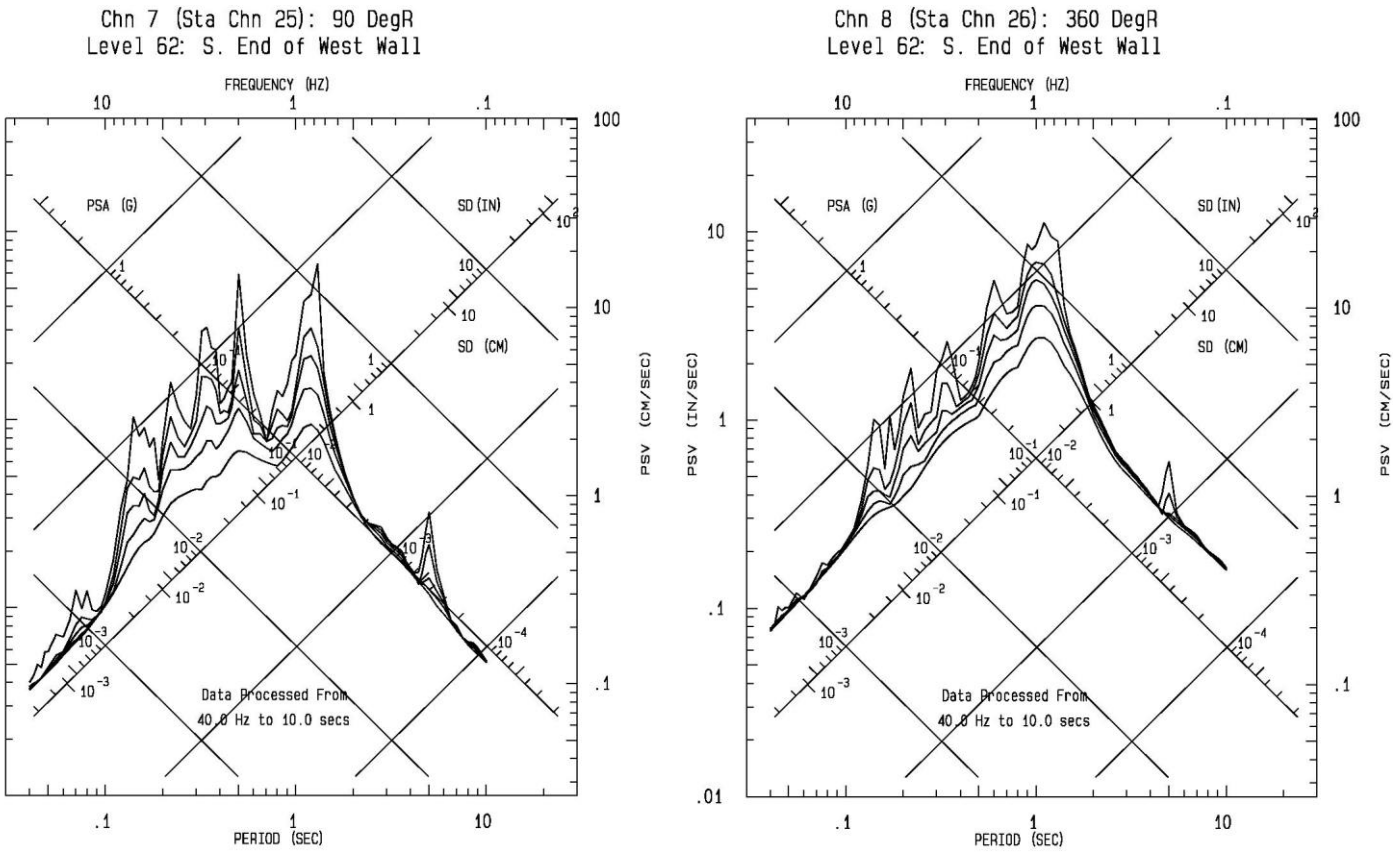

Figure 17. Tripartite response spectra plot of the M4.4 Berkeley earthquake records from the Sensors 25 and 26 at Level 62 of the Salesforce Tower. Building fundamental period of 5 seconds in each direction can be seen on the plots.

Summary

The Wilshire Grand Tower in Los Angeles and Salesforce Tower in San Francisco are two new super tall buildings in California. They have been extensively instrumented jointly by the owners and the California Strong Motion Instrumentation Program. The ambient data from the Wilshire Grand Tower show that the fundamental period is about 6.0 seconds in the transverse direction and 3.4 seconds in the longitudinal direction. The ambient data from the Salesforce Tower show that the fundamental period is about 5.0 seconds in both directions. The data recorded at Salesforce Tower show that the fundamental mode was hardly excited by the M4.4 Berkeley earthquake of January 4, 2018.

The building description and the sensor location diagrams for these two super tall buildings are included in the Center for Engineering Strong Motion Data (CESMD) at https://www.strongmotioncenter.org Ambient vibration data from these two building and the strong-motion data from the Salesforce Tower are available at the CESMD Data Center.

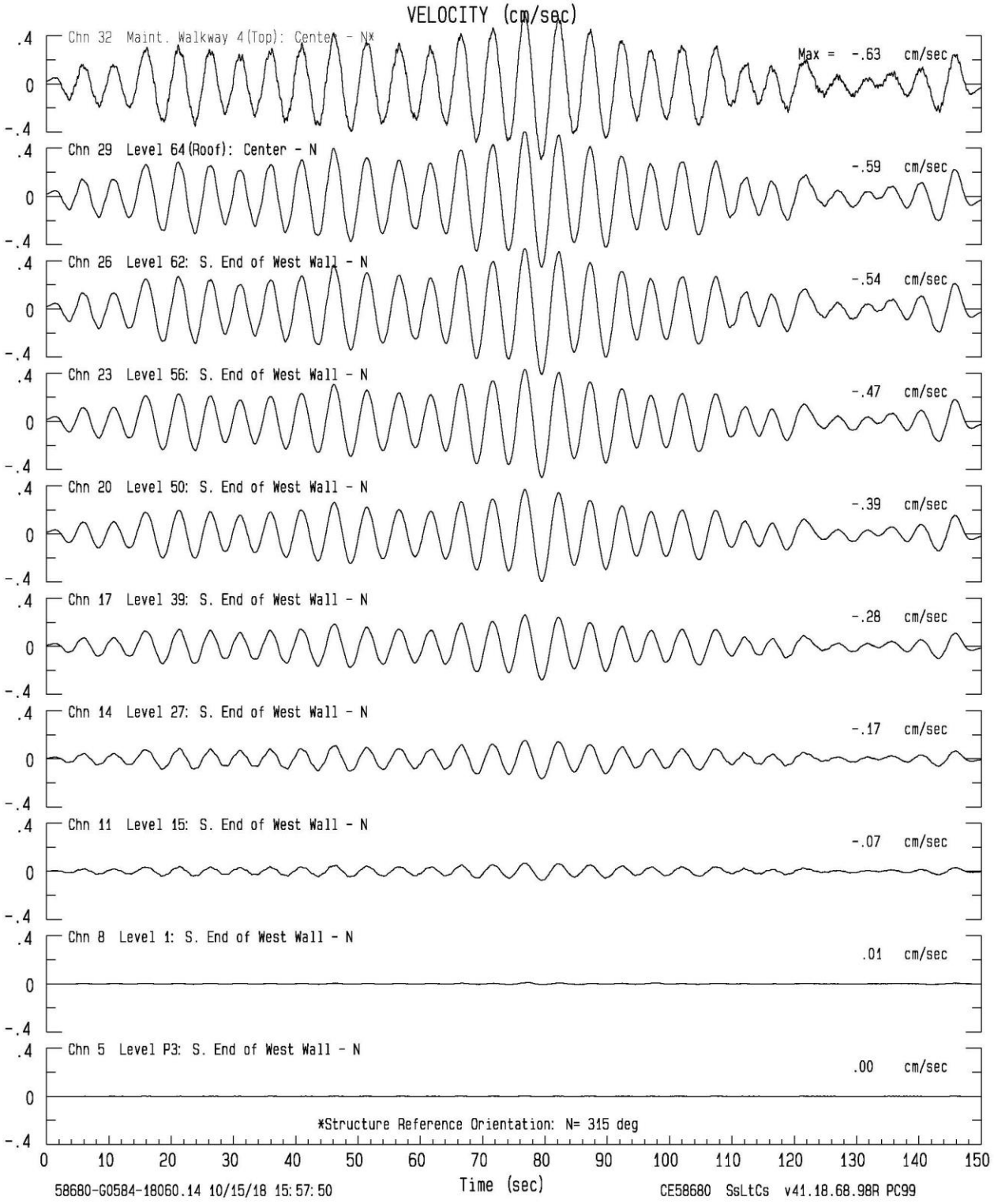

Figure 18. Velocities integrated from the ambient acceleration data from sensors in the north-south direction at ten instrumented levels of the Salesforce Tower.

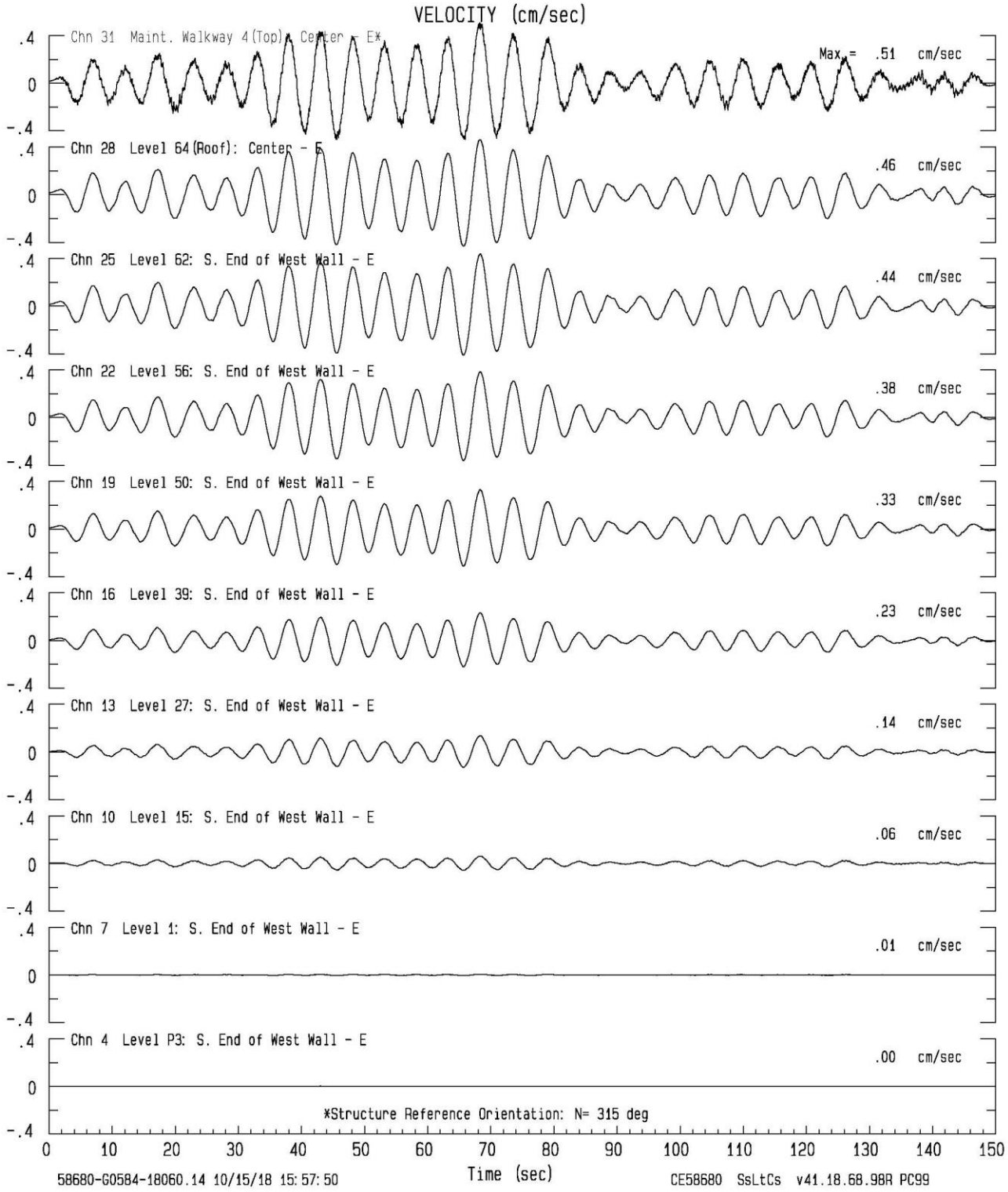

Figure 19. Velocities integrated from the ambient acceleration data from sensors in the east-west direction at ten instrumented levels of the Salesforce Tower.

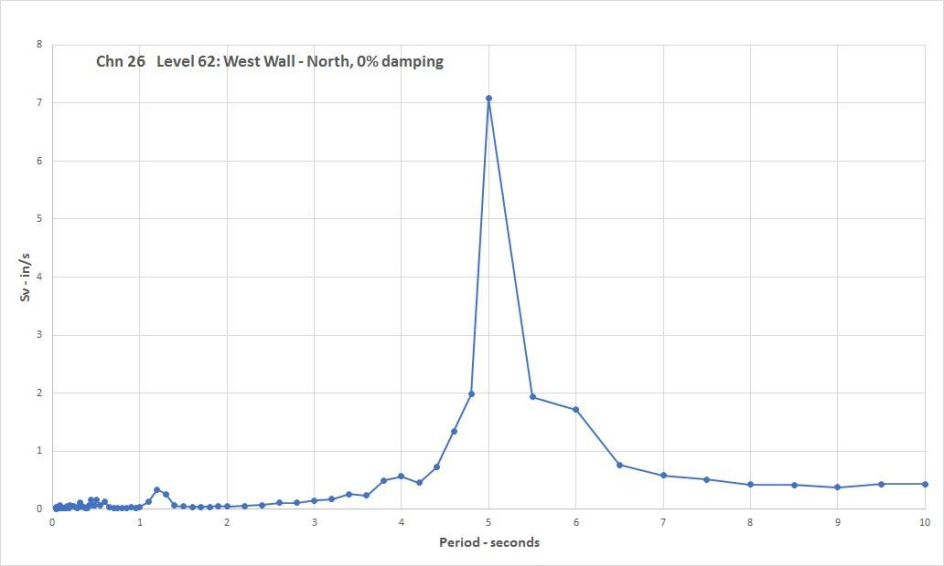

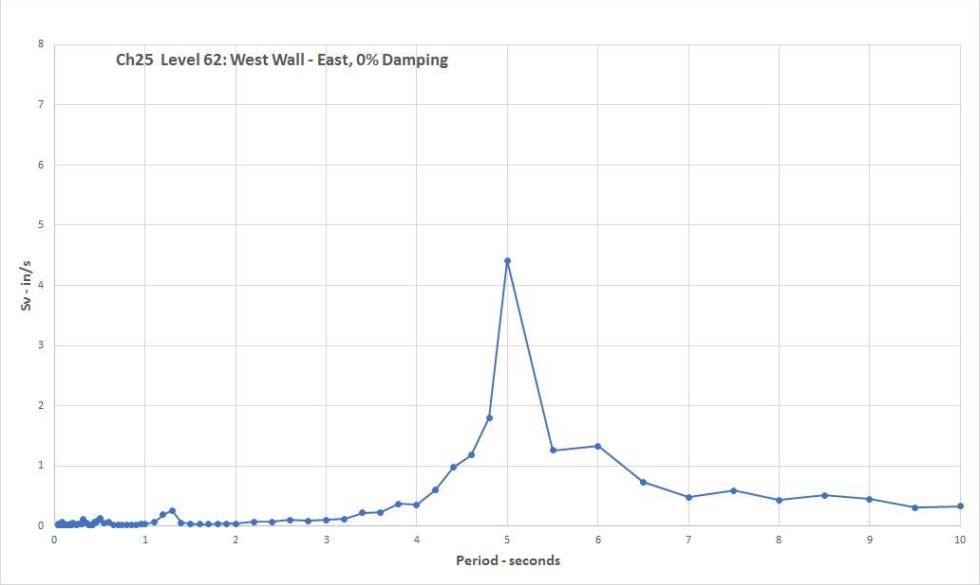

Figure 20. Zero percent damping velocity response spectra (Sv) of the ambient data from Sensor 26 (NS direction) and Sensor 25 (EW direction) on Level 62 of the Salesforce Tower.

Acknowledgements

The California Strong Motion Instrumentation Program of the California Geological Survey, Department of Conservation extends its appreciation to the owners who permitted and cooperated in the installation of strong-motion equipment in the Wilshire Grand Tower and the Salesforce Tower. The instrumentation efforts by CSMIP were directed by the Program Manager Dr. Tony Shakal and the Field Operations Manager Carl Petersen who retired at the end of 2017. CSMIP also extends its appreciation to members of the Strong Motion Instrumentation Advisory Committee and its Buildings Subcommittee for recommending the buildings for

instrumentation. Dr. Farzad Naeim of Farzad Naeim Inc. reviewed and commented on the sensor locations proposed by CSMIP. Josh Gebelein of Brandow & Johnston and Michael Valley of Magnusson Klemencic Associates assisted CSMIP in obtaining permission from the owners and reviewed the sensor locations.

References

Celebi, M., Huang, M., Shakal, A., Hooper, J., and Klemencic, R. 2012, "Ambient Response of a Unique Performance-Based Design Building with Dynamic Response Modification Features," *Proceedings of SMIP12 Seminar on Utilization of Strong-Motion Data,* Sacramento, California, October 2, 2012, p. 97-109.

Joseph, Leonard M., Gulec, C. Kerem, and Maranian, Peter J., 2014, "Performance Based Design of The Wilshire Grand Tower Los Angeles, California, USA," *Proceedings of the 2014 Annual Meeting of the Los Angeles Tall Buildings Structural Design Council,* p. 1-22.

Joseph, Leonard M., Gulec, C. Kerem, and Maranian, Peter J., 2015, "Performance Based Design of Wilshire Grand Tower," *2015 SEAOC Convention Proceedings,* p. 290-311.

Joseph, Leonard M., Gulec, C. Kerem, and Schwaiger, Justin M., 2016, "Wilshire Grand: Outrigger Designs and Details for a Highly Seismic Site," *International Journal of High-Rise Buildings,* March 2016, Vol. 5, No. 1, p.1-12.

Klemencic, Ron, Valley, Michael, and Hooper, John, 2017, "Salesforce Tower, New Benchmark in High-Rise Seismic Safety," in STRUCTURE magazine, June 2017, p. 44-48.

Los Angeles Tall Buildings Structural Design Council (LATBSDC), 2011, "An Alternative Procedure for Seismic Analysis and Design of Tall Buildings Located in the Los Angeles Region," 2011 Edition, May 2011.

Naeim, Farzad, 2013, "Instrumentation Requirements for Tall Buildings per the Los Angeles Tall Buildings Structural Design Council 2011 Alternative Analysis and Design procedure," *Proceedings of SMIP13 Seminar on Utilization of Strong-Motion Data,* p. 85-99.

Nieblas, Gerard M., 2014, "Reaching New Heights in Los Angeles," in STRUCTURE magazine, December 2014, p. 20-23.

Nieblas, Gerard M., and Phuoc Tran, 2015, "Wilshire Grand," in STRUCTURE magazine, August 2015, p. 34-36.

Valley, Michael, Klemencic, Ron, and Hooper, John, 2014, "Design of Transbay Tower, San Francisco, California," *Proceedings of the 2014 Annual Meeting of the Los Angeles Tall Buildings Structural Design Council*.